

Long-term dry storage: Temperature profiles in a cask and impact on the hydrogen behaviour in the cladding

Marc Péridis

Vollständiger Abdruck der von der TUM School of Engineering and Design der Technischen Universität München zur Erlangung eines

Doktors der Ingenieurwissenschaften (Dr.-Ing.)

genehmigten Dissertation.

Vorsitz:

Prof. Dr. rer. nat. Rudolf Neu

Prüfer*innen der Dissertation:

1. Prof. Dr. Rafael Macián-Juan
2. Prof. Dr.-Ing. Jesús Ruíz-Hervías
3. Prof. Dr.-Ing. Rafael Miró Herrero

Die Dissertation wurde am 26.09.2022 bei der Technischen Universität München eingereicht und durch die TUM School of Engineering and Design am 11.07.2023 angenommen.

Contents

Acknowledgement	vii
Publications and presentations	xi
Abstract	xv
1 Introduction and motivation of this thesis	1
1.1 Dry storage of spent nuclear fuel	1
1.2 Scope of the thesis	5
2 Temperature fields in storage casks	7
2.1 Introduction	7
2.1.1 Heat transfer mechanisms	7
2.1.1.1 Conduction	7
2.1.1.2 Convection	14
2.1.1.3 Thermal radiation	15
2.1.2 View factors and Hottel’s crossed strings method	19
2.2 Semi-analytical cask model	24
2.2.1 Cask design	24
2.2.2 Model description	26
2.2.3 Model results	30
2.2.4 Sensitivity analysis	34
2.2.5 Summary on the Python model	43
2.3 COBRA-SFS CASTOR [®] V/19 model	44
2.3.1 Short description of the thermal-hydraulic code COBRA-SFS	44
2.3.2 Model description	46

2.3.3	Model validation: code comparison	49
2.3.4	Comparison of the COBRA-SFS and Python models . .	54
2.3.5	Sensitivity analysis	58
2.3.6	Temperature calculation results	65
2.3.6.1	Cask homogeneously loaded with 39 kW	65
2.3.6.2	Drying process	66
2.3.6.3	Temperature evolution over 100 years of storage	68
2.3.6.4	Cask with inhomogeneous loading schemes . . .	70
2.3.7	Summary on the COBRA-SFS CASTOR model	75
2.4	COBRA-SFS TN-32B model	78
2.4.1	Model description	78
2.4.2	Temperature calculation results	82
2.4.2.1	Base case calculation	83
2.4.2.2	Sensitivity analysis	89
2.4.3	Summary on the TN-32B model	94
2.5	Conclusion - Temperature fields in storage casks	95
3	Hydrogen and hydride behaviour	97
3.1	Introduction	97
3.1.1	Cladding oxidation, hydriding and embrittlement	97
3.1.2	Hydrogen solubility - TSS_P & TSS_D	103
3.1.3	Diffusion mechanisms	109
3.1.4	Hydrogen diffusion in the fuel cladding	114
3.2	TSS_P/TSS_D plots and correlations	116
3.2.1	Database and uncertainties	116
3.2.1.1	Cladding materials	119
3.2.1.2	Measurement methods	121
3.2.2	ODR method	124
3.2.3	Analysis and discussion	127
3.2.4	Summary on the TSS_P/TSS_D database	133
3.3	HNGD Model	134
3.3.1	Model description	134
3.3.2	Model verification	140
3.3.3	Summary on the HNGD model	147
3.4	Hydrogen and hydride profiles - Predictions for full-length rods	148

3.4.1	Basic assumptions	148
3.4.2	Implementation of the diffusion in the model	149
3.4.3	Cladding configuration at the beginning of the dry storage	151
3.4.4	Hydrogen and hydride profiles over 100 years of storage	155
3.4.5	Hydrogen and hydride profiles over 100 years of storage with an increased diffusion coefficient	166
3.4.6	Hydrogen and hydride profiles after 100 years of storage for different diffusion coefficients	174
3.4.7	Summary on the hydrogen diffusion in a full-length rod	180
3.5	Conclusion - Hydrogen and hydride behaviour	182
4	Conclusion and outlooks	185
5	Appendices	193
5.1	View factors	193
5.1.1	2-dimensional	193
5.1.2	3-dimensional	194
5.2	Hottel's crossed strings method [26].	195
5.2.1	Implementation with Python	197
5.3	Python semi-analytical model	199
5.4	Python model, sensitivity analysis	206
5.5	Construction of a COBRA-SFS cask model	216
5.6	COBRA-SFS input groups - Writing of an input file	220
5.6.1	Group PROP	220
5.6.2	Group CHAN	221
5.6.3	Group RODS	223
5.6.4	Group SLAB	225
5.6.4.1	Solid-to-solid connections	226
5.6.4.2	Solid-to-fluid connections	228
5.6.5	Group RADG	229
5.6.6	Group HEAT	232
5.6.7	Group DRAG	233
5.6.8	Group BDRY	234
5.6.9	Group OPER	238
5.6.10	Group REST	238

5.6.11 Groups CALC and OUTFP	239
5.7 COBRA-SFS model verification	240
5.8 COBRA-SFS output - Verification of the node connections . .	248
List of Figures	251
List of Tables	261
Nomenclature	263
Bibliography	269

Acknowledgement

Als Erstes möchte ich mich bei Dir, Maik, bedanken, für alles, was Du in den letzten 5 Jahren für mich gemacht hast. Ohne Dich hätte ich meine Promotion weder angefangen, noch zu Ende gebracht. Als ich an mir und meiner Arbeit gezweifelt habe, konntest Du immer den richtigen Schub oder positiven Druck einsetzen, damit ich weiter *nach Vorne* schaue und vorankomme. Deine Ratschläge habe ich sehr geschätzt und erfolgreich einsetzen können, und Deine gute Laune und stete Energie haben Dich zu einem wertvollen Alltagskollegen gemacht. Vielen lieben Dank für alles!

Then, I would like to thank Prof. Macián-Juan, for accepting me as external PhD student at the Chair of Nuclear Technology. Thank you for always being available for support of any kind, and for all the interesting discussions and useful advice.

My sincere thanks to Prof. Neu, Prof. Ruíz-Hervías and Prof. Miró Herrero for accepting to read and comment this thesis, and to be part of the examination board.

I also thank the Federal Ministry for Economic Affairs and Climate Action for funding part of my work through the GRS projects RS 1552 and RS 1588.

Ich bedanke mich auch bei meinen ehemaligen GRS Kollegen, für die angenehme und erfolgreiche Zusammenarbeit. Einen besonderen Dank an Felix (es war schön, zusammen TUM Doktorand zu sein!), Matthias (Danke für Deine Geduld und Hilfe mit ParaView, und für die schönen Bilder, wie Fig. 2.33) und Peter (für die fachlichen Gespräche, und vor allem für die Ski-, Lauf- und Kletter-Termine!).

My grateful thanks to David Richmond, main developer of COBRA-SFS at PNNL. I really appreciated your help with COBRA-SFS and the numerous constructive discussions.

Ich bedanke mich bei Dr. Klaus-Jürgen Brammer und Dr. Jörn Becker von der BGZ, die mich in der Endphase meines Promotionsprojektes gut unterstützt haben, sowie bei den Abteilungen TBI und TZF für die gute Integration trotz der Pandemie-bedingt schwierigen Umstände bei meiner

Einstellung.

J'en viens ensuite à tous ceux qui m'ont aidé, de manière peut-être moins directe mais non moins importante.

Je commence par quelques professeurs dont les enseignements m'ont permis d'en arriver là où je suis aujourd'hui.

Pascale, merci de m'avoir accompagné tout au long de mes études, merci pour ta douceur, ta gentillesse, ta bonne humeur, ta bienveillance. Depuis plus de 20 ans, grâce à toi, le piano a toujours été là pour m'apporter détente et plaisir, réconfort dans les moments difficiles. Un grand merci également à Laurence, pour toutes ces belles années de hautbois.

Merci à Aline Degen, qui a su faire naître en moi une vraie passion pour l'Allemagne et la langue de Goethe. Je remercie également Mme Lépori et M. Klein, qui m'ont remarquablement bien préparé à ma vie en Allemagne. Enfin, si j'ai pu rédiger cette thèse, c'est bien sûr grâce à l'enseignement scientifique dont j'ai bénéficié. Je tiens à remercier Paul Roux, mon professeur de physique en MP* au lycée Fauriel, dont les cours passionnants m'auront encore bien servi pendant ce doctorat. Last but not least, je remercie Pierre-Jean Hormière, collègue mathématicien de Paul Roux. Pierre-Jean, merci pour tout ce que vous m'avez apporté : de la topologie du groupe orthogonal au manifeste pour l'UMP, des théorèmes les plus abstraits aux digressions les plus variées, vos cours ont été un délice et le berceau d'une précieuse amitié.

Je continue avec la longue liste des amis, rencontrés à différentes étapes de mon parcours.

Loïc, le premier, mon pote de la maternelle, celui qui depuis plus de 20 ans ne rate jamais un 26 février ! Depuis toutes ces années, j'ai la chance de pouvoir compter sur ce lien solide et je te remercie pour cette longue amitié. Merci à Héloïse, Julie, Marie et Sarah, qui depuis nos années de lycée sont restées de fidèles amies.

Merci aux potes de prépa : Morgan (meilleur binôme !) et Jenn, Merlin (merci de me pardonner chaque 10 septembre) et Fleur, Duch et Mathilde, Cloclo, Quentin (meilleur 5/2 !), Arthur (meilleur 3/2 !), Maxence, Estelle et Dimitri.

Merci aux ENSTA : Agathe, Aiky, Claire, Clémentine, Damien, Gabriele, Héloïse, Hugo, Léa, Nary et Sergio, pour les Zoom Covid et tous les week-ends et voyages que j'espère encore nombreux. Benjamin, Brendan, Elliot, Maxence et Romain, pour les Hauts Faits du BDA et la postérité non moins remarquable. Et Jasmine, pour être une marraine en or depuis mon entrée à l'ENSTA, et toujours là quand il faut depuis !

Vielen Dank an die Eisbabies für die regelmäßigen, erfrischenden Termine, sowie an alle Hechte für die schöne Zeit! Und Danke an Dich, Felix, für deine stete und wertvolle Unterstützung. Mei Herz schlogt boarisch!

Enfin, je remercie bien sûr ma famille, sans qui je ne serais jamais arrivé jusqu'ici. Merci à mes parents de m'avoir permis de faire les études que j'ai faites, ainsi que toutes les activités periscolaires, et merci de m'avoir toujours encouragé, soutenu et conseillé aux bons moments. Merci à Liliane, d'avoir pris soin de moi toute mon enfance. Et enfin, merci à ma soeur, Sarah. J'espère être un frère à peu près à la hauteur, en tout cas je n'aurais pu souhaiter meilleure soeur. Merci pour tout ce que tu m'as apporté !

Publications and presentations

Part of the results presented in this thesis have been published in the following articles, proceedings and reports (except for the EPJ-N article on muon radiography). These results have been presented and discussed at different conferences and events. The corresponding posters and oral presentations are listed below.

Journal articles

- T. Braunroth, N. Berner, F. Rowold, **M. Péridis** and M. Stuke: Muon radiography to visualise individual fuel rods in sealed casks, *European Physical Journal N*, Vol. 7 (12), 2021.
- **M. Péridis** and M. Stuke: Comparison of numerical and semi-analytical analyses of temperature fields of loaded dry casks, *Kern-technik* 85 (6), pp. 444-451, 2020.
- F. Boldt, **M. Péridis** and M. Stuke: SEDS benchmark for fuel rod behaviour during dry storage - preliminary results, *Kern-technik* 85 (6), pp. 426-432, 2020.
- P. Kaufholz, M. Stuke, F. Boldt and **M. Péridis**: Influence of kinetic effects on terminal solid solubility of hydrogen in zirconium alloys, *Journal of Nuclear Materials*, Vol. 510 (10), pp. 277-281, 2018.

Proceedings

- **M. Péridis**, F.-N. Sentuc, M. Sonnenkalb, J. Stewering and M. Stuke: Analysis of 3-Dimensional Temperature Fields of Loaded Dry Storage Casks, *Proceedings of the 19th International Symposium on the Packaging and Transportation of Radioactive Materials, PATRAM 2019*, New Orleans, LA, USA, August 4-9, 2019.

- F. Boldt, P. Kaufholz, **M. Péridis**, H.-G. Sonnenburg and M. Stuke: Research activities at GRS on fuel rod behaviour during extended dry storage, Kerntechnik 83 (6), pp. 476-483, 2018.
- F. Boldt, K. Hummelsheim, **M. Péridis**, F. Rowold and M. Stuke: Safety of long-term dry storage in Germany - Challenges and Perspectives, EUROSAFE 2017, 2017.

Technical reports

- M. Stuke, J. Arndt, F. Boldt, V. Hannstein, P. Kaufholz, **M. Péridis**, J. Sievers and F. Sommer: Langzeitverhalten zwischengelagerter Brennelemente bei deutlich längerer Zwischenlagerung, Report GRS-554, ISBN 978-3-947685-39-4, 2020.
- M. Stuke, F. Boldt, V. Hannstein, P. Kaufholz, **M. Péridis**, F. Sommer and H.-G. Sonnenburg: Langzeitverhalten zwischen-gelagerter Brennelemente bei deutlich längerer Zwischenlagerung (Zwischenbericht), Report GRS-534, ISBN 978-3-947685-19-6, 2018.

Posters¹

- **M. Péridis**, F.-N. Sentuc, M. Sonnenkalb, J. Stewering, M. Stuke: Analysis of 3-dimensional temperature fields of loaded dry storage casks, PATRAM 2019, 4-9 August, New Orleans, LA, USA.
- **M. Péridis**, R. Kilger, M. Sonnenkalb, J. Stewering, M. Stuke: Detailed temperature fields in loaded dry storage casks, NuMat 2018, 14-18 October, Seattle, WA, USA.
- F. Boldt, B. Grimaldi, P. Kaufholz, **M. Péridis**, M. Stuke: Statistical Analysis of Experimental Data on Terminal Solid Solubility of Hydrogen in Zr-Alloys, NuMat 2018, 14-18 October, Seattle, WA, USA.

¹The presenter is underlined.

Oral presentations

- **M. Péridis:** Hydrogen diffusion and precipitation at the scale of a full-length rod in dry storage conditions, 6th GRS Workshop on Safety of Extended Dry Storage (SEDS2022), GRS gGmbH, 02.06.2022, Garching, Germany.
- **M. Péridis:** Temperature profiles in a cask and impact on the hydrogen behaviour in the cladding, BGZ Studierendentag, BGZ Gesellschaft für Zwischenlagerung mbH, 05.05.2022, Essen, Germany.
- **M. Péridis, M. Stuke:** Update on GRS modeling work using COBRA-SFS, EPRI Extended Storage Collaboration Program (ESCP) International Thermal Modeling Benchmark, 03.02.2021, virtual meeting.
- **M. Péridis, M. Stuke:** Status update on GRS modeling work using COBRA-SFS, EPRI Extended Storage Collaboration Program (ESCP) International Thermal Modeling Benchmark, 08.10.2020, virtual meeting.
- **M. Péridis, M. Stuke:** Cladding temperature in storage casks, 4th GRS Workshop on Safety of Extended Dry Storage (SEDS2020), GRS gGmbH, 03.06.2020, virtual meeting.
- **M. Péridis:** Hüllrohrtemperaturen in Zwischen- und Endlagern, Nuclear Science Café, GRS gGmbH, 14.02.2020, Garching, Germany.
- **M. Péridis, M. Küntzel, M. Stuke:** Temperature Fields in Loaded Used Fuel Casks, 3rd GRS Workshop on Safety of Extended Dry Storage (SEDS2019), GRS gGmbH, 06.06.2019, Garching, Germany.

Abstract

Many countries around the world are currently facing the extension of the interim dry storage of spent nuclear fuel. The proper assessment of the cladding integrity over periods up to 100 years is a challenging but necessary task, including the determination of reliable and detailed temperature distributions and the prediction of the evolution of the cladding materials, in particular with regard to the mechanical properties.

The first objective of this thesis, treated in Chapter 2, was to provide realistic, time-dependent and detailed temperature distributions in storage casks. This was achieved by the development of three cask models: the first one was built using Python and based on the German CASTOR[®] V/19, while the other models were built using the thermal-hydraulic code COBRA-SFS and represented the CASTOR[®] V/19 and a TN-32B. We performed sensitivity analyses on all models, which highlighted the influence of particular parameters on the temperature distributions: the ambient temperature, the fuel assembly decay heats and the gaps between the different structure elements of the cask. We simulated various scenarios, including steady-state calculations (temperature distributions for different loading schemes and boundary conditions) and transients (accidental scenarios, drying process, daily variations of the ambient temperature).

The second objective of the thesis, treated in Chapter 3, consisted in the analysis of the hydrogen and hydride behaviour in the cladding under dry storage conditions. We analysed a database on the Terminal Solid Solubility (TSS_P/TSS_D) of hydrogen in zirconium alloys and derived correlations for the solubility limits depending on the different cladding materials and measurement methods. We observed that the distinction between TSS_P and TSS_D seems to be related to high cooling rates in experiments, which support recent new interpretations of the TSS_P limit.

Furthermore, we implemented in Python a model for precipitation and dissolution of hydrides (HNGD model), compared simulation results with the original description of the model, and discussed the discrepancies.

Finally, using temperature results from Chapter 2, we developed a model us-

ing Python to simulate the hydrogen diffusion and the hydride precipitation at the scale of a full rod, depending on temperature and time. We observed that the axial temperature profiles of the fuel rod is likely to lead to the diffusion of hydrogen toward both ends of the cladding and therefore to the accumulation of hydrides in these regions. The lack of experimental data on diffusion at these scales (time and space) does not enable any model validation at this point. However, the results achieved with the current model suggest that an increased risk of embrittlement should be considered for the upper and lower end of the fuel rods, especially for fuel assemblies presenting a high decay heat at the beginning of the storage and a low radioactive decay (e.g. high burnup MOX).

Zusammenfassung

Viele Nationen sehen sich vor der Herausforderung, die trockene Zwischenlagerung bestrahlter Brennelemente über ursprünglich geplante Zeiträume hinaus durchführen zu müssen. Die sorgfältige Prüfung der Hüllrohrintegrität über lange Zeiträume wie 100 Jahre ist eine anspruchsvolle, aber notwendige Aufgabe, die die Bestimmung von zuverlässigen und detaillierten Temperaturfeldern, sowie die Vorhersage der Entwicklung der mechanischen Eigenschaften des Hüllrohrmaterials einschließt.

Das erste Ziel dieser Dissertation war, realistische, zeitabhängige und detaillierte Temperaturverteilungen in beladenen Behältern zu diskutieren. Dies wird in Kapitel 2 anhand von 3 Behältermodellen diskutiert. Das erste Rechenmodell wurde mit Python erstellt und basiert auf dem in Deutschland verbreiteten CASTOR[®] V/19. Zwei weitere Modelle wurden für das thermohydraulische Rechenprogramm COBRA-SFS erstellt. Dabei wurde neben dem CASTOR[®] V/19 auch das Modell eines TN-32B diskutiert. Zu allen Modellen wurden Sensitivitätsanalysen durchgeführt um den Einfluss von bestimmten Eingangsparametern auf die Temperaturverteilungen zu untersuchen. Die Parameter umfassten die Umgebungstemperatur, Nachzerfallswärmeleistung und Abstände zwischen verschiedenen Strukturelementen des Behälters. Ebenfalls wurden verschiedene Szenarien simuliert,

einschließlich steady-state Rechnungen (Temperaturverteilungen für unterschiedliche Beladungen und Randbedingungen) und Transienten (Unfall-szenarios, Trocknungsprozess, tägliche Temperaturschwankungen).

Das zweite Ziel der Dissertation besteht aus der Analyse des Wasserstoff- und Hydridverhaltens im Hüllrohr unter typischen Bedingungen der trockenen Zwischenlagerung und wird im Kapitel 3 behandelt. Eine Datenbank zur Wasserstofflöslichkeit (der sog. *Terminal Solid Solubilities TSS_P und TSS_D*) in Zirkonium Legierungen wurde analysiert und Korrelationen für die Löslichkeitsgrenzen in Abhängigkeit des Hüllrohrmaterials und Messverfahrens hergeleitet. Die Interpretation der Ergebnisse lässt den Schluss zu, dass eine Unterscheidung zwischen TSS_P und TSS_D nur mit hohen Abkühlraten erklärt werden kann. Dies unterstützt neue Interpretationen der TSS_P Grenze.

Zur genaueren Untersuchung haben wir mit Python ein Modell zur Ausscheidung und Auflösung von Hydriden (das sog. HNGD Modell) implementiert und erweitert. Die Simulationsergebnisse wurden mit der originalen Beschreibung des Modells verglichen und Abweichungen diskutiert. Basierend auf den Temperaturfeldern aus Kapitel 2 wurde ein Modell entwickelt um die Wasserstoffdiffusion und Hydridausscheidung eines ganzen Brennstabs in Abhängigkeit von der Temperatur und Zeit zu simulieren. Ein Ergebnis ist, dass das axiale Temperaturprofil des Brennstabs zur Wasserstoffdiffusion zu den Hüllrohrenden führen kann. Dadurch kann eine Anhäufung von Hydriden in diesen Regionen entstehen. Der Mangel an experimentellen Daten zur Diffusion auf diesen Ebenen (Zeit und Raum) ermöglicht momentan keine Modellvalidierung. Die mit dem aktuellen Modell erreichten Ergebnisse weisen jedoch darauf hin, dass in zukünftigen Analysen die Brennstabenden näher betrachtet werden sollten.

1 Introduction and motivation of this thesis

1.1 Dry storage of spent nuclear fuel

Most nuclear reactors around the world are Light Water Reactors (LWR), which mainly include two types of reactors: Pressurized Water Reactors (PWR) and Boiling Water Reactors (BWR) [1]. Although important differences of design exist between PWR and BWR (number of loops, steam generators, temperature and pressure conditions), they also share some common characteristics:

- They are based on nuclear fission by thermal neutrons.
- Light water¹ is used as neutron moderator.
- Light water is also used as coolant.
- Low-enriched (3% to 5%) uranium oxide or mixed oxide (MOX², consisting of uranium and plutonium) is used as nuclear fuel.
- Nuclear fuel consists in fuel assemblies, bundles of fuel rods containing the fissile material.

LWR fuel assemblies are organized in square patterns, usually 10x10 rods for BWR and 15x15 to 18x18 rods for PWR, and measure around 4 m in height. Each fuel rod consists of a stack of oxide pellets (each measuring around 1 cm in length and 1 cm in diameter) enclosed in a zirconium alloy

¹We precise here *light water* to underline the difference between reactors using (normal) H₂O water, e.g. PWR and BWR reactors, and reactors using deuterium oxide D₂O, or *heavy water*, e.g. the Canadian CANDU reactors.

²Mixed oxide fuel: MOX fuel consists of plutonium oxide and uranium oxide.

tube, the cladding. The cladding has several functions to fulfil: constitute the first safety barrier³, enable the nuclear reaction (low neutron absorption and constant geometry) and efficiently transfer the heat to the coolant. The containment function of the cladding remains of highest importance after reactor operation, when the fuel is being stored. [2]

After being unloaded from a reactor core, nuclear fuel assemblies are still generating heat (decay heat). The decay power follows an exponential decrease and is particularly high during the first years of storage. As water is very efficient for heat removal, spent fuel assemblies are first wet-stored for a few years in cooling ponds. Afterwards, they can be either reprocessed in dedicated facilities (in China, France, Japan, Russia and the UK for instance) or further stored until transfer to a final repository (once-through fuel cycle). [3]

If no reprocessing is foreseen, two main ways can be distinguished for the interim storage: dry storage or wet storage. Both options offer advantages and drawbacks, and the nuclear countries around the world chose one of those options, or in some cases both. The characteristics of dry and wet storage are listed and discussed in an IRSN report [3].

In the case of dry storage, fuel assemblies are loaded and dried in casks and subsequently placed in storage facilities. Those facilities have time-limited licenses (for instance 40 years in Germany⁴) and deep geological final repositories were expected to become available on time for the transfer of the spent fuel assemblies to their final destination. However, most countries encounter difficulties to define a location and a concept for the final repository. This leads to the necessary extension of the interim storage and requires further investigations to understand and describe the long-term behaviour and degradation effects. [4]

Figure 1.1 gives an overview of the fuel life cycle depicting the above-mentioned steps. An important feature with regard to the cladding degrada-

³Three barriers are usually identified which aim at ensuring the safe enclosure of radioactive material in a power plant: the fuel cladding, the reactor vessel/first loop and the reactor building.

⁴The license duration starts with the emplacement of the first cask. The first German CASTOR[®] cask has been emplaced in April 1995 at the interim storage facility of Gorleben. The license for this facility is thus valid until 2034.

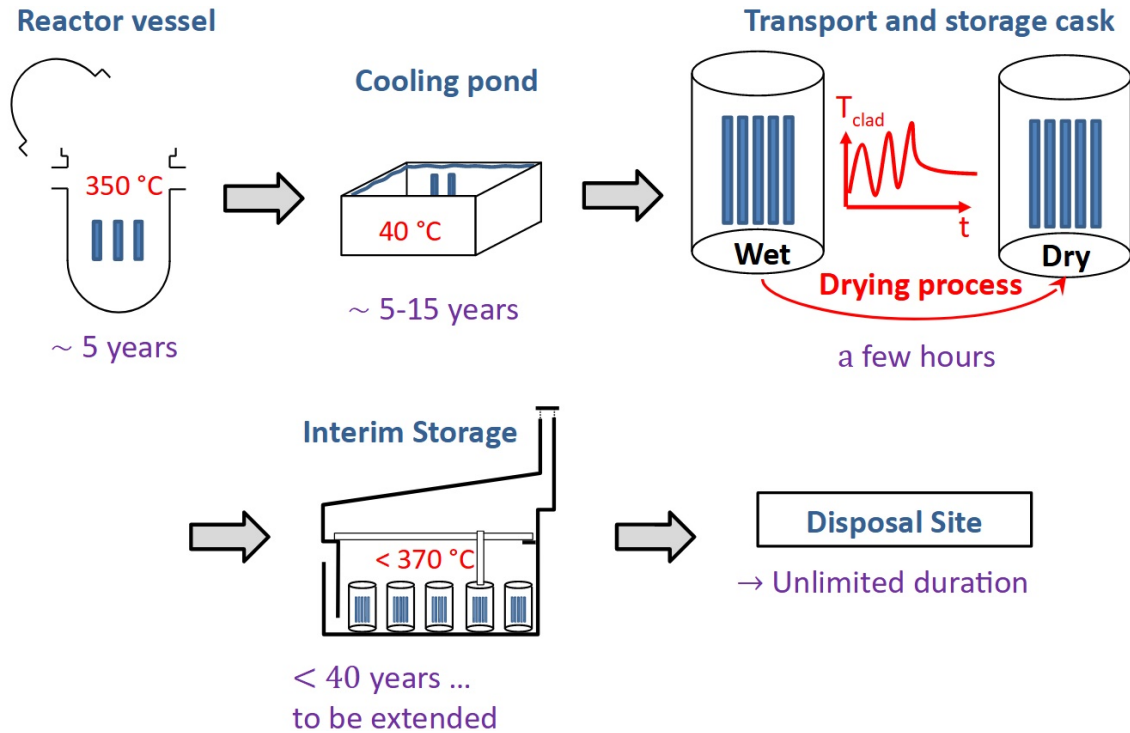


Figure 1.1: Overview of the temperature range and time scales involved over the fuel assembly life.

tion mechanisms are the various temperature and time scales appearing on this diagram, involving different boundary conditions: wet vs. dry storage, 40 °C vs. 350 °C , pseudo steady-state for several years vs. transient over a few hours. This is a major concern for the assessment of the fuel rod integrity as all major long-term material degradation effects are temperature dependent. [5–7]

The ductile-to-brittle transition temperature (DBTT, see Figure 1.2) is one of them. At low temperatures, the cladding follows a brittle behaviour which means that it can easily break even at low impact energy, e.g. in case of a mechanical shock. At higher temperatures, the cladding is more ductile and can undergo deformations and thus absorb more energy prior to failure. With the extension of the interim storage, lower cladding temperatures are expected and therefore a higher susceptibility to embrittlement.

The hydride precipitation and reorientation is a further major issue for the fuel rod integrity. During reactor operation, an oxide layer forms on the

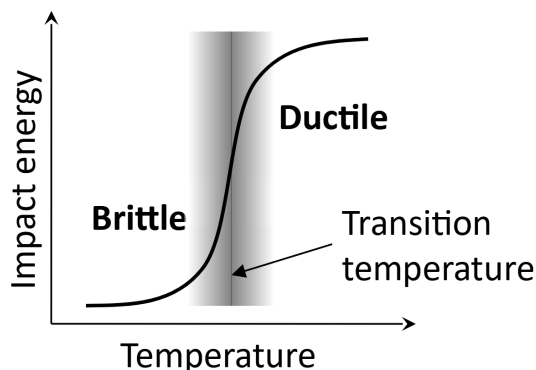


Figure 1.2: Ductile-to-Brittle Transition Temperature (DBTT). The curve depicts the absorbable impact energy prior to failure with regard to the temperature. The limit between the brittle domain (low temperature) and the ductile domain (high temperature) is marked using a grey band, as it consists in a transition involving a temperature range rather than in a clear limit at a specific temperature.

outer surface of the cladding. The oxidation reaction generates hydrogen, part of which is absorbed by the cladding. Thus, the hydrogen concentration in the zirconium alloy increases progressively and eventually leads to the formation of brittle hydrides. Hydrogen solubility and hydride precipitation strongly depend on absolute temperature values, as well as on heating and cooling kinetics [8–10]. Different types of hydrides might form in the cladding, depending on the thermal and mechanical history [11–14], which can then threaten the cladding integrity because of crack propagation assisted by hydrides. Thus, a detailed knowledge of the cladding temperature is desirable throughout the entire storage period. Table 1.1 summarizes the temperature and related phenomena expected at the different steps of the fuel assembly life.

Predicting a reliable temperature field for a loaded cask is a challenging task, as there are only few experimental data publicly available to validate the calculation models. Some of the data relevant to model a cask is proprietary and not easily accessible. Furthermore, the storage casks have shielding and containment functions to fulfil primary protection goals. Thus, a potential re-opening of a cask for experimental purposes is not straightforward. For all these reasons, the model validation to predict temperature fields of loaded casks remains challenging. [4]

	Reactor	Cooling pond	Cask Drying process	Cask Dry Storage
Temperature	High: 340-380 °C (except shutdowns)	Low: 50 °C	Cycling, short timescale, large temperature range	Initially high, slowly decreasing
Phenomena	<ul style="list-style-type: none"> • Cladding oxidation and H uptake • Hydride precipitation and dissolution (shutdowns, reloading) 	<ul style="list-style-type: none"> • Hydrides remain precipitated, as temperature remains low 	<ul style="list-style-type: none"> • Hydride dissolution, reprecipitation, reorientation • Kinetic effects (dissolution, diffusion) TSSp/TSSd 	<ul style="list-style-type: none"> • Gradual hydride formation, with temperature decrease • Thermo-dynamical equilibrium • Embrittlement

Table 1.1: Main temperature dependent phenomena affecting the cladding at the different steps of the fuel assembly life.

1.2 Scope of the thesis

This thesis aims to provide detailed simulations of the thermal conditions experienced by the spent fuel assemblies dry stored in casks and of the impact on the hydrogen behaviour in the cladding. Furthermore, it gives an insight into the related degradation mechanisms.

Chapter 2 describes the thermal modelling of spent fuel storage systems. It includes an introduction presenting the main heat transfer mechanisms involved, then it presents the different cask models that were developed during the PhD work.

The first one is a semi-analytical model, based on classical physics equations and was built using the programming language Python. This model is inspired by the German CASTOR[®] V/19, the most widely used cask in Germany for the storage of PWR fuel assemblies, designed by GNS⁵. It relies on a few number of homogenized regions only and considers simplified heat transfer exchanges. However, it offers the advantages of being easily adaptable, quick, transparent and able to provide good orders of magnitude of the temperature in the cask.

⁵GNS Gesellschaft für Nuklear-Service mbH is a company owned by energy suppliers (PreussenElektra, RWE, EnBW and Vattenfall) and providing services in the field of nuclear waste management. [15]

To obtain more detailed results, two further models were built using the thermal-hydraulic code COBRA-SFS [16–19]. One is a generic cask model, also inspired by the CASTOR[®] V/19 but fulfilling higher requirements than the semi-analytical model. The second COBRA-SFS model represents a TN-32B cask, designed by Transnuclear Inc., and was developed in the framework of a thermal-hydraulic benchmark organized by the Electric Power Research Institute (EPRI) [20]. Both COBRA-SFS models are highly detailed models, which enable to determine three-dimensional temperature fields for a whole loaded cask.

Chapter 3 describes the hydrogen behaviour in the cladding, in particular with regard to the time-dependent temperature profiles. First, we present some theoretical considerations about hydrogen dissolution and diffusion, and hydride precipitation. Then, a review of experimental work on the Terminal Solid Solubility (TSS) of hydrogen in zirconium alloys is described, including the correlations deduced from the data of the review. Afterwards, a hydrogen/hydride behaviour model (*HNGD model*) developed recently by a research group at the Pennsylvania State University [10, 21] is discussed and reproduced using the programming language Python. Verification cases are performed and the results are discussed.

Finally, temperature profiles derived in Chapter 2 are used as a basis for predictions on hydrogen and hydride behaviour at the scale of full-length rods. The diffusion equation is implemented together with the TSS equation in a simple model to simulate the hydrogen behaviour in the cladding over a long period of time (100 years of interim storage). The results should not be considered quantitatively reliable as long as no experiments are available on hydrogen diffusion at the scale of a full-length rod and over longer time scales. However, the simulations performed give some insight into possible evolutions of the hydrogen distribution in the cladding during the extended dry storage.

Chapter 4 gives outlooks and discusses possible further works. In particular, the mechanical consequences of the thermal history and the related cladding hydridation are discussed.

2 Temperature fields in storage casks

2.1 Introduction

2.1.1 Heat transfer mechanisms

Heat transfers between two systems can occur in three main types of mechanisms: conduction, convection and radiative transfers. In a thermal-hydraulics problem, these mechanisms might contribute to a greater or lesser extend to the heat transfers, depending on the characteristics and boundary conditions of the problem. In the following, these three mechanisms are reviewed and their characteristics briefly presented.

2.1.1.1 Conduction

Conduction consists in a diffusion phenomenon: particles exchange part of their kinetic energy, from neighbour to neighbour, from hotter regions to colder regions (second law of thermodynamics). It necessarily needs a medium (solid, liquid or gaseous) to occur, which constitutes a major difference with radiative transfers. Due to their diffusive nature, conduction heat transfers require longer time in the case of long heat paths. Conduction heat flow in a medium is usually described by the phenomenological Fourier's law, which basically states that the local heat flux \vec{j}_{cond} is proportional to the temperature gradient $\overrightarrow{grad} T$:

$$\vec{j}_{cond} = -\lambda \cdot \overrightarrow{grad} T \quad (2.1)$$

where λ is the thermal conductivity, in $\text{W m}^{-1} \text{K}^{-1}$.

The higher the thermal conductivity is, the better the heat conduction is: a given temperature difference between two points leads to a higher heat flux

(better heat removal) if the medium has a high thermal conductivity. From another point of view: for a given heat flux, a low thermal conductivity is responsible for larger temperature gradients. For instance, the rather low thermal conductivity of UO_2 leads to an important temperature difference between the fuel pellet centre and the pellet surface: for a linear power of 186 W cm^{-1} (normal reactor operation conditions), the temperature in the pellet varies approximately from $510 \text{ }^\circ\text{C}$ (surface) to $920 \text{ }^\circ\text{C}$ (centre), which means a temperature difference of more than $400 \text{ }^\circ\text{C}$ over about 4 mm . For a linear power of 420 W cm^{-1} , the pellet centre temperature rises to $1850 \text{ }^\circ\text{C}$, involving thermal gradients higher than $300 \text{ }^\circ\text{C mm}^{-1}$. [22]

The minus sign in Fourier's law (Eq. 2.1) ensures that the heat flux is directed from hot to cold regions. Table 2.1 gives some examples of thermal conductivities, for different materials and at different temperatures. [23]

Table 2.1: Thermal conductivity λ [$\text{W m}^{-1} \text{K}^{-1}$] of some materials at $20 \text{ }^\circ\text{C}$ and 1 bar [23].

Material	λ	Material	λ	Material	λ
Aluminium	239	Mercury	8.80	Concrete	0.1 - 1.8
Copper	386	Water	0.58	Pyrex	1.30
Silver	419	Ether	0.14	Sand	0.06
Uranium	28	Helium	0.142	PVC	0.19
Inconel	15	Hydrogen	0.168	Polyethylene	0.33 - 0.50
Cast iron	55	Argon	0.016	Wood	0.13 - 0.17
Steel	50	Water vapour	0.016	Cotton wool	0.029
Stainless steel	25	Air	0.024	Glass wool quilt	0.040

Fig. 2.1 gives a simple example of a conduction problem. The system consists of two cylinders: a small cylinder of radius R_1 , in which heat is produced with a volumetric power density p_{vol} , and a larger cylinder of radius R_2 . The height h of the cylinders is arbitrarily defined, but this quantity will not play an important role, as the problem is assumed two-dimensional. The medium between the two cylinders is characterized by a thermal conductivity¹ λ .

Due to the symmetry of the problem, both the temperature and the heat

¹The thermal conductivity is here assumed to be independent of the temperature. Actually, the thermal conductivity usually depends on temperature but this assumption is valid if the temperature range of the problem remains small. Considering the temperature dependence of the thermal conductivity, the differential equations to determine the temperature field in the system become much more complex.

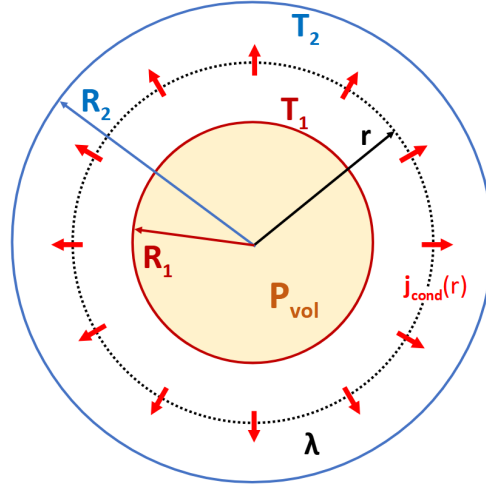


Figure 2.1: Thermal conduction in cylindrical geometry with heat production inside the inner cylinder.

flux are only depending on the radius r . The power \mathcal{P} generated in the inner cylinder is equal to:

$$\mathcal{P} = \pi R_1^2 h \cdot p_{vol}$$

If the system is at thermal equilibrium, the heat generated per unit of time, $\mathcal{P} \cdot dt$, must be equal to the heat evacuated to the environment. Furthermore, as no heat is produced between the two cylinders, the conductive heat flux $j_{cond}(r)$ integrated on any cylinder of radius r , for $R_1 \leq r \leq R_2$, corresponds to the heat generated \mathcal{P} :

$$\begin{aligned} j_{cond}(r) \cdot 2\pi r h &= \pi R_1^2 h \cdot p_{vol} \\ \Leftrightarrow j_{cond}(r) &= \frac{R_1^2}{2r} \cdot p_{vol} \end{aligned} \quad (2.2)$$

Knowing the expression of $j_{cond}(r)$, we can integrate the Fourier's law along r between R_1 and R_2 :

$$\begin{aligned}
 \int_{R_1}^{R_2} j_{cond}(r) dr &= \int_{R_1}^{R_2} -\lambda \frac{dT}{dr} dr \\
 \Leftrightarrow \frac{R_1^2}{2} \cdot p_{vol} \cdot \ln(R_2/R_1) &= -\lambda [T_2 - T_1] \\
 \Leftrightarrow T_1 - T_2 &= \frac{R_1^2}{2\lambda} \cdot p_{vol} \cdot \ln(R_2/R_1) \\
 \Leftrightarrow T_1 - T_2 &= \mathcal{R}_{th} \cdot \mathcal{P} \tag{2.3}
 \end{aligned}$$

In equation 2.3 we introduced the thermal resistance $\mathcal{R}_{th} = \frac{\ln(R_2/R_1)}{2\pi h \lambda}$, which depends on the geometry (radii and height of the cylinders) and material property (thermal conductivity). The thermal resistance enables to relate the temperature difference $T_1 - T_2$ between the two cylinders with the thermal flux (or power \mathcal{P}) traversing them. A higher thermal resistance (for instance due to a material with a lower thermal conductivity λ) would lead to a higher temperature difference between the two cylinders.

Using equation 2.3, we can for instance estimate the temperature at the inner side of a storage cask, assuming

- the cask surface temperature: $T_{surf} = 80 \text{ }^\circ\text{C}$,
- the total power loaded in the cask: $\mathcal{P} = 39 \text{ kW}$,
- the thermal conductivity of the cask wall: $\lambda = 30 \text{ W m}^{-1} \text{ K}^{-1}$ and
- its dimensions (see section 2.2.1): $R_1 = 0.75 \text{ m}$, $R_2 = 1.25 \text{ m}$, $h = 5 \text{ m}$.

$$T_{int} = 80 + \frac{\ln(1.25/0.75)}{2 \cdot 3.14 \cdot 5 \cdot 30} \cdot 39000 = 101 \text{ }^\circ\text{C}$$

Another important example of thermal resistances corresponds to the case of thermal conduction through a longitudinal element of length \mathcal{L} and section \mathcal{S} , as shown in Fig. 2.2. A similar reasoning leads to the expression of the thermal resistance \mathcal{R}_{th} :

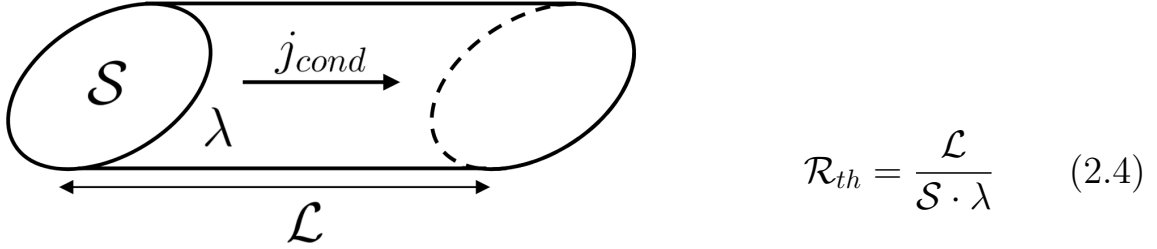


Figure 2.2: Thermal conduction in a uniaxial configuration.

This thermal resistance is simply proportional to the length of the heat path \mathcal{L} and inversely proportional to the section \mathcal{S} and thermal conductivity λ . All thermal resistances implemented in COBRA-SFS (see sections 2.3 and 2.4) are defined using this kind of expression.

Resistances in parallel or in series

In order to simplify a thermodynamics model, it can be interesting to perform some homogenization. This requires determining equivalent properties for the homogenized materials, in particular an equivalent thermal conductivity λ_{eq} . This equivalent conductivity depends on the geometrical configuration: if the materials are in parallel, the heat flux divides into two fluxes of different intensities (higher in the material with the highest conductivity), while for two materials in series, the heat flux path necessarily goes through both materials. Fig. 2.3 represents both cases: (a) two materials in parallel, (b) two materials in series.

The conditions on heat flux and temperature differences are:

- in parallel: $\Phi = \Phi_1 + \Phi_2$ and $\Delta T_1 = \Delta T_2 = \Delta T$ and
- in series: $\Delta T = \Delta T_1 + \Delta T_2$ and $\Phi_1 = \Phi_2 = \Phi$,

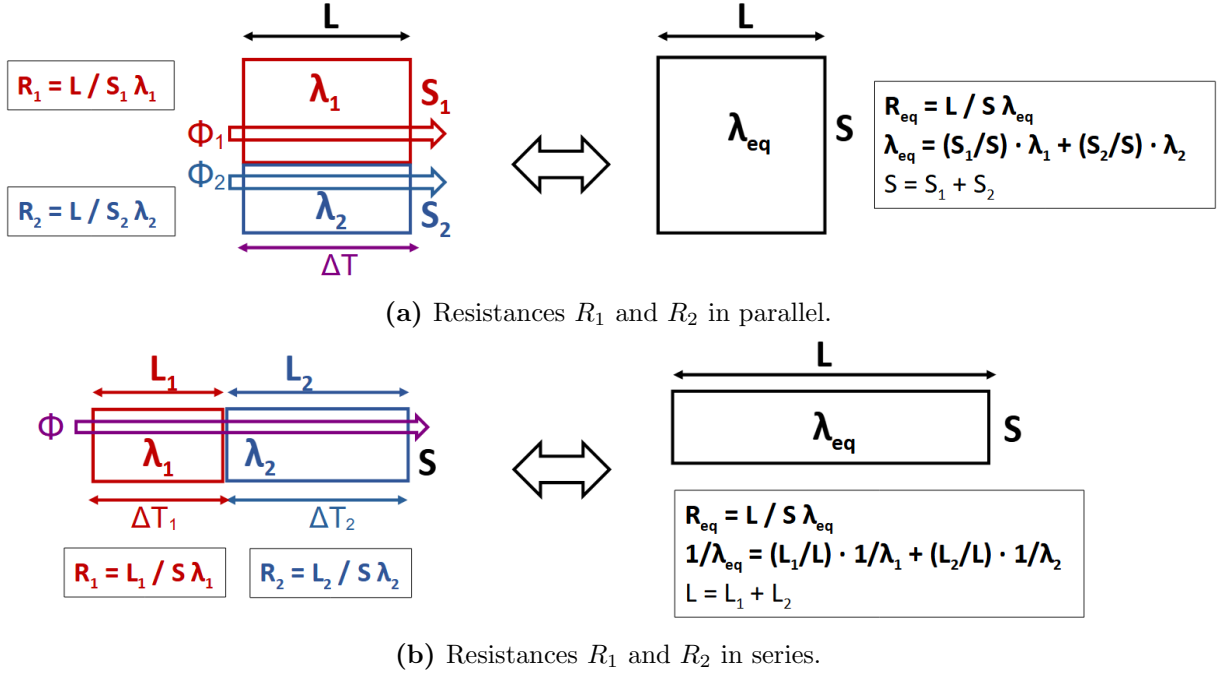


Figure 2.3: Equivalent thermal resistances R_{eq} and conductivities λ_{eq} for two materials (a) in parallel or (b) in series. L_i , S_i , Φ_i and ΔT_i refer respectively to the length of the heat path in material i , to the cross-sectional area of the heat path in material i , to the heat flux through material i and to the temperature difference resulting from the thermal resistance of material i .

where Φ_1 (resp. Φ_2) and ΔT_1 (resp. ΔT_2) are the heat flux and temperature differences through material 1 (resp. material 2), and Φ and ΔT the heat flux and temperature differences through the equivalent homogenized material.

These conditions enable to derive the equivalent thermal conductivities λ_{eq} (or resistances R_{eq}) for both cases, which are given on the right hand side of Fig. 2.3.

The difference between parallel and series plays an important role in the case of two materials with very different conductivities. For instance, if material 1 in Fig. 2.3 is an insulating material ($\lambda_1 \rightarrow 0$), then $R_1 \rightarrow \infty$ and:

- in the case of parallel materials (a), the heat flux Φ can still go through material 2 ($\Phi_1 \approx 0$ and $\Phi_2 \approx \Phi$) and the resulting temperature difference between both sides of the material remains limited: $\Delta T \approx R_2 \cdot \Phi$,
- in the case of materials in series (b), the heat flux Φ has to go through

both materials and the low conductivity of material 1 induces an important temperature gradient along the heat path in material 1: $\Delta T = \Delta T_1 + \Delta T_2 = (R_1 + R_2) \cdot \Phi \approx R_2 \cdot \Phi \rightarrow \infty$

Fig. 2.4 shows more details of the impact of the conductivity difference for two materials in series or in parallel. The plot represents the equivalent conductivity λ_{eq} in the case where λ_1 is fixed and λ_2 varies (on the x-axis) from 0 (perfect insulation) to ∞ (perfect conduction).

In the case where the two materials are in parallel (green curve), the equivalent conductivity starts at $\lambda_{eq} = \lambda_1/2$ when $\lambda_2 = 0$ (material 2 is perfectly insulating, but heat can still be conducted by material 1) and increases linearly with λ_2 .

In the case where the materials are in series, λ_2 has a stronger impact on the resulting λ_{eq} : if $\lambda_2 = 0$, then no heat can pass material 2 and as a matter of consequence $\lambda_{eq} = 0$ as well. If $\lambda_2 \rightarrow \infty$, then $\lambda_{eq} \rightarrow 2 \cdot \lambda_1$: material 2 becomes “invisible” for the heat flux but the thermal conductivity of material 1 still limits the heat conduction and induces a temperature difference independently of material 2.

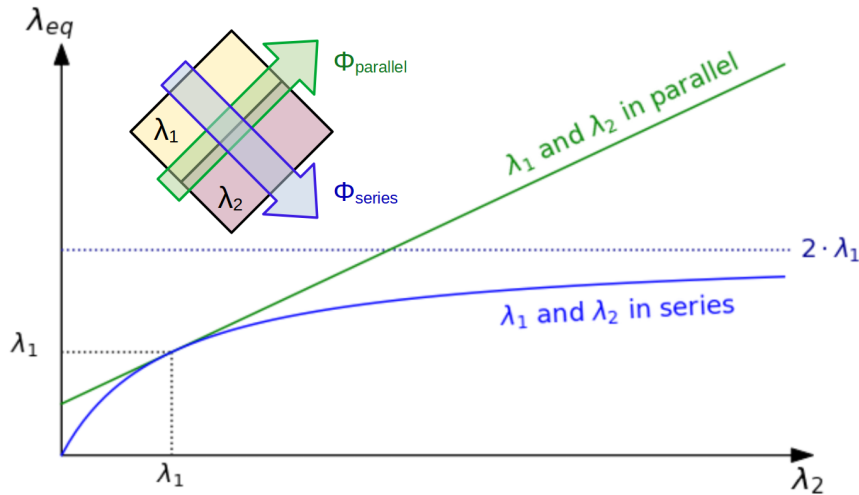


Figure 2.4: Equivalent conductivity λ_{eq} for two materials (conductivities λ_1 and λ_2) in parallel (green curve) or in series (blue curve). The plot corresponds to the case where both materials represent the same volume. λ_1 is fixed, the x-axis corresponds to λ_2 and the resulting equivalent conductivity λ_{eq} is on the y-axis.

2.1.1.2 Convection

Unlike conduction and radiative transfers, convection implies matter movements: the heat transport occurs through the matter transport. Convection thus only takes place in fluids (liquids or gases). One can distinguish natural convection and forced convection, depending on whether the fluid movement occurs only under the influence of body forces (gravity) or under the action of an external force (e.g. a ventilation system). Heat transfers by convection can apply for a system consisting solely of fluids. However, in many cases, the heat transfer of interest occurs between the surface of a solid and a fluid.

Heat transfers by convection are in general more complicated to simulate than thermal conduction or radiation, due to the matter motion involved: a precise modelling of a system including convection heat transfers requires fluid mechanics considerations. Indeed, the heat transfers by convection are directly related to the characteristics of the fluid (laminar or turbulent flow, speed of the flow). However, many correlations and formulas have been established for classical configurations, which enable to determine heat fluxes in a more simple way. In the case of a solid surface and a flow, the heat transfer is usually expressed using the Newton's law, which describes the heat flux j_{conv} as proportional to the temperature difference between the surface of the solid and the fluid [24]:

$$j_{conv} = h \cdot (T_{surf} - T_{fluid}) \quad (2.5)$$

with T_{surf} the surface temperature of the solid, T_{fluid} the temperature of the fluid², and h the “heat transfer coefficient” in $\text{W m}^{-2} \text{K}^{-1}$. Table 2.2 gives some examples of correlations for heat transfer coefficients in air at atmospheric pressure and for different geometries. To give an order of magnitude: in the case of natural convection of air at atmospheric pressure, heat transfer coefficients usually rank from 2.5 to 25 $\text{W m}^{-2} \text{K}^{-1}$ [25].

In the case of spent nuclear fuel, convection plays an important role in

²The temperature considered here corresponds to the fluid temperature at a sufficient distance from the solid surface. Indeed, in the immediate vicinity of the solid surface, the fluid flow is influenced (friction forces) by this surface and builds a “boundary layer”, which is characterized by a reduced velocity and an increased temperature. The precise modelling of the flow field falls within the scope of thermal-hydraulics but the Newton's law enables in a simpler way to indirectly take into account these effects.

Table 2.2: Correlations for free convection from various surfaces to air at atmospheric pressure [24].

Surface	Laminar	Turbulent
Vertical plane or cylinder	$h = 1.42 \left(\frac{\Delta T}{L}\right)^{1/4}$	$h = 1.31 (\Delta T)^{1/3}$
Heated plate facing upward	$h = 1.32 \left(\frac{\Delta T}{L}\right)^{1/4}$	$h = 1.52 (\Delta T)^{1/3}$
Heated plate facing downward	$h = 0.59 \left(\frac{\Delta T}{L}\right)^{1/4}$	

h = heat transfer coefficient [$\text{W}\cdot\text{m}^{-2}\cdot\text{K}^{-1}$]

$\Delta T = T_{surf} - T_{\infty}$ [K]

L = vertical or horizontal dimension [m]

cooling pond, where the convection of the water ensures an efficient heat removal. Later on, during the dry storage in interim storage facilities, convection heat transfers take place both around the storage casks (heat removal from the cask surface by the surrounding air) and within the casks (helium circulation within and around the fuel assemblies).

2.1.1.3 Thermal radiation

While conduction and convection require a medium to carry the heat, radiative transfer can occur through vacuum, as for instance the solar radiation in interplanetary medium. Any opaque solid in a transparent medium exchanges energy with its environment as the opaque surface emits and receives (with or without reflection) electromagnetic waves. Here also, one can define a radiative heat flux j_{rad} , which actually corresponds to a sum of radiative transfer over the whole range of the wave length λ of the electromagnetic radiations. In the case of a black body (body that absorbs all incident radiation) at thermal equilibrium, this sum is given by the Stefan-Boltzmann law and only depends on the surface temperature T :

$$j_{rad} = \int_0^{\infty} \frac{dj_{rad}}{d\lambda} d\lambda = \sigma T^4$$

where σ is the Stefan-Boltzmann constant: $\sigma = 5,67 \cdot 10^{-8} \text{ W m}^{-2} \text{ K}^{-4}$.

As most solid bodies are not perfect absorbers, the Stefan-Boltzmann equation is usually applied with an emissivity coefficient $0 \leq \epsilon \leq 1$:

$$j_{rad} = \epsilon \sigma T^4$$

The Stefan-Boltzmann law shows that the radiative transfers are strongly dependent on temperature and particularly important at high temperature (proportional to the fourth power). In the case of a loaded spent fuel cask, important radiative heat transfers occur between the fuel rod surfaces and the cask internal structures. Especially in large cavities filled with helium, heat transfers between surfaces standing apart from another can be very efficient by radiation, while they are much lower by conduction or convection. To calculate the radiative heat transfer between two surfaces, it is necessary to determine the heat fluxes emitted by those surfaces (Stefan-Boltzmann law), but also the geometrical configuration has to be taken into account: two surfaces will exchange more heat if they stand parallel to one another than if they are orthogonal, and the heat transfer will be larger if the distance between the two surfaces is shorter. This geometrical aspect is described by the *view factors* F_{ij} , which are discussed in section 2.1.2.

Non-blackbodies

As mentioned above, most solid bodies are not perfect absorbers. Non-blackbodies involve more complex calculations as part of the incident radiation is reflected. Indeed, when an incident radiation strikes a surface, part of it is absorbed (the corresponding fraction is defined as the absorptivity α), another part is transmitted through the surface (transmissivity τ) and the rest is reflected (reflectivity ρ). The energy conservation requires $\alpha + \tau + \rho = 1$. In the following, we establish the equation describing the radiative heat transfer between two non-blackbodies. This equation (2.8) is used by the code COBRA-SFS when radiative heat transfers have to be described. This section is adapted from [24] where more details on radiative heat transfers can be found.

To take into account the reflection and derive the corresponding equations, we may first define two new terms:

- the irradiation G : the total radiation incident upon a surface per unit time and per unit area, and
- the radiosity J : the total radiation that leaves a surface per unit time and per unit area,

which are represented in Fig. 2.5.

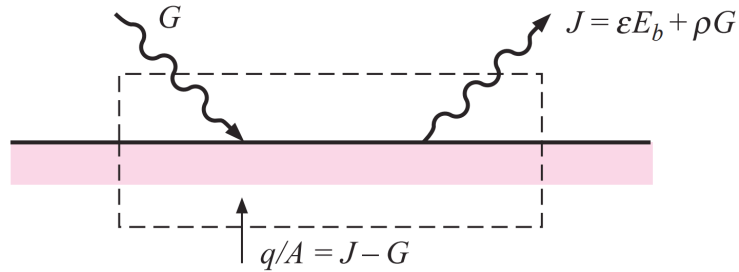


Figure 2.5: Surface energy balance for an opaque (no transmission) material. Taken from [24].

Assuming that the radiosity and irradiation are uniform over each surface, we can write the radiosity J as the sum of the emissive power of the surface (Stefan-Boltzmann law) and the reflected irradiation:

$$J = \epsilon E_b + \rho G$$

where ϵ is the emissivity, E_b is the blackbody emissive power and ρ the reflectivity. If we assume the transmissivity of the material to be zero (opaque material), we have $\rho = 1 - \alpha$, with α the absorptivity. Furthermore, Kirchhoff's identity states that the absorptivity is equal to the emissivity, $\epsilon = \alpha$, such that:

$$J = \epsilon E_b + (1 - \epsilon)G$$

Thus, the net energy leaving the surface can be written:

$$\frac{q}{A} = J - G = J - \frac{J - \epsilon E_b}{1 - \epsilon}$$

or

$$q = \frac{E_b - J}{(1 - \epsilon)/\epsilon A} \quad (2.6)$$

Equation 2.6 shows that if we consider the heat flux q as a current, the difference between the blackbody emissive power E_b and the radiosity J as a potential difference, and the denominator $(1 - \epsilon)/\epsilon A$ as a resistance, we can draw a parallel with an electrical resistance through which a current runs, leading to a potential difference. This corresponds to the first segment of the diagram in Fig. 2.6.

Considering now two surfaces, A_1 and A_2 , we can express the energy leaving surface 1 and reaching surface 2 as the product of the radiosity of surface 1, the area of surface 1 and the view factor (see section 2.1.2) from surface 1 to surface 2: $J_1 A_1 F_{12}$. Similarly, the energy leaving surface 2 and reaching surface 1 is: $J_2 A_2 F_{21}$. Using both expressions, we can calculate the net energy exchange between the two surfaces:

$$q_{1-2} = J_1 A_1 F_{12} - J_2 A_2 F_{21}$$

Due to the property of view factors stating that $A_1 F_{12} = A_2 F_{21}$ (see section 2.1.2), we can rewrite the energy exchange between the two surfaces as:

$$q_{1-2} = \frac{J_1 - J_2}{1/A_1 F_{12}} \quad (2.7)$$

In the same way as for Equation 2.6, Equation 2.7 can be considered as an electric current (the energy exchange q_{1-2}) given by the quotient of a potential difference (the potentials are the radiosities J_1 and J_2) and a resistance (the term $1/A_1 F_{12}$). This analogy enables to construct networks, in order to solve radiation heat transfer problems. In the case of a radiative heat transfer between the surfaces A_1 and A_2 , assuming that the surfaces see each other and nothing else, the network will consist of three resistances in series: a “surface-resistance” $(1 - \epsilon_i)/\epsilon_i A_i$ on each of the two surfaces and a “space-resistance” $1/A_1 F_{12}$ between the radiosity potentials. This is represented in Fig. 2.6.

The net heat transfer q_{net} corresponds then to the overall potential difference

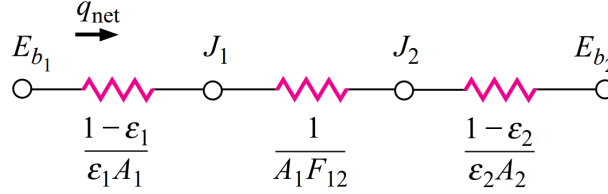


Figure 2.6: Radiation network for two surfaces that see each other and nothing else. Taken from [24].

divided by the sum of the resistances:

$$q_{net} = \frac{E_{b1} - E_{b2}}{\frac{1-\epsilon_1}{\epsilon_1 A_1} + \frac{1}{A_1 F_{12}} + \frac{1-\epsilon_2}{\epsilon_2 A_2}}$$

Thus, in terms of temperature, the radiative heat flux between two surfaces is given by:

$$q_{net} = \frac{\sigma(T_1^4 - T_2^4)}{\frac{1-\epsilon_1}{\epsilon_1 A_1} + \frac{1}{A_1 F_{12}} + \frac{1-\epsilon_2}{\epsilon_2 A_2}} \quad (2.8)$$

with A_1 and A_2 the area of the surfaces, ϵ_1 and ϵ_2 their emissivities and F_{12} the view factor from surface 1 to surface 2 (see the following section). Equation 2.8 is used in COBRA-SFS to describe the radiative heat transfers.

2.1.2 View factors and Hottel's crossed strings method

As mentioned in the previous section, the geometrical configuration of the surfaces involved in a heat transfer problem is important to determine the effective heat transfers. Indeed, if the radiation from an isothermal surface \mathcal{S}_1 can be assumed isotrope, the heat transfer from this surface to a second surface \mathcal{S}_2 will depend on two main parameters:

- the radiosity of the surface \mathcal{S}_1 , describing how much energy is diffused by \mathcal{S}_1 ,
- the view factor F_{12} from \mathcal{S}_1 to \mathcal{S}_2 , describing how well does \mathcal{S}_2 “see” \mathcal{S}_1 .

Fig. 2.7 shows for instance two surfaces in two different configurations: in (a), surface \mathcal{S}_2 sees well surface \mathcal{S}_1 , which means that an important part of the energy irradiated by surface \mathcal{S}_1 would be received by surface \mathcal{S}_2 . In configuration (b), even though both surfaces are closer from each other, surface \mathcal{S}_2 does not see surface \mathcal{S}_1 as good as in the former case and thus will not receive as much energy from surface \mathcal{S}_1 . In particular, we can see that the energy irradiated by the lower part of surface \mathcal{S}_1 cannot reach at all surface \mathcal{S}_2 .

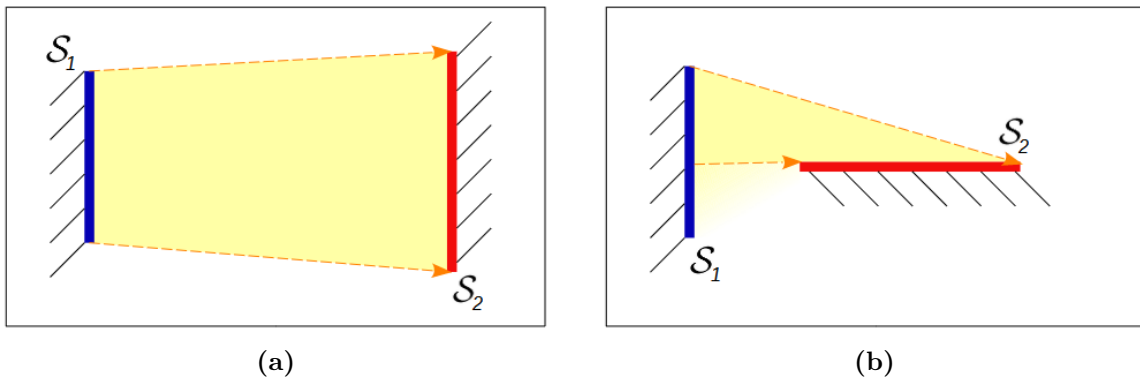


Figure 2.7: Radiative heat transfer between two surfaces in two different configurations. The radiation from surface \mathcal{S}_1 that can reach surface \mathcal{S}_2 is represented in yellow, the orange arrows draw the limits.

View factors (also referred to as “Radiation shape factors” [24]) can be defined in a more quantitative way by a double integral on the two surfaces \mathcal{S}_1 and \mathcal{S}_2 involved in the radiative heat transfer:

$$F_{12} = \frac{1}{\mathcal{S}_1} \iint_{\mathcal{S}_1 \mathcal{S}_2} \frac{\cos(\theta_1) \cos(\theta_2)}{\pi r^2} d\mathcal{S}_1 d\mathcal{S}_2 \quad (2.9)$$

with θ_1 (resp. θ_2) the angle of a ray from surface \mathcal{S}_1 to surface \mathcal{S}_2 with the normal of \mathcal{S}_1 (resp. \mathcal{S}_2) and r the length of this ray (details in Appendix 5.1 “View Factors”). In this equation, the cosine functions reflect the efficiency of the orientation of each surface: if the surfaces are facing each other, the cosines will be close to 1, while if one (or both) surface is not facing the other, the corresponding cosine will take values close to 0. The denominator coefficient πr^2 reflects the attenuation of the isotropic radiation. Per definition, view factor values lay between 0 (no radiation from \mathcal{S}_1 can reach \mathcal{S}_2) and 1 (all radiation from \mathcal{S}_1 reaches \mathcal{S}_2): $0 \leq F_{12} \leq 1$.

An important property is the reciprocity of the view factors:

$$\mathcal{S}_1 \cdot F_{12} = \mathcal{S}_2 \cdot F_{21} \quad (2.10)$$

The demonstration of Equation 2.10 is evident using the view factor definition of Equation 2.9. From a more physical point of view, this equality indicates that if both surfaces present the same radiosity, then the energy per unit time³ leaving \mathcal{S}_1 and received by \mathcal{S}_2 is equal to the energy per unit time leaving \mathcal{S}_2 and received by \mathcal{S}_1 (any given line joining the two surfaces can correspond to a ray traveling in either direction).

Another property of view factors is the summation: for an enclosure of N surfaces \mathcal{S}_j ,

$$\sum_{j=1}^N F_{ij} = 1 \quad \forall i \in [1; N] \quad (2.11)$$

This property simply means that all the radiation leaving a surface \mathcal{S}_i which is part of an enclosure, will be received by a surface of this enclosure. Equation 2.11 is not valid anymore if the surfaces considered do not form a closed enclosure, as part of the radiation emitted by \mathcal{S}_i could then exit the system.

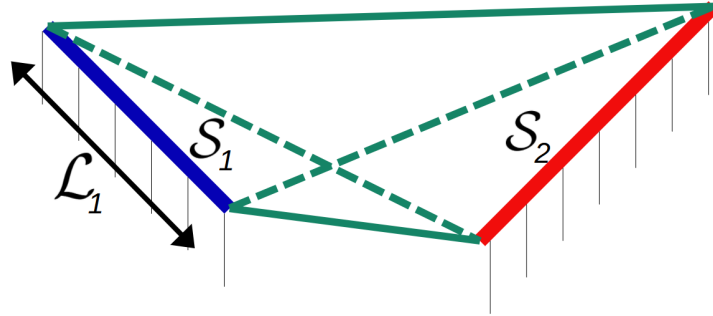


Figure 2.8: Crossed and uncrossed strings between two surfaces exchanging radiative heat. To determine the view factor from \mathcal{S}_1 to \mathcal{S}_2 , the Hottel's method can be applied using the crossed strings (green dotted line) and the uncrossed strings (green plain lines).

Equation 2.9 enables to determine view factors between surfaces. However, the integrals may complicate the calculation in most situations. Therefore, some other formulas might be very useful, as for instance the “Hottel's

³The “energy per unit time” corresponds to the radiosity integrated over the emitting surface.

formula”, or “Crossed strings method” [19, 26]. This formula applies only for two-dimensional systems but provides then a very simple expression to calculate view factors. Indeed, this expression only uses the lengths of the crossed and uncrossed strings joining the ends of the surfaces concerned, as well as the length \mathcal{L}_1 of the emitting surface⁴ (see Fig. 2.8):

$$F_{12} = \frac{\text{crossed strings} - \text{uncrossed strings}}{2 \cdot \mathcal{L}_1} \quad (2.12)$$

Finally, Fig. 2.9 gives an example of view factor calculation. The system consists of two surfaces: a plate \mathcal{S}_1 of length \mathcal{L} , which closes a half cylinder \mathcal{S}_2 . There are thus 4 view factors to determine: the self view factors F_{11} and F_{22} , and the reciprocal view factors F_{12} and F_{21} . We can first note that as \mathcal{S}_1 is a flat surface, $F_{11} = 0$. Furthermore, $F_{11} + F_{12} = 1$ (summation of the view factors of surface \mathcal{S}_1), and thus $F_{12} = 1$.

On the contrary, \mathcal{S}_2 is concave, so that part of the radiation emitted by \mathcal{S}_2 is then received by itself, which means that $F_{22} > 0$. Knowing F_{12} , we can deduce F_{21} from the reciprocity property:

$$F_{21} = \frac{\mathcal{L}}{\pi \mathcal{L}/2} F_{12} = \frac{2}{\pi}$$

The summation of the view factors of surface \mathcal{S}_2 yields then:

$$F_{22} = 1 - \frac{2}{\pi}$$

The application of the Hottel’s formula would also yield the same result: for F_{12} , the crossed strings between \mathcal{S}_1 and \mathcal{S}_2 would coincide with the segment \mathcal{S}_1 and thus have a length \mathcal{L} , while the uncrossed strings have a zero length. The length of the emitting surface \mathcal{S}_2 is $\pi \mathcal{L}/2$ and thus, according to the Hottel’s formula:

$$F_{21} = \frac{(\mathcal{L} + \mathcal{L}) - (0 + 0)}{2 \cdot (\pi \mathcal{L}/2)} = \frac{2}{\pi}$$

These view factors could also have been calculated using the mathematical definition given by Equation 2.9, but it would have been more complex and time-consuming.

⁴It might seem misleading to speak here of the “length” of a “surface”, but one should keep in mind that even though view factors apply per definition to surfaces, the Hottel’s correlation applies only to two-dimensional problems and thus involves lengths which actually characterize surfaces.

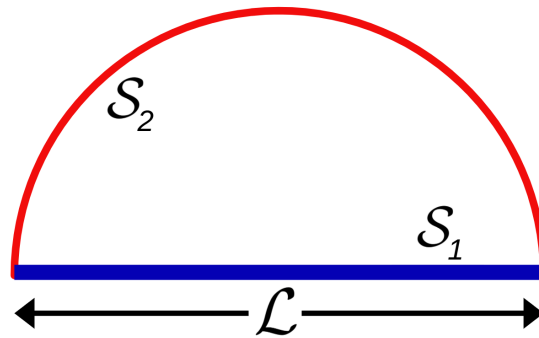


Figure 2.9: Radiative heat transfer in a closed half cylinder of diameter \mathcal{L} .

Further explanation on the mathematical definition of the view factor F_{12} , as well as some demonstrations concerning the Hottel's crossed strings method can be found in the appendixes 5.1 "View factors" and 5.2 "Hottel's crossed strings method", or in [26] or [24] ("Radiation shape factors").

2.2 Semi-analytical cask model

The first cask model presented in this thesis is a semi-analytical model inspired by the CASTOR[®] V/19, a transport and storage cask designed by GNS. It uses fundamental equations, includes strong homogenization assumptions and is implemented with the programming language Python. It has been developed as a direct application of the heat transfer theory presented in the previous section and provides temperatures in both steady-state and transient cases.

In the following, we first present the CASTOR[®] V/19 cask. Then, we describe the semi-analytical model (referred to as *Python model* in the following) inspired by the CASTOR[®] V/19. Finally, we discuss some results yielded by this model: a steady-state calculation (39 kW homogeneously loaded, with a room temperature of 25°C), accidental scenarios corresponding to fire conditions, and a sensitivity analysis of 10 parameters of the model.

2.2.1 Cask design

The CASTOR[®] V/19 is a transport and storage cask designed by GNS. It is the most common cask in Germany for the storage of PWR spent fuel assemblies and can host up to 19 fuel assemblies. For Germany, it is foreseen that the fuel assemblies can have a maximum average burnup of 55 GWd/t_{HM} and a power limit of 39 kW. The 19 fuel assemblies can include up to four *special assemblies* placed in the inner cavity ring: MOX assemblies with a maximum average burnup of 55 GWd/t_{HM} or Uranium assemblies with a maximum average burnup of 65 GWd/t_{HM} [27]. In the following, we will refer to fuel assemblies as *FA*, in particular when referring to their identification: for instance, *FA 10* for the central fuel assembly in Fig. 2.18.

The CASTOR[®] V/19 is 5.94 m in height and has an external diameter (including cooling fins) of 2.44 m. The cask body is made of cast iron, in which polyethylene rods are inserted for neutron shielding. The inner cavity



Figure 2.10: CASTOR[®] V/19 cask from GNS. On the upper left picture, we can see the configuration of the basket and 19 fuel assemblies in the cask cavity. On the lower left picture, we can observe the closing system including a primary lid and a secondary lid. A protection plate (blue painted) comes on top of the double-lid system. The two rows of polyethylene moderator rods (white rods and round spots in the cask body) can be seen on the vertical cask. On the external surface of the cask, cooling fins are used to enhance the heat removal. Taken from [28].

is 5.03 m in height, 1.48 m in diameter and includes fuel compartments made of aluminium and stainless steel, in which the fuel assemblies can be inserted. This cavity is filled with helium, which is both an inert gas and a good thermal conductor. The cask is closed using two bolted lids. The geometry of the CASTOR[®] V/19 can be seen in Fig 2.10 [28].

2.2.2 Model description

The Python model was built in parallel to the development of the first COBRA-SFS model (*CASTOR model*, presented in section 2.3). We modelled the cask with 5 homogenized radial zones for the cask cavity filled with internal structures and fuel assemblies, and one zone for the cask body (see Fig. 2.11). The radii of the 5 zones were set in such a way that the 5 zones representing the cask interior have the same surface areas: $R_1 = R_{int}$, $R_2 = \sqrt{4/5} R_{int}$, $R_3 = \sqrt{3/5} R_{int}$, $R_4 = \sqrt{2/5} R_{int}$, and $R_5 = \sqrt{1/5} R_{int}$, with R_{int} the radius of the cask cavity. The choice of this particular division presents an advantage: we can see in Fig. 2.11 that

- the 12 external fuel assemblies are located in the zones 1, 2 and 3,
- the 6 intermediate fuel assemblies are approximately half in zone 4 and half in zone 5, and
- the central fuel assembly is in zone 5.

Considering this spatial distribution of the fuel assemblies over the zones, we attributed the following powers to the homogenized zones:

- for zone 1, 2 and 3: $12 \times \frac{1}{3} \times P_{tot}/19 = 4/19 P_{tot}$
- for zone 4: $6 \times \frac{1}{2} \times P_{tot}/19 = 3/19 P_{tot}$
- for zone 5: $(6 \times \frac{1}{2} + 1) \times P_{tot}/19 = 4/19 P_{tot}$

with P_{tot} the total power loaded in the cask.

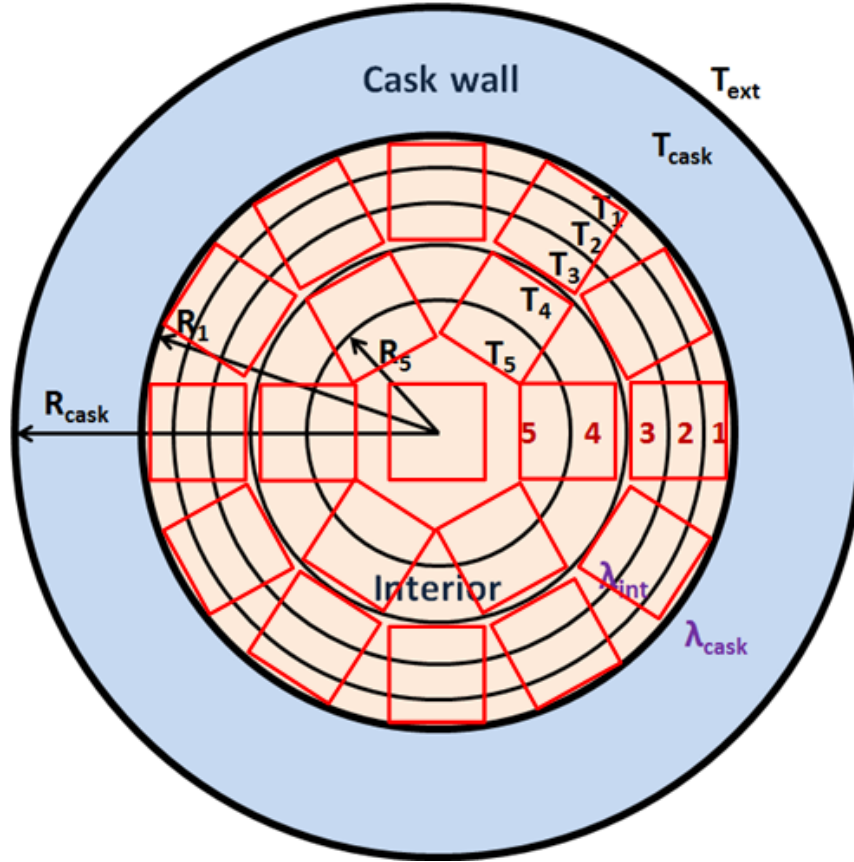


Figure 2.11: Diagram of the semi-analytical cask model. The model consists of six homogenized zones: one for the cask body and five for the internal part of the cask, including basket structures and fuel assemblies. Fuel assembly positions are indicated by the red squares on the diagram but the assemblies are not considered in detail in the model, due to the homogenization assumptions.

The constant parameters used for the model are gathered in Table 2.3: cask height H , inner and outer cask diameters R_i , characteristic dimensions of the fuel rods (height h and radii r_i), masses m_i , total power P_{tot} , emissivities ϵ_i , densities ρ_i , Stefan-Boltzmann constant σ , heat capacities c_i , cask wall thermal resistance⁵ R_{par}^{th} , and conductivity of cast iron λ_{GGG} . Further parameters were then defined as functions of the temperature: thermal conductivity of the polyethylene (PE), of the homogenized cask body, of the homogenized cask interior area, thermal resistances from one zone of the

⁵In the following, we will use the exponent “th” to refer to *thermal* resistances (R_{par}^{th} , $R_{i+1,i}^{th}$) and distinguish them from radii (R_i). In R_{par}^{th} , the index “par” refers to *parietal*.

model to the next one, and heat capacities.

Table 2.3: Parameters used in the Python semi-analytical model.

Parameter	Value	Unit	Parameter	Value	Unit
H	4.95	m	P_{tot}	39000	W
R_{int}	0.74	m	ρ_{clad}	6560	kg m ⁻³
R_{cask}	1.15	m	ρ_{alum}	2700	kg m ⁻³
h_{rod}	400	cm	ρ_{steel}	7800	kg m ⁻³
r_{fuel}	0.403	cm	ρ_{fuel}	13600	kg m ⁻³
$r_{clad,i}$	0.411	cm	ρ_{He}	0.166	kg m ⁻³
$r_{clad,o}$	0.475	cm	σ	5.67×10^{-8}	W m ⁻² K ⁻⁴
$r_{GT,i}$	0.555	cm	c_{PE}	2150	J kg ⁻¹ K ⁻¹
$r_{GT,o}$	0.616	cm	c_{clad}	330	J kg ⁻¹ K ⁻¹
m_{GGG}	85906	kg	c_{alum}	896	J kg ⁻¹ K ⁻¹
m_{PE}	2514	kg	c_{steel}	500	J kg ⁻¹ K ⁻¹
ϵ_{int}	0.8	-	c_{fuel}	303	J kg ⁻¹ K ⁻¹
$\epsilon_{cask,o}$	0.93	-	c_{He}	3115	J kg ⁻¹ K ⁻¹
$\epsilon_{cask,i}$	0.25	-	R_{par}^{th}	2.60×10^{-3}	K W ⁻¹
ϵ_{room}	1	-	λ_{GGG}	36	W m ⁻¹ K ⁻¹

Heat exchanges between the zones consist of two contributions: conduction and radiation. Convective heat transfers are not taken into account in this model. They mainly impact the axial temperature profiles in the cask (the helium convection in the cask tends to transfer heat from the lower part of the fuel assemblies towards the upper part), but as the model at hand does not consider the axial dimension of the cask, the modelling of convection would have been probably ill-defined.

Conduction heat flux derives from the Fourier's law (see section 2.1.1.1):

$$\vec{j}_{cond} = -\lambda \overrightarrow{grad} T \quad (2.13)$$

Radiative heat transfers are given by the Stefan-Boltzmann law (see section 2.1.1.3):

$$j_{rad}^* = \epsilon \sigma T^4 \quad (2.14)$$

From the integration of equations 2.13 and 2.14, we derived the expression for the heat flux $\Phi_{i+1,i}$ from zones $i + 1$ to zone i :

$$\Phi_{i+1,i}(t) = \frac{T_{i+1}(t) - T_i(t)}{R_{i+1,i}^{th}(T(t))} + 2\pi R_{i+1} H \sigma(\epsilon_{i+1} T_{i+1}^4 - \epsilon_i T_i^4) \quad (2.15)$$

where $R_{i+1,i}^{th}$ is the thermal resistance between the zones $i+1$ and i (see section 2.1.1.3, Equation 2.3), defined by:

$$R_{i+1,i}^{th}(T) = \frac{1}{2\pi H \lambda_{i+1}(T)} \times \ln\left(\frac{R_i + R_{i+1}}{R_{i+1} + R_{i+2}}\right) \quad (2.16)$$

and T is the temperature considered for the thermal resistance, defined as the mean value of the temperatures T_{i+1} and T_i : $T = \frac{T_{i+1} + T_i}{2}$.

Then, the energy balance for each zone i can be written time-step-wise and leads to the temperature evolution, involving the heat fluxes $\Phi_{i+1,i}$ and $\Phi_{i,i-1}$, the thermal capacity C_i and the power generated by decay heat P_i :

$$T_i(t + dt) = T_i(t) + \frac{P_i + \Phi_{i+1,i} - \Phi_{i,i-1}}{C_i} \times dt \quad (2.17)$$

Using Equations 2.17 and 2.15, we defined the following functions (the corresponding scripts can be found in Appendix 5.3):

- *temp_eq*(T_{room} , $dt = 10$, $delta = 1e-6$)
temp_eq yields the equilibrium temperature values (in °C) for each zone, according to the room temperature T_{room} given in parameter. The user can also define the time step dt (default is $dt = 10$ s) and the convergence criterion (default is $delta = 1e-6$ K).
- *temp*(T_{init} , T_{room_list} , t , dt , $scale = "lin"$)
temp plots the temperature (in °C) evolution for each zone, starting from the initial condition T_{init} (list of the initial temperatures for each zone), according to room temperature conditions (list of tuples (*time*, *temperature*) which enables boundary condition changes with time), over a time duration t and with a time step dt . The time scale can be linear (default) or logarithmic.

These functions have been used to calculate the temperature distributions and evolutions in different conditions.

2.2.3 Model results

Using the function *temp_eq*, we first determined the equilibrium temperatures in the case of a total power of 39 kW and a room temperature of 25 °C. We obtained the following results:

- The zone modelling the cask body has a temperature of 79 °C
- Zone 1 has a temperature of 145 °C
- Zone 2 has a temperature of 215 °C
- Zone 3 has a temperature of 259 °C
- Zone 4 has a temperature of 289 °C
- Zone 5 has a temperature of 311 °C

With regard to the available literature [29–31], these temperature values seem to provide good orders of magnitude for the cask body and for the interior of the cask.

Then, using the function *temp*, we simulated the temperature evolutions under different boundary conditions. Thus, Fig. 2.12 shows the temperature evolution for the different zones of the model under accidental conditions, where the cask would undergo a temperature of 600 °C for one hour. The plot starts from the equilibrium state corresponding to a room temperature of 25 °C, as determined above. Then, after 100 s, a room temperature of 600 °C is applied for one hour (blue dotted line in Fig. 2.12), before being set back on 25 °C. During the temperature step, only the cask body is really affected by the change of boundary conditions and presents an exponential increase of temperature of approximately 100 °C: from 79 °C up to 180 °C. Its temperature also immediately decreases when the room temperature returns to normal. The temperatures of the internal zones of the model present smaller and smoother variations. The maximum temperatures of these zones are reached at different times:

- after 3.5 hours (from the start of the temperature step) for zone 1,

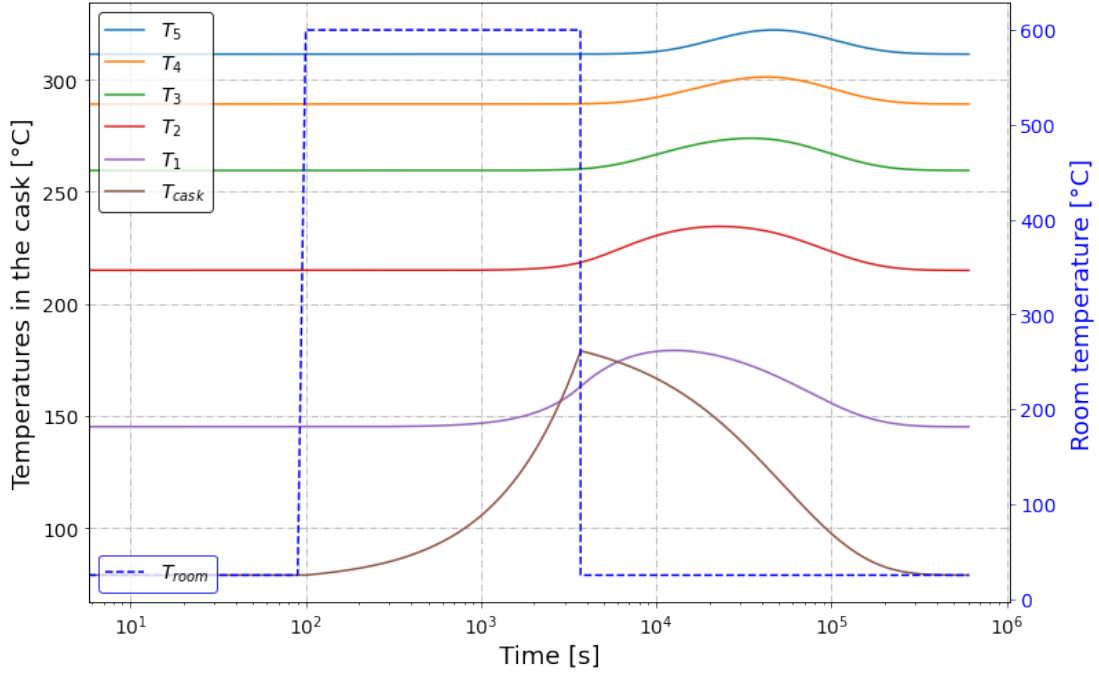


Figure 2.12: Temperature evolution with a step of 1 hour at 600 °C (logarithmic time scale). The blue dotted line indicates the room temperature: from 25 °C at the beginning of the simulation, it increases to 600 °C for 1 hour before being set back on 25 °C. The six plain lines show the evolution of the different zone of the model. The cask body (brown line) immediately starts to increase (resp. decrease) when the room temperature increases (resp. decreases), while the five zones corresponding to the cask cavity and fuel assemblies present some delay. For instance, the innermost zone reaches a temperature maximum only 14.5 h after the room temperature increase.

- after 7 h for zone 2,
- after 10.5 h for zone 3,
- after 13 h for zone 4 and
- after 14.5 h for zone 5.

The temperature variation caused by the temperature step ranges from 12 °C for the most internal zone (T_5 reaches a maximum temperature of 323 °C) up to 32 °C for the external zone (T_1 reaches 177 °C). This indicates that the nearer the fuel rods are from the cask centre, the more the effect of

the temperature step will be delayed and reduced. Finally, the temperatures in the cask are back to the initial equilibrium values after about 4 days.

Fig. 2.13 presents a similar scenario, but with a temperature step of 30 minutes at $T_{room} = 800$ °C. The temperature evolution is very similar to the former case. This scenario corresponds to the accident conditions of transport defined by the IAEA in its Safety Standards [32] and also considered in the U.S. NRC Regulations as “hypothetical accident conditions” [33].

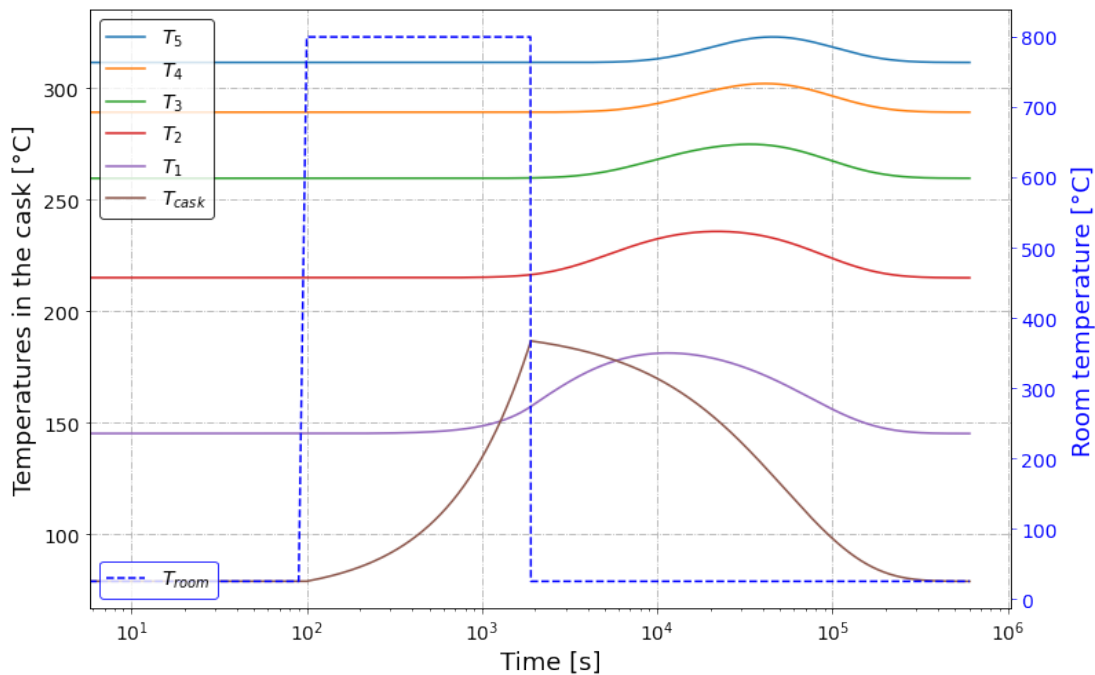
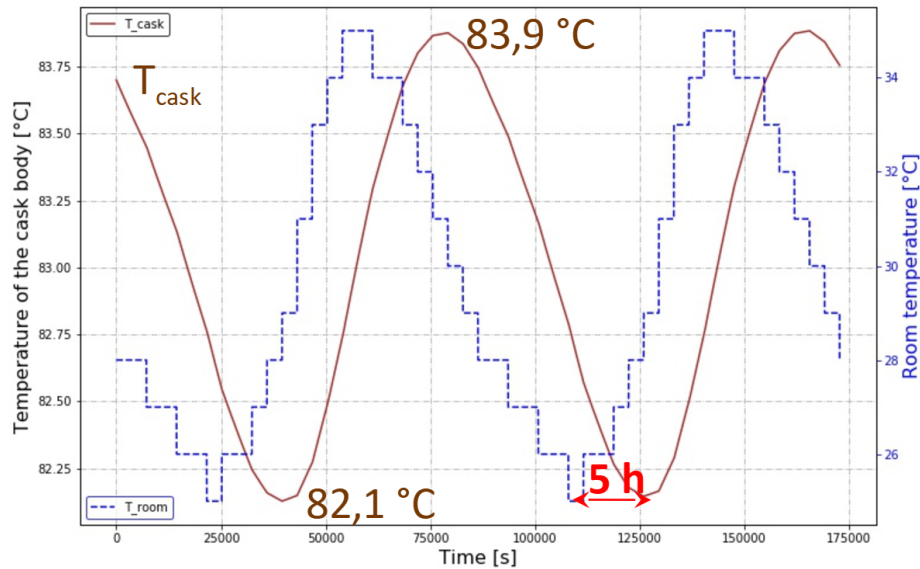


Figure 2.13: Temperature evolution with a step of 30 min at 800 °C (logarithmic time scale).

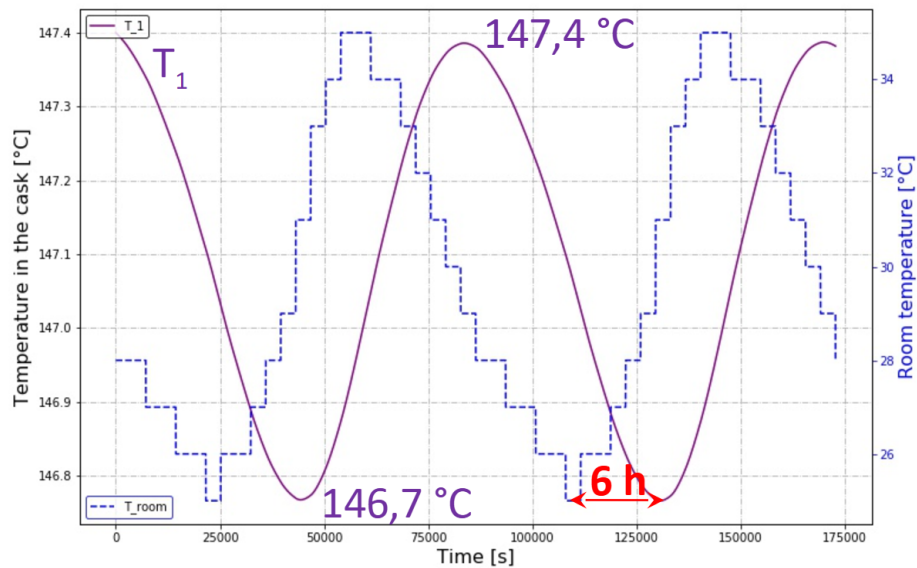
Further scenarios can be simulated with this model, such as daily fluctuations of the room temperature. For instance, Fig. 2.14a and Fig. 2.14b show, respectively, the temperature evolutions of the cask body and of the zone 1, in the case of a generic daily fluctuation of the room temperature. The amplitude of this fluctuation was defined with T_{room} varying from 25 °C to 35 °C over a day. We can see that the cask body temperature follows the room temperature variations with a delay of about 5 hours, and with an amplitude of around 1.8 °C. The temperature of zone 1 presents a similar

2.2 Semi-analytical cask model

evolution, but with a longer delay (about 6 hours) and a smaller amplitude (less than 1 °C).



(a) Cask body temperature.



(b) Temperature of zone 1 (most external).

Figure 2.14: Evolution of the cask temperature under generic daily fluctuations of the room temperature. The room temperature varies between 25 °C and 35 °C with a period of 24 hours (2 days are simulated). The cask body temperature (a) presents similar temperature variations but with an amplitude of 1.8 °C and a delay of 5 hours. The amplitude of the temperature variations of zone 1 is even lower (0.8 °C) but with a longer delay (6 hours).

2.2.4 Sensitivity analysis

A major advantage of the Python model consists in the very short calculation time: equilibrium temperatures are yielded within a few seconds. This enables to perform large numbers of simulations in a reasonable time and without special computational capacities. Therefore, we conducted a sensitivity analysis on 10 parameters and including 7000 simulations. The detail of the distributions used for the parameter sampling is shown in Table 2.4. The distributions for the emissivity coefficients were chosen as uniform, in order to define fixed limits (in particular to ensure $\epsilon \leq 1$) and as we had no further information on the distributions. For the other parameters, we chose normal distributions, as the only information for each parameter consists in its mean value and the fact that the parameter is more likely to present values near to this mean value. The conductivity for cast iron λ_{GGG} is defined as an absolute value ($36 \text{ W m}^{-1} \text{ K}^{-1}$) while the conductivities for polyethylene, fuel assemblies and helium are given as normalized parameters. This is due to the differences in definition in the Python model (constant value for λ_{GGG} , correlations for the other conductivities).

Table 2.4: Parameters used in the sensitivity analysis of the Python model.

Parameter	Distribution type	Mean value	Standard deviation
ϵ_{int}	Uniform	0.8	$0.75 \leq \epsilon_{int} \leq 0.85$
$\epsilon_{cask,o}$	Uniform	0.93	$0.90 \leq \epsilon_{cask,o} \leq 0.96$
$\epsilon_{cask,i}$	Uniform	0.25	$0.2 \leq \epsilon_{cask,i} \leq 0.3$
P_{tot}	Gaussian	39000	1000
T_{room}	Gaussian	25	5
λ_{GGG}	Gaussian	36	3
$Factor\lambda_{PE}$	Gaussian	1	0.05
$Factor\lambda_{FA}$	Gaussian	1	0.05
$Factor\lambda_{He}$	Gaussian	1	0.05
$Heat\ transfer\ coeff$	Gaussian	3.3	0.1

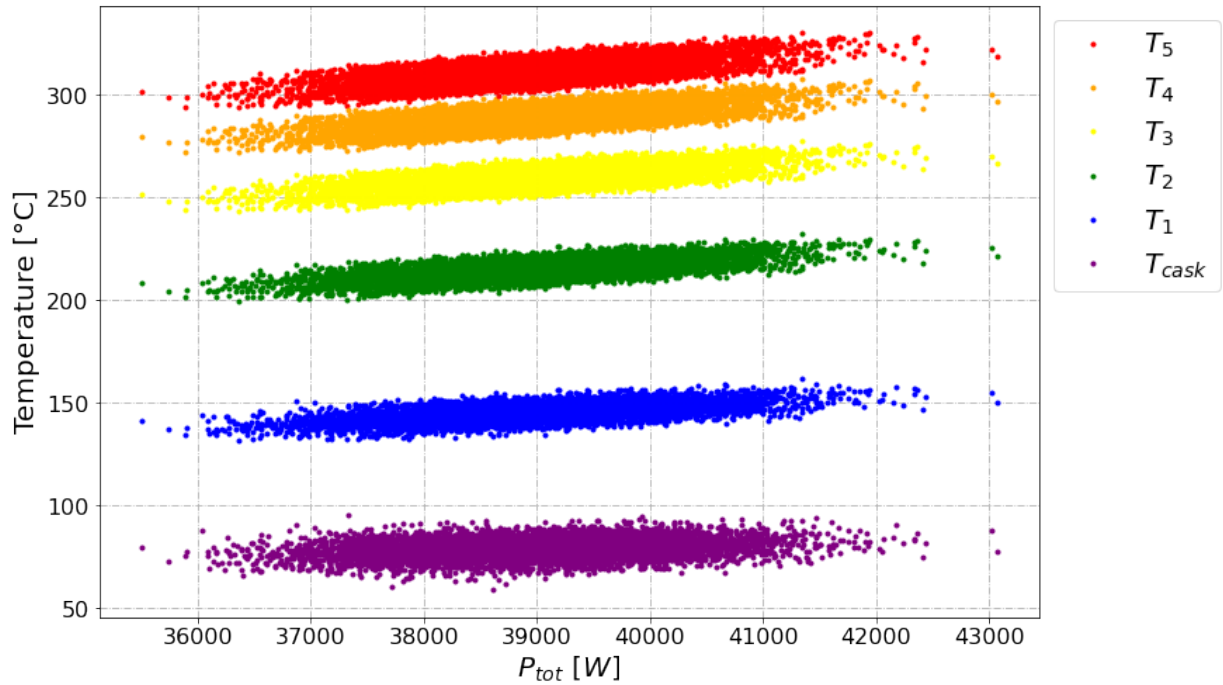
Using the results of the 7000 simulations, it is possible to determine which of the parameters are correlated to the temperatures yielded by the model. Two parameters are said *correlated* (resp. *anticorrelated*) if high values of one parameter can be associated with high values (resp. low values) of the

other parameter. This is important because if a parameter is strongly correlated to the temperature of the cask, then this means that large uncertainties on this parameter can be expected to lead to large uncertainties in the model output.

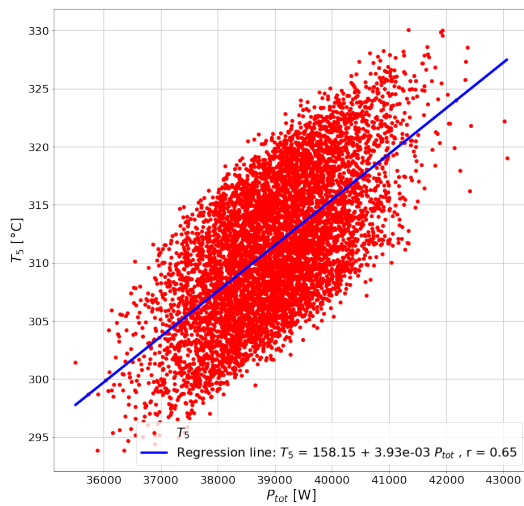
Fig. 2.15 and Fig. 2.16 are scatter plots depicting the temperatures yielded by the model, with regard to the total power P_{tot} and to the room temperature T_{room} . For both figures, three scatter plots are included: (a) with the temperatures of all 6 zones of the Python model, (b) with the temperature of zone 5 (most internal zone) and (c) with the temperature of the cask body. Linear regression lines have been drawn on the scatter plots (b) and (c).

In Fig. 2.15, we can observe that the temperature in the cask tends to increase with P_{tot} . In particular, this correlation is stronger for the internal zones of the cask than for the cask body: the temperature T_5 of zone 5 in Fig. 2.15b clearly tends to be higher for high values of P_{tot} . This is less clear with the cask body temperatures T_{cask} in Fig. 2.15c. On the contrary, in Fig. 2.16 the room temperature appears better correlated with T_{cask} (Fig. 2.16c) than with T_5 (Fig. 2.16b).

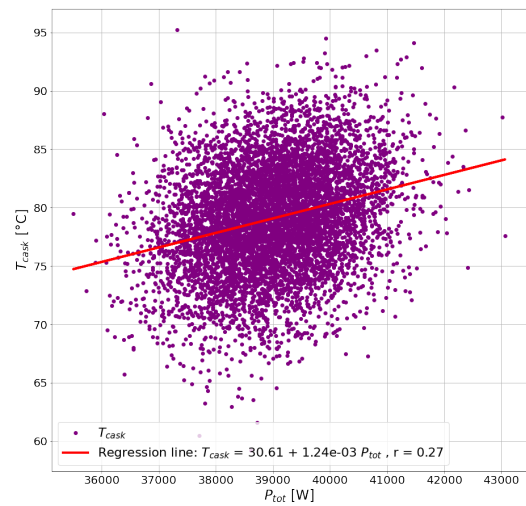
The scatter plots of the 6 zones of the model for each of the 10 parameters listed in Table 2.4 can be found in Appendix 5.4. Fig. 5.1 provides an example of anticorrelation, as the temperatures inside the cask tend to be lower for higher emissivity coefficients.



(a) All 6 zones of the model.



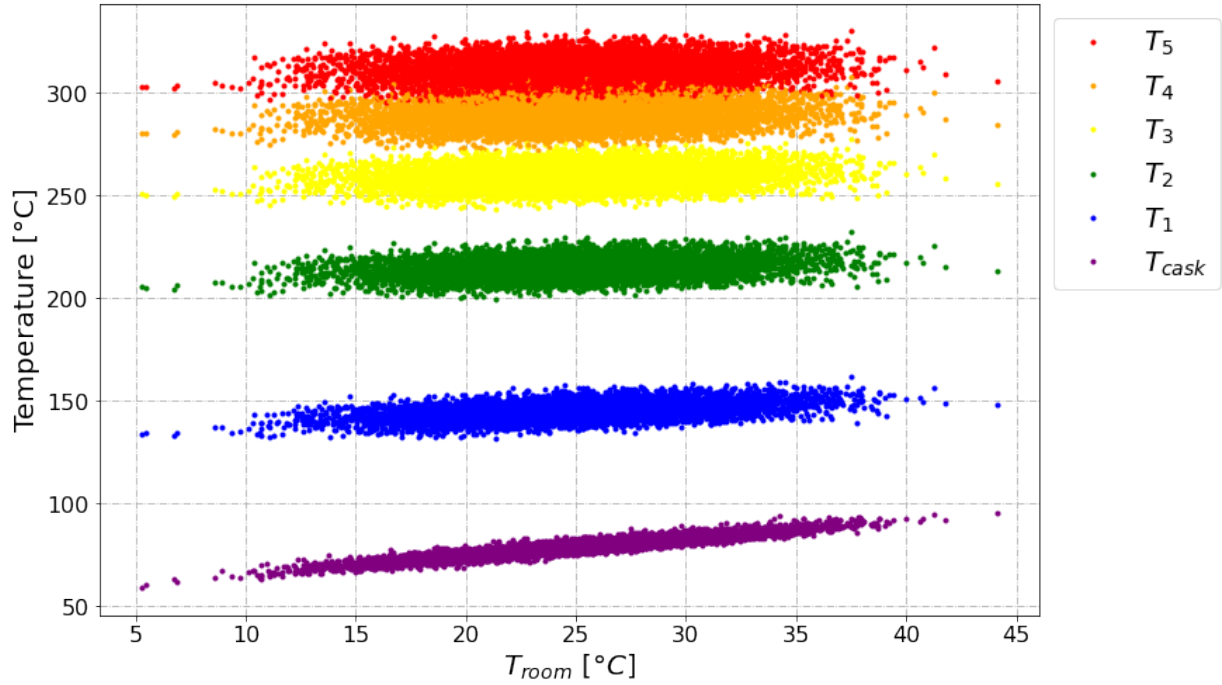
(b) Zone 5 (most internal).



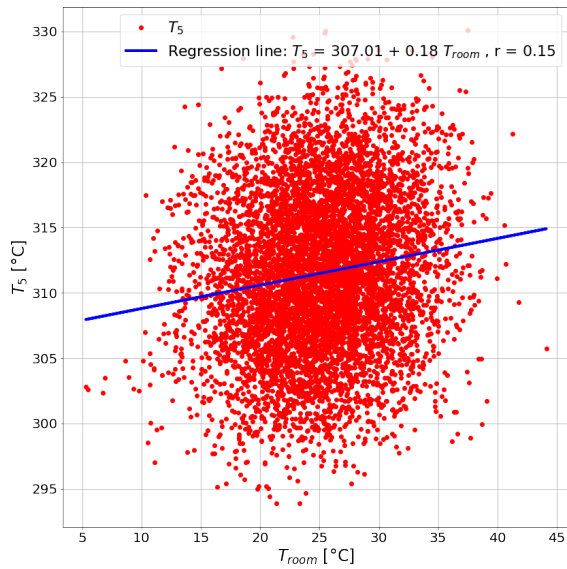
(c) Cask body.

Figure 2.15: Scatterplot showing the temperatures of the 6 zones of the Python model with regard to the total power.

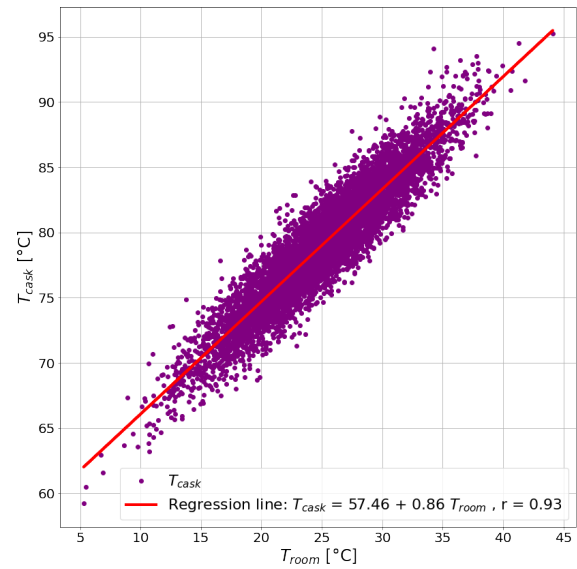
2.2 Semi-analytical cask model



(a) All 6 zones of the model.



(b) Zone 5 (most internal).



(c) Cask body

Figure 2.16: Scatterplot showing the temperatures of the 6 zones of the Python model with regard to the room temperature.

Pearson correlation coefficient, correlation matrix and linear regression

To assess in a more quantitative way the correlation level of the different parameters, a correlation matrix was calculated using the function *corrcoeff* from the Python library NumPy [34]. This correlation matrix is based on Pearson correlation coefficients $r_{x,y}$.

The Pearson correlation coefficients $r_{x,y}$ [35] are defined as the quotient of the covariance $cov(x, y)$ of two variables x and y , with the standard deviations $\sigma(x)$ and $\sigma(y)$:

$$r_{x,y} = \frac{cov(x, y)}{\sigma(x) \cdot \sigma(y)} = \frac{\sum_{i=1}^N (x_i - \bar{x})(y_i - \bar{y})}{\sqrt{\sum_{i=1}^N (x_i - \bar{x})^2} \sqrt{\sum_{i=1}^N (y_i - \bar{y})^2}} \quad (2.18)$$

with \bar{x} and \bar{y} the mean values of x and y : $\bar{x} = \frac{1}{n} \sum_{i=1}^n x_i$ and $\bar{y} = \frac{1}{n} \sum_{i=1}^n y_i$.

The Pearson correlation coefficient ranges from -1 to 1 and determines the strength of the linear relationship between two variables [35]. The sign indicates whether the two variables are correlated ($r_{x,y} > 0$) or anti-correlated ($r_{x,y} < 0$). The absolute value measures the correlation level. A correlation coefficient equal to 1 (resp. -1) indicates a perfect correlation (resp. anti-correlation): all points (x_i, y_i) lie perfectly on a straight line with a positive (resp. negative) slope. A correlation coefficient equal to 0 indicates that no trend can be found: high values for x_i can be associated neither with high values nor with low values for y_i .

In Fig. 2.15, we already observed that P_{tot} appears better correlated with T_5 than with T_{cask} . This is confirmed by the correlation coefficients: $r = 0.65$ for the correlation between T_5 and P_{tot} , and $r = 0.27$ for the correlation between T_{cask} and P_{tot} . In Fig. 2.16, we can see that the correlation is even stronger between T_{room} and T_{cask} : the data points appear well concentrated around the regression line and the high correlation coefficient $r = 0.93$ confirms that T_{cask} and T_{room} are strongly correlated.

Using the function *linregress* from Python library SciPy (subpackage *stats*) [36], we also plotted on the scatter plots the corresponding linear regressions. The aim of a linear regression is to have a function which provides the best prediction of y for a given x . If we call \hat{y} the estimated value of y for a

given x using the regression function $\hat{y} = ax + b$, we can define for each data point (x_i, y_i) the residual ϵ_i as: $\epsilon_i = y_i - \hat{y}_i = y_i - (ax_i + b)$. The residuals represent the errors between the real data y_i and the estimation \hat{y}_i . The linear regression should minimize these errors, therefore we can determine the coefficients a and b by looking for the minimum of the function $F(a, b) = \sum_{i=1}^n [y_i - (ax_i + b)]^2$, sum of the squared residuals on all data points (x_i, y_i) . This is achieved by solving the two equations $\frac{\partial F}{\partial a} = 0$ and $\frac{\partial F}{\partial b} = 0$.

$$\begin{aligned} \frac{\partial F}{\partial b} = 0 &\Leftrightarrow \sum_{i=1}^n 2(y_i - ax_i - b) \cdot (-1) = 0 \\ &\Leftrightarrow \sum_{i=1}^n y_i - a \sum_{i=1}^n x_i - \sum_{i=1}^n b = 0 \\ &\Leftrightarrow \bar{y} = a\bar{x} + b \end{aligned}$$

We can note that this first equation indicates that the barycentre of the (x_i, y_i) data points is located on the regression line.

$$\begin{aligned} \frac{\partial F}{\partial a} = 0 &\Leftrightarrow \sum_{i=1}^n 2[y_i - ax_i - b] \cdot (-x_i) = 0 \\ &\Leftrightarrow \sum_{i=1}^n x_i [y_i - ax_i - (\bar{y} - a\bar{x})] = 0 \\ &\Leftrightarrow \sum_{i=1}^n x_i [(y_i - \bar{y}) - a(x_i - \bar{x})] = 0 \\ &\Leftrightarrow a = \frac{\sum_{i=1}^n x_i (y_i - \bar{y})}{\sum_{i=1}^n x_i (x_i - \bar{x})} \\ &\Leftrightarrow a = \frac{\sum_{i=1}^n (x_i - \bar{x})(y_i - \bar{y})}{\sum_{i=1}^n (x_i - \bar{x})^2} \\ &\Leftrightarrow a = \frac{cov(x, y)}{var(x)} \end{aligned}$$

with $cov(x, y) = \frac{1}{n} \sum_{i=1}^n (x_i - \bar{x})(y_i - \bar{y})$ and $var(x) = \frac{1}{n} \sum_{i=1}^n (x_i - \bar{x})^2$.

In order to make the covariance and variance appear, we introduced additional $-\bar{x}$ terms in the second to last equivalence, at the numerator and

denominator. They do not change the equation, as

$$\sum_{i=1}^n -\bar{x}(y_i - \bar{y}) = \sum_{i=1}^n -\bar{x}y_i + \sum_{i=1}^n \bar{x}\bar{y} = -n\bar{x}\bar{y} + n\bar{x}\bar{y} = 0$$

Thus, the coefficients of the linear regression are given by:
$$\begin{cases} a = \frac{cov(x,y)}{var(x)} \\ b = \bar{y} - a\bar{x} \end{cases}$$

Fig. 2.17 shows the correlation matrix containing the Pearson coefficients $r_{i,j}$ obtained with the 7000 simulations. We can first note that this matrix verifies usual properties of correlation matrices: it is symmetric ($cov(i,j) = cov(j,i)$ and therefore $r_{i,j} = r_{j,i}$) and its diagonal is filled with 1 (trivially, any variable is perfectly correlated with itself). The colorbar enables to distinguish whether the parameters are correlated (red), anticorrelated (blue) or uncorrelated (white). The more intense the colour is, the stronger the correlation (or anticorrelation) is.

We can observe that the upper left 6x6 elements of the matrix are strongly correlated. This is not surprising as they correspond to the temperatures yielded by the model. If a set of model parameters leads to a particularly high (resp. low) temperature for one zone of the cask model, we might expect that the whole cask will be particularly hot (resp. cold), i.e. that the other zones will also present a rather high (resp. low) temperature. We might note that the correlation is lower between T_{cask} and the temperatures of the other zones, in particular with the most internal zones: while the correlation between T_{cask} and T_1 (external zone) is 0.64, the correlation between T_{cask} and T_5 (internal zone) only reaches 0.32. This can be understood considering that the description of the cask body includes mainly specific parameters (conductivity, surface heat transfer, emissivity) which are distinct from the parameters describing the zones modelling the cask cavity. Furthermore, the spatial configuration of the model (cask body in contact with zone 1 but separated from zone 5) can explain the stronger correlation between T_{cask} and T_1 .

The lower right 10x10 coefficients are (except for the diagonal) all very close to zero. This was expected as they correspond to the correlation coefficients between the 10 parameters that are randomly generated for each simulation. Therefore, they should be de facto independent and, as a consequence, uncorrelated.

The remaining coefficients describe the correlations between the parameters of the Python model and the temperatures of the different zones. The correlation matrix indicates that three parameters are significantly correlated (or anticorrelated) with the temperatures:

- ϵ_{int} , the cladding emissivity.
 ϵ_{int} is anticorrelated with the temperatures of the internal zones, in particular with the most internal ones: the correlation coefficients range from $r_{\epsilon_{int},T_1} = -0.54$ to $r_{\epsilon_{int},T_5} = -0.73$. On the contrary, ϵ_{int} is not at all correlated with the cask body temperature T_{cask} ($r_{\epsilon_{int},T_5} = -0.02$).
- P_{tot} , the total power loaded in the cask.
 P_{tot} is well correlated with the internal zones, with correlation coefficients ranging from 0.6 (r_{P_{tot},T_1}) to 0.65 (r_{P_{tot},T_5}). On the contrary, the correlation between P_{tot} and T_{cask} is rather weak ($r_{P_{tot},T_{cask}} = 0.27$).
- T_{room} , the room temperature.
 T_{room} is strongly correlated with the cask body temperature: $r_{T_{room},T_{cask}} = 0.93$. However, it is less correlated with the internal zones: $r_{T_{room},T_1} = 0.48$ indicates still a certain correlation, but already with zone 2 the correlation coefficient drops: $r_{T_{room},T_2} = 0.29$. The correlation with the most internal zone is weak: $r_{T_{room},T_5} = 0.15$.

The other parameters of the model present very low (< 0.26 in all cases and < 0.1 in most cases) correlation coefficients with the temperatures.

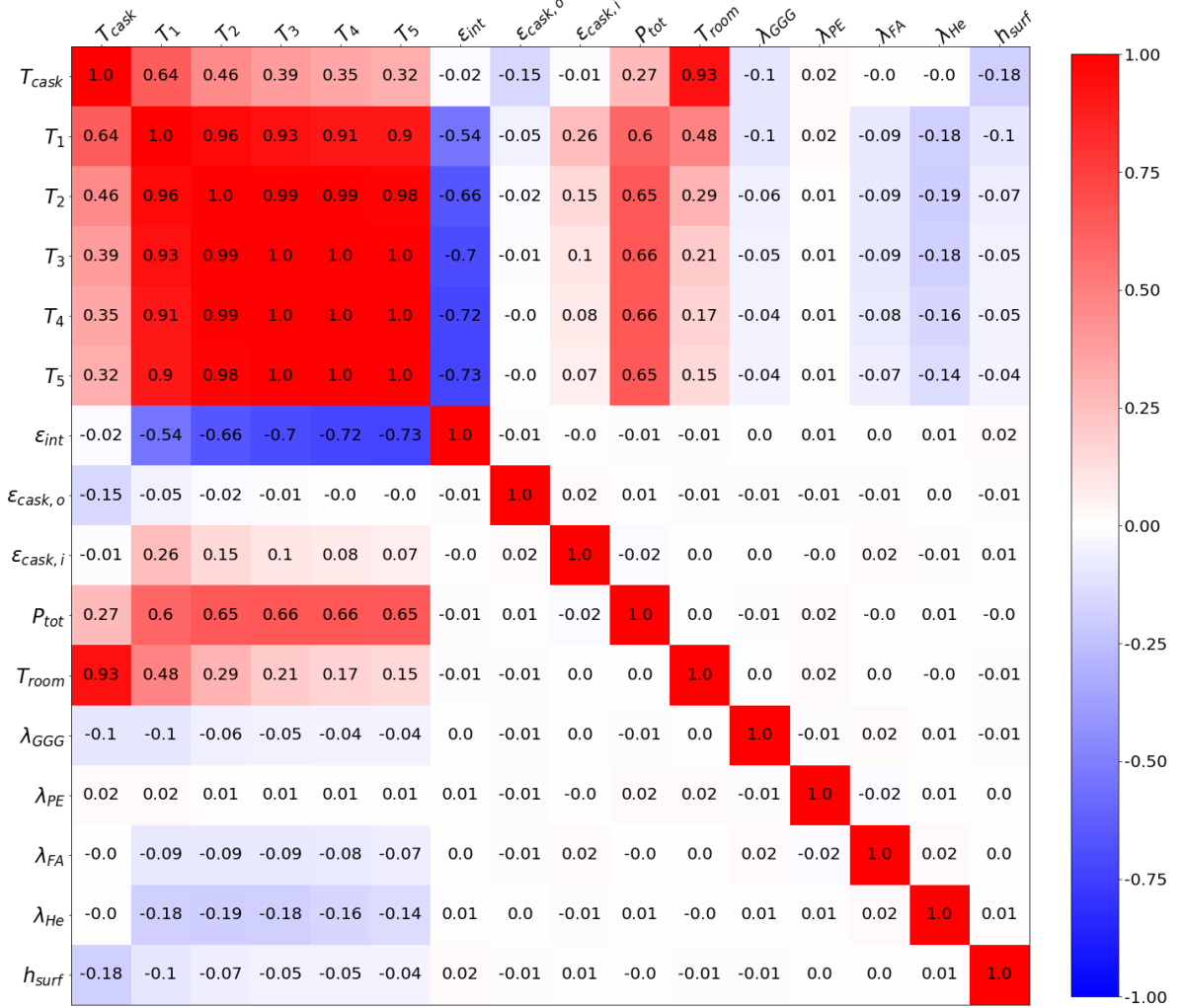


Figure 2.17: Correlation matrix consisting of the Pearson coefficients r for each couple of parameters and/or temperature results from the Python model. The temperatures of the different zones of the model are strongly correlated (upper left red sub-matrix), except for the cask body, which is less correlated to the more internal zones. The parameters of the model are randomly generated for the simulations and therefore independent. This can be seen with the near zero coefficients (white cells) for the lower right part of the matrix. Concerning the correlations between parameters and temperature results, three parameters appear particularly correlated. The cladding emissivity ϵ_{int} is anticorrelated (deep blue cells) with the 5 zones corresponding to the cask internal part (r ranges from -0.54 to -0.73) but not with the cask body ($r = -0.02$). P_{tot} is correlated with the same zones (r ranges from 0.6 to 0.65 for T_1 to T_5 , but $r = 0.27$ with T_{cask}). And T_{room} is correlated mainly with the cask body ($r = 0.93$) but less with the internal zones: $r = 0.48$ with T_1 , but decreases to 0.29 with T_2 and 0.15 with T_5 .

2.2.5 Summary on the Python model

In this section, we presented a semi-analytical cask model (*Python model*) inspired by the CASTOR[®] V/19 cask. This model is based on fundamental physics equations, includes strong homogenization assumptions and is implemented with the programming language Python. The results provide good orders of magnitude of the temperatures expected in a loaded cask.

The model can be easily adapted to both steady-state and transient calculations, and for different boundary conditions. Thus, we first determined the temperature distribution in the case of a cask loaded with 39 kW for a room temperature of 25 °C. Then transient calculations corresponding to accidental scenarios have been performed: starting from a room temperature of 25 °C, this temperature has been increased to 600 °C (resp. 800 °C) for 1 hour (resp. 30 min), before returning to 25 °C (Fig. 2.12 and Fig. 2.13). Finally, the effect of daily room temperature variations on the cask temperature has been investigated with a further transient calculation (Fig. 2.14).

The simplicity of the Python model offers further advantages. It would be easy to couple this model to further models or codes, for instance fuel performance codes, to analyse temperature-dependent mechanical properties of fuel rods. Furthermore, due to the short computational time, a sensitivity analysis involving 7000 simulations has been performed to identify the most relevant parameters. The resulting correlation matrix between 10 input parameters and the temperatures has been determined and discussed (Fig. 2.17). Room temperature, decay heat and cladding emissivity were found to be the most relevant ones.

2.3 COBRA-SFS CASTOR[®] V/19 model

In the previous section, we presented a semi-analytical model based on fundamental physics equations and including strong homogenization assumptions. Although this model offers many advantages, it is not sufficient when detailed temperature distributions are required. The following section presents a new model, also inspired by the CASTOR[®] V/19 cask from GNS, but built with the thermal-hydraulic code COBRA-SFS [19]. The level of details of this model is significantly higher than for the Python model and, consequently, the results are much more detailed.

This section first includes a brief description of the thermal-hydraulic code COBRA-SFS. Then, the cask model is described, as well as its validation through the comparison with other codes. A sensitivity analysis is conducted, focussing on the influence of the room temperature and the gaps between adjacent solid structures. Finally, different application cases are presented: a steady-state for a homogeneous load of 39 kW, a drying process (transient, with a vacuum phase followed by a helium refill), 100 years of storage (gradual decay heat decrease resulting in a temperature decrease), and different inhomogeneous loading schemes (missing fuel assemblies or *special assemblies* with increased decay heats).

2.3.1 Short description of the thermal-hydraulic code COBRA-SFS

COBRA-SFS is a thermal-hydraulic code derived from the COBRA code family. It is developed and validated since 1986 at Pacific Northwest National Laboratory (PNNL), Richland, USA. COBRA-SFS was specifically developed to model spent fuel storage and transportation systems, in steady-state as well as in transient conditions. It uses a finite-difference approach to predict flow and temperature distributions in the spent fuel storage system and the fuel assemblies. Heat exchanges include two-dimensional radiative and three-dimensional conductive heat transfers, as well as natural or forced convection [16–19].

COBRA-SFS does not provide any graphical user interface, neither for the

Table 2.5: Summary of input groups for COBRA-SFS [19].

Group	Description
PROP	Specifies fluid and solid material properties.
CHAN	Specifies flow field geometry.
VARY	Optional: specifies axial variation in channel flow area, and axial variation in width of flow path for lateral flow.
RODS	Specifies fuel rod geometry and thermal connections between fluid channels and rods.
SLAB	Specifies slab node geometry, defines slab thermal connection types, and interconnecting “map” of solid conduction nodes.
RADG	Specifies input to define thermal radiation exchange factors for rod arrays and slab nodes.
HEAT	Specifies input for Nusselt number correlations for the total system energy solution (fluid, rods, and slabs).
DRAG	Specifies input for wall friction and form drag correlations for fluid energy solution.
BDRY	Specifies thermal boundary conditions for the radial side(s) of the model, and defines the geometry and boundary conditions for the optional upper and lower plenum models.
OPER	Specifies overall flow or pressure drop axial boundary conditions, and heat generation rate in fuel rods.
REST	Special addition to simplify the input of heat generation rates: for each assembly, the heat generation rate is specified in Watts.
CALC	Specifies calculational parameters for numerical solution, including damping options and convergence criteria; specifies time step size and overall duration for (optional) transient calculations.
OUTP	Specifies user-defined parameters governing output options for channels, rod, slab nodes, fluid flow gaps; specifies time interval(s) for standard output and other special output options in transient calculations.
ENDD	Final group flag to terminate reading of COBRA-SFS input file and signals the code to stop looking for additional input groups.

input nor for the output processing. The input is complex and rigorously structured, with exacting format requirements. Input files are divided into input groups, some are always required while other are optional, depending on the model and simulation conditions (transient or steady-state for

instance). The input groups are listed and briefly described in Table 2.5. A more detailed description of the main input groups is included in Appendix 5.6. Furthermore, a general overview of the different steps required for the development of a new COBRA-SFS model is given in Appendix 5.5.

2.3.2 Model description

The COBRA-SFS generic cask model inspired by the CASTOR[®] V/19 (referred to as *CASTOR model* in the following) consists of 568 solid nodes, shown in Fig. 2.18, and 36 axial layers. Each layer is 12.25 cm in height, thus the 36 layers cover 441 cm, which corresponds to the height of the fuel assemblies. The 568 solid nodes are distributed as follows: 196 nodes for the 19 fuel assembly compartments made of steel (green numbering in Fig. 2.18), 120 nodes for the aluminium structures (violet nodes and numbering in Fig. 2.18) and 252 nodes for the cask body (blue numbering). The 252 nodes of the cask body are divided into 7 rings of 36 nodes each, corresponding successively to a pure cast iron region, a homogenized ring including cast iron and a row of polyethylene rods, a second pure cast iron ring, a second homogenized ring corresponding to cast iron and polyethylene rods, a third pure cast iron ring, the cooling fins (also made of cast iron) and the cask surface (zero thickness, but useful to define boundary conditions on the cask surface and determine the surface temperature).

The model includes 18x18-24 PWR fuel assemblies, which are modelled pin by pin. Thus, the model yields temperature values for each of the 18x18 rods from all 19 fuel assemblies and at each of the 36 axial layers. We assumed a single cladding type, characterized by a thermal conductivity $\lambda = 17.3 \text{ W m}^{-1} \text{ K}^{-1}$ ($10 \text{ Btu h}^{-1} \text{ ft}^{-1} \text{ }^\circ\text{F}^{-1}$). Cladding heat capacity and density, as well as UO₂ conductivity, thermal capacity and density are also defined (input group RODS, subgroup RODS.4), but are only used for transient calculations. Indeed, in the case of steady-state calculations, the fuel material is expected to have a limited influence on the temperature results and the fuel rod power is applied at the inner surface of the cladding as a boundary condition. Spacer grids are not directly modelled but loss coef-

2.3 COBRA-SFS CASTOR[®] V/19 model

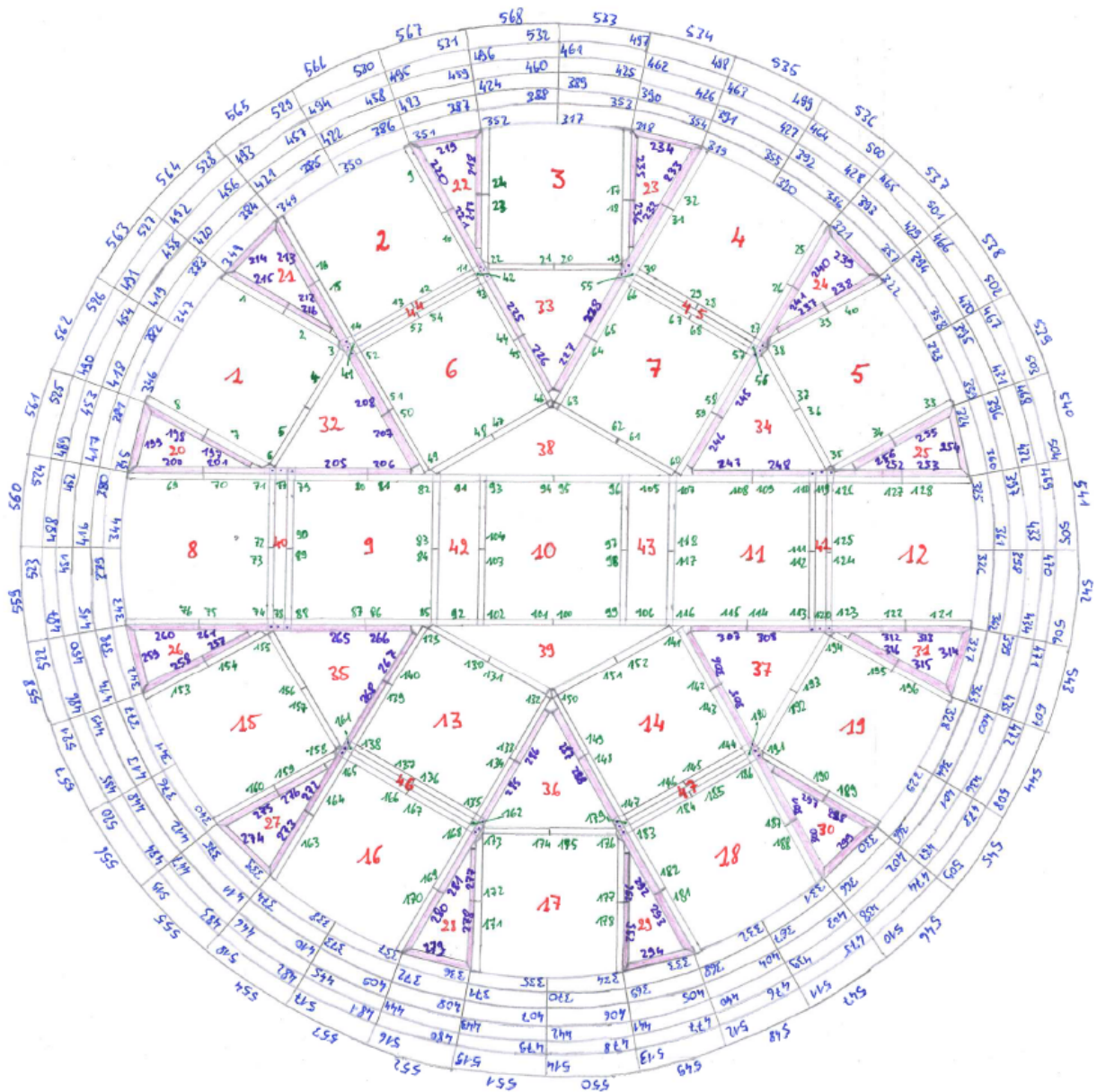


Figure 2.18: Diagram of the generic model. The red numbers identify the assemblies: first the fuel assemblies (1 to 19), then the *unrodded assemblies* (20 to 47). The other numbers identify solid nodes. The green numbering concerns steel structures (fuel compartments), from node 1 to node 196. The purple numbering concerns aluminium structures (corresponding nodes have been coloured in purple to distinguish them from steel nodes, which are left blank), from node 197 to node 316. Finally, the blue numbering corresponds to nodes representing the cask body. It starts with node 317 and ends with node 568, building 7 rings corresponding to the different layers (and materials) of the cask body. Note that the cask body is not on scale.

ficients for the helium flow are applied at the axial locations of the grids. The cask is filled with helium at a pressure slightly below 1 bar. Within each fuel assembly, 19x19 helium channels are modelled, 4 rods defining the corners of one channel. Within the basket structures, 28 further helium channels (much larger than the fuel assembly channels) are modelled. Helium properties were taken from NIST database [37].

A few homogenization assumptions were taken concerning the cask body. A homogenized medium is defined for the 2nd and 4th rings of nodes in the cask body, to take into account the polyethylene rods included in the cast iron. An equivalent thermal conductivity has been calculated assuming polyethylene and cast iron to be in parallel (resp. in series) for thermal connections along the radial and axial (resp. azimuthal) directions. The theory of equivalent conductivities has been detailed in section 2.1.1.

In the final model, many geometrical gaps (imperfect connection between two structural elements) have been taken into account. Those gaps are explicitly defined within the thermal resistances as additional terms given by $R_{gap} = \mathcal{W}/(\lambda \cdot \mathcal{S})$ (Equation 2.4 from section 2.1.1.1), with \mathcal{W} the width of the gap, λ the thermal conductivity (without temperature dependency) of the gas filling the gap and \mathcal{S} the surface of the nodes facing the gap.

Heat transfer mechanisms include conduction (with consideration of gaps), convection and radiation. Conduction is calculated by COBRA-SFS both in solids and gas (helium). Convection correlations are used for helium in the cask and at the external cask surface for air. Radiative heat transfers are calculated within the fuel assemblies (from rod to rod as well as between rods and basket structures), within the basket structures and between the cask external surface and the environment. View factors are defined to precisely determine the radiative exchanges inside the cask.

Concerning the boundary conditions, at the top and bottom of the model, COBRA-SFS provides options to model “plenum regions”. This consists in defining a series of regions to connect the top (resp. bottom) of the fuel assembly region to the environment, using thermal connections. In the CASTOR model, we defined both upper and lower plenums.

Different loading schemes have been simulated, as for instance a homogeneous loading of 39 kW (maximum power for this type of cask), corresponding to 2052 W per fuel assembly. Concerning the decay heat profile, different profiles have been tested including simple, flat profiles and more detailed profiles, such as the one given in the GRS benchmark specification [38] (decay heat calculation performed with the GRS code OREST [39]). Each calculation, for a given loading scheme and a given decay heat axial profile, corresponds to a specific COBRA-SFS input file.

The model provides, at each of the 36 axial layers, temperature results for all 568 solid nodes, 18x18 fuel rods of the 19 fuel assemblies, 19x19 helium channels of the 19 fuel assemblies, and 28 helium channels within the basket structures. COBRA-SFS needs around 10 minutes to perform one steady-state simulation with this model, using a single processor.

2.3.3 Model validation: code comparison

The model validation represents a major challenge in the case of the CASTOR model. No measurements of temperatures inside a CASTOR[®] cask loaded with spent fuel assemblies are publicly available. A difficulty in recording these temperatures is due to the containment function of the cask, which should not be reopened once it has been closed. Temperature measurements for the cask surface are much more likely to have been performed, yet such data would not be easy to access either.

As no comparison of our model with experimental data was possible, we compared the results of the COBRA-SFS model with the results from two other models [29], shown in Fig. 2.19 and Fig. 2.20. Those models are also inspired by the CASTOR[®] V/19 cask and were built with COCOSYS [40] and ANSYS CFX [41]. They are briefly presented in the following and the temperature calculation results for the central fuel assembly are then discussed.

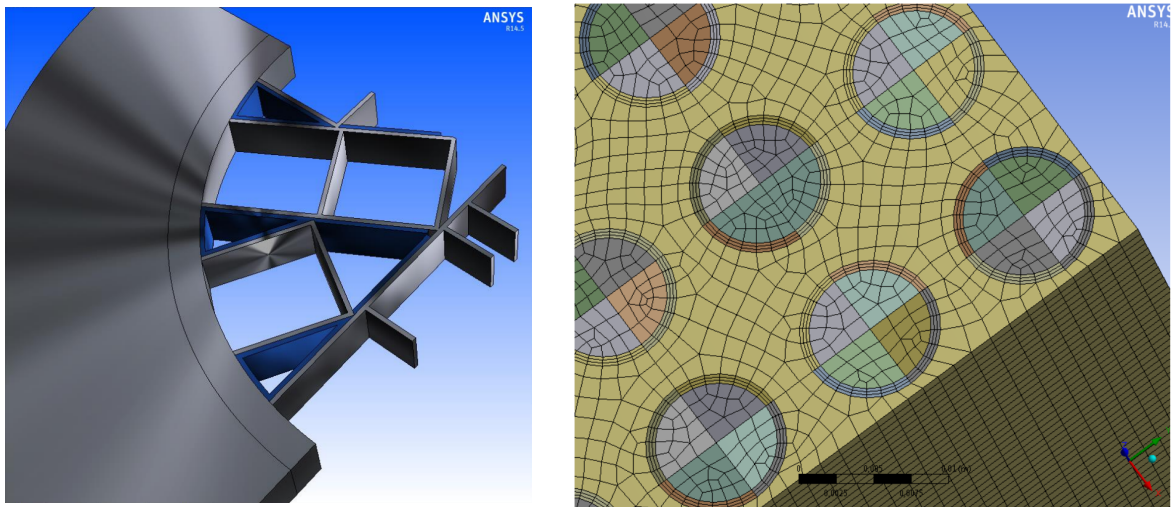
COCOSYS model and results

COCOSYS (**C**ontainment **C**ode **S**ystem) [40] is a thermal-hydraulic program developed at the German Gesellschaft für Anlagen- und Reaktorsicherheit (GRS) gGmbH. It has been mainly developed for the simulation of severe accidents, in particular with regard to containment issues. Unlike COBRA-SFS, it is not specifically dedicated to the modelling of storage systems and therefore does not offer as many capabilities for this type of simulation.

The cask model built with COCOSYS is two-dimensional and consists in an axial section of a quarter of the cask, as shown in Fig. 2.19a. As a consequence, only a quarter of the central fuel assembly (FA 10 in Fig. 2.18) is modelled. For this central assembly, the model includes 9 different types of fuel rods (B01 to B09 in Fig. 2.19b). For the other fuel assemblies, the model considers only four *heat slabs*: S2A and S2I for the intermediate assemblies⁶ and S1A and S1I for the external assemblies (see Fig. 2.19a). Radiative heat transfers between the fuel rods are modelled, as well as heat transfers to the surrounding fuel basket structures. Convection of the helium gas within the cask/assembly is neglected, which might have a significant impact on the temperature: increase of the average temperature. To limit this effect, heat conduction is modelled within the helium between the fuel rods and between the external rods and the surrounding fuel basket, in addition to the heat conduction in the solid structures. Another important simplification consists in the assumption that for the central assembly all rods in a row are similar. This might also have a significant impact on the results. Indeed, according to the COBRA-SFS and ANSYS CFX models, the temperature difference between the rods on the outermost row (B09 in Fig. 2.19b) can reach 20 °C. This effect is even stronger for the other fuel assemblies, as each of them is modelled with only two different heat slabs.

⁶Three categories of fuel assemblies can be distinguished in the CASTOR[®] cask: FA 10 is the *central assembly*, FA 6, 7, 9, 11, 13 and 14 are referred to as *intermediate assemblies*, and the other assemblies as *external assemblies*. See Fig. 2.18.

condition for the fuel assembly basket. The fuel assembly baskets and cask body were modelled in another simulation with ANSYS CFX, excluding the fuel assemblies (see Fig. 2.20a). It was found with this model of the fuel assembly baskets that the temperature of the basket structure surrounding the central fuel assembly would be about 13 °C higher, compared to COCOSYS results.



(a) ANSYS CFX model for the cask body and basket structures.

(b) Visualization of the nodalization of a quarter of the central fuel assembly with ANSYS CFX.

Figure 2.20: Modelling work inspired by the CASTOR[®] V/19 and performed using ANSYS CFX. It includes two models: one for the cask body and basket structures (a) and one for the central fuel assembly (b). For the central fuel assembly, the model represents a 10 cm long axial segment of a quarter of the assembly and uses nearly 1.5 million elements. Taken from [29].

Discussion of results

Results yielded by COCOSYS, ANSYS CFX, and COBRA-SFS models are plotted in Fig. 2.21. They correspond to a cask loaded with 39 kW equally distributed between the 19 fuel assemblies. The cladding temperature is given for two different series of fuel rods, corresponding respectively to the hottest (“upper” temperatures) and coldest (“lower” temperatures) rods of each row (see diagram in the bottom left-hand corner of Fig. 2.21). Only one curve corresponds to COCOSYS, as all rods of a row are assumed similar. For the other two models, two curves are plotted.

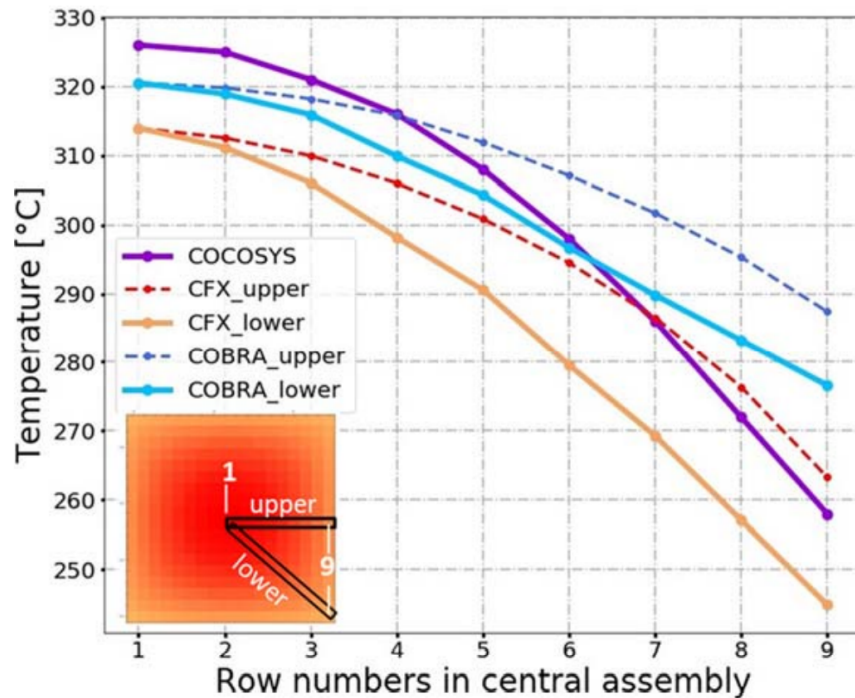


Figure 2.21: Comparison of the COBRA-SFS model with COCOSYS and CFX models. The curves represent the temperature of rods from different rows of the central fuel assembly. Row 1 corresponds to the central rods, while row 9 consists of the rods on the edge of the assembly. As all rods from a row do not present the same temperature, two temperatures per row have been plotted: the hottest (*upper*) and the coldest (*lowest*). The row numbering and the position of the *upper* and *lower* rods is shown in the bottom left-hand diagram. For COCOSYS, only one temperature per row appears as the model assumes that the temperature is the same for all rods of a row. Taken from [42].

The COCOSYS model was built using the most conservative assumptions in the fuel assemblies: no helium convection, but heat conduction within the helium, and radiative exchanges, but limited to neighbouring rods. The ANSYS CFX model also includes conservatism due to some homogenization, a limited consideration of convection and a fixed temperature of the fuel assembly basket based on COCOSYS results. The conservatism in COCOSYS and ANSYS CFX models could explain the stronger temperature gradients (especially by COCOSYS results, but also by ANSYS CFX) between the inner and the outer rods. The temperature differences within the assembly come to approximately 70 °C with COCOSYS, 65 °C with ANSYS CFX

and 45 °C with COBRA-SFS. We can also observe with COBRA-SFS and ANSYS CFX results that, for a given row of rods, ANSYS CFX yields the largest temperature variations. This can also be explained by more conservatism in the heat transfers.

Furthermore, as mentioned in the ANSYS CFX model description, the second simulation (representing the cask body and the basket structures without fuel assemblies) found that the temperature applied as boundary condition was too cold: according to the second ANSYS CFX model, the temperature of the basket structure enclosing the central assembly should have been 13 °C hotter. Concerning the basket structure, the COBRA-SFS model yields the highest temperature: approximately 270 °C at the hottest axial zone. The COBRA-SFS model includes further thermal resistances to take account of the imperfect connection between the basket structures and the cask body (see Fig. 2.28 for more details on the influence of the gaps on the temperature fields).

With regard to the uncertainties on the cask design and considering the differences in the assumptions and modelling choices, the results provided by the three models are still in good agreement. The comparison of the three models is not an optimal means of validation of the COBRA-SFS model, but given the lack of experimental data, this provides at least some additional confidence in the model results.

2.3.4 Comparison of the COBRA-SFS and Python models

To gain further confidence in the COBRA-SFS CASTOR model, we compared its results with the results from the Python model. In Fig. 2.22, steady-state calculations corresponding to the cask homogeneously loaded with 39 kW and by a room temperature of 25 °C are presented for both models: COBRA-SFS with the blue line and Python with the red line. The temperature profiles plotted correspond to the temperature along the cask section marked with the green dashed line on the background. [4]

COBRA-SFS modelling enables to visualize detailed temperature profiles within each of the five fuel assemblies crossed by the green line, as well

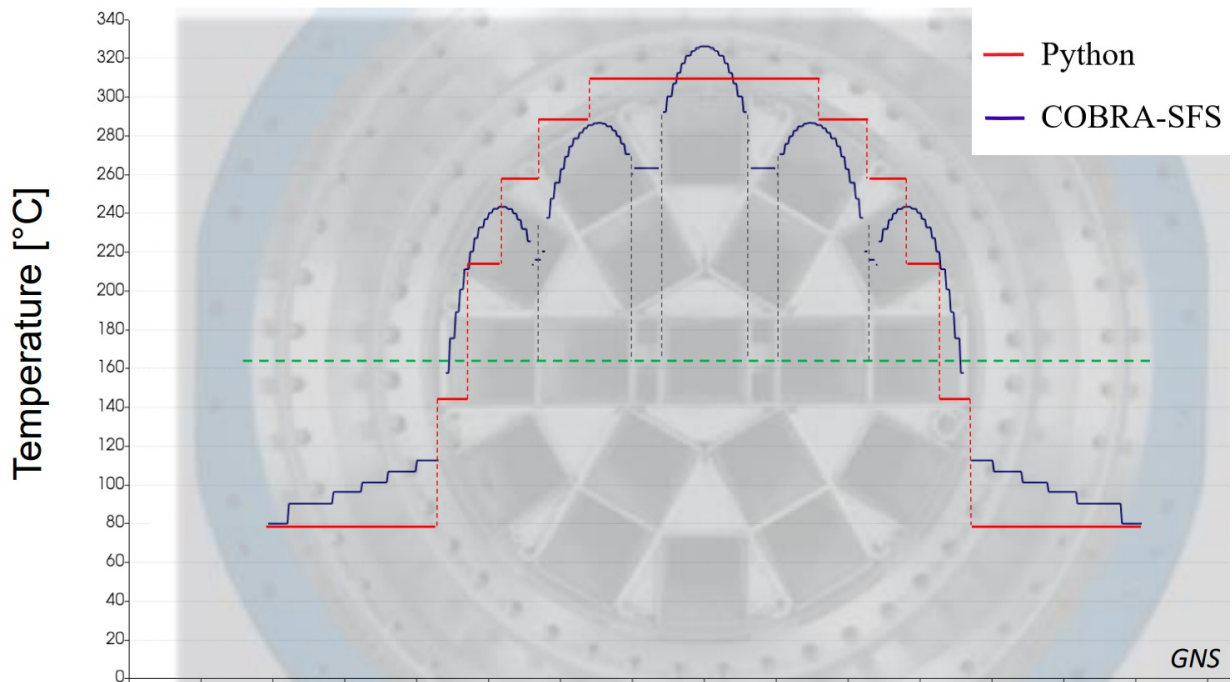


Figure 2.22: Comparison of the temperature calculated with the Python model and with COBRA-SFS for a homogeneous load of 39 kW and a room temperature of 25 °C. The temperatures plotted correspond to the temperature along the cask section marked with the green dashed line on the background. COBRA-SFS provides detailed results (blue line): the five fuel assemblies crossed by the green line can be well identified on the temperature profile and the cask body presents six temperature values as it consists of six rings in the COBRA-SFS model. The temperature profile calculated by the Python model (red line) only presents six temperatures as the model consists of six homogenized zones. Although the models have very different levels of detail, both models are in good agreement and correspondences can be established between the 6 zones of the Python model and the more detailed CASTOR model. Taken from [4].

as the temperature in the cask body. Thus, the two external fuel assemblies exhibit a temperature ranging from 157 °C to 243 °C, the intermediate assemblies ranging from 238 °C to 287 °C and the central assembly from 292 °C to 325 °C. Due to the modelling assumptions, the temperature in the cask body follows a step function with 6 values, ranging from 80 °C to 113 °C, as the cask body consists of six layers in the COBRA-SFS model (see Fig. 2.18 in section 2.3.2).

The temperature profile yielded by the Python model is simpler with in

total only six values, corresponding to the six zones of the model. However, we can observe that the six values reflect well the global shape of the temperature profile yielded by COBRA-SFS. It is thus possible to establish some equivalences:

- The zone modelling the cask body has a temperature of 79 °C, which corresponds to the temperature calculated by COBRA-SFS for the external part of the cask body.
- Zone 1 presents a temperature of 145°C, which approximately corresponds to the temperature of the coldest rods of the external fuel assemblies according to the COBRA-SFS model.
- Zone 2 presents a temperature of 215°C, which could correspond to an average temperature for the external assemblies.
- Zone 3 presents a temperature of 259 °C, which can represent an upper limit for the temperature of the external assemblies, or could correspond to cold fuel rods from the intermediate assemblies.
- Zone 4 presents a temperature of 289 °C, which approximately corresponds to the peak temperature in the intermediate fuel assemblies, or to cold fuel rods from the central assembly.
- Zone 5 presents a temperature of 311 °C, which could correspond to an average temperature for the central fuel assembly according to COBRA-SFS results.

Fig. 2.23 shows another comparison of both models, in the case of a transient calculation. The simulation corresponds to the first part of a drying process, when the loaded cask is taken out of the cooling pond, the water pumped out and vacuum drawn in the cask to further remove water. The cask is loaded with 39 kW and the simulation starts with a homogeneous temperature of 40 °C, which is assumed to be the thermal equilibrium for the cask in the cooling pond. At $t = 0$, we set vacuum conditions so that the temperature starts to increase. 80 hours under vacuum conditions are then simulated. This transient has been simulated with COBRA-SFS for

a thermomechanical benchmark organized by GRS [38] and is presented in more detail (including a further phase with helium refill) in section 2.3.6.2, Fig. 2.31.

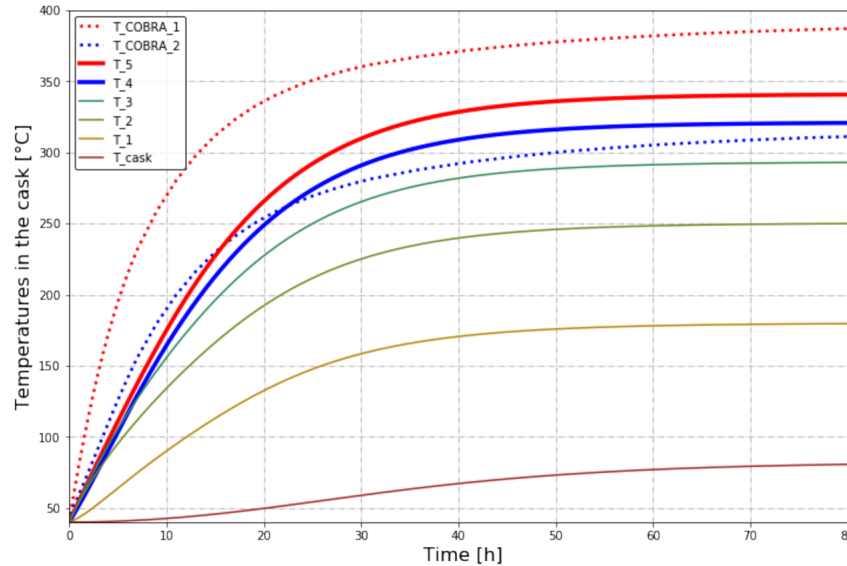


Figure 2.23: Comparison of COBRA-SFS and Python models on a transient calculation simulating the vacuum step of the drying process. The simulation starts with a homogeneous temperature of 40 °C corresponding to the cooling pond conditions, then the temperature increases as vacuum conditions are simulated. Plain line curves show the results of the Python model (6 zones), while COBRA-SFS results are plotted with dotted lines. The COBRA-SFS results are for the hottest (red curve) and coldest (blue curve) rods of the central fuel assembly. The model comparison on steady-state calculations indicated that zone 5 of the Python model could correspond to an average temperature for the central assembly, while zone 4 approximately corresponds to the cold fuel rods of the central assembly. These equivalences are still valid for this transient.

In Fig. 2.23, the temperature evolutions of the 6 zones of the Python model are plotted with the plain lines, while the two dotted curves represent COBRA-SFS results for the hottest and for the coldest rods of the central fuel assembly. The steady-state calculation presented in Fig. 2.22 suggested some equivalences between the two models. This can be observed on this transient too. In particular, we noted with the steady-state calculation that zone 5 of the Python model could correspond to an average temperature of the central fuel assembly. This remains valid on the transient calculation:

the red plain line (temperature of zone 5 from the Python model) lies mainly between the two dotted lines (hottest and coldest rods of the central fuel assembly, according to COBRA-SFS). Similarly, we noted on the steady-state calculation that zone 4 of the Python model corresponds approximately to the coldest rods of the central fuel assembly. This can also be observed in Fig. 2.22, as both blue lines present similar profiles.

We might note that the Python model predicts a slower temperature increase of the temperature. This might be due to the strong homogenization assumption. Indeed, during the transient, in a given zone the heat is homogeneously accumulated: the heat capacity of all materials included in this zone is used for any temperature variation. In the case of the COBRA-SFS model, the different elements of the model (fuel rods, helium, basket structures, cask body) are distinct and the heat generated by the fuel rods first heat up the rods from where it originates.

Although both models predict slightly different temperature evolutions, this transient further supports the validity of the CASTOR model, as well as the idea that the simplified model can provide good orders of magnitude. Furthermore, it is worth noting that the temperature distribution in a cask under normal storage conditions is rather smooth, independently of the different media (fuel, cladding, helium, steel). At the scale of the fuel assemblies, the fuel rods do not show any significant influence on the temperature distribution, as shown in Fig. 2.24. At the scale of the whole cask, the temperature distribution is also rather smooth and the temperature gradient is mainly radially oriented (see Fig. 2.25). This might be considered favourable for a homogenized model involving radial zones.

2.3.5 Sensitivity analysis

We performed a sensitivity analysis of the COBRA-SFS CASTOR model, focussing on the influence of the room temperature and of the gaps between adjacent solid structures.

Fig. 2.26 shows the temperature profiles of the hottest rod of the cask (centre of the central fuel assembly) in red, one of the coldest rods of the

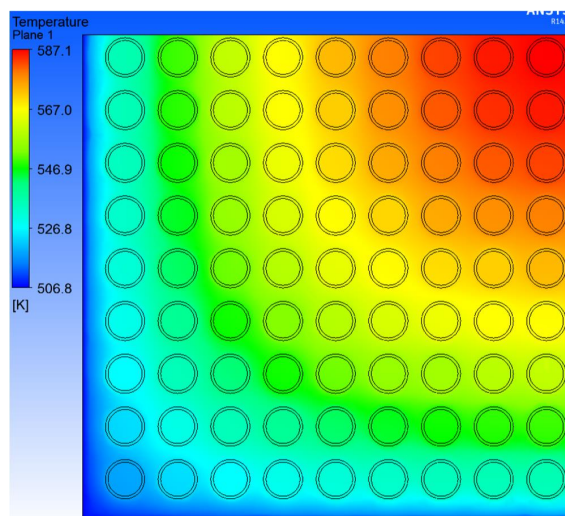


Figure 2.24: Temperature distribution in a quarter of the central fuel assembly, determined by the ANSYS CFX model. Taken from [29].

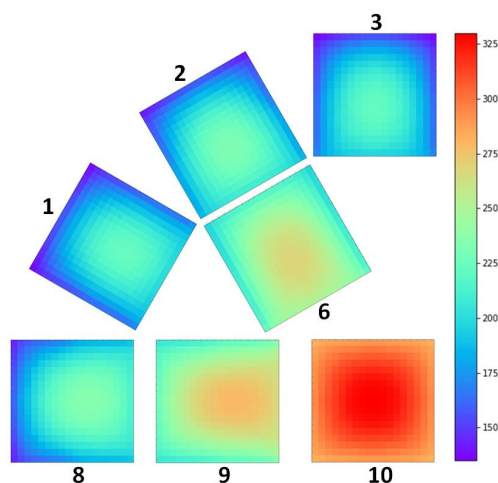


Figure 2.25: Temperature map for a quarter of the COBRA-SFS CASTOR model.

cask (“external rod”, facing the cask body) in green and the cask body in blue, for three different room temperatures: 10 °C, 25 °C and 40 °C.

We can first note that the room temperature variations have almost the same impact on the hottest rod, as on the external rod and on the cask body. The increase of 30 °C in room temperature leads to an increase of 26 °C for the cask body, of 24 °C (at the top) to 26 °C (at the bottom) for the external rod and of 21 °C (top) to 26 °C (bottom) for the hottest rod. This strong effect of the room temperature is not surprising: variations of the room temperature do not significantly change the heat fluxes inside the cask (the geometry and the related thermal resistances remain unchanged, as well as the heat sources), but set a new reference for the thermodynamic equilibrium. This point is described in more detail in section 2.4.2.2.

The slighter temperature variation (21 °C) at the top of the hottest rod might be related to the stronger influence of convective and radiative heat transfers in this region (upper part of the cask and hottest fuel assembly).

Another important parameter in the model consists in the imperfect connections between the different structures. Indeed, the basket structures are not perfectly bonded to the cask body internal surface. Similarly, aluminium

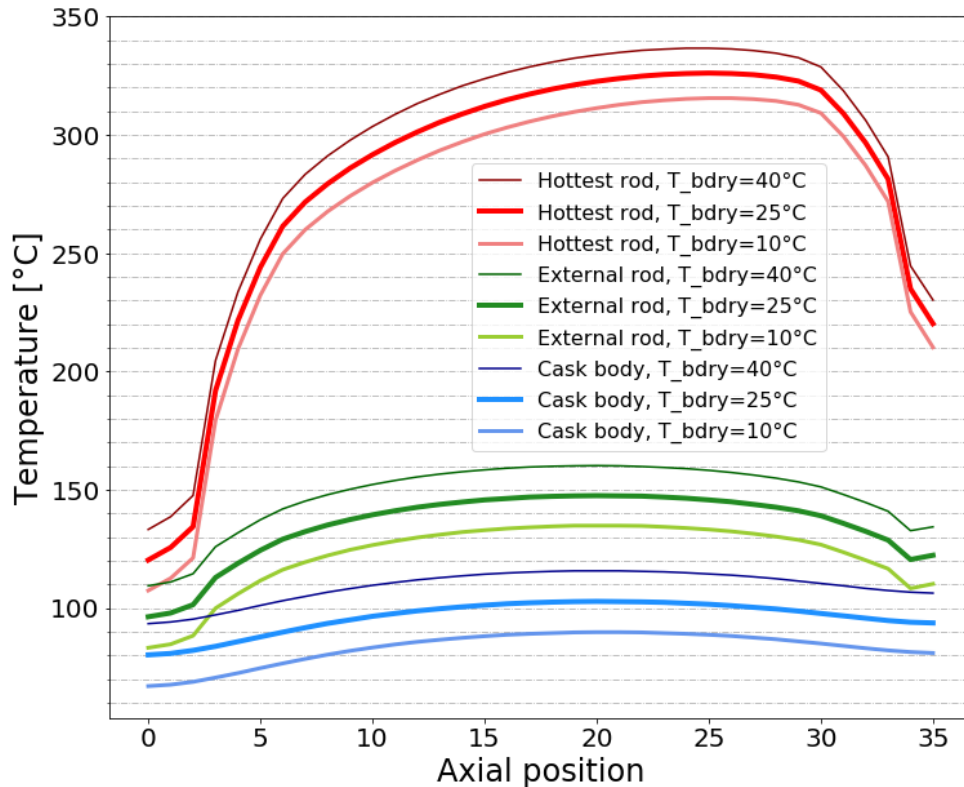


Figure 2.26: Temperature profiles of the hottest rod in red, an “external” rod (adjacent to the cask body internal surface) in green and the cask body in blue, for three different room temperatures: 10 °C, 25 °C and 40 °C.

and steel structures forming the fuel compartments are not perfectly bonded together. A perfect bond is neither easily feasible nor desirable, due to the large temperature variations the cask is expected to undergo: the different materials present different thermal expansion coefficients and therefore the temperature variations would result in internal stresses in case of strong bonds between the structures. Fig 2.27 shows a CASTOR[®] V/19 during loading operations. We can see that the different structures of the cask are not all perfectly connected but present clear separations.

Concerning the heat transfers, the imperfect connections, or gaps, between the different structures result in additional thermal resistances. Simulations were performed with the CASTOR model, in which we defined gap resistances corresponding to different gap thicknesses. Three configurations were

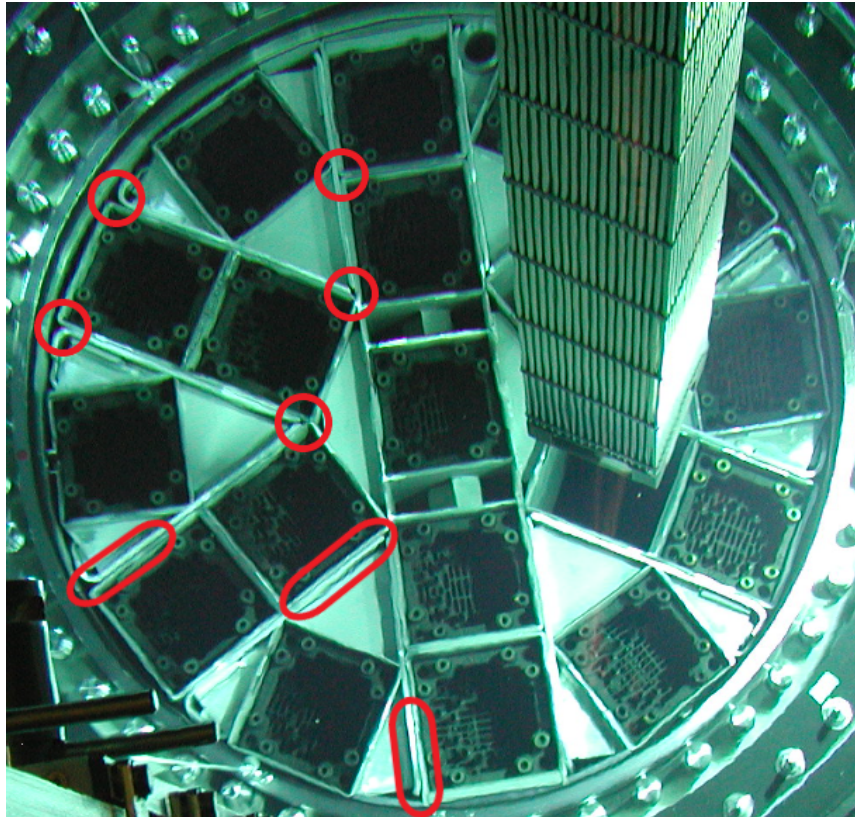


Figure 2.27: Picture of a CASTOR[®] V/19 under water during loading operations. Some of the most distinct gaps between the different components of the internal structures are highlighted in red. Adapted from [43].

simulated, based on discussion and qualitative assessment⁷:

- no gaps taken into account,
- 0.5 mm between aluminium and steel plates (basket structures) and 1 mm between basket structures and cask body internal surface, and
- 1 mm between aluminium and steel plates (basket structures) and 2.5 mm between basket structures and cask body internal surface.

Fig. 2.28 presents temperature profiles for the central assembly corresponding to the three configurations: (a) without gaps, (b) with small gaps and

⁷It seems impossible to determine exact gaps, but we can expect that a configuration with no gap and a configuration with a constant gap (concentric fuel basket inside the cask) of 2.5 mm constitute realistic boundary cases.

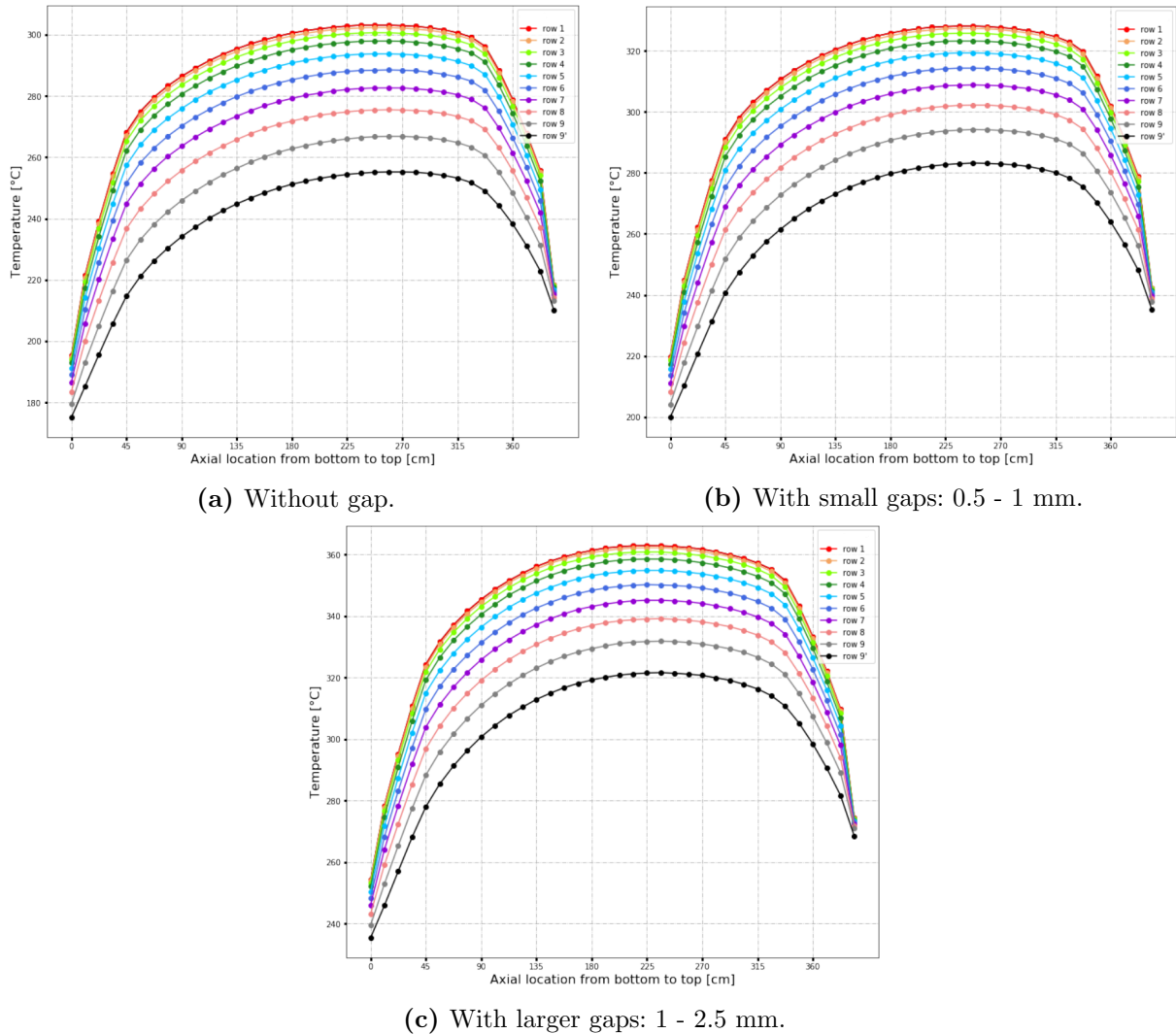


Figure 2.28: Temperature profiles in the central fuel assembly for a model a) without gap, b) with small gaps (0.5 - 1 mm) and c) with larger gaps (1 - 2.5 mm).

(c) with larger gaps. On each figure, we plotted the temperature profiles of the 9 rods located on the centre of each row (“upper” rods on the diagram of Fig. 2.21) and of the rod located at the corner of the fuel assembly (coldest rod of the fuel assembly). We can first observe that the gaps do not impact the shape of the temperature profiles. However, the overall temperature levels are strongly depending on the gaps: for instance, the maximum temperature reaches 303 °C without gap, 329 °C with small gaps (0.5 and 1 mm) and 363 °C with larger gaps (1 and 2.5 mm). Table 2.6 provides more precise temperature values. The last two columns show the tempera-

ture differences between the different cases: the small gap (1 mm) leads to an increase of 24 °C to 29 °C, while the larger gap (2.5 mm) further increases the temperature of 32 °C to 38 °C. We can retain the order of magnitude of + 25 °C per mm of gap.

Table 2.6: Impact of the gap thicknesses on the temperature of the central fuel assembly. This table presents the temperatures of the hottest rod (T_1), the rod in the middle of the 9th row (T_9) and the corner rod ($T_{9'}$) of the central assembly, in three cases: (a) without gap, (b) with small gaps (0.5-1 mm) and (c) with larger gaps (1-2.5 mm). The indices *max*, *bottom* and *top* refer respectively to the maximal temperature, the temperature at the bottom of the rod and the temperature at the top of the rod. The last two columns indicate the temperature differences between cases (a) and (b), and between cases (b) and (c).

Temperature	Case (a)	Case (b)	Case (c)	(b)-(a)	(c)-(b)
$T_{1,max}$	303 °C	329 °C	363 °C	26 °C	34 °C
$T_{9,max}$	267 °C	294 °C	332 °C	27 °C	38 °C
$T_{9',max}$	255 °C	284 °C	322 °C	29 °C	38 °C
$T_{1,bottom}$	195 °C	220 °C	255 °C	25 °C	35 °C
$T_{9,bottom}$	180 °C	204 °C	239 °C	24 °C	35 °C
$T_{9',bottom}$	175 °C	200 °C	236 °C	25 °C	36 °C
$T_{1,top}$	219 °C	243 °C	275 °C	24 °C	32 °C
$T_{9,top}$	213 °C	238 °C	271 °C	25 °C	33 °C
$T_{9',top}$	210 °C	236 °C	268 °C	26 °C	32 °C

We can conclude that the gaps between the different structures of a cask have a strong impact on the temperatures in the cask. Small gaps might induce significant increases in temperature. Unfortunately, it is impossible to determine precisely a “correct” gap. First, the exact design data from the constructor is proprietary and therefore unknown here. Second, the gaps are expected to vary anyway with time and space: the temperature variations over the cask lifetime are directly related to variations of the gap thickness due to expansion or contraction of the materials, and at a given time the gaps are not expected to be symmetrical. For instance, the basket can lean against one side of the cask body, closing the gap on this side but resulting in a larger gap on the opposite side.

We did not try to implement non-symmetrical gaps in the COBRA-SFS model: this would require to define specific thermal connections for each

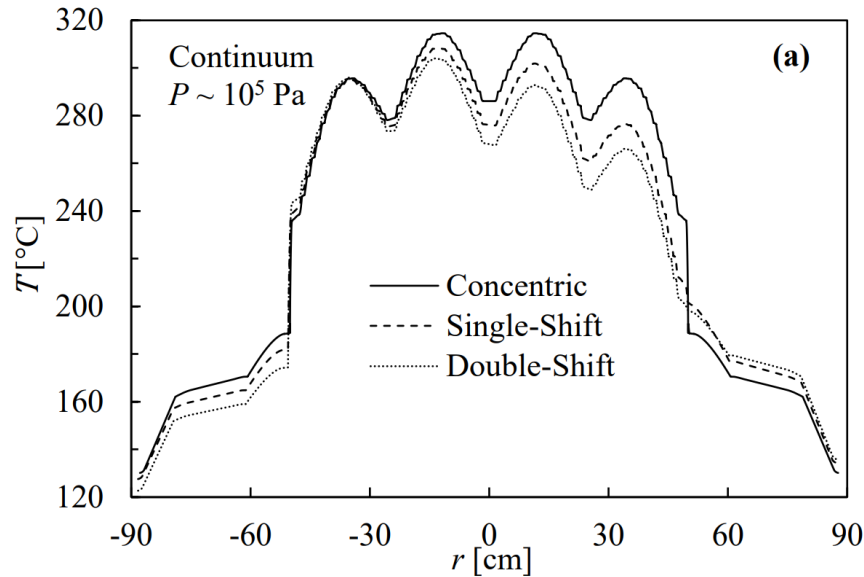


Figure 2.29: Temperature profile along a diagonal line through a TN-32 cask (identical to the cask presented in section 2.4), modelled using ANSYS. The three curves correspond to the cases of a concentric geometry (constant gap), a single-shift (the basket leans on one side of the cask) and a double-shift (the basket leans on two sides of the cask). The four humps correspond to fuel assemblies, while the more external parts with lower temperatures correspond to aluminium rails (and helium) and to the cask body (for $|r| \geq 60$ cm). Taken from [44].

of the 36 nodes that constitute the internal surface of the cask body and to proceed with the related necessary changes in the input file (see Appendix 5.6 for more details on the input groups). Yet, this issue was tackled by a research group at the University of Nevada, Reno. Their results are presented in [44] and show in particular that a constant gap (concentric fuel basket inside the cask) leads to the highest peak temperature, as shown in Fig. 2.29. If the basket leans on one side of the cask, this results in a concentration of the heat flux along this direction, leading to lower temperatures in the fuel assemblies on this side (better heat removal) but to a slight increase in the cask body temperature (higher heat flux). The opposite side of the cask is little impacted: in Fig. 2.29, the temperature of the left fuel assembly remains unchanged in all three cases plotted. This might be explained by the fact that, on the one hand, the increased gap restrains the heat flux but, on the other hand, more heat is removed through the opposite side

(i.e. towards the right in Fig. 2.29), which reduces the heat flux on the side of the increased gap (i.e. towards the left in Fig. 2.29). This reduced heat flux on the side with the increased gap can explain the lower cask body temperature on this side. On the contrary, on the right part of Fig. 2.29, the temperature of the cask body increases when the basket leans on the cask, which can be explained by a higher heat flux.

2.3.6 Temperature calculation results

In this section, we present some results obtained with the CASTOR model for steady-state and transient calculations.

2.3.6.1 Cask homogeneously loaded with 39 kW

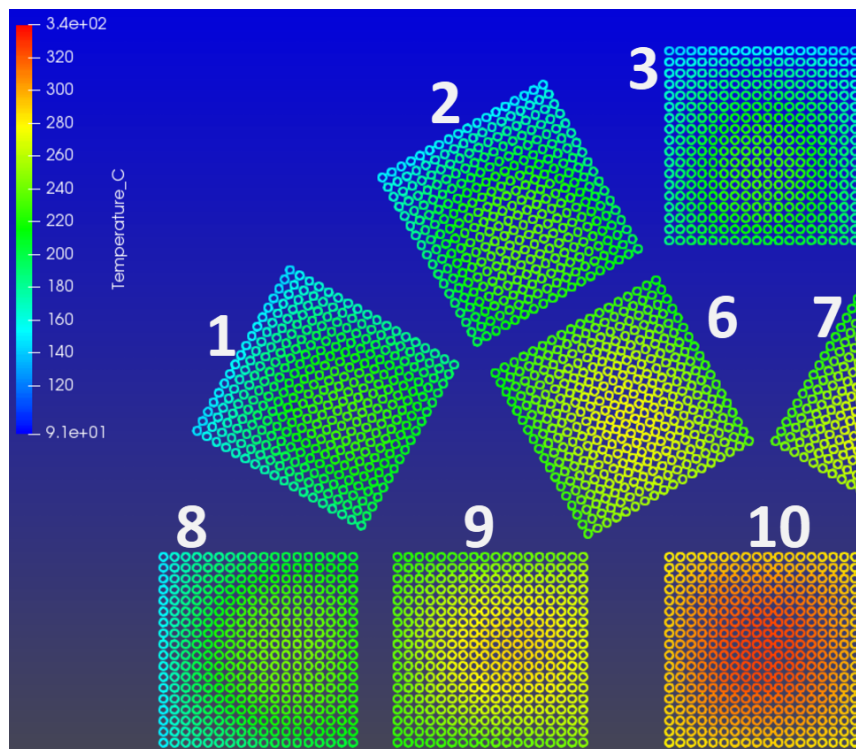


Figure 2.30: Temperature distribution [°C] at the hottest axial position (294 to 306 cm) for a total power load of 39 kW equally distributed between the 19 fuel assemblies and for a room temperature of 25 °C. Taken from [42].

Fig. 2.30 shows the temperature distribution in the cask for the hottest axial position (from 294 to 306 cm) assuming a homogeneous maximum load (39 kW) and a typical axial power profile. The temperature ranges from 150 °C to 240 °C for the external assemblies, from 220 °C to 285 °C for FA 9, and from 280 °C to 325 °C for FA 10. FA 9 is slightly hotter than FA 6 due to the influence of FA 10. Similarly, FA 2 and FA 8 are hotter than FA 1 and FA 3, due to the influence of FA 6 and FA 9 respectively. We can also note that, except for FA 10, the hottest spots of the assemblies are slightly shifted from the centre of each assembly towards the centre of the cask. [42]

2.3.6.2 Drying process

Fig. 2.31 presents the results of a transient calculation performed with COBRA-SFS. This simulation aimed at modelling the drying process, initial step of the dry storage, which follows the wet storage in cooling pond. For the simulation, we assumed the central fuel assembly to have a power of 2208 W and the remaining 18 fuel assemblies a power of 2044 W ⁸. Prior to the transient, the equilibrium state was calculated assuming the cask being filled with helium and at an ambient temperature of 25 °C.

As starting point of the simulation, the temperature of the whole cask (including fuel assemblies, internal structures and cask body) is set to 40 °C, which is the assumed temperature of the cooling pond. In COBRA-SFS, this was achieved by turning off the decay heats of all fuel assemblies (no power generated) and setting the boundary temperature on 40 °C. Under those conditions, as no heat is generated in the cask, this preliminary steady-state calculation trivially yields a homogeneous temperature of 40 °C in the whole cask.

⁸For a realistic loading scheme, we would not expect to find the highest decay heat placed at the centre of the cask. The loading scheme simulated here resulted from a decay heat calculation performed in the frame of the GRS thermomechanical benchmark [38], for which the decay heat of the central fuel assembly was calculated for 100 years of storage according to given reactor operation conditions. The decay heat of the other 18 fuel assemblies (2044 kW) was defined so that the total power loaded in the cask corresponds to 39 kW at the beginning of the dry storage and afterwards decreases proportionally to the decay heat of the central fuel assembly.

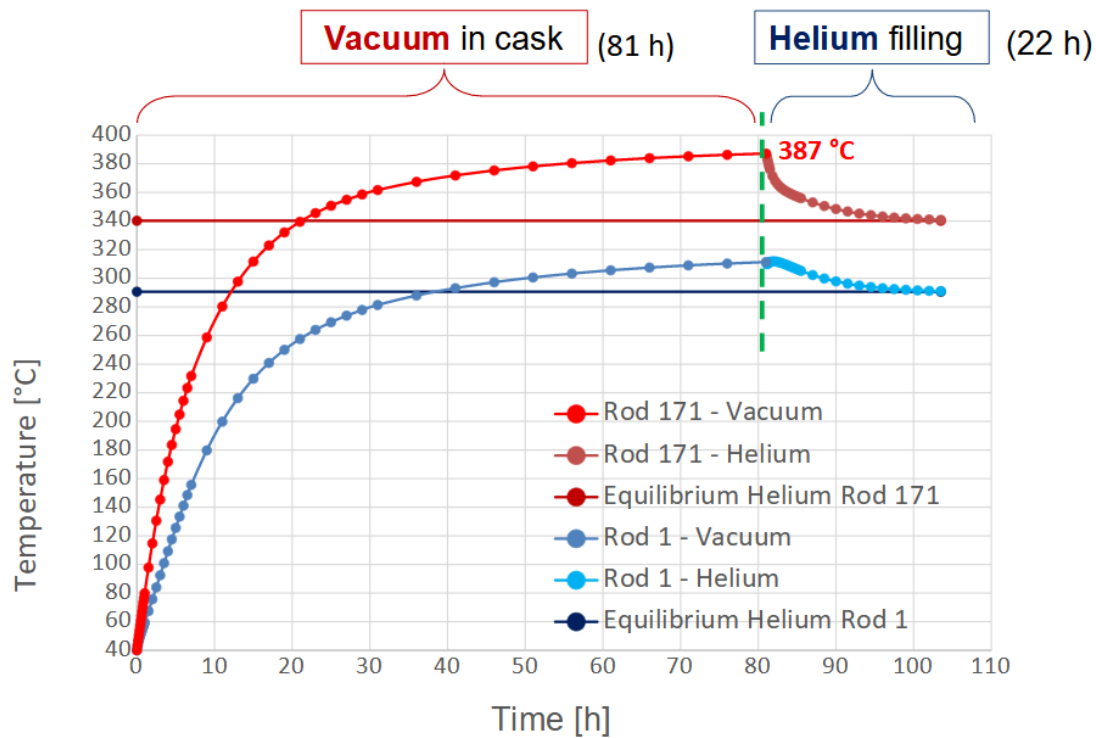


Figure 2.31: Temperature evolution from cooling pond to dry storage: At the beginning of the simulation, the whole cask (including the fuel assemblies) is at a temperature of 40 °C, corresponding to the cooling pond conditions. Then, the simulation consists in two phases: the first 81 hours correspond to vacuum conditions, while in the following 22 hours the cask is filled with helium. The red curve shows the temperature of the hottest rod of the central fuel assembly, while the blue curve shows the temperature of the coldest rod of the central fuel assembly. The red and blue straight lines correspond to the equilibrium temperatures of the hottest and coldest rods respectively, for the cask filled with helium.

The decay heat generation is then turned on at $t = 0$ s (beginning of the drying process transient) and the fluid properties are deliberately changed to limit the heat transfer mechanisms inside the cask to conduction and thermal radiation, thus assuming no effective convection due to the very low gas pressure in the cask. This approach neglects any transition between wet storage and vacuum conditions (in practice, water from the cask is not instantaneously pumped out of the cask) but seems a reasonable approximation: the temperature increase is progressive over several hours (even days) due to the high heat capacity of the cask, and the relatively short pump

out operations present conditions similar to the cooling pond (efficient heat removal by water at a temperature between 40 °C and 100 °C).

After 81 h in vacuum conditions, the fluid parameters are changed again: convection is turned back on as the cask is now assumed to be refilled with helium. After refill, 22 h were simulated, which was a sufficient time to reach an equilibrium state.

In Fig. 2.31, four curves are drawn. The hottest rod (central rod) and the coldest rod (corner rod) of the central fuel assembly are considered. For both of them the cladding temperature evolution over the transient is plotted as well as a straight line corresponding to the final equilibrium temperature of the rod in helium atmosphere.

At first, the cladding temperature increases quickly. After 21 h under vacuum conditions, the temperature of the hottest rod already exceeds the peak cladding temperature reached with helium atmosphere (340 °C). At the end of the 81 h under vacuum conditions, the temperature reaches 387 °C. The helium refill leads then to a decrease of the temperature. The temperature of the hottest rod decreases immediately and, within the 22 h simulated after refill, the temperature drops to the equilibrium temperature of 340 °C. The temperature of the corner rod does not decrease instantaneously: an inertia effect probably occurs because of the extra heat accumulated in the central rods of the fuel assembly. The corner rod also reaches its equilibrium temperature (290 °C) within the 22 h. [4]

2.3.6.3 Temperature evolution over 100 years of storage

The following results were obtained by using the described model with slightly enhanced assumptions. Namely, the thermal connections defined by thermal resistances without temperature dependence were changed to definitions involving geometrical factors and enabling to take into account the temperature dependence of the material thermal properties (see Appendix 5.6, Listing 5.5, for more details on the different ways to define thermal connections between solid nodes). Furthermore, in this version of the model, a more detailed modelling of the plenum regions (uppermost and lowest parts of the cask) was implemented and the boundary temperature

at the bottom of the cask was set to 40 °C instead of 25 °C as used in the former simulations. These changes led to slightly higher temperatures within the cask: the peak cladding temperature in the case of a cask homogeneously loaded with 39 kW reached 341 °C, instead of 325 °C in the case of the simulation presented in Fig. 2.30. It is worth noting that the described enhanced assumptions do not significantly change the previously discussed sensitivities in section 2.3.5.

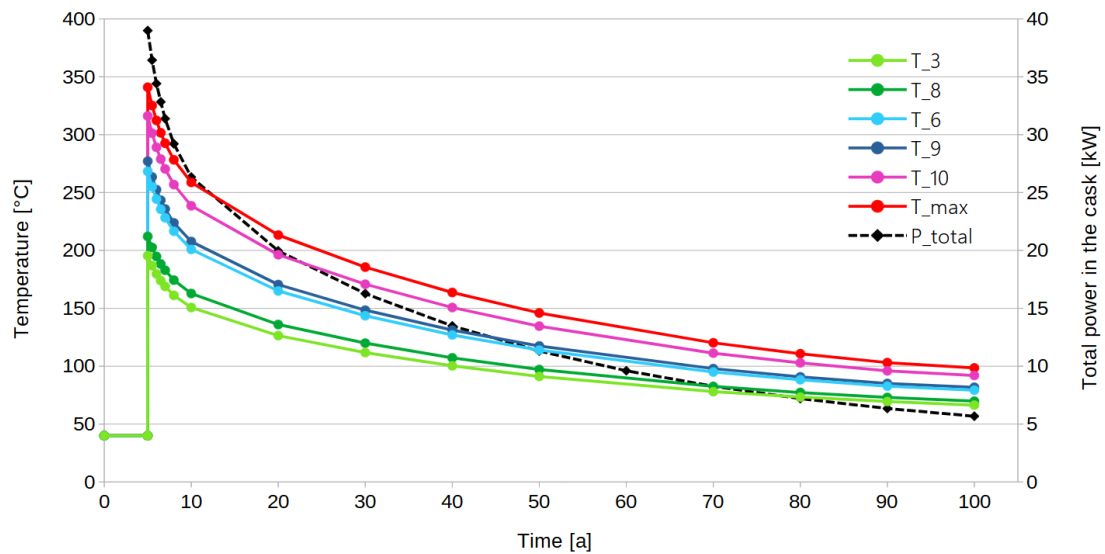


Figure 2.32: Temperature evolution over 100 years of storage. The first 5 years represent the wet storage, for which we assumed a temperature of 40 °C. Then, the sudden increase of the temperature corresponds to the beginning of the dry storage (drying process). Over the following 95 years, the temperature values result from COBRA-SFS calculations. The temperature decreases progressively due to the decay heat decrease. The curves correspond to the average temperatures of FA 3, 6, 8, 9 and 10, as well as the maximum temperature of the cask. The total power in the cask is plotted with the black dotted line (right-hand side y-axis).

Fig. 2.32 presents the evolution of the assembly-average temperatures of FA 3, FA 6, FA 8, FA 9 and FA 10, as well as the maximum temperature of the cask (central rod in FA 10), at the hottest axial position and for 100 years. $t = 0$ is assumed to be the end of reactor operations and the first 5 years correspond to wet storage, during which the temperature of the fuel assemblies remains low (set to 40 °C on the figure). At $t = 5a$, the dry storage starts and the decay heat evolution is plotted, as well as the tem-

perature curves calculated by COBRA-SFS. The decay heat, plotted with the dotted black line (y-axis on the right-hand side of the diagram) starts at 39 kW and decreases progressively, proportionally to the decay heat calculation presented in [38]. At the beginning of the dry storage, the maximum temperature reaches 341 °C and the coldest fuel assembly (FA 3) presents an average temperature of 200 °C. The temperature decreases quickly in the first years: the maximum temperature falls below 300 °C after 2 years of dry storage, below 250 °C after 7 years and below 200 °C after 20 years. In accordance with the exponential decrease of the decay heat, the temperature drop slows down with time: 43 years of dry storage are necessary for the maximum temperature to fall below 150 °C and finally, after 95 years of dry storage (100 years after the end of reactor operations), no temperature exceeds 100 °C within the cask.

2.3.6.4 Cask with inhomogeneous loading schemes

Finally, Table 2.7 and Table 2.8 present the results of further calculations with COBRA-SFS, simulating different loading schemes. In Table 2.7, the first line corresponds to the homogeneous loading, each of the 19 fuel assemblies having a decay heat of 2052 W so that the total power reaches 39 kW. The following lines correspond to simulations in which one or several fuel assemblies are missing, while the other assemblies still present a decay heat of 2052 W. The assembly-averaged temperatures T_i at the hottest axial position are provided for FA 1, 2, 3, 6, 8, 9 and 10, as well as the maximum temperature in the cask T_{max} . The grey cells indicate missing fuel assemblies, which means that the temperatures correspond to helium without local heat generation.

We can first observe that a single missing fuel assembly has a limited impact on the other assemblies although the defined decay heat, 2052 W, is a relatively high value for a fuel assembly being dry stored. It mainly influences the temperature of the direct neighbouring fuel assemblies, in particular the fuel assemblies on the same radial alignment.

Table 2.7: Temperatures in the CASTOR[®] cask for different loading schemes: 39 kW homogeneously distributed (2052 W per fuel assembly) on the first line, one missing fuel assembly for the five following lines (the other assemblies still present a decay heat of 2052 W), and 4 (resp. 6) missing fuel assemblies for the second last (resp. last) line. The assembly-averaged temperatures T_i at the hottest axial position are provided for FA 1, 2, 3, 6, 8, 9 and 10, as well as the maximum temperature in the cask T_{max} . The grey coloured cells indicate missing assemblies, therefore the temperatures in these cells correspond to helium, without heat generation.

	T_{max}	T_{10}	T_9	T_8	T_6	T_3	T_2	T_1
39 kW Homogeneous	341 °C	316 °C	277°C	212 °C	268 °C	196 °C	208 °C	197 °C
36.95 kW Missing FA 10	288 °C	238 °C	260°C	208 °C	256 °C	195 °C	207 °C	196 °C
36.95 kW Missing FA 9	326 °C	300 °C	207°C	190 °C	256 °C	195 °C	203 °C	187 °C
36.95 kW Missing FA 8	334 °C	308 °C	260°C	153 °C	260 °C	195 °C	203 °C	185 °C
36.95 kW Missing FA 6	330 °C	304 °C	265°C	206 °C	192 °C	184 °C	183 °C	185 °C
36.95 kW Missing FA 2	335 °C	310 °C	269°C	207 °C	250 °C	183 °C	150 °C	184 °C
30.79 kW, Missing FA 6,7,13,14	297 °C	269 °C	240°C	200 °C	172 °C	176 °C	182 °C	186 °C
26.68 kW, Missing FA 6,7,9,11,13,14	266 °C	237 °C	163°C	180 °C	153 °C	175 °C	177 °C	176 °C

- In the case of FA 10 (central assembly) missing, the average temperature of FA 6 and FA 9 (intermediate assemblies) is reduced by 12 °C and 17 °C respectively. FA 9 is more impacted as it directly faces FA 10. The other assemblies (external assemblies) show a temperature drop of only 1 °C to 4 °C (the latter in the case of FA 8, as it is in the alignment of FA 10 and FA 9).
- For FA 9 missing, FA 8 and FA 10 are the most impacted (directly facing FA 9), with temperature drops of 22 °C and 16 °C respectively. For FA 1 and FA 6 (neighbouring assemblies, but not directly facing

FA 9), the drops reach 10 °C and 12 °C respectively. For FA 3, which is well separated from FA 9, the temperature drop is of only 1 °C.

- Similarly, for FA 8 missing, the main impact is observed on FA 9 (-17 °C) and on FA 1 (-12 °C), while the temperature drops are very low for FA 2 and FA 3 (5 °C and 1 °C respectively).
- For FA 6 missing, FA 2 is the most impacted, with a temperature drop of 25 °C. This was expected, as it is radially perfectly aligned (facing) FA 6. FA 1, FA 3, FA 9 and FA 10 all four present a moderate temperature drop of 12 °C, which is explained by their positions: they are all indirectly neighbouring FA 6, being separated by large helium channels. FA 8 is less impacted by FA 6 missing and presents a temperature drop of 6 °C.
- For FA 2 missing, the strongest impact is observed on FA 6 with a temperature drop of 18 °C, while FA 1 and FA 3 present a moderate temperature drop of 13 °C. FA 8, FA 9 and FA 10 are less impacted, with temperature drops of 5 °C to 8 °C.

We can also observe that the maximum temperature T_{max} is always in FA 10 (except when FA 10 is missing) and that it drops by 6 °C to 15 °C when one fuel assembly is missing, the largest drop occurring when FA 9 is missing. If FA 10 is missing, T_{max} is reached in FA 6 (and in the symmetrical assemblies: FA 7, FA 13 and FA 14) with a temperature of 288 °C.

In the case of several fuel assemblies missing, the temperature drops are larger, in particular on the central (FA 10) and intermediate (FA 9 when not missing) assemblies.

- For 4 intermediate fuel assemblies missing (FA 6, 7, 13 and 14), the temperature drop reaches 47 °C for FA 10 and 37 °C for FA 9. The temperature drop is of 26 °C for FA 2, as it directly faces FA 6. FA 3 is indirectly (through large helium channels) neighbouring both missing FA 6 and FA 7 and presents a temperature drop of 20 °C. Finally, FA 8 and FA 1 are less impacted, with respectively -12 °C and -11 °C.

- For all 6 intermediate fuel assemblies missing, the temperature drop of FA 10 reaches 79 °C. Concerning the external fuel assemblies, the temperature drop is of 21 °C for FA 3 and FA 1, which are separated from the missing assemblies by large helium channels, and of 31 °C (resp. 32 °C) for FA 2 (resp. FA 8), which directly faces FA 6 (resp. FA 9).

Table 2.8 presents temperatures in the CASTOR[®] cask in the case of inhomogeneous loads due to special fuel assemblies (see section 2.2.1) at positions 6, 7, 13 and 14. The five configurations all present a total loaded power of 39 kW but with different decay heat ratios *special assemblies / normal assembly* $\mathcal{R}_{S/N}$: 1 (homogeneous load), 1.5, 2, 2.5 and 3. This means that the decay heat of the four special assemblies increases from 2052 W (homogeneous load) to 4333 W ($\mathcal{R}_{S/N} = 3$), while the decay heat of the other assemblies decreases from 2052 W to 1444 W. The same temperatures as in Table 2.7 are given and we added the maximum temperatures of FA 10 ($T_{10,max}$) and FA 6 ($T_{6,max}$).

We can first observe that the maximum temperature in the cask T_{max} is located in FA 10 if $\mathcal{R}_{S/N}$ is equal to 1 or 1.5, but that T_{max} is reached in the special assemblies (FA 6 in the table) if $\mathcal{R}_{S/N}$ is equal to 2 or greater. As a consequence,

- T_{max} decreases from 341 °C to 338 °C when the $\mathcal{R}_{S/N}$ increases from 1 to 1.5 due to the decrease of decay heat (and temperature) for FA 10, but
- T_{max} increases for higher ratios, from 343 °C for $\mathcal{R}_{S/N} = 2$ to 374 °C for $\mathcal{R}_{S/N} = 3$, as it is then determined by the special fuel assemblies whose decay heats (and temperatures) increase.

Concerning the average temperatures of the assemblies, different behaviours can be observed:

- T_{10} remains constant, equal to 316 °C. This is probably due to two effects offsetting each other. On the one hand, the decay heat in FA 10

Table 2.8: Temperatures in the CASTOR[®] cask for loadings involving special fuel assemblies. The first line corresponds to the homogeneous case: 39 kW equally distributed between the fuel assemblies (2052 W per assembly). On the following 4 lines, the fuel assemblies at positions 6, 7, 13 and 14 have been defined with increased decay heat (special fuel assemblies, see section 2.2.1). In each case, the total power loaded in the cask is 39 kW, but the ratio $\mathcal{R}_{S/N}$ between the decay heat of the special assemblies and the decay heat of the normal assemblies varies from 1.5 up to 3. The assembly-averaged temperatures (T_i) at the hottest axial position are provided for FA 1, 2, 3, 6, 8, 9 and 10, as well as the maximum temperatures $T_{i,max}$ in FA 6 and FA 10, and the maximum temperature T_{max} in the cask.

	T_{max}	$T_{10,max}$	T_{10}	T_9	T_8	$T_{6,max}$	T_6	T_3	T_2	T_1
Homogen. $\mathcal{R}_{S/N} = 1$	341 °C	341 °C	316 °C	277°C	212 °C	295 °C	268 °C	196 °C	208 °C	197 °C
Special FA $\mathcal{R}_{S/N} = 1.5$	338 °C	338 °C	316 °C	274°C	203 °C	322 °C	287 °C	192 °C	206 °C	191 °C
Special FA $\mathcal{R}_{S/N} = 2$	343 °C	336 °C	316 °C	272°C	196 °C	343 °C	302 °C	190 °C	205 °C	186 °C
Special FA $\mathcal{R}_{S/N} = 2.5$	360 °C	335 °C	316 °C	270°C	190 °C	360 °C	314 °C	188 °C	204 °C	183 °C
Special FA $\mathcal{R}_{S/N} = 3$	374 °C	333 °C	316 °C	268°C	185 °C	374 °C	324 °C	187 °C	203 °C	181 °C

decreases when $\mathcal{R}_{S/N}$ increases and therefore the temperature gradient within the assembly decreases (this is confirmed by the decrease of $T_{10,max}$). On the other hand, the decay heat increase of the special assemblies surrounding FA 10 leads to an increase in the overall temperature of FA 10.

- T_6 increases significantly, due to the important increase in decay heat.
- The other assemblies present decreases in temperature, which are more or less strong depending on their positions relative to the special fuel assemblies:
 - T_2 presents a very slight decrease (-5 °C when $\mathcal{R}_{S/N}$ increases from 1 to 3), as FA 2 is directly facing FA 6 and therefore strongly under the influence of its increasing decay heat.

- T_3 and T_9 present a larger decrease (-9 °C), as FA 3 and FA 9 are both neighbouring two special assemblies but indirectly, being separated by large helium channels.
- T_1 and T_8 present the largest temperature decreases (-16 °C and -27 °C respectively), as the special assemblies are located relatively far and therefore less compensate the decay heat decrease in FA 1 and FA 8.

2.3.7 Summary on the COBRA-SFS CASTOR model

In this section, we presented and discussed a cask model inspired again by the CASTOR[®] V/19, built with the thermal-hydraulic code COBRA-SFS. This model includes 568 nodes representing the different structures of the cask. For each fuel rod, the temperatures of 36 axial zones of equal length are calculated. The same axial zones are defined for the entire cask. Therefore, temperature profiles consisting of 36 values are provided for each fuel rod, as well as for the 568 nodes of the model. As for the fuel rods, temperature profiles are provided for each subchannel within the fuel assemblies. Thus, detailed 3-dimensional temperature distributions can be calculated for an entire cask by this model. The short computational time of a few minutes per simulation constitutes a major advantage of COBRA-SFS compared to CFD simulations, the main alternative for a detailed temperature analysis.

Due to the lack of publicly available experimental data, we compared the results of the COBRA-SFS model to the ones derived using the codes COCOSYS and ANSYS CFX (Fig. 2.21), assuming identical boundary conditions for loading scheme and room temperature. We found that there is a good agreement between the three models and any differences can be explained by the intrinsic different modelling capabilities of the codes. COBRA-SFS offers the possibility to take all three-dimensional heat transfer mechanisms into account, combined with much shorter calculation times compared to ANSYS CFX.

A comparison of the COBRA-SFS model with the Python model enabled

to establish interesting equivalences between both models (Fig. 2.22 and Fig. 2.23): for instance, the most internal zone of the homogenized Python model corresponds to an average temperature of the central fuel assembly according to the COBRA-SFS model. These correspondences have been observed in both steady-state and transient cases and offer a further cross validation check for both models.

The impact of key parameters has been analysed, assessed and explained. We have shown that a room temperature increase by 30 °C (from 10 °C to 40 °C) leads to a temperature increase between 21 °C and 26 °C for the fuel assemblies, as well as in the cask body (Fig. 2.26). The impact of the gaps between the different components (e.g. cask body and fuel basket) has also been analysed and we observed that for a constant gap (concentric fuel basket in the cask cavity), a 1 mm gap leads to a temperature increase by approximately 25 °C for the fuel assemblies (Fig. 2.28).

A detailed temperature distribution corresponding to a cask homogeneously loaded with 39 kW has been presented. We found that three types of temperature ranges can be distinguished for the fuel assemblies, depending on their position: central, intermediate or external fuel assemblies (Fig. 2.30).

A drying process has been simulated, including a vacuum drying phase followed by a helium refill (Fig. 2.31). It showed that in vacuum conditions, starting from 40 °C (cooling pond conditions), the temperature needs approximately one day to reach temperatures equivalent to its equilibrium at the beginning of the dry storage. A longer vacuum drying leads to cladding temperatures exceeding the equilibrium state expected under helium conditions.

The fuel assembly temperature profiles have been determined for a storage period of 100 years (Fig 2.32) assuming a cask loaded with 39 kW. It showed that the temperature decreases rapidly during the first years and therefore that high temperatures (above 300 °C) can be expected only at the beginning of the dry storage. After 20 years of dry storage, the peak temperature in the cask does not exceed 200 °C.

Finally, different loading schemes have been simulated. We analysed the

impact of missing fuel assemblies (Table 2.7), as well as the influence of the *special assemblies* (Table 2.8) on the temperature distributions.

This second cask model provides an efficient way to determine very detailed three-dimensional temperature distributions in an entire cask, for both steady-state and transient cases.

2.4 COBRA-SFS TN-32B model

The second COBRA-SFS cask model presented in this thesis was developed within the framework of an international benchmark. This benchmark is organized by the Electric Power Research Institute (EPRI) as part of the Extended Storage Collaboration Program (ESCP) and aims at comparing different codes used for the modelling of storage systems. The conditions of the model development differed on many aspects from the conditions of development of the first model.

First, almost all input data was provided in a detailed manner within the benchmark specifications [20], as the organizers wanted to reduce as much as possible the divergences between the participants, regarding possible modelling assumptions. Thus, the cask design was clearly presented, as well as the materials and their properties.

Another major difference was that it consisted in an open benchmark, which means that experimental measurement results were provided from the beginning. This made the verification of the model more straightforward.

Finally, the TN-32B benefited from the experience gained through the development of the first COBRA-SFS model (CASTOR model). A detailed description of the error tracking for this model can be found in Appendix 5.7.

The TN-32B cask is 4.67 m in height, 2.59 m in diameter and can host 32 fuel assemblies. The basket structures hosting the fuel assemblies are made of stainless steel and aluminium. The cask body is made of steel including aluminium boxes filled with borated polyester for neutron shielding. The cask cavity is 4.15 m in height, 1.75 m in diameter and filled with helium at a pressure of 2.2 bar. More details on the cask geometry and materials can be found in the benchmark specifications (EPRI report) [20].

2.4.1 Model description

The COBRA-SFS TN-32B model consists of 629 solid nodes, shown in Fig. 2.33, and 40 axial layers. Each layer is 10.16 cm (4 in) in height, thus the 40 layers cover 406 cm (160 in), which corresponds to the height of the

cask cavity region. The 629 solid nodes are distributed as follows: 197 nodes for the 32 fuel assembly compartments made of steel and aluminium, 180 nodes for the rails made of aluminium and 252 nodes for the cask body. The 252 nodes of the cask body are divided into 7 rings of 36 nodes each, corresponding successively to the inner confinement shell, the gamma shield, the inner side of the neutron shield boxes, the neutron shield resin, the outer side of the neutron shield boxes, the outer shell and the cask surface (zero thickness). Detailed drawings used for the development of this model can be found in the benchmark specifications (EPRI report) [20].

The model includes 17x17 PWR fuel assemblies (Westinghouse design), which are modelled pin by pin. Thus, the model yields temperature values for each of the 17x17 fuel rods from all 32 fuel assemblies and at each of the 40 axial layers. Fuel assembly design data were taken from [45]. We assumed a single cladding type, characterized by a thermal conductivity $\lambda = 15.6 \text{ W m}^{-1} \text{ K}^{-1}$ ($9 \text{ Btu h}^{-1} \text{ ft}^{-1} \text{ }^\circ\text{F}^{-1}$). Fuel material is not considered in the model as it is expected to have a limited influence on the temperature results in the case of steady-state calculations. The fuel rod power is thus applied at the inner surface of the cladding as a boundary condition. Spacer grids are not directly modelled but loss coefficients are applied at the axial locations of the grids. As we developed a full cask model, the detailed loading scheme provided in the benchmark specifications has been used: we assigned the corresponding power to each of the 32 fuel assemblies. Furthermore, the decay heat profile provided in the specifications has also been included in the model. The cask is filled with helium at a pressure of 2.2 bar. Within each fuel assembly, 18x18 helium channels are modelled, 4 rods defining the corners of one channel. Within the rails, 32 further helium channels (much larger than the fuel assembly channels) are modelled. Helium properties were taken from NIST database [37].

A few homogenization assumptions were taken, concerning the basket structures and the cask body. The basket structures consist of aluminium and stainless steel, but are considered in the model as made of one homogenized media⁹. The material properties defined for the homogenized media include

⁹See section 2.1.1.1, paragraph *Resistances in parallel or in series*, for more details on homogenized media and equivalent thermal conductivities.

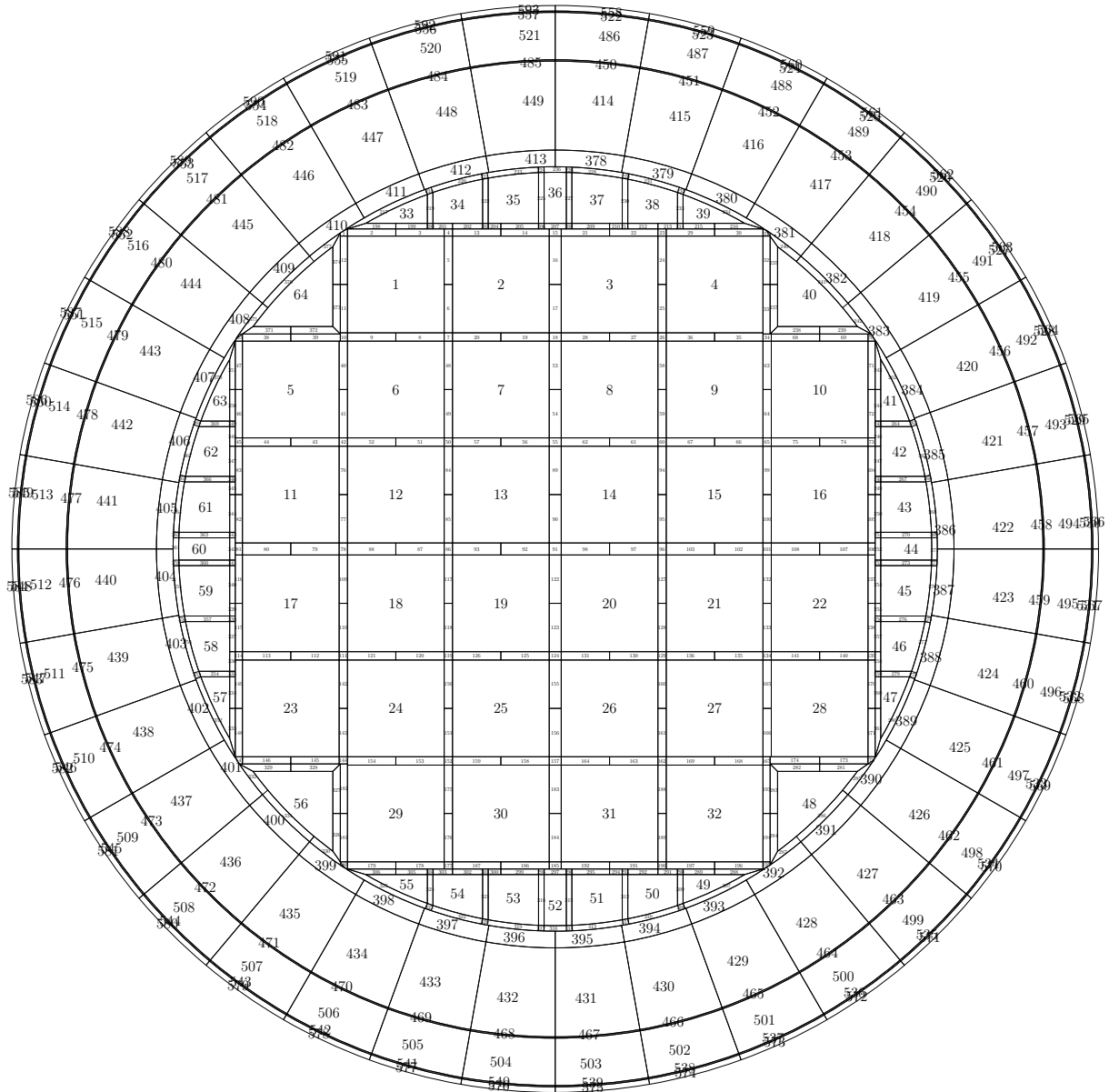


Figure 2.33: Diagram of the TN-32B model showing the numbering used for the fuel assemblies, helium channels and solid nodes. The 32 fuel assemblies (*rodded assemblies*) are first numbered with the large numbers in the middle of the diagram, then the large helium channels (*unrodded assemblies*) inside the rails surrounding the fuel assemblies are numbered from 33 to 64. Another numbering identifies the solid nodes of the model: first, the nodes for the fuel compartments from 1 (corner of FA 1) to 197 (at FA 32), then the nodes for the rail structures from 198 (at helium channel 33) to 377 (at helium channel 64) and finally the nodes for the cask body from 378 to 593. 36 further nodes (594 to 629) are used to represent the surface of the cask but are not depicted on this diagram.

a thermal conductivity which corresponds to the basket plate (aluminium), a gap (helium) and the fuel compartment (stainless steel) in parallel. In order to take into account the discrepancy in case of thermal conduction for a configuration in series, a correcting factor was included in the concerned thermal resistances. This factor corresponds to the ratio between the thermal conductivities in both cases (in parallel and in series), evaluated at 200 °C. Similarly, a homogenized medium is defined for the fourth ring of nodes in the cask body, to consider the borated polyester resin and the aluminium from the shield boxes. An equivalent thermal conductivity has been calculated assuming aluminium and polyester resin to be in parallel (resp. in series) for thermal connections along the radial and axial (resp. azimuthal) directions.

All gaps mentioned in the benchmark specifications [20] have been taken into account, except the gap at the basket plate ends. Most of the gaps are explicitly defined within the thermal resistances as additional terms given by $R_{gap} = W/(\lambda \cdot \mathcal{S})$, with W the width of the gap, λ the thermal conductivity (no temperature dependency) of the gas filling the gap and \mathcal{S} the surface of the nodes facing the gap. The only exception is for the gap between fuel compartment and basket plate, as this gap has been included in a homogenized node, together with basket plate and fuel compartment. Heat transfer mechanisms include conduction (with consideration of gaps), convection and radiation. Conduction is calculated by COBRA-SFS both in solids and in helium. Convection correlations are used for helium in the cask and at the external cask surface for air. Radiative heat transfers are calculated within the fuel assemblies (from rod to rod as well as between rods and basket structures), within the rail structures and between the cask external surface and the environment. View factors are defined to precisely determine the radiative exchanges inside the cask.

Concerning the boundary conditions at the top and bottom of the model, COBRA-SFS provides options to model *plenum regions*. This consists in defining a few regions to connect the top (resp. bottom) of the fuel assembly region to the environment, using thermal connections. In our model, we defined both upper and lower plenums. The lower plenum includes regions

successively for helium, the cask inner liner, an air gap, the gamma shield and air convection underneath the cask. The upper plenum includes regions for helium, the top shield plate, the cask lid and air convection above the cask. The ambient temperature is assumed to be 24 °C (75 °F) on the sides, top and bottom of the cask, and thermal radiation as well as convection are taken into account. Natural convection correlations were taken from [24]. On the bottom face of the cask, convection was assumed to be in laminar regime, involving a heat transfer coefficient given by $h = 0.59 (\Delta T/L)^{1/4}$. On the top face of the cask, a turbulent flow was assumed, corresponding to $h = 1.52 (\Delta T)^{1/3}$. On the sides of the cask, the flow was expected to be at the transition between laminar (lower part of the cask) and turbulent (upper part), but as we could assign only one correlation for the whole height of the cask, we assumed a turbulent flow with a reduced heat transfer coefficient: $h = 1.07 (\Delta T)^{1/3}$. This heat transfer coefficient determines the temperature difference between the cask surface and the room temperature. As the room temperature is given by the specifications, this means that the heat transfer coefficient actually determines the cask surface temperature. To fix the reduced coefficient in the expression of h , we considered the experimentally measured cask surface temperature (as this is an “open benchmark”, measured temperatures were accessible to the participants) in the middle of the cask and we chose a reduced coefficient ensuring a good agreement between measurement and simulation for the surface temperature.

The model provides, at each of the 40 axial layers, temperature results for all 629 solid nodes, 17x17 fuel rods of the 32 fuel assemblies, 18x18 helium channels of the 32 fuel assemblies, and 32 helium channels within the rails. COBRA-SFS needs about 20 minutes to perform one steady-state simulation with this model, using a single processor.

2.4.2 Temperature calculation results

In this section, we present the calculation results that were obtained for the EPRI international thermal modelling benchmark. The results include a base case calculation, which simulates the conditions of the experimental

measurements on the real TN-32B cask. This constitutes the first phase of the benchmark. The second phase of the benchmark will consist in a sensitivity analysis of the models, but it has not been achieved yet. However, some preliminary sensitivity calculations were already performed during the first phase and are also presented here. Verification methods based on the model symmetry have been applied to the TN-32B model and are detailed in Appendix 5.7.

2.4.2.1 Base case calculation

For the phase 1 of the benchmark, we had to simulate the TN-32B cask loaded with fuel assemblies presenting different decay heats in accordance with the real loading scheme (experimental measurements). This plan is shown in Fig. 2.34 and the decay heats vary from 573.8 W for FA 13 to 1142.4 W for FA 7. We should then provide 7 temperature axial profiles corresponding to 7 given guide tubes in different fuel assemblies and 3 temperature axial profiles on the cask surface corresponding to 3 different azimuthal coordinates (referred to as columns A, B and C). The 7 temperature profiles are located within fuel assemblies 2, 6, 14, 19, 24, 28 and 31, in each case approximately at mid-distance between the centre and the edge of the assembly (the precise location can be found in the benchmark specifications [20]) and correspond to guide tubes in which thermocouple lances were inserted. Each lance has 9 thermocouples at different axial positions. Details on the experiment and on the measurements are provided in [20].

Fig. 2.35a presents the results of the base case calculation for the 7 guide tubes. The temperature profiles from the COBRA-SFS simulation are plotted with plain lines, while the experimentally measured temperatures are plotted with dotted lines. To enable a direct comparison, we determined for each of the 7 temperature profiles from COBRA-SFS a corresponding temperature at the 9 axial positions using linear interpolation (the COBRA-SFS model presents 40 axial layers and thus provides in output temperature profiles consisting of 40 values).

	1 912.2 W	2 978.2 W	3 914.4 W	4 799.5 W	
5 800.9 W	6 1008.6 W	7 1142.4 W	8 1121.2 W	9 975.1 W	10 814.5 W
11 802.6 W	12 1135.0 W	13 573.8 W	14 1037.0 W	15 1124.8 W	16 941.3 W
17 961.7 W	18 1131.1 W	19 920.2 W	20 646.2 W	21 1135.8 W	22 941.2 W
23 934.7 W	24 914.2 W	25 1133.7 W	26 1136.3 W	27 988.2 W	28 916.9 W
	29 914.2 W	30 968.0 W	31 927.7 W	32 804.3 W	

Figure 2.34: Power of the 32 fuel assemblies loaded in the TN-32B cask.

Due to their central positions in the cask, FA¹⁰ 14 and FA 19 present the highest temperatures, significantly higher than the other assemblies. FA 14 is slightly hotter (maximum temperature on the simulated profile: 226.3 °C) than FA 19 (222.6 °C), which can be explained by the difference in their respective decay heats: 1037 W and 920.2 W.

FA 6 and FA 24 present intermediate temperatures as they are located neither in the centre of the cask nor on the edge. FA 6 has a higher decay heat than FA 24 (1008.6 W and 914.2 W respectively), leading to higher temperatures (maximum temperatures from the simulation: 211.9 °C and 204.7 °C respectively).

FA 2 and FA 31 are located on the edge of the fuel assembly load, facing the inner side of the cask body. However, they are not corner assemblies and therefore are not in direct contact with the cask body (unlike FA 28). They present colder temperature profiles than the previous ones, with a maximum simulated temperature of 196.6 °C for FA 2 and 194.7 °C for FA 31. We can note that this is again in accordance with the difference in their respective

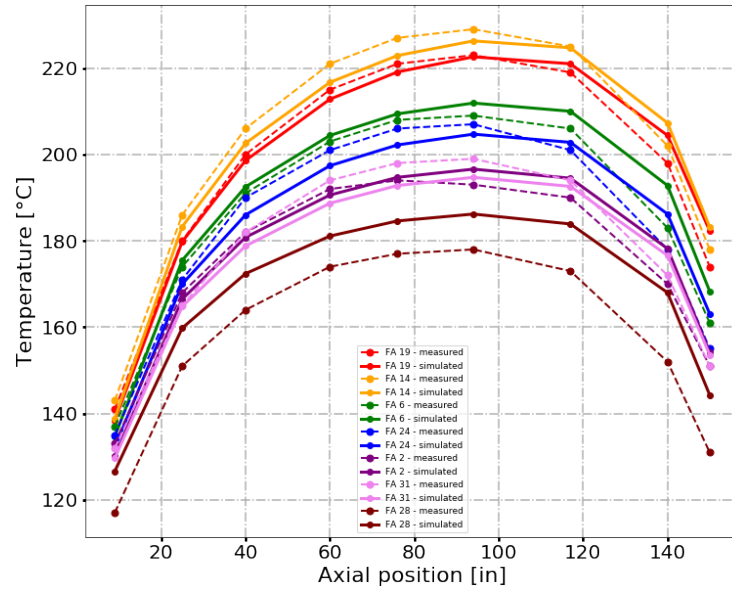
¹⁰We will talk here of FA, but the temperature profiles actually correspond to one precise guide tube per fuel assembly. Each fuel assembly could provide many other temperature profiles (peak cladding temperature, temperature profiles of each single rod or mean temperature profile), but as we had to consider only one precise guide tube per assembly in the frame of the benchmark, there can be no confusion and this simplify the notation.

decay heats: 978.2 W for FA 2 and 927.7 W for FA 31. On the contrary, according to the measured temperatures, FA 31 is hotter than FA 2. There is no obvious explanation for it, as even the neighbouring assemblies from FA 2 have in average a higher decay heat than the neighbours of FA 31. However, we should keep in mind that all 4 profiles (2 measured and 2 simulated) remain nearly equal, within 10 °C, which is rather negligible with regard to the measurement and simulation uncertainties.

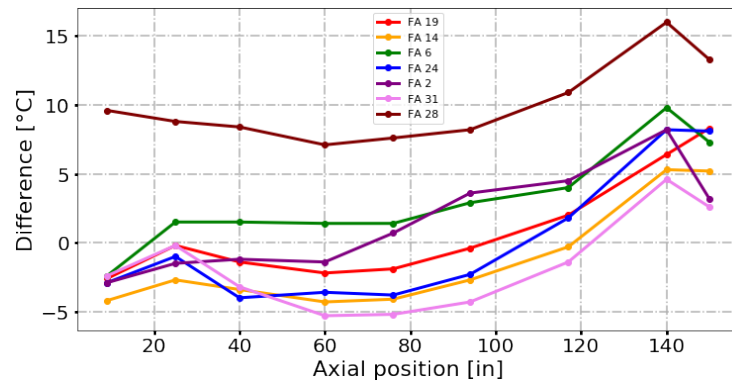
Finally, FA 28 presents as expected the lowest temperature profile, due to its location. As a “corner fuel assembly”, FA 28 is better (more directly) connected to the cask body, which ensures lower temperatures: the maximum simulated temperature reaches 186.2 °C. The stronger influence of the cask body on corner assemblies compared to other assemblies had already been observed during the verification phase of the model, which is presented in Appendix 5.7 (see Fig. 5.17 in particular). FA 28 presents the highest discrepancy between simulation result and experimental measurement, with temperature differences up to 16 °C. This could be related to an underestimation of the thermal connection between the basket structure surrounding the corner assemblies and the cask body. However, a difference of 15 °C still constitutes a very satisfying result for a cask model.

The details of the temperature differences between the simulated and the measured profiles can be seen in Fig. 2.35b. As already mentioned, FA 28 presents the highest discrepancy, the simulation being about 10 °C too hot on most of the height and up to 16 °C too hot in the upper part of the cask. For the other assemblies, the temperature differences remain mostly below 5 °C, except for the upper part of the cask, where the simulated temperatures are up to 10 °C too hot. This may have several explanations:

- The correlation for the heat transfer coefficient applied on the cask surface is the same over the whole height of the cask, whereas different regimes of flow and convective heat transfer should be expected: laminar in the lower part of the cask (resulting in a lower heat removal) and turbulent in the upper part (better heat removal). The choice of a turbulent correlation with a reduced coefficient might result in some increase of the temperature in the upper part of the cask.



(a) Temperature profiles experimentally measured (dotted lines) and simulated with the COBRA-SFS model (plain lines).



(b) Difference between simulation results and measurements.

Figure 2.35: Comparison of the measured (dotted lines) and simulated (plain lines) temperature profiles of guide tubes from 7 fuel assemblies loaded in the TN-32B cask.

- The plenum model, defining the possible heat removal paths through the top and bottom of the cask, also has an impact on the upper and lower parts of the temperature profiles. If the overall thermal resistance of the upper plenum has been overestimated, this would result in overestimated temperatures for the upper part of the cask.
- Finally, the helium convection within the cask also significantly im-

pacts the temperature profile. This was stated and discussed during benchmark meetings by participants who initially neglected the convection (in particular, participants using Finite Element Method) and observed that without helium convection the hump of the resulting temperature profiles were clearly shifted towards the bottom. Indeed, within the fuel assemblies the ascending helium flux transports heat towards the top of the cask. This leads to a decrease in temperature in the lower part of the fuel assemblies (enhanced heat removal) but shifts the maximum of the temperature profiles towards the top of the cask, as helium itself warms up while it goes through the fuel assemblies.

Fig. 2.36 shows the temperature profiles for the cask surface calculated with COBRA-SFS (plain line) and measured (dotted line). The measured temperature profiles consist of only 5 points each, but COBRA-SFS results are plotted including all 40 axial positions. As the COBRA-SFS model only covers a height of 160 in (corresponding to the length of the fuel assemblies), the lowest point of the measured A column is out of the domain covered by the simulation.

Simulation results and experimental measurements are in good agreement, the difference does not exceed 5 °C. The adjustment of the heat transfer coefficient (see section 2.4.1) ensured that the simulation results would fit well with the experimental measurements in the middle of the cask, but Fig. 2.36 shows that more generally the temperature profiles are in good agreement over the whole height.

We can observe that all three simulated temperature profiles are almost perfectly superposed. This is probably due to the fact that the loading scheme is rather well equilibrated and that the cask body is thick enough, so that the outgoing heat flux is homogeneously shared between all azimuthal directions (the 36 nodes of the cask body rings). Furthermore, the boundary condition consists in a room temperature of 24 °C for all sides of the cask, which together with the azimuthal-invariant heat flux ensures a surface temperature profile independent of the azimuthal angle.

On the contrary, the measurements show some differences between the three profiles. This may most probably result from slightly inhomogeneous bound-

ary conditions (one side of the cask might be better exposed to the air flow entering the facility) or simply from measurement uncertainties, as the differences remain very small: mainly below 2 °C and about 5 °C for the lowest part of the profiles. However, the comparison of column A with column B or C can be discussed, as the lowest points of those profiles do not correspond to the same axial positions.

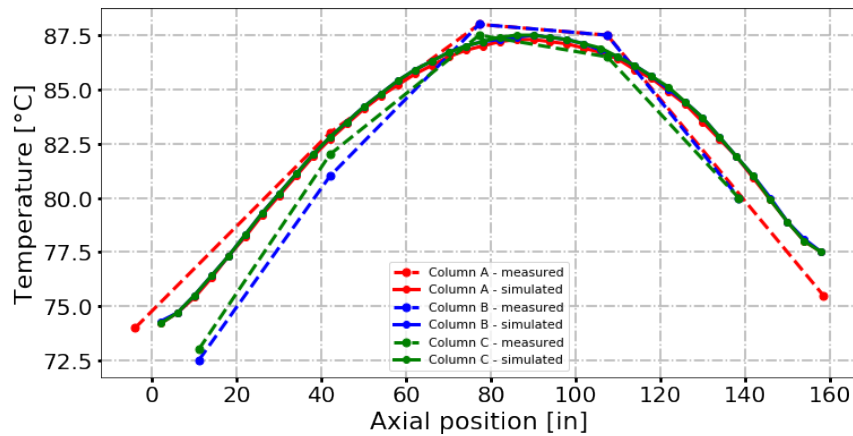


Figure 2.36: Comparison of the measured (dotted lines) and simulated (plain lines) surface temperature of the TN-32B cask. Three profiles are represented, corresponding to three different azimuthal coordinates.

A first comparison of the results from the different participants has been shown and discussed on the Winter ESCP Meeting 2021 [46]. The main takeaways from phase 1 of the benchmark have been listed as:

- Wide variations in temperature predictions have been observed, up to 70 °C.
- Most groups predicted the shape of the temperature profiles well.
- Boundary conditions can likely be traced to a lot of the variations.
- The lack of details as built information and purposeful skewing of the design specifications may also have an impact.

Wide variations have not been observed with our model, whose results remained within 20 °C from the experimental data. The final report should be published by EPRI by the end of 2022. [46]

2.4.2.2 Sensitivity analysis

A sensitivity analysis was performed using the TN-32B model to analyse the influence of the decay heat and room temperature on the resulting temperature profiles. In Fig. 2.37, 2.38, 2.39 and 2.40, we represented

- on the upper diagrams: the temperature profile of the base case in blue, the temperature profile in case of increased decay heat (+ 5 %) or room temperature (+ 15 °F = + 8.3 °C) in red and the temperature profile in case of reduced decay heat (- 5 %) or room temperature (- 15 °F = - 8.3 °C) in green,
- on the lower diagrams: the difference between the hottest and coldest profiles from the upper diagrams.

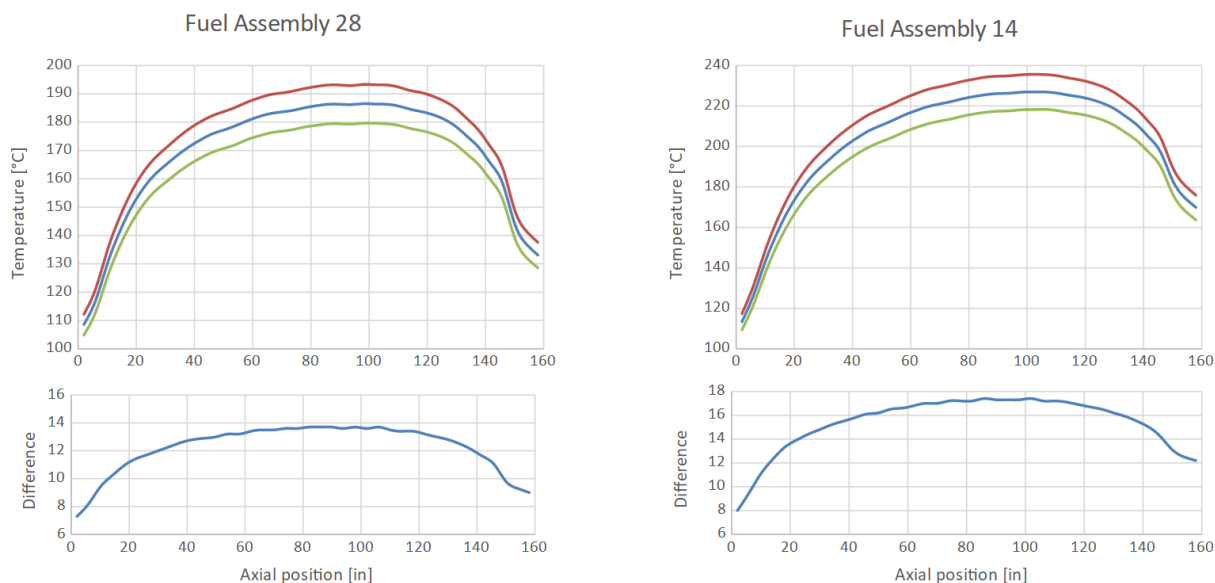


Figure 2.37: Temperature variation with decay heat. Results are presented for FA 28 (corner fuel assembly) on the left and for FA 14 on the right (central fuel assembly). For both assemblies, three curves are plotted on the upper diagrams corresponding to the base case result and to the increased (+5%) and reduced (-5%) decay heats. On the lower diagrams, we plotted the temperature difference between the calculations with the increased and reduced decay heats.

Fig. 2.37 presents the influence of the decay heat on the temperature profile

of FA 28 (coldest profile, see Fig. 2.35) and FA 14 (hottest profile). As expected, the higher the decay heat is, the higher the temperatures are. The difference plot is similar to the temperature profiles: for FA 28 (resp. FA 14), the minimum difference is at the bottom of the cask by 7.3 °C (resp. 8 °C), then the difference increases up to 13.7 °C (resp. 17.6 °C) in the middle of the cask and decreases at the top, down to 9 °C (resp. 12 °C).

The temperature differences are larger for FA 14 than for FA 28. This can be explained by the difference in decay heat (for the base case: 1037 W vs. 914.2 W): a higher decay heat leads to larger variations (in absolute terms) and therefore to larger temperature differences. This also explains that the profile of the difference curves follows the profile of the temperature curves (which themselves correspond roughly to the decay heat profile).

Another interesting point is that the upper part of the cask is more sensitive to decay heat variations: while the temperature difference between the high decay heat and low decay heat curves is around 8 °C at the bottom for both FA 14 and FA 28, the difference reaches 12 °C at the top for FA 14, but only 9 °C for FA 28. This might be related to the stronger influence of the convection in FA 14 (higher temperatures). The helium at the bottom of the cask is assumed mixed (uniform temperature) by COBRA-SFS, which explains the limited difference between FA 14 and FA 28 at the bottom, but when helium reaches the top of the fuel, the temperatures might present important differences depending on the fuel assembly.

Fig. 2.38 shows the surface temperature profiles¹¹ obtained with the same variations of decay heat. The amplitude of the difference curve is smaller than for the fuel assemblies: 3.8 °C at the bottom, 4.9 °C in the middle and 3.9 °C at the top. Here also, the profile of the difference curve corresponds to the temperature and decay heat profiles: the decay heat is higher in the middle part of the cask, therefore the heat flux is also higher, which leads to higher surface temperatures.

Fig. 2.39 is similar to Fig. 2.37 but concerns the influence of the room temperature (± 8.3 °C compared to the base case). Here again, we can first

¹¹As the simulations do not show any difference between the three columns concerning the surface temperature, we consider only one temperature profile per case.

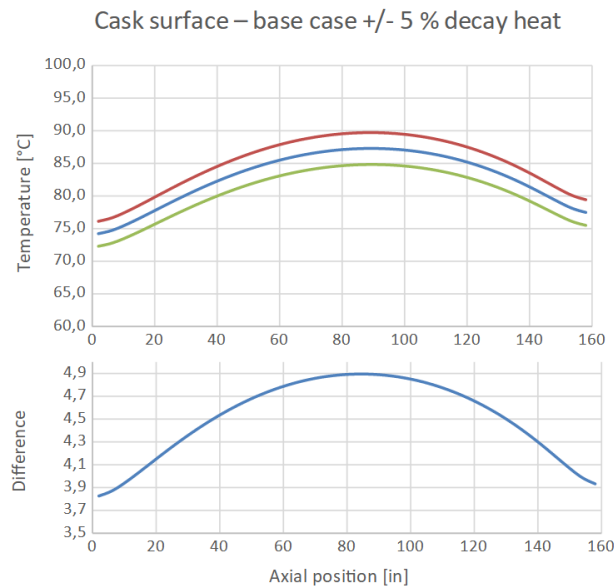


Figure 2.38: Temperature variation of the cask surface with decay heat. The three curves plotted on the upper diagram correspond to the base case result and to the increased (+5%) and reduced (-5%) decay heats. On the lower diagram, we plotted the temperature difference between the calculations with the increased and reduced decay heats.

note that with increasing room temperature, the overall temperature within the cask increases. Thus, an increase of 16.6 °C of the room temperature leads to an increase of 10 to 14 °C for FA 28 and 10 to 16 °C for FA 14.

Fig. 2.40 shows the temperature profiles for the cask surface, obtained with the different room temperatures. We can first note that the influence of the room temperature on these profiles is strong: for a room temperature increase of 16.6 °C, the surface temperature increases by around 13 °C. This increase is in the same order of magnitude than for the fuel assemblies. We can here observe the difference with the decay heat: The decay heat variations also lead to a significant increase of the temperature in the fuel assemblies (8 to 18 °C) but have less impact on the temperature of the cask surface (less than 5 °C).

To understand this overall influence of the room temperature on both the cask and the fuel assemblies, we can draw again a parallel with an electricity problem involving a resistance R through which a current I is passed, as shown in Fig. 2.41. If the current I and the resistance R are fixed, then the

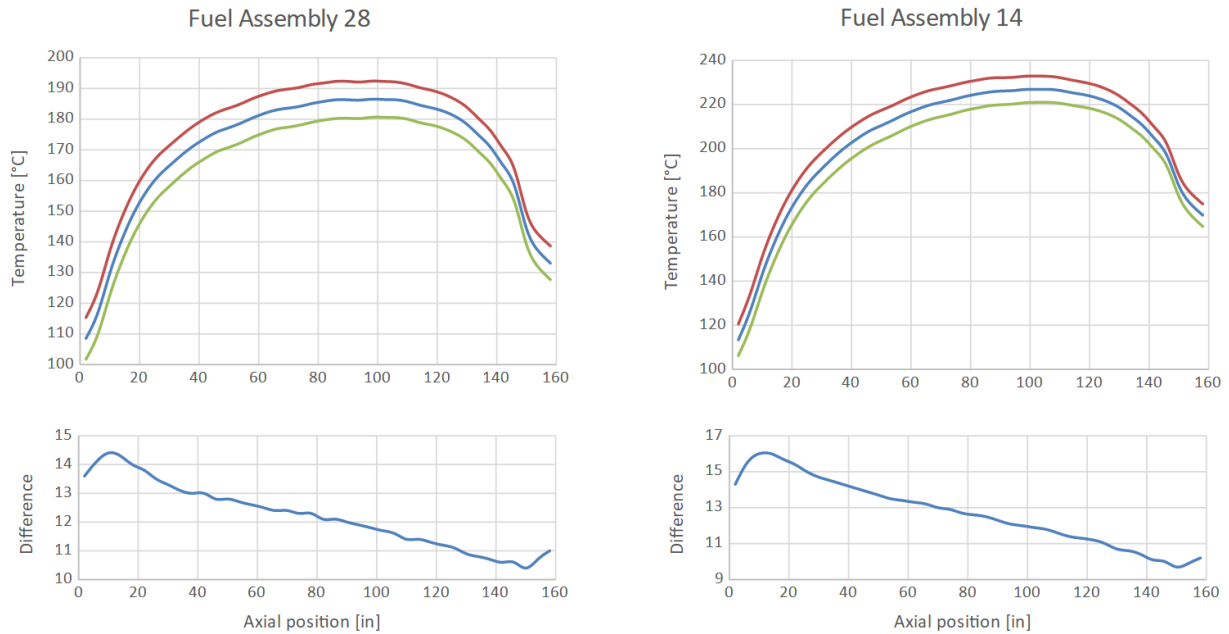


Figure 2.39: Temperature variation with room temperature. Results are presented for FA 28 (corner fuel assembly) on the left and for FA 14 on the right (central fuel assembly). For both assemblies, three curves are plotted on the upper diagrams corresponding to the base case result and to the increased (+8.3 °C) and reduced (-8.3 °C) room temperatures. On the lower diagrams, we plotted the temperature difference between the calculations with the increased and reduced room temperatures.

potential difference $V_1 - V_0 = R \times I$ is also fixed and any change of the (reference) potential V_0 results in the same change for the potential V_1 . In the case of the cask, the heat flux Φ corresponds to the current and is fixed (when the decay heats of the fuel assemblies are fixed) and the thermal resistance R_{th} is fixed as the material properties and the cask geometry are fixed. It is a rough approximation to say that we can define a simple thermal resistance between any given point of the cask and the environment, as the heat paths are complex and the heat transfers are not linear (especially the radiative and convective heat transfers), but the idea that from a given point to the environment the heat encounters a certain resistance remains valid. If the end point of the heat flux - the room temperature T_{room} - is raised then the whole path (including the starting point T_{int}) should be expected to be raised too.

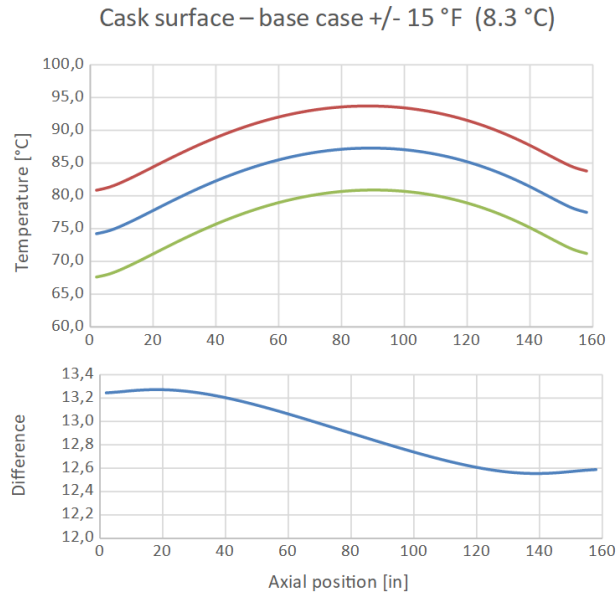


Figure 2.40: Temperature variation of the cask surface with room temperature. The three curves plotted on the upper diagram correspond to the base case result and to the increased (+8.3 °C) and reduced (-8.3 °C) room temperatures. On the lower diagram, we plotted the temperature difference between the calculations with increased and reduced room temperatures.

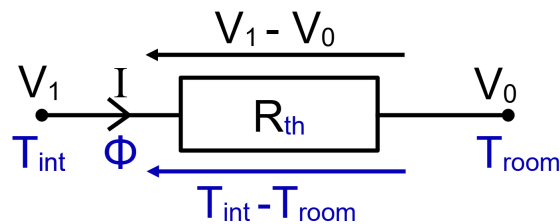


Figure 2.41: Analogy between temperatures and electrical potentials. If the current I (resp. the heat flux Φ) and resistance R (resp. thermal resistance R_{th}) are fixed, then the potential difference $V_1 - V_2$ (resp. the temperature difference $T_{int} - T_{room}$) is known and any variation of the potential V_0 (resp. the temperature T_{room}) results in the same variation for the potential V_1 (resp. the temperature T_{int}).

2.4.3 Summary on the TN-32B model

In this section, we presented and discussed a COBRA-SFS cask model, developed in the frame of an international thermal modelling benchmark. The cask modelled is a TN-32B, which can host up to 32 PWR fuel assemblies. The first phase of the benchmark aimed to provide the results (a list of temperature profiles) of a base case calculation corresponding to a given power loading scheme.

The specifications of the benchmark were very detailed. Experimental temperature data were provided, which enabled an efficient validation of the model. The result of phase 1 of the benchmark gave further evidence that COBRA-SFS can provide very realistic results in a detailed manner and without high computational costs: the simulation results are mainly within 10 °C from the experimental measurements, with an exception for one temperature profile presenting a maximum difference of 16 °C (Fig. 2.35 and Fig. 2.36). A report on the results of this first phase should be published by EPRI by the end of 2022.

Preliminary sensitivity calculations have been performed too, focussing on the effect of the room temperature and decay heat on the temperature distribution. We observed that room temperature variations affect the temperature of both the fuel assemblies and the cask body: an increase of the room temperature by 16.6 °C results in an increase of approximately 13 °C for the cask surface (Fig. 2.40) and of 10 to 16 °C for the fuel assemblies (Fig. 2.39).

Concerning the decay heat, the effect of a $\pm 5\%$ variation appeared stronger on the fuel assemblies than on the cask surface: the fuel assembly temperature varies by 8 to 18 °C (Fig. 2.37), while the cask surface temperature varies by less than 5 °C (Fig. 2.38).

The upcoming phase 2 of the benchmark foresees more comprehensive sensitivity analyses and should start in 2022.

2.5 Conclusion - Temperature fields in storage casks

This chapter presented three models used to determine cask temperature distributions and evolutions.

The first model (*Python model*) is inspired by the German CASTOR[®] V/19, a cask widely used in Germany for the storage of PWR spent fuel assemblies. It consists in a semi-analytical model, based on classical, fundamental heat transfer equations, which are solved using the programming language Python. The model includes 6 homogenized zones and this simplicity of the model offers many advantages: it can be easily adapted to new boundary conditions or application cases, it would be convenient to couple with a further program (e.g. for the analysis of the thermo-mechanical behaviour of the fuel rods), it enables to perform many simulations in a short time without the need of high performance computing infrastructures (thus, we conducted a sensitivity analysis involving 7000 simulations on our laptop within 8 hours) and finally, it ensures a good overview and understanding of its constitutive elements. Furthermore, although the model yields only 6 temperature values, it can provide good orders of magnitude as discussed in section 2.3.4. The model is well adapted for the simulation of transients, including accidental scenarios and drying process, or even investigations related to the final repository, for e.g. different host rock environments.

As a detailed knowledge of the temperature distribution and evolution in a cask is necessary for the prediction of the cladding behaviour during long-term storage, a more detailed model has been built using the thermal-hydraulic code COBRA-SFS. This second model (*CASTOR model*) is also inspired by the CASTOR[®] V/19. It includes a large number of elements (568 solid nodes, 6887 helium channels, 6156 rods and 36 axial layers) and yields correspondingly detailed temperature results: each single rod is taken into account independently, different powers can be assigned to the 19 fuel assemblies with specific axial power profiles and the boundary conditions can be defined in a precise manner (surface temperatures, surface heat fluxes). A simulation for a steady-state case is performed within only a

few minutes using a standard laptop.

Due to the lack of publicly available experimental data, the model has been cross-validated by comparison with two CASTOR[®] V/19 inspired models built using different codes. The comparison of the COBRA-SFS model with the Python model enabled to determine some equivalences and further validated the two models.

A sensitivity analysis was performed on the CASTOR model and showed that the room temperature and the gaps between the different structures of the cask have a significant impact on the temperature distribution.

Different loading schemes were simulated and showed for instance the influence of the *special assemblies* on the temperature distribution.

The third model presented in this chapter is also built using COBRA-SFS and models a TN-32B cask, which is mainly used for experimental purposes in the USA. This model is also very detailed, including 627 solid nodes, 10400 helium channels, 9248 rods and 40 axial layers. The development of this model was motivated by the participation to an international thermal benchmark organized by EPRI.

The outcomes of phase 1 of the EPRI benchmark showed that COBRA-SFS (and in particular the model presented in this thesis) can yield results very close to the experimental measurements (maximal difference of 16 °C but mainly below 10 °C). A first sensitivity analysis confirmed the strong impact of the room temperature on the overall temperature distribution, as already observed with the CASTOR model. It also showed that the uncertainty on the decay heat values can lead to important temperature variations too, in particular within the fuel assemblies (less in the cask body).

The results of the first phase of the benchmark will be published by EPRI in a report by the end of 2022. Phase 2 should start in 2022 and will consist in a more comprehensive sensitivity analysis of the models developed for phase 1.

3 Hydrogen and hydride behaviour

The second part of this thesis describes the hydrogen behaviour in the cladding. As all main phenomena (dissolution, precipitation, diffusion) are strongly dependent on the temperature, Chapter 2 constitutes a logical prerequisite for the issues discussed in Chapter 3.

3.1 Introduction

3.1.1 Cladding oxidation, hydriding and embrittlement

LWR fuel assemblies spend in general 4 to 5 years in reactor. During this period, they are immersed in water at high temperature (in the order of 325 °C for PWR and 285 °C for BWR [47]) and pressure (in the order of 155 bar for PWR and 75 bar for BWR [47]), and permanently irradiated by a high neutron flux. An oxidation reaction between the zirconium of the cladding and the water from the primary circuit leads to the formation of an oxide layer on the outer surface of the cladding, according to the equation:



This zirconium oxide layer presents different drawbacks. First, it has a thermal conductivity significantly lower than metal zirconium (1-3 W m⁻¹ K⁻¹ for zirconium oxide vs. 14-17 W m⁻¹ K⁻¹ for zirconium alloy, for temperatures ranging from ambient temperature to 400 °C [48–51]), which leads to an increase of the temperature in the fuel rod. In particular, the temperature increases at the interface of zirconium oxide and metal (the order of magnitude of +1 °C when the oxide layer grows by 4 µm is given in [52] for Zircaloy-4 cladding), where the oxidation reaction takes place. The temperature increase at this interface furthers even more the oxidation reaction, as

the thickness of the oxide layer increases.

When the oxide layer reaches a certain thickness (in the order of 100 μm), an important risk of desquamation has to be taken into account: the mechanical properties of the zirconium oxide are not as good as for the zirconium alloy and the zirconium oxide can peel off from the underlying zirconium alloy. This leads to variations in the cladding thickness and to cold spots in the cladding where the oxide peeled off, which in turn impacts the cladding hydridation. In [53], the IRSN reports that corrosion thickness measurements performed by EDF on fuel rods from the French 1300 MWe NPPs revealed that 5 % of the rods present a corrosion thickness above 108 μm at the end of operation, and 35 % a thickness above 80 μm .

Furthermore, parallel to the formation of an oxide layer, the zirconium alloy bulk of the cladding becomes thinner as the oxidation progresses. The mechanical characteristics of the cladding are directly impacted: the azimuthal and axial stresses in the cladding are approximately inversely proportional to the cladding thickness (see Equations 3.2), and thus the stress in the cladding increases as the oxidation progresses.

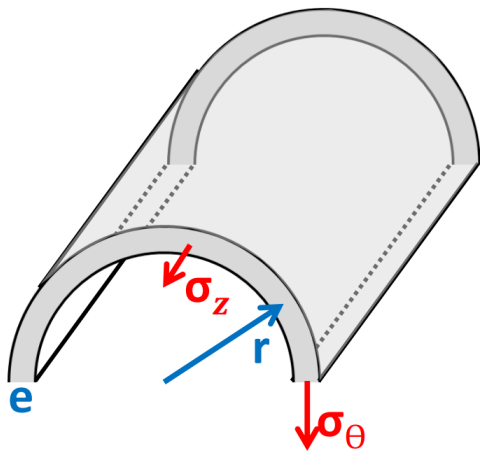


Figure 3.1: Axial and circumferential stresses in a cylinder.

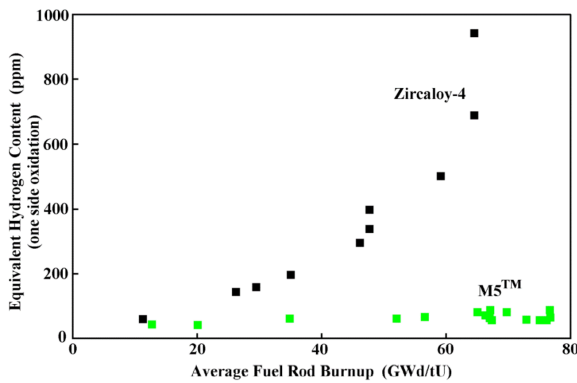
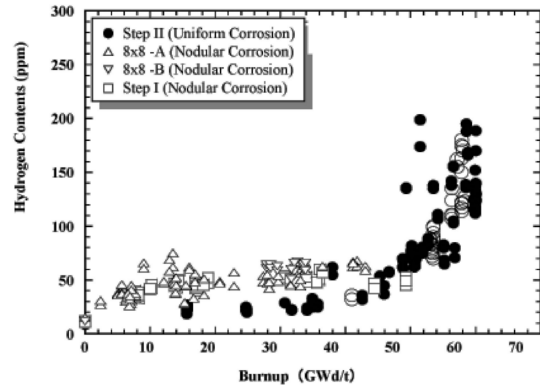
Barlow's formula for a thin-walled tube:

$$\begin{aligned}\sigma_{\theta} &= \frac{r \cdot (P_{int} - P_{ext})}{e} \\ \sigma_z &= \frac{r \cdot (P_{int} - P_{ext})}{2e}\end{aligned}\quad (3.2)$$

with r the cladding radius, e the cladding thickness, and P_{int} (resp. P_{ext}) the internal (resp. external) rod pressure.

Another important aspect of the cladding oxidation is the related hydrogen uptake. Indeed, part of the hydrogen (10 to 20 % [22]) generated by the oxidation reaction is absorbed by the cladding. Depending on the zirconium alloy type, the cladding oxidation is more or less severe and the hydrogen

uptake thus results in hydrogen contents varying from a few tens up to several hundreds of wt.ppm. Thus, for a burnup of 50 MWd/t_{HM}, Zircaloy-4 cladding presents a hydrogen concentration of 300 to 400 wt.ppm, while other materials such as M5TM or Zircaloy-2 with liner usually remain well below 100 wt.ppm, as can be seen in Fig. 3.2 (a) and (b). According to the temperature and total hydrogen concentration, the hydrogen can be either dissolved (hydrogen in solid solution) or precipitated as hydrides.

(a) Zircaloy-4 and M5TM. Taken from [54].

(b) Zircaloy-2 with Zr-liner. Taken from [55].

Figure 3.2: Hydrogen content in cladding with regard to the burnup.

The determination of the hydride morphology is important, as it can strongly impact the mechanical properties of the cladding. While metal zirconium presents a ductile behaviour, hydrides are brittle and hydrided cladding is thus more susceptible for crack propagation and loss of integrity. The fracture toughness K_{IC} , which measures the resistance of a material to crack propagation, is represented for Zircaloy-4 in Fig 3.3 with regard to the temperature and for different hydrogen concentrations [56]. We can observe ductile to brittle transition temperatures (rapid increase in the middle of the S-shaped curves) for almost all concentrations. For each curve, the linear domain at high temperature starts approximately at the temperature ensuring total dissolution of the hydrogen:

- TSS_D(270 °C) \approx 40 wt.ppm
- TSS_D(340 °C) \approx 100 wt.ppm
- TSS_D(410 °C) \approx 200 wt.ppm

- $TSS_D(500\text{ }^\circ\text{C}) \approx 400\text{ wt.ppm}$
- $TSS_D(560\text{ }^\circ\text{C}) \approx 600\text{ wt.ppm}$
- $TSS_D(650\text{ }^\circ\text{C}) \approx 1000\text{ wt.ppm}$

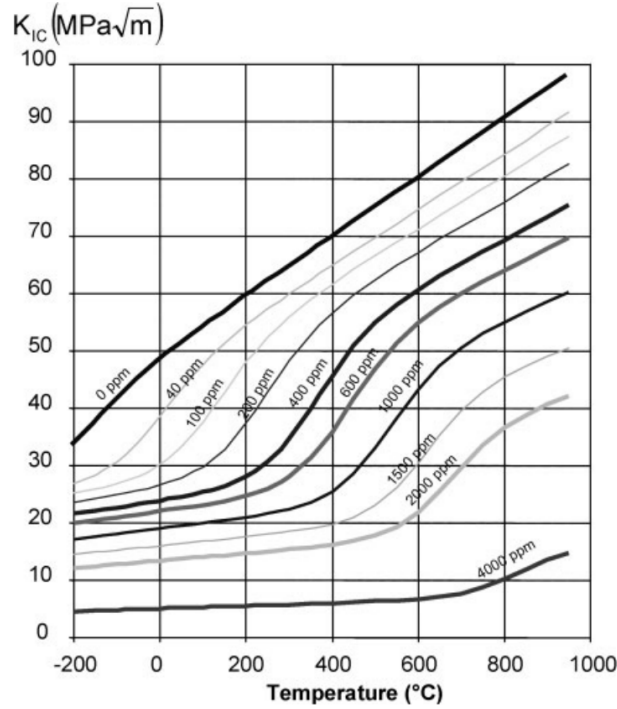


Figure 3.3: Influence of hydrogen content and temperature on Zircaloy-4 fracture toughness. The curves correspond to a correlation established by IRSN and based on a literature review of fracture toughness values. Taken from [56].

At a temperature above $300\text{ }^\circ\text{C}$, like in reactor or at the beginning of the dry storage in a cask (realistic estimation for a cask loaded with a rather high power), a large amount of hydrogen is dissolved as the solubility is in the order of 100 wt.ppm . On the contrary, if the cladding temperature is around $50\text{ }^\circ\text{C}$, the hydrogen solubility is near zero so that almost all hydrogen is precipitated as hydrides. This corresponds to temperatures during the wet storage in cooling pond or in a cask after a long storage time (lower power due to decay).

To describe the hydrogen precipitation behaviour in zirconium alloy, numerous experimental works have been performed and solubility limit curves

have been determined. This point will be presented in more detail in section 3.1.2. However, the determination of a solubility limit depending on the temperature is not sufficient to predict the behaviour of a fuel rod with regard to the hydrogen. Indeed, the diffusion has to be taken into account, too: hydrogen can diffuse in the cladding (especially over long periods of time, e.g. the extended dry storage), under the influence of different factors:

- temperature gradients
- concentration gradients
- stress gradients

Hydrogen diffusion is discussed in more detail in section 3.1.3.

Another important parameter is the overall stress distribution in the cladding, which can impact the hydride morphology. While circumferential hydrides are commonly observed at the end of operation when the fuel is cooled, radial hydrides might be formed later. For instance, if the cladding is heated up and then cooled down under a high tensile stress (resulting from high internal fuel rod pressure or from pellet cladding contact), the tensile stress along the circumferential direction can foster the formation of hydrides radially oriented. This is not desirable, as cracks propagate through the cladding much easier along hydrides (brittle material) than in the zirconium alloy bulk (ductile). If the hydrides are radially oriented, the crack propagation can occur more easily and the risk of a cladding opening is increased. [57–63]

Finally, we can mention that during a cooling period (such as the dry storage), the initial configuration is believed to be important: hydride growth requires less energy than the nucleation of new hydrides. Thus, even if under a given stress level one should expect the precipitation of radial (resp. circumferential) hydrides, the presence of circumferential (resp. radial) hydrides in the cladding might avoid the formation of radial (resp. circumferential) hydrides.

The work presented in [12] gives some evidences that the threshold stress for the precipitation of radial hydrides rather than circumferential hydrides

depends on the total hydrogen concentration (see Fig. 3.4) and on the peak cladding temperature (which determines, how many hydrides remain precipitated over the whole experiment time). This threshold stress presents a minimum at the hydrogen concentration corresponding to the hydrogen solubility limit at the peak temperature. For instance, in Fig. 3.4b (experimental results for a peak temperature of 400 °C), the minimum threshold stress (≈ 50 MPa) is reached for a hydrogen content of approximately 200 wt.ppm, which corresponds to the hydrogen solubility at the peak temperature of the experiments: $TSS_D(400 \text{ °C}) \approx 200 \text{ wt.ppm}$.

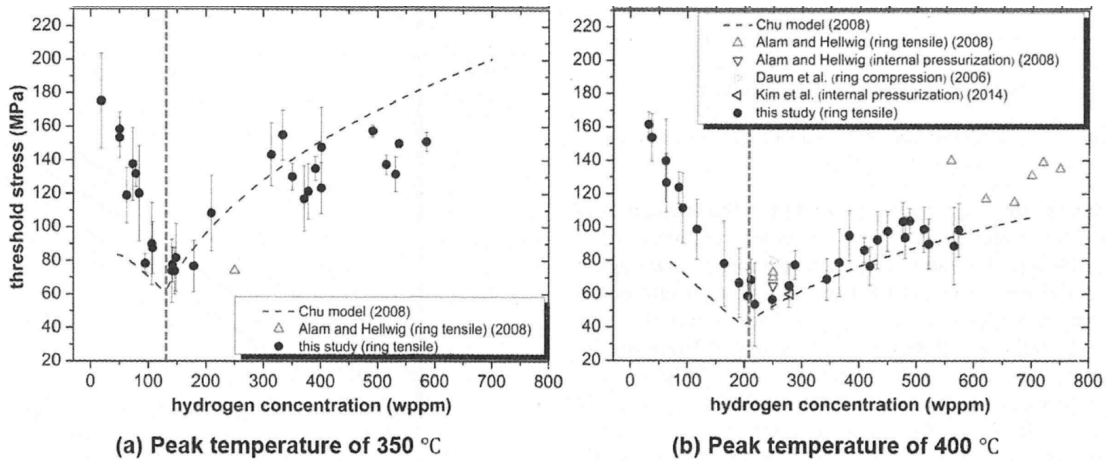


Figure 3.4: Threshold stress for hydride reorientation, depending on the hydrogen content and on the peak temperature. Taken from [12].

For hydrogen concentrations below this limit, the threshold decreases with increasing hydrogen content (the higher the concentration, the easier it is to build radial hydrides), while for concentrations above this limit, the threshold increases with increasing hydrogen content: increased hydrogen content means more hydrides remaining (circumferentially) precipitated at the peak temperature, on which the dissolved hydrogen can precipitate during cooling.

This shows that a low concentration of hydrides is not necessarily a good condition (contrarily to what was widely believed): it can lead to complete dissolution of the hydrides when the peak temperature is reached, and enable later the precipitation of radial hydrides rather than circumferential hydrides [62, 63]. For instance, a cladding having a hydrogen concentration of 150 wt.ppm presents a threshold stress around 80 MPa if the cladding un-

dergoes a heating to 350 °C (Fig. 3.4a), while for a cladding with a hydrogen concentration of 350 wt.ppm the threshold stress is around 140 MPa.

Hydrogen and hydride behaviour has been an important research topic in the last decades due to this safety aspect and significant improvements have been achieved in the understanding of the precipitation mechanisms. However, the prediction of the hydrogen distribution and hydride morphology at the scale of a full rod and over long periods of time remains difficult.

3.1.2 Hydrogen solubility - TSS_p & TSS_D

Fig. 3.5 presents the phase diagram of the Zr-H binary system¹. For the temperature range encountered during normal conditions of operation and storage (≤ 400 °C), zirconium is in the α -phase, a hexagonal close-packed (HCP) low-temperature phase with some solubility of hydrogen [64]. The temperature and hydrogen range corresponding to normal operations and storage conditions is marked by a red rectangle. In this red rectangle, two domains can be observed:

- α -phase if the temperature is high enough and the hydrogen content sufficiently low. In this case, all hydrogen is dissolved in the zirconium and thus only one phase is present. The hydrogen dissolved in the α -zirconium matrix forms a *solid solution*.
- α - and δ -phases if the hydrogen content is too high or the temperature too low. In this case, part of the hydrogen precipitates in δ -hydrides. Both α and δ phases coexist.

¹This diagram has been known since the 1950's. Fig. 3.5 has been published in 1962 and only minor changes have been performed since then. In particular, the zirconium higher temperature phase, β -phase, was characterized as body-centered cubic in early literature (e.g. in Fig. 3.5), but is now largely accepted to be orthorhombic [64]. The main changes relevant for spent fuel storage concern the precise determination of the hydrogen solubility limit (limit between α and $\alpha + \delta$ domains) which is discussed in detail in the following.

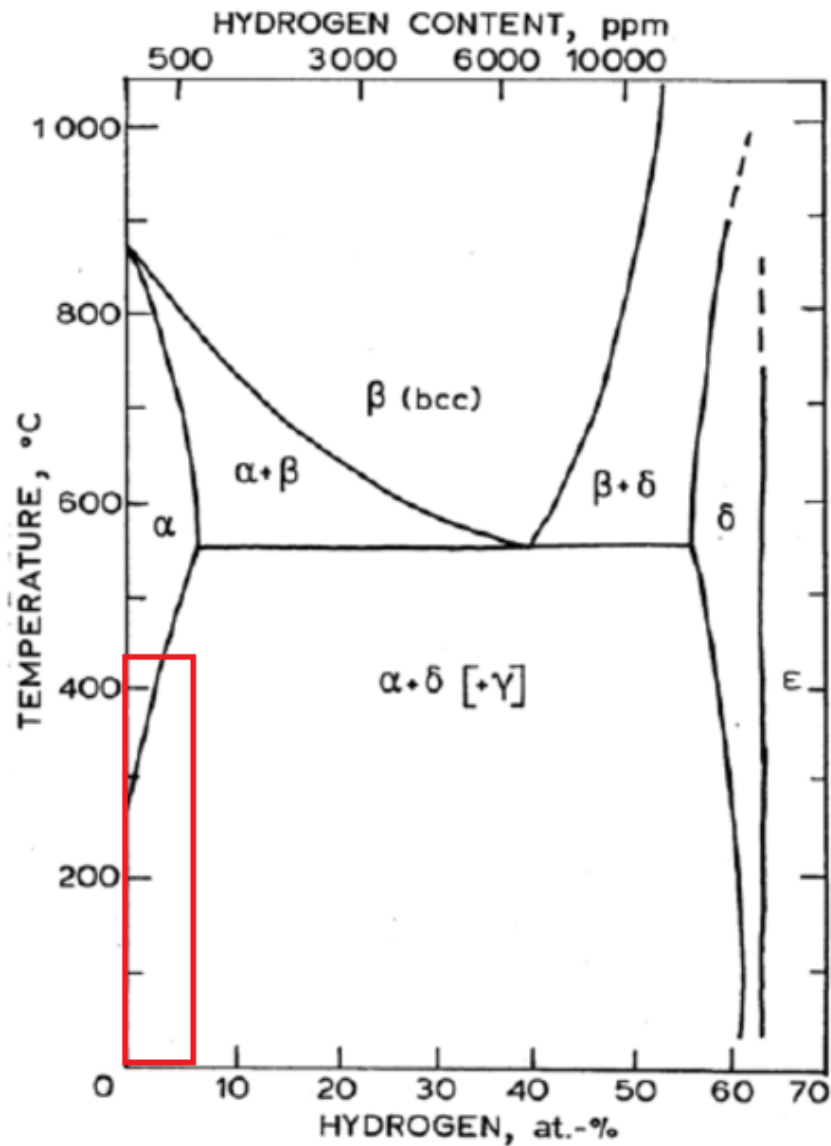


Figure 3.5: Phase diagram for Zr-H binary system. For normal reactor operations and spent fuel storage, only the lower left part of the diagram (red rectangle) is relevant: temperatures up to 400 °C and hydrogen contents of a few hundred wt.ppm. These conditions enable two configurations of the system: if the temperature is high enough and the hydrogen content low enough, then all hydrogen is dissolved (*solid solution*) and there is only one phase (α -phase). Otherwise, if the temperature is too low or the hydrogen content too high, then part of the hydrogen forms hydrides and the binary system consists in two phases (α -zirconium and δ -hydrides). Adapted from [65].

Furthermore, the phase diagram indicates

- the temperature-dependent solubility limit of hydrogen in zirconium, given by the line separating the α domain from the $\alpha+\delta$ domain, and
- the stoichiometry of the δ -hydrides, given by the line separating the $\alpha+\delta$ domain from the δ domain at around 60 at.% of hydrogen: 60 at.% of H and 40 at.% of Zr corresponds to $\text{ZrH}_{1.5}$.

Thus, the α -phase can contain only a relatively low amount of hydrogen without forming a further phase. The concentration limit is called *Terminal Solid Solubility* (TSS) and depends mainly on the temperature. It corresponds to the amount of hydrogen that can be dissolved in zirconium at a given temperature. The higher the temperature is, the more hydrogen can be dissolved in the zirconium. This binary diagram does not consider the influence of alloying elements used in zirconium-based cladding materials. These elements are thought to influence the oxidation behaviour and amount of hydrogen uptake. However, according to [64], they are not expected to influence the hydride formation and reorientation directly, rather details of kinetics and perhaps some morphology as the precipitates may influence nucleation sites. Early experimental works (1967) already observed that alloying elements in Zircaloy-2, Zircaloy-4 and Zr-2.5wt%Nb have no significant effect on the Terminal Solid Solubility, which remains very nearly the same as that in unalloyed zirconium [66,67].

In many experimental works [13,66–81], the hydrogen solubility limit in zirconium alloys has been studied and correlations have been derived. While originally a single solubility limit TSS was considered [66–69], heating and cooling experiments revealed later that different limits could be defined: in cooling experiments, the solubility appeared higher than in heating experiments. The difference was explained by the volumetric misfit strain: hydrides have a lower density than zirconium alloys (approximately 12-17%) and therefore the precipitation of hydrides (during cooling) necessitates more energy to deform the zirconium matrix [74,82]. To distinguish the different solubility limits, the terms of Terminal Solid Solubility for Precipitation

(TSS_P) and Terminal Solid Solubility for Dissolution (TSS_D) have been introduced and widely used in later works [13, 70–81].

Fig. 3.6 gives an example of TSS_P/TSS_D curves. We can observe that both curves present an exponential profile, starting with a hydrogen solubility nearly null at room temperature. TSS curves are thus usually described by an Arrhenius law:

$$TSS(T) = TSS_0 \cdot \exp\left(-\frac{E}{RT}\right) \quad (3.3)$$

with TSS_0 a pre-exponential coefficient, E the activation energy, R the gas constant and T the temperature.

The TSS_P curve is above the TSS_D which means that at a given temperature, the hydrogen solubility observed during cooling (precipitation) experiments is higher than the solubility observed during heating (dissolution) experiments.

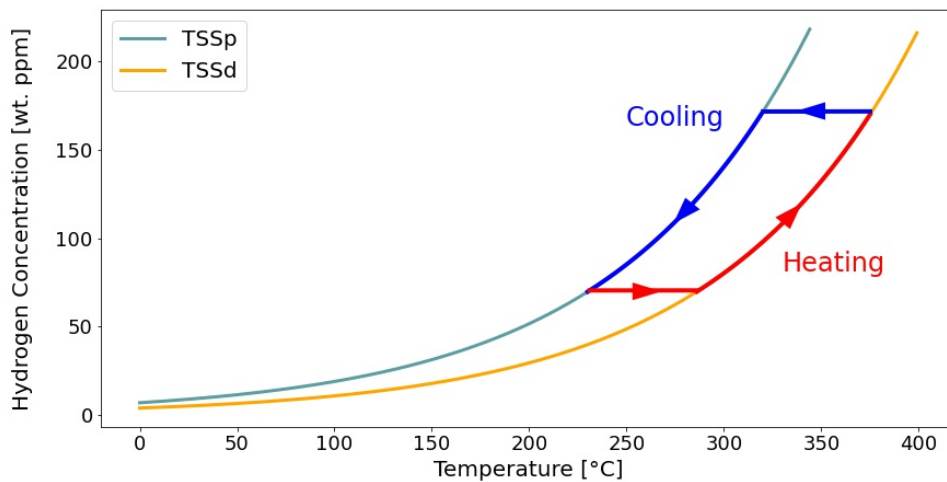


Figure 3.6: Generic curves representing the Terminal Solid Solubility for Dissolution (TSS_D) and Precipitation (TSS_P) of hydrogen in zirconium as function of the temperature.

A thermal cycle is also represented on the diagram. It corresponds to a material with (at least) 170 wt.ppm hydrogen, which undergoes a cooling from 375 °C to 230 °C, followed by a heating back to the initial temperature of 375 °C.

Starting at a temperature of 375 °C, the hydrogen solubility is around 170 wt.ppm (upper right point of the thermal cycle). From this point, the temperature is then decreased (blue curve). First, the dissolved hydrogen concentration does not change but remains equal to 170 wt.ppm (horizontal segment of the blue curve). Only when the temperature has dropped down to 320 °C, the blue curve reaches the TSS_P curve, which means that hydride precipitation will start with further cooling. Thus, as the temperature further decreases from 320 °C to 230 °C, the dissolved hydrogen concentration decreases (i.e. hydrides precipitate), following the concentration given by the TSS_P curve.

The heating phase (red curve) starts when the temperature has reached 230 °C. At first, the heating from 230 °C to 285 °C (red horizontal segment) does not induce any change in the concentration of dissolved hydrogen: the temperature must first increase until it reaches the TSS_D curve and only then the hydride dissolution starts. During the further heating, the dissolved hydrogen concentration follows the TSS_D curve: it increases until it reaches the initial concentration of 170 wt.ppm, when the temperature is back to 370 °C.

This example shows the role played by the two different solubility limits, TSS_D and TSS_P. In particular, they induce a certain delay in precipitation and dissolution, which has been referred to as *hysteresis* in the literature [13, 69, 71, 72, 74, 78, 80].

The understanding of the different solubility limits significantly improved over the years. The dependence of the TSS_P values on experimental parameters (cooling rate, peak temperature) has been noted for a long time. Thus, in [71], the authors defined a TSS_{P1} and a TSS_{P2}, obtained respectively by cooling from an upper- and a lower-bound maximum temperature. A *memory effect* has also been described, responsible for variations in TSS_P: a former hydride precipitation is likely to result in pre-existing dislocation nests which facilitate re-precipitation of hydrides² [13, 71, 76].

More recent works [8, 9] provided new insights into the solubility limit: the

²This *memory effect* is thought to be strongly dependent on the temperature evolution, especially on peak temperature: high temperatures can anneal out the dislocations caused by former hydride precipitation and therefore annul the *memory effect*. [71]

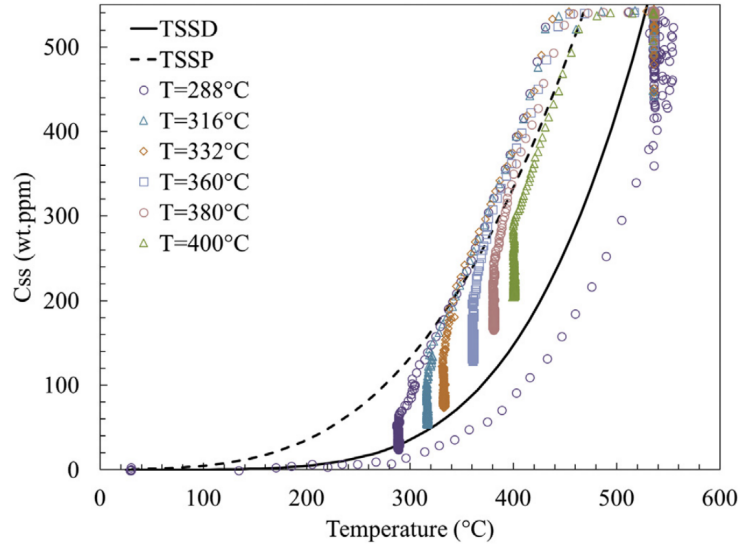


Figure 3.7: Experimental results on a sample loaded with 541 wt.ppm hydrogen. The sample is first heated to 535 °C and held for 30 min at this temperature, which ensures total dissolution of the hydrides. Then it is quickly cooled (2 °C/s) to a given target temperature (6 cases on the figure, ranging from 288 °C to 400 °C) and held for 2 h at this temperature. We can see on the picture that the concentration of dissolved hydrogen falls below TSS_P , continuing to decrease towards TSS_D . This indicates that precipitation can occur in the “hysteresis region” and suggests that TSS_D is the equilibrium solubility. Taken from [9].

TSS_P can be interpreted as the result of a kinetic effect while the TSS_D corresponds to the thermodynamic equilibrium. In [9], experimental results gave evidence that if a sufficient hold time (in the order of some hours) was included after cooling, hydride precipitation continues during this temperature hold and the dissolved hydrogen slowly decreases from TSS_P towards TSS_D (see Fig. 3.7).

In [8], the authors proposed to introduce a kinetic adjustment for the precipitation of zirconium hydrides in zirconium alloys. They argue that the precipitation of further hydrides on pre-existing hydrides is subjected to the diffusion of hydrogen. In the case of high cooling rate, hydrogen would not have enough time to diffuse to the energetic minimum and would therefore precipitate locally³, forming thereby new hydrides. This is in accordance

³Characteristic lengths for diffusion of hydrogen in a zirconium alloy are provided in the next section, Table 3.1.

with former experimental works. [62, 63]

The fact that most experiments were performed with relatively high cooling rates compared to those expected during dry storage results in TSS_P values valid only in these specific conditions. Thus, most data and correlations obtained from the former experimental works might be well valid for applications to fast thermal transients (e.g. during reactor operation), but the TSS_P curves from the literature should be considered with caution, especially for assessment of long-term cladding behaviour.

3.1.3 Diffusion mechanisms

This section has been adapted from [83] and aims to present the main equations and characteristics of the diffusion, which are essential prerequisites for predictions on the hydrogen behaviour in the cladding.

Particle diffusion is an irreversible phenomenon driven by thermal agitation. The higher the temperature is, the more efficient the diffusion is. Furthermore, diffusion tends to homogenize the media: if there is a concentration gradient, the particles will diffuse from the higher concentration towards the lower concentration region. Diffusion under a concentration gradient is usually described by the phenomenological Fick's law. The influence of temperature gradients is commonly referred to as Soret effect or thermophoresis.

In the following, we present the notions of particle flux and particle current density, and we establish the conservation equation. Then we introduce the Fick's law and Soret effect, which enable to derive the diffusion equation under the influence of concentration and temperature gradients. Finally, we provide a few examples of characteristic lengths for hydrogen diffusion in a zirconium alloy.

Particle flux through a surface and current density vector

We call particle flux Φ through a surface S the particle flowrate through this surface. The number of particles going through S during a time dt is

then given by:

$$dN = \Phi dt$$

We can then introduce the vector particle current density $\vec{j}(M, t)$ whose flux through S yields the particle flux previously defined:

$$\Phi = \iint_{M \in S} \vec{j}(M, t) \cdot \vec{dS}_M$$

The number of particles dN going through S between t and $t + dt$ is thus given by:

$$dN = \Phi dt = \left(\iint_{M \in S} \vec{j}(M, t) \cdot \vec{dS}_M \right) dt \quad (3.4)$$

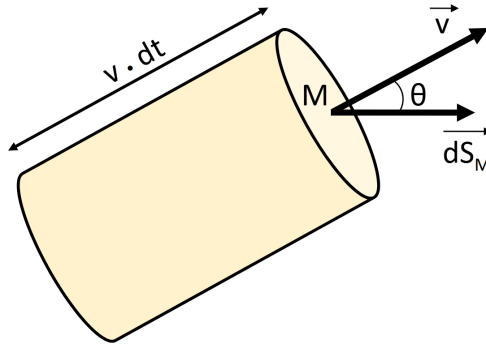


Figure 3.8: Particle current density vector.

Considering particles with a velocity \vec{v} , if $n(M, t)$ is the local particle density and \vec{dS}_M an oriented elementary surface making an angle θ with \vec{v} , we can calculate the number of particles d^2N that will cross \vec{dS}_M between t and $t + dt$. These particles are located in the cylinder whose generators are parallel to \vec{v} and of length $v dt$ (see Fig. 3.8). The volume of this cylinder is :

$$d\tau = dS_M v dt \cos \theta = \vec{v} \cdot \vec{dS}_M dt$$

and the number of particles d^2N is :

$$d^2N = n d\tau = (n \vec{v}) \cdot \vec{dS}_M dt$$

Using the definition of the particle current density vector:

$$d^2N = d\Phi dt = \left(\vec{j}(M, t) \cdot \vec{dS}_M \right) dt$$

We can then identify the particle current density vector at point M and time t as:

$$\vec{j}(M, t) = n(M, t) \vec{v}(M, t) \quad (3.5)$$

Conservation and diffusion equations

Let \mathcal{V} be a volume, fixed and non-deformable, delimited by the surface \mathcal{S} . The variation of the number N of particles in the volume \mathcal{V} between t and $t + dt$ is:

$$dN = N(t + dt) - N(t) = \frac{d}{dt} \left(\iiint_{M \in \mathcal{V}} n(M, t) d\tau_M \right) dt$$

at first order in dt . As \mathcal{V} is fixed and non-deformable, we can invert the order of the time derivative and the space integral:

$$dN = \iiint_{M \in \mathcal{V}} \frac{\partial n(M, t)}{\partial t} d\tau_M dt$$

The number of particles entering the volume \mathcal{V} between t and $t + dt$ is:

$$\delta N_{ext \rightarrow \mathcal{V}} = - \oiint_{P \in \mathcal{S}} \vec{j}(P, t) \cdot d\vec{\mathcal{S}}_P dt = - \iiint_{M \in \mathcal{V}} \text{div } \vec{j}(M, t) d\tau_M dt$$

The negative sign comes from the fact that $d\vec{\mathcal{S}}_P$ is pointing outwards of the volume \mathcal{V} while $\delta N_{ext \rightarrow \mathcal{V}}$ are particles entering the volume \mathcal{V} . The second equality is a direct application of the Ostrogradsky's theorem⁴.

⁴The Ostrogradsky's theorem states that if \vec{V} is a continuously differentiable vector field, then the integral of \vec{V} over a closed surface \mathcal{S} is equal to the integral of the divergence of \vec{V} over the volume inside \mathcal{S} . To highlight the importance of the hypothesis *closed surface*, the surface integral is usually written with a circle symbol on it (double closed integral).

We can then write the conservation equation as:

$$\begin{aligned} dN &= \delta N_{ext \rightarrow \mathcal{V}} + dN_{prod} \\ \Leftrightarrow \iiint_{M \in \mathcal{V}} &\left(\frac{\partial n(M, t)}{\partial t} + \text{div } \vec{j}(M, t) - n_{prod}(M, t) \right) d\tau_M dt = 0 \end{aligned}$$

with n_{prod} the density of particle production.

As this equation should be valid for any volume \mathcal{V} , we can write the local conservation equation:

$$\frac{\partial n(M, t)}{\partial t} + \text{div } \vec{j}(M, t) = n_{prod}(M, t) \quad (3.6)$$

Fick's law is a phenomenological law which states that the particle flux is proportional to the local concentration gradient:

$$\vec{j}_{Fick}(M, t) = -D \overrightarrow{\text{grad}} n(M, t) \quad (3.7)$$

The proportionality coefficient D is called *diffusion coefficient*, or *diffusivity*, and has dimension of $\text{m}^2 \text{s}^{-1}$.

In addition to the effect of concentration gradients, temperature gradients can also influence diffusion. The Soret effect, or thermophoresis, describes the diffusion due to temperature gradient [14, 70, 84] and can be expressed as:

$$\vec{j}_{Soret}(M, t) = -\frac{D Q^* n}{R T^2} \overrightarrow{\text{grad}} T(M, t) \quad (3.8)$$

where D is the diffusion coefficient, Q^* the heat of transfer, n the concentration of the diffusing particles, R the gas constant and T the temperature.

We can derive the diffusion equation (under concentration and temperature gradients) by combining the conservation equation (Equation 3.6) with the particle flux due to the concentration gradient (Equation 3.7) and temperature gradient (Equation 3.8):

$$\frac{\partial n(M, t)}{\partial t} - \text{div} \left(D \overrightarrow{\text{grad}} n(M, t) + \frac{D Q^* n}{R T^2} \overrightarrow{\text{grad}} T(M, t) \right) = n_{prod}(M, t) \quad (3.9)$$

with D the diffusion coefficient in $\text{m}^2 \text{s}^{-1}$.

In the case of diffusion problem without significant temperature gradient, we can neglect the Soret effect and assume the diffusion coefficient D to be constant so that it can be taken out of the second derivative. Thus, Equation 3.9 can be rewritten as:

$$\frac{\partial n(M, t)}{\partial t} - D \cdot \Delta n(M, t) = n_{prod}(M, t) \quad (3.10)$$

Characteristic dimensions

We can derive a simple relation between characteristic time and diffusion length by dimensional analysis (non-dimensionalization) of equation 3.10. Indeed, if τ and L are the characteristic time and length, and t^* and x^* the corresponding non-dimensional variables, equation 3.9 (without production term) leads to:

$$\frac{1}{\tau} \frac{\partial n}{\partial t^*} = \frac{D}{L^2} \frac{\partial^2 n}{\partial x^{*2}}$$

Thus, the characteristic time and diffusion length are linked by:

$$\tau = \frac{L^2}{D} \quad \text{or} \quad L = \sqrt{D\tau} \quad (3.11)$$

Equation 3.11 enables to quickly determine an order of magnitude of the time required for particles to diffuse over a given distance, or to estimate the extent of the diffusion after a given time. Table 3.1 provides some examples of characteristic lengths for diffusion of hydrogen in Zircaloy-2 at different temperatures and over different periods of time. These characteristic lengths are calculated using diffusion coefficients determined experimentally and provided in [68].

We should note that these characteristic lengths correspond to diffusion under concentration gradients but without taking the effect of temperature gradients into account. Depending on their orientation, temperature gradients might either accelerate or slow down the diffusion.

Table 3.1: Characteristic length of diffusion at different temperatures and for different diffusion times: an hour, a day, a week, a month and a year. The diffusion coefficients have been measured in Zircaloy-2 [68].

Temperature	Diffusion coefficient	Characteristic length				
		Hour	Day	Week	Month	Year
261 °C	$0.80 \cdot 10^{-6} \text{ cm}^2 \text{ s}^{-1}$	0.054 cm	0.26 cm	0.70 cm	1.5 cm	5.0 cm
315 °C	$1.70 \cdot 10^{-6} \text{ cm}^2 \text{ s}^{-1}$	0.078 cm	0.38 cm	1.0 cm	2.1 cm	7.3 cm
358 °C	$2.94 \cdot 10^{-6} \text{ cm}^2 \text{ s}^{-1}$	0.10 cm	0.50 cm	1.3 cm	2.8 cm	9.6 cm
408 °C	$4.71 \cdot 10^{-6} \text{ cm}^2 \text{ s}^{-1}$	0.13 cm	0.64 cm	1.7 cm	3.5 cm	12 cm

3.1.4 Hydrogen diffusion in the fuel cladding

Fig. 3.9 represents the influence of the temperature and concentration gradients on the hydrogen diffusion in the cladding: hydrogen diffuses from high concentration regions towards lower concentration regions (Fick's law) and from high temperatures towards low temperatures (Soret effect). Both effects lead to an equilibrium distribution: the temperature gradient supports diffusion towards the cold region, and the resulting higher concentration in the cold region counterbalances progressively the diffusion due to Soret effect. In the case of fuel rods, stress gradients are assumed to be negligible compared to temperature and concentration gradients. Indeed, due to the cylindrical geometry of the cladding, no significant stress gradient should be expected along the axial direction, nor along the radial direction (consistent with the Barlow's formula applied in the conditions of a thin tube). However, stress gradients can play an important role in the case of local "defects", such as cracks: the stress concentration at the tip of a crack attracts hydrogen and eventually leads to the formation of hydrides which embrittle the material and promote further crack propagation.

Hydrogen distribution along the radial dimension of the cladding has been

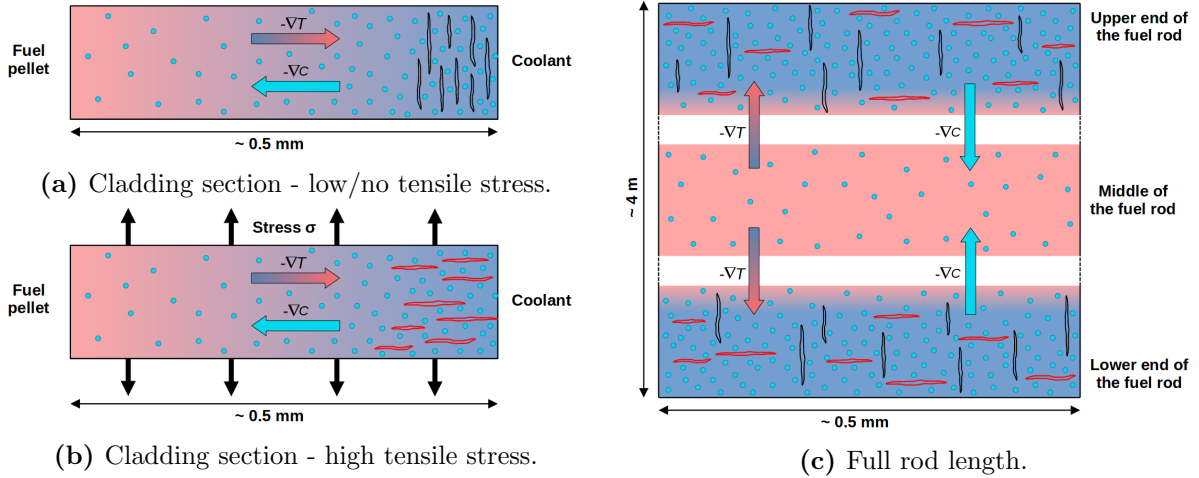


Figure 3.9: Hydrogen diffusion and hydride morphology under temperature, concentration and stress gradients. Dissolved hydrogen is represented with light blue points, hydrides with black (circumferential) and red (radial) plates. The background colour indicates temperature gradients (blue for cold regions, red for hot regions). Arrows on the diagrams show the influence of the Fick's law ($\vec{\nabla}c$) and Soret effect ($\vec{\nabla}T$). (a) and (b) represent radial cuts of a cladding, while (c) corresponds to the axial dimension. We should note that the characteristic length for diffusion involved in (c) (order of magnitude: m) is significantly longer than in (a) and (b) (order of magnitude: mm). In (b), the cladding undergoes a high circumferential tensile stress, which resulted in the formation of radial hydrides. While (a) and (b) configurations have been observed in many experimental works, (c) should be considered with more care as there are less results for full-length rods. Section 3.4 examines this topic.

experimentally observed in many works. In particular, during reactor operations, high radial temperature gradients lead to high concentration gradients with lower hydrogen concentrations in the inner side of the cladding and higher hydrogen concentrations on the outer side. This is represented in Fig. 3.9a and Fig. 3.9b. Furthermore, the impact of stress is shown by the black arrows in Fig. 3.9b: high tensile stresses along the circumferential direction might lead to the formation of radial hydrides (perpendicular to the tensile stress) instead of circumferential hydrides. The threshold stress for the formation of radial hydrides has been described in different experimental works. [12, 57, 61–63]

Fig. 3.9c concerns the diffusion at the scale of a full rod. This topic will be examined in more detail in section 3.4.

3.2 TSS_P/TSS_D plots and correlations

In section 3.1.2, we discussed the importance of the hydrogen solubility to predict the hydrogen and hydride behaviour in zirconium alloys. A database has been built using experimental data on the Terminal Solid Solubility from different works [13, 66–68, 70–74, 76–78, 80, 81]. The data points have been collected by Felix Boldt, the careful assessment of the uncertainties has been conducted by Felix Boldt, Bastien Grimaldi, Peter Kaufholz, Maik Stuke and me. Afterwards, I produced the plots and correlations presented in this section.

The review of the data led to two questions:

Can we derive reliable correlations from these data?

Is there a clear separation between the TSS_P and TSS_D?

3.2.1 Database and uncertainties

In a first step, the published experimental values of TSS have been collected in a database. After extensive review, further information has been stored for each experiment, for example year of publishing, material type and experimental method. Uncertainties were also added, trying to remain as little conservative as possible. Where it was stated, uncertainties were determined from the information provided in the publications. Some were given in percent, other in absolute values. In some cases, we contacted the authors for more details. We tried very carefully to not over or underestimate the uncertainties.

The database consists of

- 672 data points, including uncertainties,
- 48 experimental series,
- 12 research projects,
- 7 materials, irradiated and unirradiated, and
- 5 different measurement methods.

Table 3.2: TSS_D/TSS_P database references. The 12 research projects are listed with the name of the first author and the reference, the year of publication, the materials investigated, the measurement method applied and the type of solubility (TSS_D and/or TSS_P).

Author	Year	Material	Method	TSS
Kearns [66]	1967	Zr, Zry-2, Zry-4	Diffusion	D
Kammenzind [70]	1996	Zry-4	Diffusion	D & P
Pan [71]	1996	Zr-2.5Nb	DEM	D & P
McMinn [72]	2000	Zry-2, Zry-4	DSC	D & P
Vizcaíno [73]	2002	Zry-4	DSC	D
Une [74]	2003	Zry-2, HighFeZry	DSC	D & P
Singh [76]	2004	Zry-2, Zr-2.5Nb	Dilatometry	D & P
Une [77]	2009	Zry-2	DSC	D & P
Tang [78]	2009	M5, N18, Zry-4	DSC	D & P
Colas [13]	2012	Zry-2	In-situ XRD	D & P
Kim [80]	2014	Zry-4	DSC	D & P
Blackmur [81]	2015	Zry-4	In-situ XRD	P

Fig. 3.10 depicts the temperature versus the hydrogen concentration for all TSS values stored in the database. Data points are colour coded according to publication, regardless of measurement methods or materials.

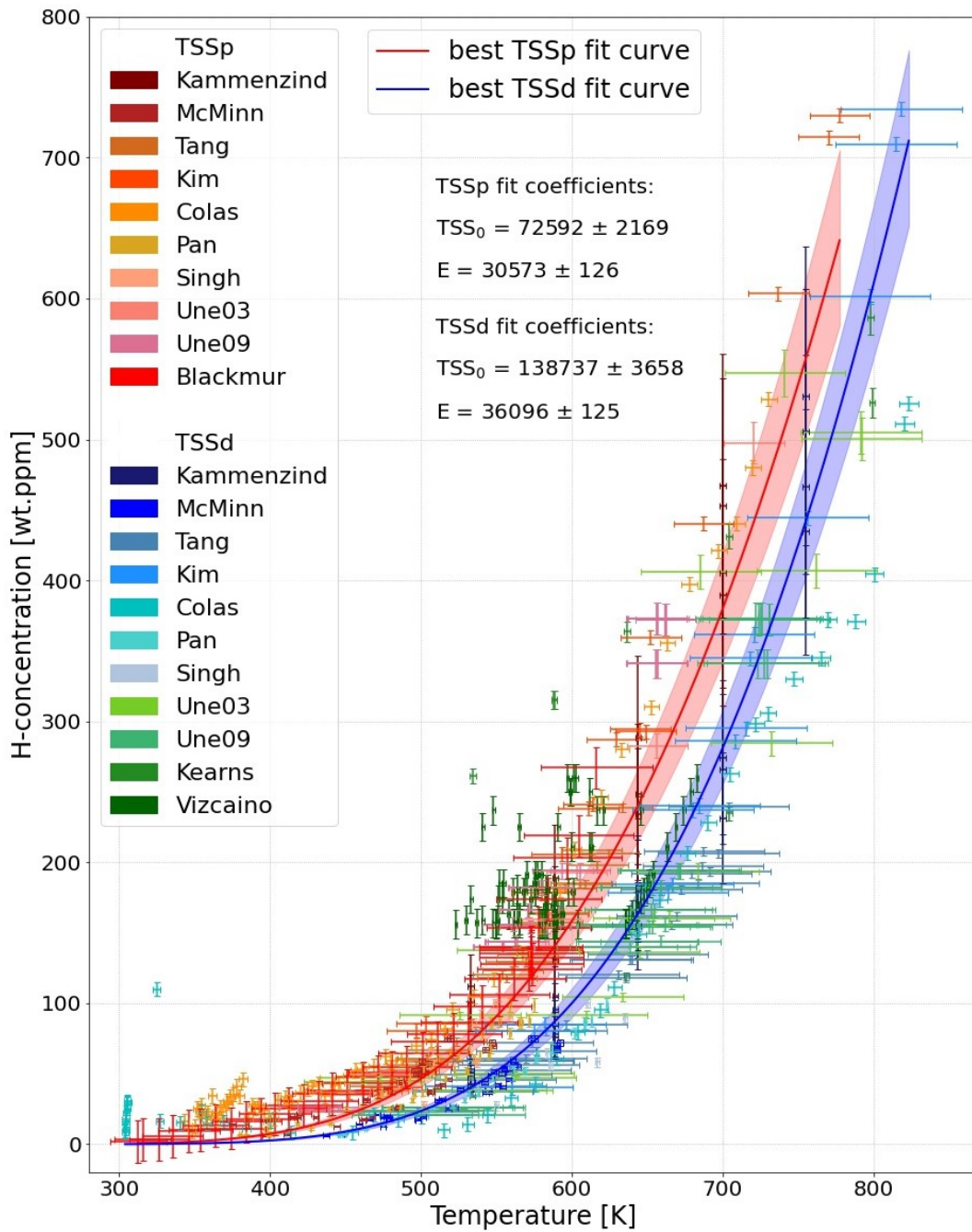


Figure 3.10: Plot of all TSS_P and TSS_D points from the database as a function of the temperature and with uncertainties. The best fit curves for TSS_P and TSS_D are plotted and the fit coefficients (with standard deviations) of both curves are indicated on the figure. 95% confidence intervals (1.96σ) are drawn around the fit curves.

3.2.1.1 Cladding materials

Zirconium alloys are widely used as cladding materials for nuclear fuel. This choice is motivated by the low thermal neutron absorption cross section of zirconium, combined with good mechanical properties and corrosion resistance, and a satisfying thermal conductivity. While Zircaloy-4 and Zircaloy-2 have been the most common alloy variants for PWR and BWR respectively, the permanent search of higher burnups and more flexibility in operation led to the development of further alloys, such as M5[®] for PWR and HiFi[®] for BWR.

Table 3.3: Composition [wt.-%] of Zircaloy-2, Zircaloy-4, Zr-2.5Nb, M5[®], N18 and HiFi[®], including the principle alloying elements. For a given alloy type, the standard composition might have changed with time and information in the literature was not always consistent. Therefore, the values presented in this table should not be considered too strictly. [85–92]

Element	Zircaloy-2	Zircaloy-4	Zr-2.5Nb	M5 [®]	N18	HiFi [®]
Sn	1.20 - 1.70	1.20 - 1.70	–	–	0.80 - 1.20	1.20 - 1.70
Nb	–	–	2.4 - 2.8	0.80 - 1.20	0.20 - 0.40	–
O	0.10 - 0.14	0.10 - 0.14	0.09 - 0.13	0.11 - 0.16	–	–
Fe	0.07 - 0.20	0.18 - 0.24	< 0.065	< 0.05	0.30 - 0.40	0.25 - 0.50
Cr	0.05 - 0.15	0.07 - 0.13	–	–	0.05 - 0.10	0.05 - 0.15
Ni	0.03 - 0.08	–	–	–	–	0.03 - 0.08
Zr	Balance	Balance	Balance	Balance	Balance	Balance

The development of zirconium alloys as cladding materials started in the 1950s, prompted by the development of nuclear submarines [90]. Zircaloy-2 was designed specifically for nuclear applications in a high-temperature water environment. The alloying agents - tin, iron, chromium, and nickel - were added to neutralize the detrimental effect on corrosion resistance of

the impurities - nitrogen, aluminium, and carbon - and for their strengthening effect. The low neutron absorption cross section of pure zirconium was not increased significantly by those alloying elements [93]. Zircaloy-2 is still the industry standard for BWR fuel cladding and is currently mainly used with an inner liner⁵, which aims to protect the cladding against damage induced by pellet cladding interaction. [94]

Zircaloy-4 was developed from Zircaloy-2 with the principal aim of reducing the hydrogen pick up in reactor. Thus, both alloys present very similar compositions, except for a few elements. In particular, nickel is removed (limited to 0.007%) from the alloy composition of Zircaloy-4 [93]. Zircaloy-4 has been the industry standard for PWR fuel for many decades, starting in the 1960s. To increase the oxidation resistance and therefore improve the mechanical properties and enable higher burnups, cladding designs including an outer liner have been developed. [91]

Zr-2.5Nb is a common zirconium alloy, which has been used for pressure tubes in CANDU (Canada Deuterium Uranium) and RBMK (Reaktor Bolshoy Moshchnosti Kanalnyy) reactors for over 40 years [87]. Compared to Zircaloy-2 and Zircaloy-4, it does not contain tin, but 2.4 to 2.8 wt.ppm niobium.

M5[®] is a cladding material for PWR fuel assemblies developed in the 1990s by Framatome. It is fully re-crystallized, includes 1 wt.% niobium and presents significant improvements compared to Zircaloy-4: low corrosion and very low hydrogen pickup. It enables higher burnups and provides more flexibility for nuclear operations without sacrificing margin for accidents [85,95]. It is now a standard cladding material for PWR fuel.

N18 is an alloy developed in China in the 1990s. While Zircaloy-2 and Zircaloy-4 belong to Zr-Sn series, and Zr-2.5Nb and M5 to the Zr-Nb series, N18 is a Zr-Sn-Nb alloy. [88,92]

High Fe Zr alloy has been developed for use as BWR fuel claddings and spacer material at high burnups. It was originally developed by NFI (start-

⁵Initially, in the 1970s, this inner liner was made of pure zirconium. In the 1990s, it was replaced by low-alloyed zirconium (e.g. 0.4% Fe). [91]

ing in the mid-1980s) and builds on the performance experience acquired with Zircaloy-2 cladding but with minor changes aiming at improving the resistance to hydrogen uptake [96]. It is now commercialized under the commercial name of HiFi[®] and constitutes a new generation of BWR cladding material, meeting increasing demands for higher fuel duties and burnup. For instance, Westinghouse new BWR fuel assembly TRITON11[™] uses HiFi[®] as cladding material (with a ZrSn-liner) [97]. The final composition of HiFi[®] remains unchanged compared to Zircaloy-2, except for the iron level which is above the upper limit of Zircaloy-2 chemical specifications. [74, 86]

3.2.1.2 Measurement methods

This section shortly presents the five measurement methods used to obtain the TSS_P and TSS_D values gathered in the database. The following descriptions of the measurement methods are taken from [8], where more details can be found. Only the description of the Dynamic Elastic Modulus (DEM) method derives from other sources.

Diffusion techniques

Early experiments focusing on the determination of the effect of temperature on the terminal solid solubility of hydrogen in alloys were carried out either as diffusion couple experiments or as thermo-diffusion experiments [66–68]. The diffusion couple experiments use the thermal diffusion of dissolved hydrogen between a hydrogen charged and an uncharged specimen connected by welding. The hydrogen-rich metal contains a higher hydrogen concentration than the expected terminal solid solubility at the temperature of the experiment. The welded specimens were afterwards heated to allow hydrogen to diffuse into the uncharged specimen of the couple. As diffusion only takes place with dissolved hydrogen, one can calculate the terminal solid solubility of hydrogen at the diffusion temperature knowing the amount of hydrogen diffused into the hydrogen free specimen. From the hysteresis point of view, the diffusion couple is heated to dissolve zirconium hydrides at the level of TSS_D into the matrix. After reaching diffusion equilibrium,

a cool-down of the couple would lead to hydrogen concentrations equal to the TSS_D in the low hydrogen part of the specimen.

In thermo-diffusion experiments, a hydrided specimen is exposed to a temperature gradient where the distribution of hydrogen is guided by thermo diffusion. At a certain point within the gradient, the solubility of hydrogen is exceeded, resulting in the precipitation of zirconium hydrides. The hydrogen concentration at the transition between the area containing zirconium hydrides and dissolved zirconium area is taken as terminal solid solubility. However, from the hysteresis point of view, the terminal solid solubility derived by this method at the boundary concentration to precipitation depicts the TSS_P . [8]

Dilatometry

This method uses the change in dimensions of a specimen during hydride precipitation. As zirconium hydrides have a significantly lower density compared to the α -Zr matrix in the alloy, every precipitation of zirconium hydrides results in a deformation of the lattice and an overall change in length of the specimen. In dilatometric hydride analysis, hydrided specimen are heated while the change in length is recorded as a function of the temperature. Measurements can be carried out during heating and cooling, depicting the TSS_D in the heating experiment mode and TSS_P in the cooling experiment mode. Due to the direct response in the measurement and the possibility to perform consecutive heating and cooling experiments using the same material, the method is ideal for the determination of the TSS-curves. [8]

Differential Scanning Calorimetry

With the further development of measurement technologies, new methods became available to analyse the solubility of hydrogen in zirconium alloys. The technology of differential scanning calorimetry (DSC) opened a new option for the determination of the hydrogen terminal solid solubility. The method is based on calorimetric measurements of absorbed heat during a heating process. The detection of the affiliated heat of the specimen allows for the quantitative description of the dissolution of hydrides. However, the

method is sensitive to deviations in the type of zirconium hydrides as they exhibit different formation enthalpies. An additional factor of uncertainty in this technique is the interpretation of the measurements raw data. As shown in [73], a variation of about 20 °C in TSS-values can be related to different interpretation. [8]

Dynamic Elastic Modulus

Elastic Moduli are quantities measuring the ability of a material to resist elastic deformation⁶ under an applied stress. They are usually measured by destructive tests consisting in applying a load (stress) and recording the corresponding deformation (strain): the elastic modulus⁷ is defined as the slope of the recorded stress-strain curve. In this case, it is called *Static Elastic Modulus*.

Alternatively, new techniques have been developed to determine the *Dynamic Elastic Modulus*, based on sonic or ultrasonic resonance methods [98]. This avoids destructing the specimens and enables to perform multiple tests on one specimen for a range of temperature. These techniques require very small strain and have a great precision in the measurement of the elastic modulus.

In the case of zirconium alloy containing hydrogen, the plot of elastic modulus with regard to the temperature presents a “knee” point associated with the dissolution (during heating) or precipitation (during cooling) of hydrides. For a specimen with a hydrogen concentration c , it is thus possible to determine the temperatures T_D and T_P for which $TSS_D(T_D) = c$ and $TSS_P(T_P) = c$. [71,99]

X-ray diffraction

The modern application of X-ray diffraction for the analysis of hydride reori-

⁶In solid mechanics, two main types of deformations can be distinguished: elastic deformations (corresponding to the elasticity of the atomic bonds in the case of metal) which are completely recoverable and plastic deformations which are not recoverable (related to the breaking of atomic bonds).

⁷For isotropic solids, we can distinguish the Young’s modulus E and the shear modulus G , depending on the type of stress (normal or shear) considered. Both E and G are termed *Elastic Moduli*. The Young’s modulus is the most frequently examined.

entation and hydride precipitation opens an option to get a direct response from zirconium hydrides. Using X-ray diffraction, it is possible to observe hydride dissolution and precipitation kinetics in-situ at high temperatures. The method is extensively used to investigate the effect of stress on the crystallization orientation of zirconium hydrides [81, 100, 101]. While the determination of TSS_P in the traditional methods is linked to a full dissolution of zirconium hydrides, followed by a cooling process to obtain the first precipitation, in-situ X-ray analysis opens an option to observe the precipitation within a specimen with existing zirconium hydrides. [8]

3.2.2 ODR method

To fit the data, we used the Orthogonal Distance Regression (ODR) method, which enables to account properly for the uncertainties on both variables: the solubility limit and the temperature. The ODR method is presented in detail in the User's Reference Guide for ODRPACK⁸ [103], from which the following summary is adapted.

Least squares methods consist in finding the parameters $\beta \in \mathbb{R}^p$ of a mathematical model f that defines a relationship between variables that are subject to errors. f can be linear or non-linear in its parameters β . Sometimes one of the variables is distinguished as being a *response* that is *dependent* upon the remaining variables, which are commonly called the *explanatory*, *regressor* or *independent* variables. In these cases, the explanatory variables are often used to predict the behaviour of the response variable.

We say that there is an *explicit* relationship f between the variables (x, y) if $y \approx f(x; \beta)$, where y is a response variable, x an explanatory variable, and y is assumed to be only approximately equal to $f(x; \beta)$ because of measurement errors in y and possibly x . If only y is subject to measurement error, the parameters of the explicit model can be obtained using ordinary least squares procedures. The regression lines presented in section 2.2.4 of Chapter 2 are an example of ordinary least squares procedures. If both y

⁸ODRPACK is FORTRAN-77 library for performing ODR with possibly non-linear fitting functions. An object-oriented interface to ODRPACK is provided in the Python library SciPy (scipy.odr package). [102, 103]

and x present measurement errors, then the parameters β can be found by orthogonal distance regression. In the case of the TSS data analysis, the temperature is the explanatory variable, the TSS values are the response variables, and the Arrhenius law represents the (non-linear) model consisting of two parameters ($\beta \in \mathbb{R}^2$): the pre-exponential coefficient TSS_0 and the activation energy E in Equation 3.3.

We define the explicit orthogonal distance regression problem as follows: let (x_i, y_i) , $i = 1, \dots, n$ be an observed set of data⁹. Suppose that the values of y_i are a nonlinear function of x_i and a set of unknown parameters $\beta \in \mathbb{R}^p$, but that both the x_i and the y_i contain actual but unknown errors $\delta_i^* \in \mathbb{R}^1$ and $\epsilon_i^* \in \mathbb{R}^1$ respectively. The superscript \star denotes such actual but unknown quantities. The observed value of y_i satisfies

$$y_i = f(x_i + \delta_i^*; \beta^*) - \epsilon_i^* \quad i = 1, \dots, n \quad (3.12)$$

for some actual but again unknown value β^* .

The explicit orthogonal distance regression problem is to approximate β^* by finding the β for which the sum of the squares of the n orthogonal distances from the curve $f(x; \beta)$ to the n data points is minimized (see Fig. 3.11). This is accomplished by the minimization problem

$$\min_{\beta, \delta, \epsilon} \sum_{i=1}^n (\epsilon_i^2 + \delta_i^2)$$

subject to the constraints $y_i = f(x_i + \delta_i; \beta) - \epsilon_i \quad i = 1, \dots, n$.

The ϵ_i can be eliminated from the minimization problem, which then only depends on β and the δ_i :

$$\min_{\beta, \delta} \sum_{i=1}^n ([f(x_i + \delta_i; \beta) - y_i]^2 + \delta_i^2) \quad (3.13)$$

⁹We assume that $x_i \in \mathbb{R}^1$ and $y_i \in \mathbb{R}^1$ for simplicity. This corresponds to the case of the TSS data.

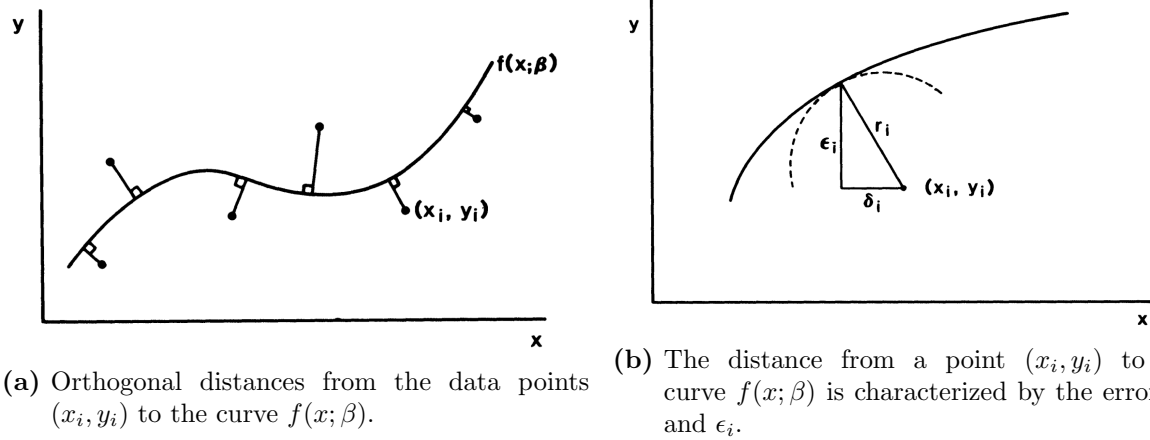


Figure 3.11: Orthogonal Distance Regression (ODR) problem. The problem consists in finding the parameters β of the model f , which minimize the sum of the squares of the distances from the experimental data points (x_i, y_i) to the curve $f(x; \beta)$. Taken from [104].

Finally, we can generalize Equation 3.13 to the weighted orthogonal distance regression problem

$$\min_{\beta, \delta} \sum_{i=1}^n (w_{\epsilon_i} [f(x_i + \delta_i; \beta) - y_i]^2 + w_{\delta_i} \delta_i^2) \quad (3.14)$$

by introducing the weights $w_{\epsilon_i} \in \mathbb{R}^1$ and $w_{\delta_i} \in \mathbb{R}^1$, $i = 1, \dots, n$, which are sets of non-negative numbers and can be used for instance to account for unequal precision on y_i and x_i . In the case of the TSS data analysis, the uncertainties on the temperature and on the TSS values have been taken into account as weighting factors for the determination of the parameters of the Arrhenius fit functions. [103]

Different methods exist for the resolution of non-linear least squares problems. All these methods are iterative: from a starting point β_0 the method produces a series of vectors β_1, β_2, \dots , which hopefully converges to β^* . [105] In the odr package from the Python library SciPy, a modified trust-region Levenberg-Marquardt-type algorithm is implemented to estimate the function parameters [102]. The reader is referred to [104] for a detailed description of this algorithm. The arguments required by the ODR method in the case of the TSS data analysis consisted of:

- the data values x_i (temperature) and y_i (TSS),
- the standard deviations s_{x_i} and s_{y_i} ,
- the model $f(\beta; x)$ (Arrhenius function) and
- an initial guess β_0 of the model parameters (TSS_0 and E).

3.2.3 Analysis and discussion

Fig. 3.12, 3.13 and 3.14 present the results of the ODR method applied to different sets of data from the TSS database, corresponding respectively to experiments on Zircaloy-2, experiments on Zircaloy-4 and experiments using the DSC measurement method. In each case, we considered two sets of data: one for the TSS_P and one for the TSS_D. The data points are plotted with their uncertainties, in shades of red-orange for the TSS_P data and in shades of blue-green for the TSS_D data. For both data sets, the coefficients of the best fit curve have been determined using the ODR method and are written on the figures. The standard deviation σ for each coefficient is provided after the \pm sign. The 95% confidence intervals (1.96σ) are drawn around the fit curves: the best fit curves have a probability of 95% to be contained in these domains (the fit coefficients have a probability of 95% to be contained within the 1.96σ intervals).

Zircaloy-2

In Fig. 3.12, data from 5 different research projects on Zircaloy-2 is plotted, which includes

- 156 data points for TSS_P¹⁰: McMinn (32 points), Colas (74), Singh (5), Une03 (9), Une09 (36)
- 135 data points for TSS_D: McMinn (33 points), Colas (47), Singh (4), Une03 (9), Une09 (42)

¹⁰Corresponding references are summarized in Table 3.2.

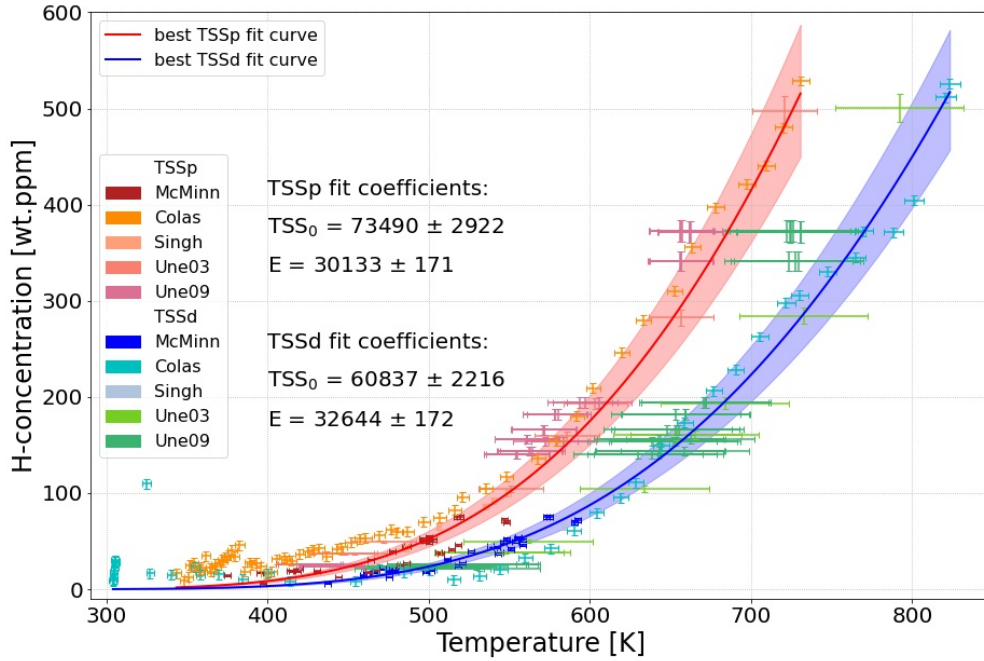


Figure 3.12: Plot of all TSS_P and TSS_D values from the database corresponding to Zircaloy-2. The data points are plotted with uncertainties and the best fit curves for TSS_P and TSS_D , determined by the ODR method, are plotted as well with their respective 95% confidence intervals.

The two fit curves, including the 95% confidence intervals are clearly distinct. The 95% confidence intervals are rather tight around the best fit curves, which is probably due to the large number of data points with small uncertainties. We might note that the TSS_P data from Colas tend to be above the TSS_P fit curve. This might be related to the influence of the cooling rates: 60 °C/min in the measurements from Colas, while it is of 10 °C/min in the measurements from Une (Une03 and Une09) and of 5 °C/min in the measurements from McMinn. This would be in agreement with the kinetic effect discussed in section 3.1.2, according to which a high cooling rate tends to over-estimate the solubility limit.

Zircaloy-4

Fig. 3.13 presents data on Zircaloy-4, corresponding to 6 research projects and including

- 88 data points for TSS_P: Kammenzind (12 points), McMinn (10), Tang (12), Kim (15), Blackmur (39)
- 150 data points for TSS_D: Kammenzind (22 points), McMinn (10), Tang (12), Kim (15), Vizcaíno (91)

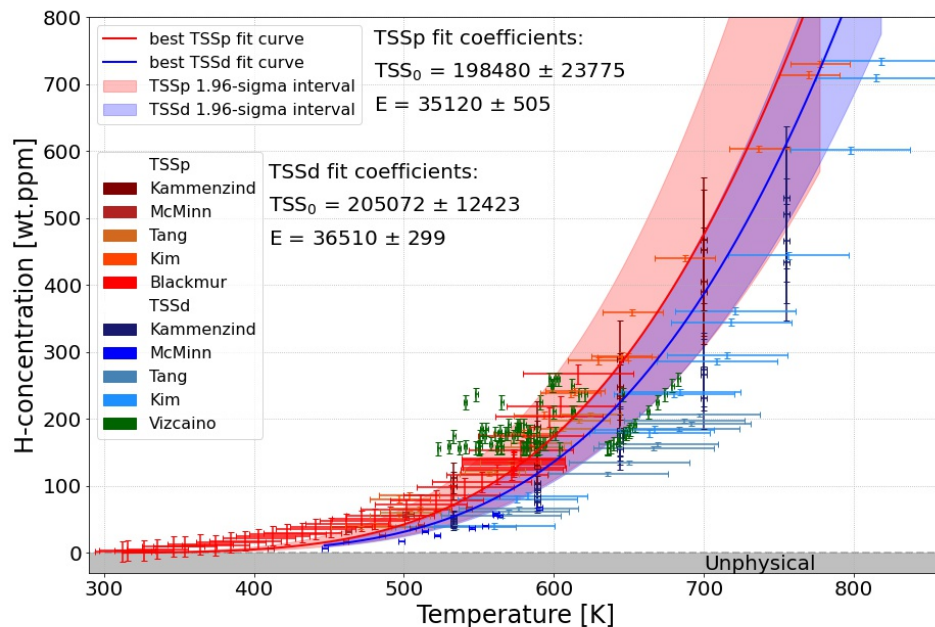


Figure 3.13: Plot of all TSS_P and TSS_D values from the database corresponding to Zircaloy-4. The data points are plotted with uncertainties and the best fit curves for TSS_P and TSS_D, determined by the ODR method, are plotted as well with their respective 95% confidence intervals.

For this data set, the two best fit curves are still distinct, with $TSS_D < TSS_P$ at any temperature, but the 95% confidence interval of the TSS_D fit is completely included in the 95% confidence interval of the TSS_P fit. The larger confidence interval around the TSS_P curve might be explained by rather large uncertainties on most of the TSS_P data points (especially from

Blackmur). Concerning the TSS_D data, we can first observe that the data points from Vizcaíno differ from the rest of the data set, as they are mainly located above the TSS_P fit curve. Furthermore, as they present relatively small uncertainties, they probably tend to increase the resulting TSS_D best fit curve. As a consequence, numerous TSS_D data points are located under the 95% confidence interval of the TSS_D best fit curve. This confidence interval is tighter than for the TSS_P data set, due to a larger number of data points with small uncertainties.

The cooling rates applied for the TSS_P were of 5 °C/min in the work of Blackmur and McMinn, 10 °C/min in the work of Tang and 20 °C/min in the work of Kim. Thus, compared to the Zircaloy-2 data, the Zircaloy-4 data derives from lower cooling rates, which might explain that the distinction between TSS_D and TSS_P is not as clear as for the Zircaloy-2.

Differential Scanning Calorimetry (DSC)

Fig. 3.14 depicts the data points corresponding to experiments using the DSC method to measure the TSS values. It includes data from 6 different research works:

- 134 data points for TSS_P : McMinn (42 points), Tang (32), Kim (15), Une03 (9), Une09 (36)
- 253 data points for TSS_D : McMinn (55 points), Tang (30), Kim (15), Une03 (20), Une09 (42), Vizcaíno (91)

In this case, the two fit curves do not present the classical configuration with $TSS_D < TSS_P$: for temperatures higher than 700 K, the TSS_D curve rises above the TSS_P curve. Furthermore, for temperature above 650 K, the 95% confidence intervals largely overlap. In this case too, the cooling rates involved are lower than for the Zircaloy-2: 5 °C/min for McMinn data (42 points), 10 °C/min for Tang, Une03 and Une09 (77 points) and 20 °C/min for Kim (15 points), which might explain that the distinction between TSS_D and TSS_P is not as clear as for the Zircaloy-2 data. The 95% confidence intervals are rather tight, particularly for the TSS_D fit curve, which is based

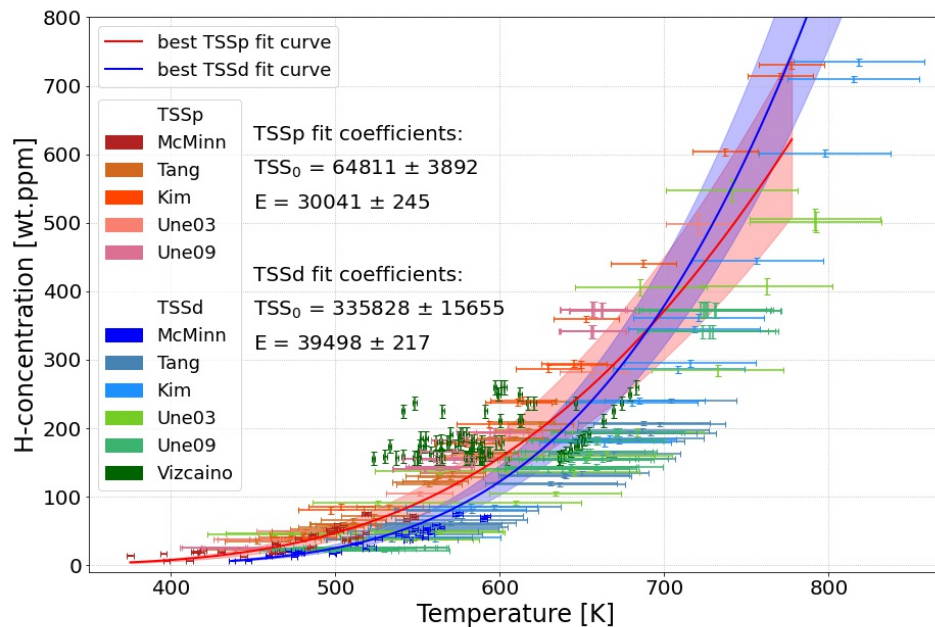


Figure 3.14: Plot of all TSS_P and TSS_D values from the database measured using Differential Scanning Calorimetry (DSC). The data points are plotted with uncertainties and the best fit curves for TSS_P and TSS_D, determined by the ODR method, are plotted as well with their respective 95% confidence intervals.

on a large number of data points. As for the Zircaloy-4 fit, a significant number of TSS_D points appear under the TSS_D fit curve, probably related to the Vizcaíno data.

Further correlations have been derived for data sets corresponding to the other cladding materials and for the other measurement methods. However, they include a lower number of data points, corresponding in no case to more than two different research projects. The complete collection of correlations is provided in Table 3.4, including the standard deviation of each coefficient.

Table 3.4: Arrhenius fit functions for TSS_D and TSS_P calculated with the ODR method. The standard deviations are indicated for each coefficient.

Data set	TSS_D	TSS_P
Zircaloy-2	$(60837 \pm 2216) \exp\left(\frac{-32644 \pm 172}{RT}\right)$	$(73490 \pm 2922) \exp\left(\frac{-30133 \pm 171}{RT}\right)$
Zircaloy-4	$(205072 \pm 12423) \exp\left(\frac{-36510 \pm 299}{RT}\right)$	$(198480 \pm 23775) \exp\left(\frac{-35120 \pm 505}{RT}\right)$
N18	$(58952 \pm 94136) \exp\left(\frac{-32335 \pm 8580}{RT}\right)$	$(36968 \pm 24657) \exp\left(\frac{-26551 \pm 3168}{RT}\right)$
M5	$(87936 \pm 233355) \exp\left(\frac{-34328 \pm 12498}{RT}\right)$	$(33153 \pm 37798) \exp\left(\frac{-26516 \pm 4807}{RT}\right)$
Zr-2.5Nb	$(54477 \pm 4054) \exp\left(\frac{-33016 \pm 327}{RT}\right)$	$(30898 \pm 1763) \exp\left(\frac{-27524 \pm 229}{RT}\right)$
High Fe Zry	$(61206 \pm 42288) \exp\left(\frac{-30310 \pm 3795}{RT}\right)$	
Diffusion	$(107023 \pm 6623) \exp\left(\frac{-34033 \pm 337}{RT}\right)$	$(40960 \pm 25778) \exp\left(\frac{-26957 \pm 3255}{RT}\right)$
DSC	$(335828 \pm 15655) \exp\left(\frac{-39498 \pm 217}{RT}\right)$	$(64811 \pm 3892) \exp\left(\frac{-30041 \pm 245}{RT}\right)$
DEM & dilatometry	$(64127 \pm 4488) \exp\left(\frac{-33642 \pm 313}{RT}\right)$	$(36193 \pm 1987) \exp\left(\frac{-28070 \pm 223}{RT}\right)$
In-situ XRD	$(96955 \pm 10572) \exp\left(\frac{-35473 \pm 651}{RT}\right)$	$(21185 \pm 1044) \exp\left(\frac{-22918 \pm 246}{RT}\right)$
All points	$(138737 \pm 3658) \exp\left(\frac{-36096 \pm 125}{RT}\right)$	$(72592 \pm 2169) \exp\left(\frac{-30573 \pm 126}{RT}\right)$

3.2.4 Summary on the TSS_P/TSS_D database

In this section, we presented a database on the Terminal Solid Solubility (TSS) of hydrogen in zirconium alloys. The database includes experimental data from 12 research projects with 48 experimental series, including a total of 672 data points with uncertainties, involving 7 materials and 5 different measurement methods. The different cladding materials and measurement methods have been described, as well as the Orthogonal Distance Regression (ODR) method. The ODR method (`odr` package from the Python library `SciPy`) has been applied to different sets of data from the database, sorted by material type or measurement method, and correlations have been determined. We presented the results corresponding to the Zircaloy-2 and Zircaloy-4 data sets (Fig. 3.12 and 3.13), and to the DSC data set (Fig. 3.14). We observed that the distinction between TSS_P and TSS_D was not always statistically significant, since there was an overlap of the respective 95% confidence intervals. A statistically significant difference between the two solubility limits was observed for the data set involving the highest cooling rates (Zircaloy-2), while for data sets involving lower cooling rates, the confidence intervals around the TSS_P and TSS_D fit curves were largely overlapping. This might be regarded as a further indication of the kinetic effect discussed in section 3.1.2.

3.3 HNGD Model

This section presents an adaptation of a model which has been recently developed by a research group at the Pennsylvania State University [10,21] and aims to describe the hydrogen behaviour in zirconium alloy. This model is called HNGD model which stands for **H**ydride **N**ucleation-**G**rowth-**D**issolution. Subsection 3.3.1 describes the model and some verification cases are discussed in Subsection 3.3.2. We found slightly different solutions compared to the ones published in [10] and discussed the possible origin of these differences. In section 3.4, predictions for full-length rods are made using similar equations but with specific assumptions adapted to dry storage conditions: long-term slow cooling.

3.3.1 Model description

This model takes into account the two classical solubility limits for hydrogen in zirconium alloy, the TSS_D and the TSS_P , but presents a new interpretation of the *hysteresis* region described in former research works [13, 69, 71, 72, 74, 78, 80].

Indeed, the HNGD model distinguishes the hydrogen precipitation by nucleation of new hydrides, or by growth of existing hydrides. As shown in Fig. 3.15, the nucleation of new hydrides occurs only if the concentration is above the TSS_P , while growth happens for hydrogen concentrations over TSS_P but also between TSS_P and TSS_D (i.e. in the historically so-called *hysteresis* region). TSS_D corresponds to the maximum concentration of hydrogen in zirconium alloy at the thermodynamic equilibrium and therefore, in the domain below this curve all hydrides dissolve. Thus, there is no more hysteresis region, but a region where precipitation occurs only by growth, involving longer time scales compared to nucleation. This is in accordance with experimental observations (see Fig. 3.7) which showed that by a cooling followed by a temperature hold, the hydrogen concentration follows the TSS_P curve during the cooling but then, during the temperature hold, slowly decreases further towards the TSS_D . [9, 21]

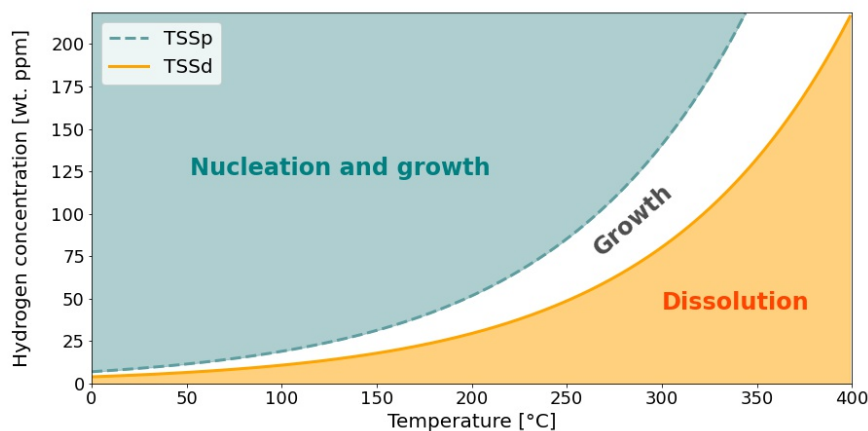
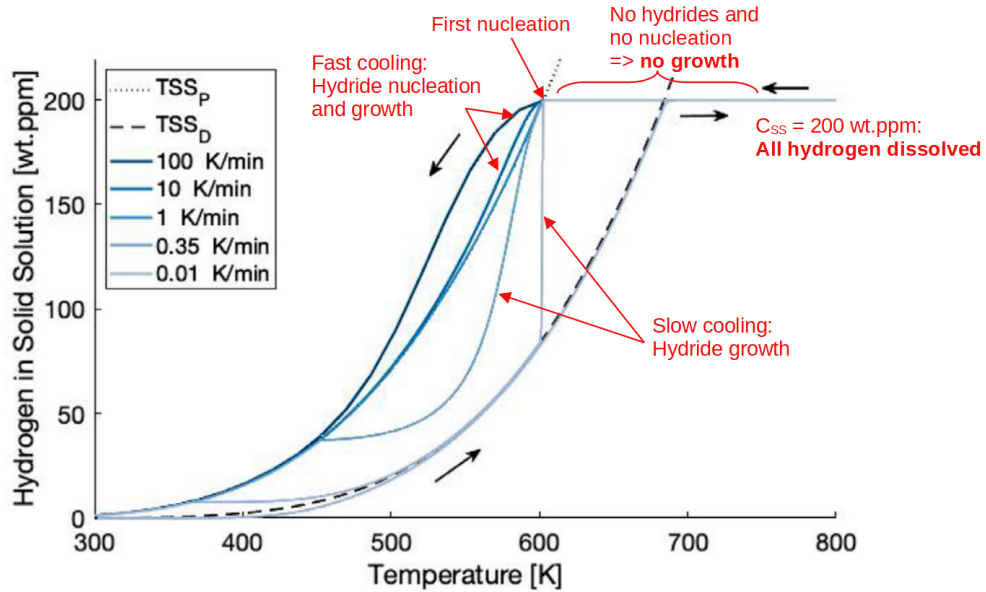


Figure 3.15: Precipitation (nucleation/growth) and dissolution domains considered by the HNGD model.

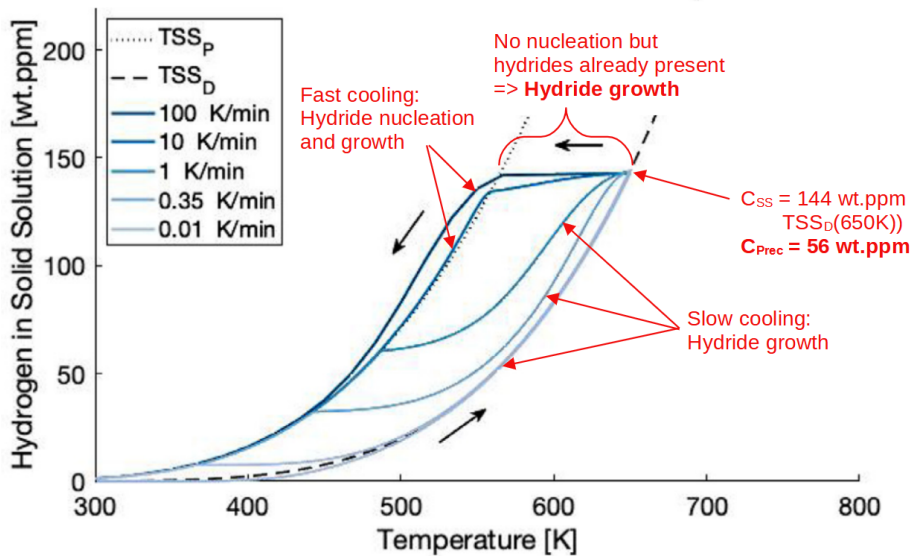
Furthermore, this model distinguishes the cooling from a state where all hydrogen is dissolved and the cooling from a state where some hydrides are still present at the beginning of the cooling. The difference between both cases can be seen in Fig 3.16a and 3.16b, which show the evolution of hydrogen in solid solution for a sample with 200 wt.ppm hydrogen, for different thermal cycles, simulated by the HNGD model of the Pennsylvania State University.

In Fig. 3.16a, the thermal cycles start at room temperature and consist in heating up to 800 K and cooling down back to room temperature with different cooling rates. In this case, the peak temperature leads to a complete dissolution of the hydrides, as the $TSS_D(800\text{ K})$ is higher than 200 wt.ppm. As a consequence, the temperature has first to decrease until TSS_P is reached before any precipitation can start. Then, nucleation starts and growth is therefore activated too. Depending on the cooling rate, nucleation or growth have more or less importance in the precipitation of the hydrides.

In Fig. 3.16b, similar thermal cycles are simulated, but the peak temperature is 650 K. At this temperature, the solubility of hydrogen is lower than the total amount of hydrogen considered in the simulation: $TSS_D(650\text{ K}) = 144\text{ wt.ppm}$ while $C_{\text{tot}} = 200\text{ wt.ppm}$. Thus, 56 wt.ppm of hydrides are still present at the beginning of the cooling. This enables hy-



(a) Thermal cycle with total dissolution of the hydrides.



(b) Thermal cycle with partial dissolution of the hydrides.

Figure 3.16: Simulation results from the HNGD model developed at the Pennsylvania State University. The curves represent the hydrogen concentration in solid solution during thermal cycles including a heating phase leading to a total (a) or partial (b) dissolution of the hydrides, and followed by a cooling phase at different cooling rates (from 0.01 K/min to 100 K/min). The different cooling rates strongly impact the contribution of nucleation and growth to the hydride precipitation. Adapted from [10].

hydride precipitation by growth immediately when the cooling starts. The difference with the previous case is particularly important by low cooling rates, when hydrides have time to precipitate by growth. For high cooling rates (10 to 100 K/min), the temperature decreases quickly, the TSS_P curve is thus reached before much precipitation by growth can occur, and afterwards most of the hydride precipitation occurs by nucleation.

To describe the hydride dissolution, nucleation and growth, the HNGD relies on following differential equations:

$$\text{Dissolution : } \frac{\partial C_{SS}}{\partial t} = -K_D (C_{SS} - TSS_D) \quad (3.15)$$

$$\text{Nucleation : } \frac{\partial C_{SS}}{\partial t} = -K_N (C_{SS} - TSS_P) \quad (3.16)$$

$$\text{Growth : } \frac{\partial C_{SS}}{\partial t} = -K_G (C_{tot} - TSS_D) p (1 - x) (-\ln(1 - x))^{1-1/p} \quad (3.17)$$

with C_{SS} the hydrogen concentration in solid solution, K_D , K_N and K_G the kinetic parameters for dissolution, nucleation and growth, C_{tot} the total content of hydrogen, p the Avrami parameter¹¹, and x the advancement of the precipitation reaction, defined by $x = \frac{C_{tot} - C_{SS}}{C_{tot} - TSS_D}$.

The kinetic parameters are defined as:

$$K_D = K_{D0} \exp\left(-\frac{E_D}{RT}\right) \quad (3.18)$$

$$K_N = K_{N0} f_\alpha \exp\left(-\frac{E_{th}}{RT}\right) \quad (3.19)$$

$$K_G = (1/K_{mob} + 1/K_{th})^{-1} \quad (3.20)$$

with f_α the volume fraction of α -phase.

The formation energy E_{th} of the δ -hydrides is described with a polynomial expression depending on the temperature:

$$E_{th} = -E_{th0} + E_{th1} T - E_{th2} T^2 + E_{th3} T^3 \quad (3.21)$$

¹¹This parameter corresponds to the dimensionality of the growth, introduced in the Johnson-Mehl-Avrami-Kolmogorov (JMAK) model for crystallization reactions. It would be 1 for a needle, 3 for a sphere and is here set to 2.5 for platelets. [21, 106]

Equation 3.20 accounts for the competition between diffusion rate (K_{mob}) and reaction rate (K_{th}) as limiting factors for hydride growth (see [10, 21] for more details).

The hydrogen diffusion is described by the following differential equation:

$$\frac{\partial C_{SS}}{\partial t} = -\nabla \left(-D\nabla C_{SS} - \frac{DQ^*C_{SS}}{RT^2} \nabla T \right) \quad (3.22)$$

with Q^* the heat of transport and D the diffusion coefficient:

$$D(T) = D_0 \exp\left(\frac{-E_D}{RT}\right) \quad (3.23)$$

Equation 3.22 takes into account the effect of the concentration gradients (Fick's law) and temperature gradients (Soret effect). See Equation 3.9 in section 3.1.3 for more details.

The solubility limits are given by classical Arrhenius equations:

$$TSS_P = TSS_{P0} \cdot \exp\left(\frac{-Q_P}{RT}\right) \quad (3.24)$$

$$TSS_D = TSS_{D0} \cdot \exp\left(\frac{-Q_D}{RT}\right) \quad (3.25)$$

The parameters used in the model are summarized in Table 3.5. They are mainly taken from [10] but some of them have been taken from the online documentation of the INL code BISON [107] in which the model has been implemented. The differences consist essentially in rounding issues but it appeared that values from [107] enabled to reproduce the results of [10] with a better precision than with parameter values from [10]. The values of K_{th0} and K_{mob0} have been switched and corrected¹².

Using the programming language Python, we reproduced part of the results (verification cases) from the work of Passelaigue et al. [10]. These results

¹²The values as presented in Table 3.5 can be found in [21]. K_{th} and K_{mob} are both expected to influence the hydride growth kinetics, since at low temperature the diffusion is the limiting factor while at higher temperature the precipitation rate becomes the limiting factor. From this point of view, the values in [21] seem more plausible compared to the values given in [10].

Table 3.5: Parameters used in the reproduction of the HNGD model. [10, 107]

Parameter	Value	Unit
TSS_P (Eq. 3.24)		
TSS _{P0}	30853	wt.ppm
Q _P	25249	J mol ⁻¹
TSS_D (Eq. 3.25)		
TSS _{D0}	102000	wt.ppm
Q _D	35459	J mol ⁻¹
Diffusion (Eq. 3.23)		
D ₀	1.08×10^{-2}	cm ² s ⁻¹
E _D	44000	J mol ⁻¹
Pre-exponential terms (Eq. 3.15 to 3.17)		
K _{D0}	1110	s ⁻¹
K _{N0}	2.75×10^{-5}	s ⁻¹
K _{th0}	1.6×10^{-5}	s ⁻¹
K _{mob0}	5.53×10^5	s ⁻¹
Formation energy of δ-hydrides (Eq. 3.21)		
E _{th0}	54000	eV at ⁻¹
E _{th1}	38.58	eV at ⁻¹ K ⁻¹
E _{th2}	0.01929	eV at ⁻¹ K ⁻²
E _{th3}	2.894×10^{-5}	eV at ⁻¹ K ⁻³
Activation energy (Eq. 3.20)		
E _G	86806	J mol ⁻¹
Heat of transport (Eq.3.22)		
Q*	25500	J mol ⁻¹
Gas constant		
R	8.314	J K ⁻¹ mol ⁻¹
Atomic weights ¹³		
M _H	1.0078	u
M _{Zr}	91.224	u

are presented in the next section. The simulations only concern local dissolution, nucleation and growth of hydrogen, without considering any spatial dimension (no diffusion). Diffusion issues will be tackled in section 3.4, in which full-length rods are analysed.

3.3.2 Model verification

The first verification case concerns the hydride dissolution in a zirconium alloy and is shown in Fig. 3.17. It assumes that 250 wt.ppm of hydrogen are initially fully precipitated as hydrides and the temperature is then set to 550 K. At this temperature, the hydrogen solubility is $TSS_D^{550} = 44$ wt.ppm. Thus, hydrides dissolve until the hydrogen concentration in solid solution reaches 44 wt.ppm. The dissolution occurs relatively quickly, within less than 2 min. An analytical solution can be derived from Equation 3.15 [10]:

$$C_{SS}(t) = TSS_D^{550} \left(1 - e^{-K_D^{550}t} \right) \quad (3.26)$$

This solution is plotted with a black dashed line in Fig. 3.17 and shows that the solution yielded by Python using a timestep of 1 s is nearly identical to the analytical solution. This simulation is in perfect agreement with the results presented in [10].

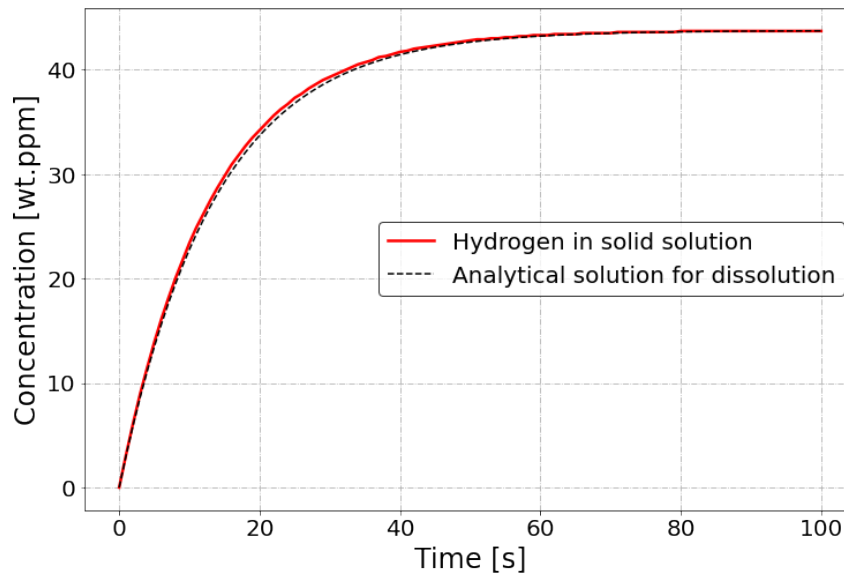


Figure 3.17: Verification case for hydride dissolution: 250 wt.ppm of hydrogen are initially fully precipitated and the temperature is set to 550 K. This leads to the partial dissolution of the hydrides, as $TSS_D^{550} = 44$ wt.ppm. The concentration of dissolved hydrogen calculated by the simulation is plotted with the red plain line, while the black dashed line corresponds to the analytical solution given by Equation 3.26.

The next verification case concerns the hydride nucleation and is shown

in Fig. 3.18. The initial hydrogen amount is 540 wt.ppm and is assumed completely dissolved in the zirconium alloy. The temperature is set to 600 K. At this temperature, the solubility limit for precipitation is $TSS_P^{600} = 195$ wt.ppm. We can observe that the hydrogen concentration in solution immediately decreases due to hydride nucleation and reaches the TSS_P within approximately 6 min. Over a longer simulation time, hydrogen would further precipitate due to hydride growth (no nucleation but hydride growth in the domain between TSS_P and TSS_D), until the concentration of dissolved hydrogen reaches the TSS_D .

Equation 3.16 also has an analytical solution¹⁴ [10]:

$$C_{SS}(t) = TSS_P^{600} \left(C_{tot} - TSS_P^{600} e^{-K_N^{600}t} \right) \quad (3.27)$$

This analytical solution is plotted with a black dashed line in Fig. 3.18. In this case too, the solution provided by Python (with a timestep of 1 s) is nearly identical to the analytical solution and corresponds to the results presented in [10].

Fig. 3.19 presents the results of a verification case concerning hydride growth. It assumes an initial concentration of dissolved hydrogen of 288 wt.ppm and the temperature is set to 650 K. At this temperature, the solubility limits are $TSS_P^{650} = 289$ wt.ppm and $TSS_D^{650} = 144$ wt.ppm. As the initial concentration (288 wt.ppm) is between TSS_P and TSS_D , hydrogen precipitation can only happen as hydride growth. No nucleation takes place for dissolved hydrogen concentrations below TSS_P . In order to observe hydride growth, the amount of hydrides in the simulation is initialized to $C_{prec}(t = 0) = 10^{-6}$ wt.ppm. We can thus observe that the decrease in hydrogen concentration starts very slowly (at first, there are few hydrides on which hydrogen can further precipitate) but progressively accelerates. However, hydride growth is significantly slower than nucleation: while 350 wt.ppm hydrogen precipitates within 6 min in Fig. 3.18, the precipitation of 120 wt.ppm hydrogen by hydride growth requires around 2 days (172800 s) in Fig. 3.19.

¹⁴In this case, the volume fraction of the zirconium α -phase is assumed equal to 1, in order to ensure that the nucleation kinetic parameter K_N is constant. This is a reasonable assumption as the amount of hydride is low compared to the volume of zirconium alloy. See [10] for more details.

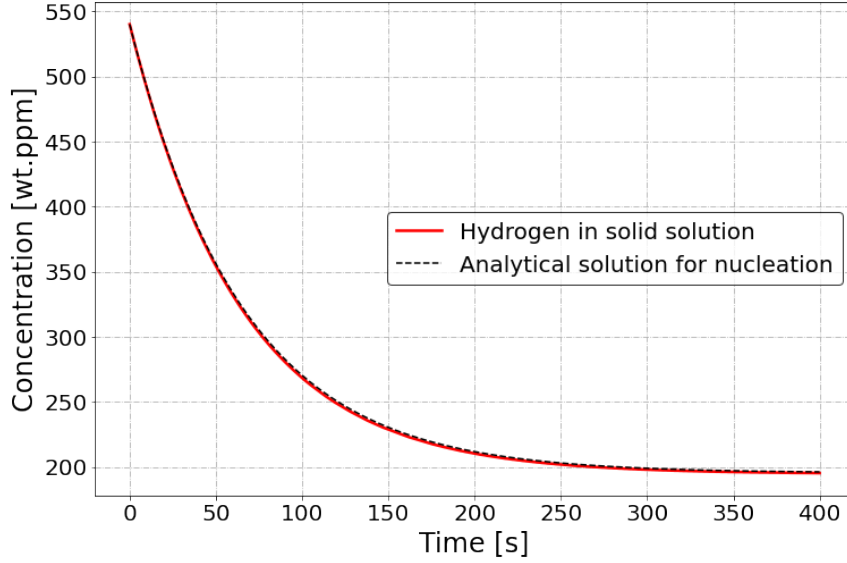


Figure 3.18: Verification case for hydride nucleation: 540 wt.ppm of hydrogen are initially fully dissolved and the temperature is set to 600 K. This leads to the partial precipitation of the hydrogen, as $TSS_p^{600} = 195$ wt.ppm. The concentration of dissolved hydrogen calculated by the simulation is plotted with the red plain line, while the black dashed line corresponds to the analytical solution given by Equation 3.27.

In this case too, an analytical solution to Equation 3.17 can be derived [10]:

$$C_{SS}(t) = TSS_D^{650} \left(C_{SS}(t=0) - TSS_D^{650} e^{-(K_G^{650}t)^p} \right) \quad (3.28)$$

This analytical solution is plotted with a dotted blue line in Fig. 3.19 and we can observe that the Python solution (with a timestep of 100 s) is nearly equal to the analytical solution in this case too. However, it appeared that it does not correspond to the results presented in [10]: the evolution of the hydrogen concentration from 288 wt.ppm down to 170 wt.ppm are similar (progressive increase of the precipitation rate) but the time scales are different by a factor 22: 8000 s in [10] and 175000 s in this thesis. The origin of the discrepancy could not be identified, though the analytical solution suggests that it must be related to the definition of the kinetic factor K_G . In the case of rapid (up to a few hours) thermal transients, the hydride growth rate is important as it determines whether hydrogen precipitates by growth or by nucleation of new hydrides. For longer evolutions without rapid thermal transients, e.g. during dry storage, the growth rate is less

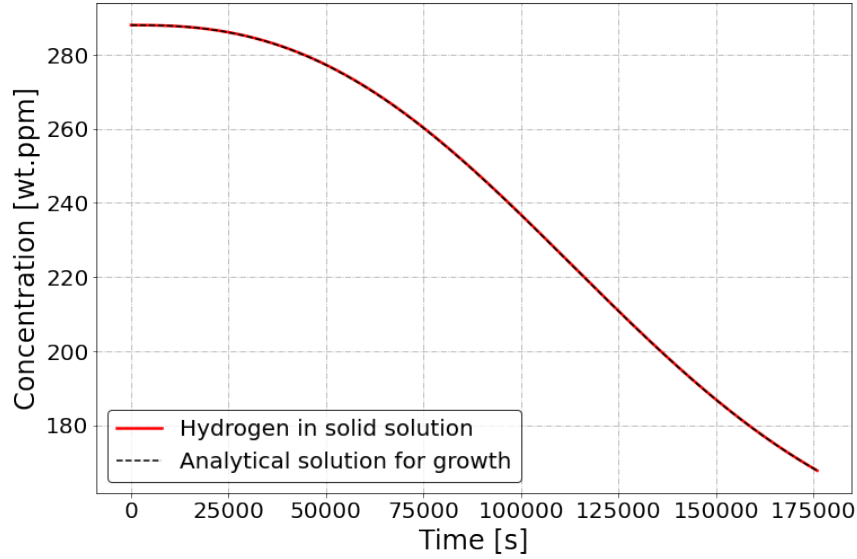


Figure 3.19: Verification case for hydride growth: 288 wt.ppm of hydrogen are initially dissolved and the temperature is set to 650 K. At this temperature, $TSS_P^{650} = 289$ wt.ppm and $TSS_D^{650} = 144$ wt.ppm. Therefore, no hydride nucleation occurs but hydrogen precipitates by hydride growth. The hydride concentration is initialized to 10^{-6} wt.ppm so that hydride growth can start. The concentration of dissolved hydrogen calculated by the simulation is plotted with the red plain line, while the black dashed line corresponds to the analytical solution given by Equation 3.28.

important for hydride prediction as the dissolved hydrogen concentration can be expected to follow the local TSS_D value. This will be discussed in section 3.4.

Fig. 3.20 and 3.21 present two simulations involving thermal cycles with various cooling rates. They correspond respectively to the figures 4a and 4b from [10] which are presented and discussed above in Fig. 3.16. The same behaviour as in [10] can be observed:

In the case of a total hydride dissolution at the end of the initial heating (Fig. 3.20), the hydrogen concentration has to reach the TSS_P first, before any precipitation occurs: as all hydrides have dissolved during initial heating, hydride growth is impossible and hydride nucleation only starts when TSS_P is reached.

In the case of an incomplete hydride dissolution at the end of the heating (Fig. 3.21), hydride growth begins as soon as the cooling starts and even-

tually nucleation starts later when the hydrogen concentration reaches the TSS_P due to sufficient temperature decrease.

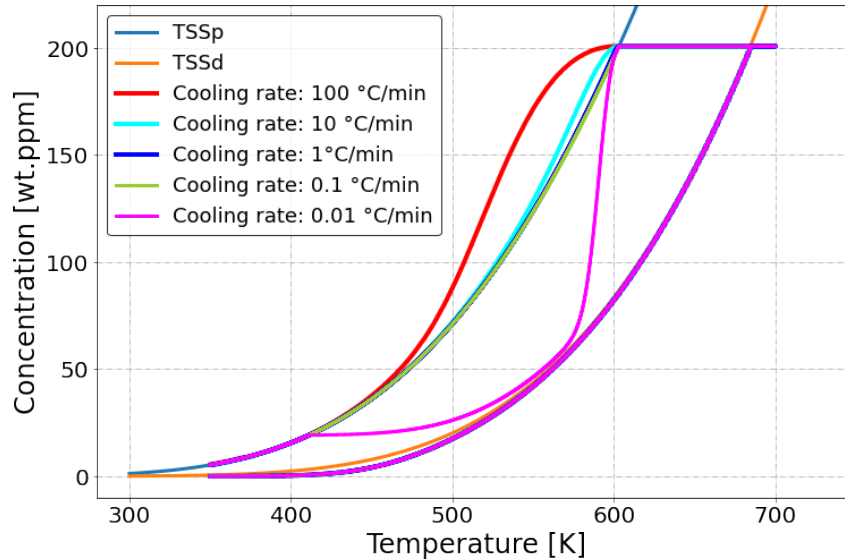


Figure 3.20: Thermal cycles simulated with the HNGD model, involving the total dissolution of hydrogen in a zirconium alloy and different cooling rates. The total hydrogen content is 200 wt.ppm and the simulation starts at 350 K. The temperature is first increased to 700 K, which results in an increase of the dissolved hydrogen concentration (y -axis) following the TSS_D curve. When 700 K is reached, $TSS_D^{700} = 230$ wt.ppm and thus the 200 wt.ppm hydrogen are fully dissolved. Then, the temperature is decreased back to 350 K with various cooling rates, ranging from 0.01 °C/min to 100 °C/min. As the hydrogen is fully dissolved at the end of the heating, no hydrides are present at the beginning of the cooling. Therefore, hydride precipitation starts only when TSS_P is reached (600 K): at this point, nucleation starts and enables hydride growth too. Depending on the cooling rate, precipitation by nucleation (red curve) or by growth (fuchsia curve) predominates.

Depending on the cooling rate, different scenarios can be observed. In Fig. 3.20, we can see that for cooling rates higher than 1 °C/min the hydrogen concentration exceeds the TSS_P curve as the cooling is too fast compared to hydride precipitation rate. For cooling rates between 0.1 and 1 °C/min, the hydrogen concentration follows the TSS_P curve during cooling, while for the lowest cooling rate (0.01 °C/min), the hydride growth starting after the first hydride nucleation is faster than the cooling rate and the hydrogen concentration drops below the TSS_P curve towards the TSS_D curve.

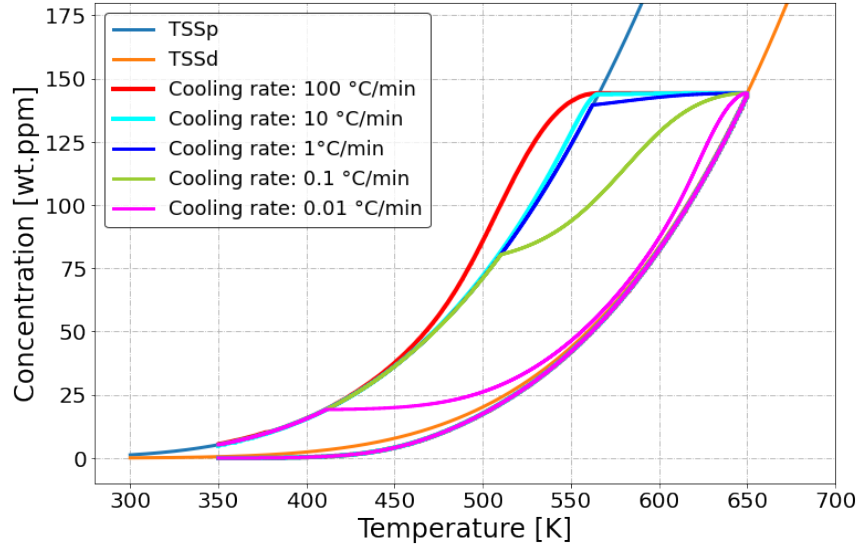


Figure 3.21: Thermal cycles simulated with the HNGD model, involving partial dissolution of hydrogen in a zirconium alloy and different cooling rates. The total hydrogen content is 200 wt.ppm and the simulation starts at 350 K. The temperature is first increased to 650 K, which results in an increase of the dissolved hydrogen concentration (y-axis) following the TSS_D curve. At 650 K, $TSS_D^{650} = 144$ wt.ppm and thus 56 wt.ppm hydrogen remain precipitated as hydrides. Then, the temperature is decreased back to 350 K with various cooling rates, ranging from 0.01 °C/min to 100 °C/min. As hydrides are still present at the beginning of the cooling, hydride precipitation by growth can start immediately. For cooling rates equal to or higher than 1 °C/min, the cooling rate is too high compared to the hydride growth rate and therefore the TSS_P is reached without significant hydride precipitation by growth, and afterwards nucleation is responsible for most of the hydride precipitation. For cooling rates lower than 1 °C/min, we can observe that the concentration of dissolved hydrogen decreases significantly before the TSS_P curve is reached, which indicates that hydride growth is the main precipitation mechanism.

In Fig. 3.21, the role of hydride growth is even more evident: precipitation by growth starts immediately after beginning of the cooling (at 650 K) so that the hydrogen concentration immediately decreases (contrary to Fig. 3.20, there is no initial plateau from TSS_D to TSS_P). For cooling rates above 1 °C/min, the growth rate is low compared to the cooling rate so that the temperature decreases until the TSS_P curve is reached, without significant hydride precipitation. Afterwards, the highest cooling rate (100 °C/min,

red curve) leads to a hydrogen concentration exceeding the TSS_P as even the nucleation rate is too low compared to the cooling rate. For cooling rates lower than $1\text{ }^\circ\text{C}/\text{min}$, hydride precipitation by growth ensures that the hydrogen concentration remains longer below the TSS_P curve. In the case of the lowest cooling rate ($0.01\text{ }^\circ\text{C}/\text{min}$, fuchsia curve), the hydrogen concentration nearly follows the TSS_D curve, as hydride growth is sufficient to ensure hydride precipitation of the hydrogen above the thermodynamic solubility limit.

These two simulations show some discrepancy with the results presented in [10]. The difference is related to the hydride growth rate, as already identified with the verification case concerning hydride growth (Fig. 3.19). In Fig. 3.21, the curves corresponding to cooling rates of $0.1\text{ }^\circ\text{C}/\text{min}$ and $0.01\text{ }^\circ\text{C}/\text{min}$ correspond approximately to the cooling rates of $1\text{ K}/\text{min}$ and $0.35\text{ K}/\text{min}$ in Fig. 3.16b, respectively. Thus, the factor 22 observed with Fig. 3.19 also applies in the case of Fig. 3.20 and 3.21.

3.3.3 Summary on the HNGD model

Using the HNGD model, we performed some simulations to verify the hydride dissolution, nucleation and growth rates (Fig. 3.17, 3.18 and 3.19) and compared our results to the ones presented in [10]. For the hydride dissolution and nucleation, we found identical results. For the hydride growth rate, we observed a much lower rate (factor 22 on the time scale) than in [10]. This is probably related to the kinetic parameter K_G , which depends on the diffusion rate and on the precipitation reaction rate. This discrepancy has been observed on further verification cases (Fig. 3.20 and 3.21), on which thermal cycles involving different cooling rates have been simulated.

We might note here that even if the hydride growth rate seems to be underestimated in our reproduced model, a cooling rate of 0.01 °C/min nearly ensures the thermodynamic equilibrium (TSS_D) throughout the cooling. This cooling rate is significantly higher than the expected cooling rates during dry storage: a decrease of 30 °C over the first 6 months (peak cladding temperature in Fig. 2.32) corresponds to a cooling rate of 0.0001 °C/min and constitutes an upper bound. Therefore, the hydride precipitation rate during long-term dry storage should not be affected by the hydride growth rate: The concentration of precipitated hydrides is expected to follow the thermodynamic equilibrium given by the hydrogen solubility limit TSS_D . This last point constitutes a fundamental assumption for the model presented in the next section, which simulates the hydrogen behaviour in full-scale rods under dry storage conditions.

3.4 Hydrogen and hydride profiles - Predictions for full-length rods

In this section, we will present and discuss simulations which aim to predict the hydrogen behaviour at the scale of a full-length rod during dry storage. This requires to know the temperature profile in the rod over the whole storage time, the hydrogen concentration in the cladding at the end of operation, the solubility limit for hydrogen in the cladding material and the diffusion parameters. The following results should be considered as qualitative rather than quantitative, as it would be unwise to rely on a model without experimental validation. Experimental programs focussing on diffusion over longer time and at larger scale are expected in the coming years. Furthermore, the primary purpose of the simulations presented in the following was to identify possible phenomena regarding the hydrogen diffusion and the evolution of the hydride profile over time.

3.4.1 Basic assumptions

The model used to predict the hydrogen behaviour is based on the following assumptions:

- The hydrogen and hydride concentrations are not depending on the r and θ coordinates (cylindrical coordinate system) of the cladding, but only on the z coordinate (axial dimension).
- The temperature evolution with time is so slow, that there is no kinetic effect. At any axial location with hydrides, hydrides and hydrogen are at the thermodynamic equilibrium and the solubility limit is given by the TSS_D curve.
- Diffusion of dissolved hydrogen is driven by concentration gradients (Fick's law) and temperature gradients (Soret effect). Stress gradients are assumed not relevant.
- Hydrides do not impact the diffusion.

- Locally, the divergence of the dissolved hydrogen flux impacts the total hydrogen (sum of dissolved hydrogen and hydrides) concentration.

The last point requires some further explanation: Considering a section of rod presenting a temperature gradient and having a hydrogen concentration above the solubility limit, hydrides are present in this rod section and the concentration of dissolved hydrogen presents a gradient (consistent with the temperature gradient). If we consider the difference between the outgoing and ingoing hydrogen fluxes (particle balance) over a given time, it is likely to be non-zero. In a simple diffusion problem without source term, this would lead to a change in the concentration profile of the diffusing particles. However, as hydride dissolution and precipitation are faster than hydrogen diffusion, we can expect that the hydrides locally act as a source or a sink for the hydrogen deficit or excess resulting from the diffusion. Therefore, the local dissolved hydrogen concentration will remain equal to the solubility limit TSS_D , which is itself determined by the temperature.

If the rod section considered presents a hydrogen concentration lower than the solubility limit, no hydrides are present and the hydrogen diffusion impacts the concentration profile of the dissolved hydrogen (which in this case also corresponds to the total hydrogen). Thus, we might keep in mind that:

- The hydrogen diffusion due to concentration gradients (Fick's law) and temperature gradients (Soret effect) is determined using the concentration of dissolved hydrogen.
- The hydrogen diffusion impacts the profile of the total hydrogen concentration. In particular, if hydrides are present then the dissolved hydrogen concentration remains constant and equal to TSS_D .

3.4.2 Implementation of the diffusion in the model

The model is discretized in 36 axial zones in order to match the 36 axial zones of the COBRA-SFS CASTOR model and therefore the 36 values of the temperature profiles. We defined three arrays containing concentration profiles: one for hydrides, one for dissolved hydrogen and one for the total

amount of hydrogen (sum of the other two). The hydrogen flux between the 36 axial zones is then calculated using the dissolved hydrogen concentration and the temperature according to the diffusion equation (Equation 3.9). In our case, the local production term corresponds to hydrides dissolving or precipitating, depending on the divergence of the hydrogen flux.

$$\frac{\partial C_{diss}(M, t)}{\partial t} - \frac{\partial}{\partial x} \left(D \cdot \frac{\partial C_{diss}(M, t)}{\partial x} + \frac{D Q^* C_{diss}}{R T^2} \frac{\partial T(M, t)}{\partial x} \right) = - \frac{\partial C_{prec}(M, t)}{\partial t}$$

As $C_{diss} + C_{prec} = C_{tot}$, the equation can be rewritten as:

$$\frac{\partial C_{tot}(M, t)}{\partial t} = \frac{\partial}{\partial x} \left(D \cdot \frac{\partial C_{diss}(M, t)}{\partial x} + \frac{D Q^* C_{diss}}{R T^2} \frac{\partial T(M, t)}{\partial x} \right) \quad (3.29)$$

The diffusion coefficient is calculated according to an Arrhenius law:

$$D(T) = D_0 \cdot \exp\left(\frac{-E_D}{RT}\right) \quad (3.30)$$

with $D_0 = 1.08 \times 10^{-2} \text{ cm}^2 \text{ s}^{-1}$ and $E_D = 4.4 \times 10^4 \text{ J mol}^{-1}$ the pre-exponential term and activation energy of the diffusion coefficient Arrhenius law used in the HNGD model [10].

To determine the evolution of the total hydrogen concentration $C_{tot,i}^n$ in zone i at timestep n , Equation 3.29 is discretized as:

- For $i = 0$,

$$dC_{tot,0}^n = \frac{D(T_{0/1})}{d^2} \left[(C_{diss,1} - C_{diss,0}) + \frac{(T_1 - T_0) \cdot Q^* \cdot C_{diss,0/1}}{R \cdot T_{0/1}^2} \right]$$

$$C_{tot,0}^{n+1} = C_{tot,0}^n + dt \cdot dC_{tot,0}^n$$

- For i in $[1 ; 34]$,

$$dC_{tot,i}^n = \frac{D(T_{i/i+1})}{d^2} \left[(C_{diss,i+1} - C_{diss,i}) + \frac{(T_{i+1} - T_i) \cdot Q^* \cdot C_{diss,i/i+1}}{R \cdot T_{i/i+1}^2} \right] - \frac{D(T_{i-1/i})}{d^2} \left[(C_{diss,i} - C_{diss,i-1}) + \frac{(T_i - T_{i-1}) \cdot Q^* \cdot C_{diss,i-1/i}}{R \cdot T_{i-1/i}^2} \right]$$

$$C_{tot,i}^{n+1} = C_{tot,i}^n + dt \cdot dC_{tot,i}^n$$

- For $i = 35$,

$$dC_{tot,35}^n = - \frac{D(T_{34/35})}{d^2} \left[(C_{diss,35} - C_{diss,34}) + \frac{(T_{35} - T_{34}) \cdot Q^* \cdot C_{diss,34/35}}{R \cdot T_{34/35}^2} \right]$$

$$C_{tot,35}^{n+1} = C_{tot,35}^n + dt \cdot dC_{tot,35}^n$$

with d the length of the axial sections of rod, T_i the temperature in axial section i , $C_{diss,i}$ the dissolved hydrogen concentration in axial section i and dt the time step. Indices $i/i+1$ refer to mean values of two adjacent axial sections. Exponents n are omitted on all T_i and $C_{diss,i}$ in order to make the expressions more readable.

This numerical scheme corresponds to a Forward Time Centered Space (FTCS) method [108–110].

Knowing the total hydrogen concentration profile at timestep $n+1$, the concentration profiles of dissolved hydrogen and hydrides is simply deduced as:

$$C_{diss,i}^{n+1} = \min [TSS_D(T_i^{n+1}), C_{tot,i}^{n+1}] \quad \text{for } i \in [0; 35]$$

$$C_{prec,i}^{n+1} = C_{tot,i}^{n+1} - C_{diss,i}^{n+1} \quad \text{for } i \in [0; 35]$$

3.4.3 Cladding configuration at the beginning of the dry storage

The following figures present some examples of hydride and hydrogen profiles at the beginning of the dry storage.

Fig. 3.22, 3.23 and 3.24 correspond to different rod configurations at the beginning of the dry storage: a fuel rod with 250 wt.ppm hydrogen in Fig. 3.22, a fuel rod with 100 wt.ppm hydrogen in Fig. 3.23 and a fuel rod with 50 wt.ppm hydrogen in Fig. 3.24. The x-axis represents the axial dimension of the fuel rods, while the different concentrations (total amount of hydrogen, dissolved hydrogen and hydrides) are on the y-axis. The cladding temperature is on the right-hand side y-axis. In each case, we simply assumed the total amount of hydrogen (red line) to be homogeneously distributed over the whole rod length. A realistic temperature profile provided by a COBRA-SFS calculation has been applied in each case¹⁵ (blue dotted line,

¹⁵This profile corresponds to a calculation performed in the frame of the GRS thermo-mechanical benchmark [38]. Temperature profiles at different time points of the dry storage can be seen in Fig. 3.25.

to be read on the right-hand side y-axis) and the corresponding TSS_D profile is plotted with a black dotted line. Then, according to the assumptions presented above, the profile of the dissolved hydrogen has been determined as the minimum of TSS_D and total hydrogen: either the total amount of hydrogen is below the solubility limit and all hydrogen is dissolved, or it is above the solubility limit and the dissolved hydrogen concentration is equal to TSS_D while the rest is precipitated as hydrides. Finally, the hydride concentration (blue curve) is calculated as the difference between the total amount of hydrogen and the dissolved hydrogen. The coloured domains in the diagrams show the concentrations of hydride (blue) and dissolved hydrogen (orange).

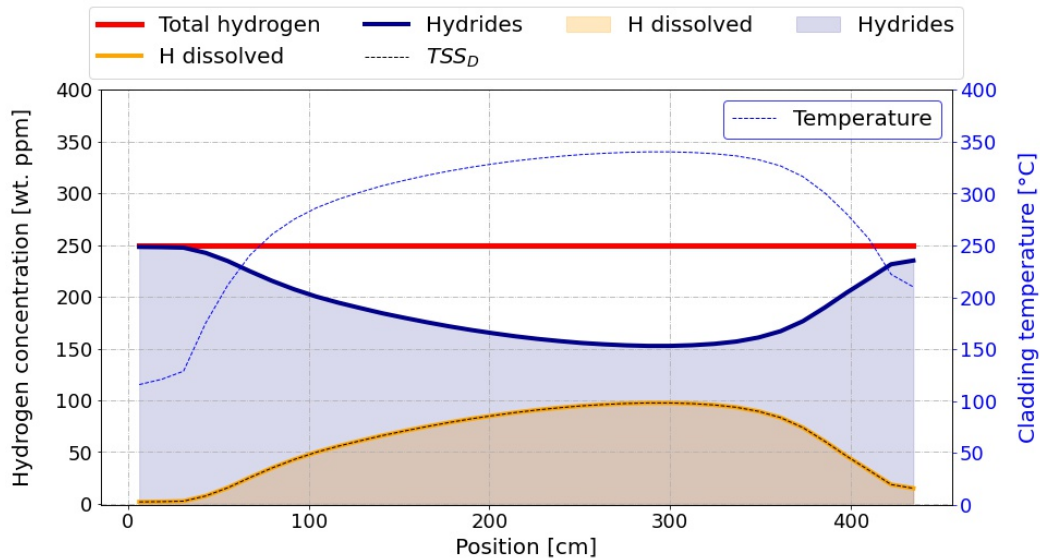


Figure 3.22: Hydrogen and hydride profiles at the beginning of the dry storage, for a total hydrogen concentration of 250 wt.ppm.

In Fig. 3.22, the total amount of hydrogen is rather high (250 wt.ppm) so that even in the centre part of the rod by 340 °C, the main part of the hydrogen remains precipitated (approximately 150 wt.ppm hydrides and 100 wt.ppm dissolved hydrogen). At both ends of the rod, the temperature is significantly lower and almost all hydrogen is precipitated as hydrides.

In Fig. 3.23, the total amount of hydrogen is of 100 wt.ppm. The dissolved hydrogen profile is identical to the previous case as the temperature profile

3.4 Hydrogen and hydride profiles - Predictions for full-length rods

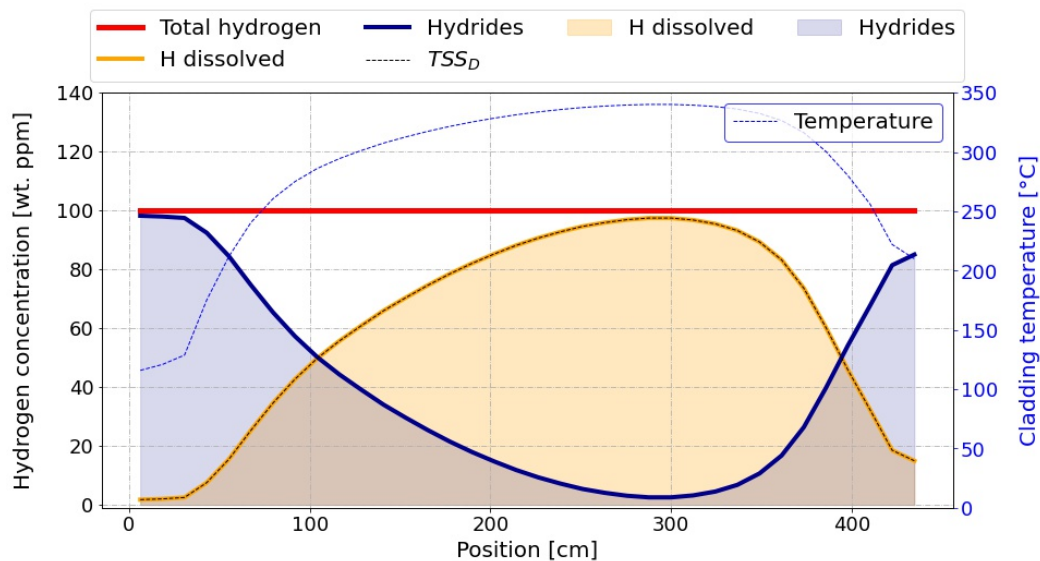


Figure 3.23: Hydrogen and hydride profiles at the beginning of the dry storage, for a total hydrogen concentration of 100 wt.ppm.

(and therefore the TSS_D profile) is unchanged. However, the amount of hydride is reduced by 150 wt.ppm over the whole rod length. Thus, in the hottest section of the rod, nearly all hydrogen is dissolved (the blue coloured domain almost splits at $x = 300$ cm).

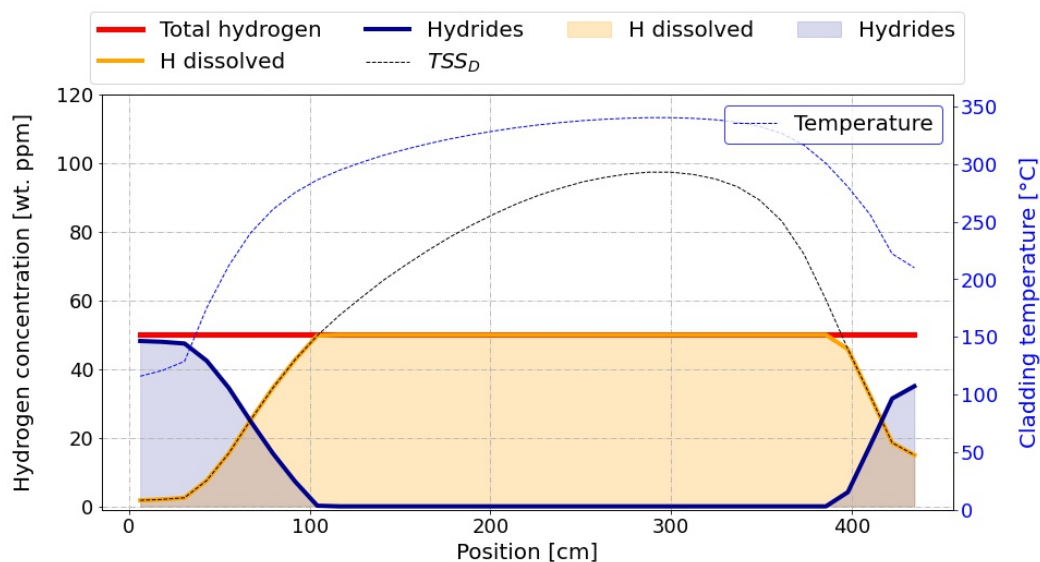


Figure 3.24: Hydrogen and hydride profiles at the beginning of the dry storage, for a total hydrogen concentration of 50 wt.ppm.

In Fig. 3.24, the low hydrogen concentration (50 wt.ppm) results in the total dissolution of the hydrides over the main part of the rod, corresponding to the rod section for which the cladding temperature exceeds 286 °C ($TSS_D(286\text{ °C}) = 50\text{ wt.ppm}$).

Considering these concentration profiles, it appears that both Fick's law and Soret effect can be expected to influence the diffusion in the same direction. Thus, we can expect that the hydrogen fluxes will tend to reduce the hydrogen amount in the central part of the rod (highest dissolved hydrogen concentration and temperature) and to increase it at the lower and upper parts of the rod. The questions then arise:

- To which extent does this hydrogen redistribution occur?
- Can all hydrogen from the central part of the rod diffuse to the cold ends?
- Will the hydride concentration in the uppermost and lowest part of the rod have significantly increased after 100 years of dry storage?

3.4.4 Hydrogen and hydride profiles over 100 years of storage

In the following, we present the results of three simulations of fuel rods stored for 100 years (5 years of wet storage followed by 95 years of dry storage) corresponding to the initial states presented in the previous section:

- a fuel cladding with 250 wt.ppm hydrogen,
- a fuel cladding with 100 wt.ppm hydrogen and
- a fuel cladding with 50 wt.ppm hydrogen.

Fig. 3.25 shows the temperature profiles that have been used in the following simulations. These profiles correspond to calculations performed in the frame of the GRS thermo-mechanical benchmark [38] and provide temperatures at $t = 5$ years (beginning of dry storage after 5 years of wet storage), 5.5, 6, 7, 8, 10, 20, 30, 40, 50, 70 and 100 years.

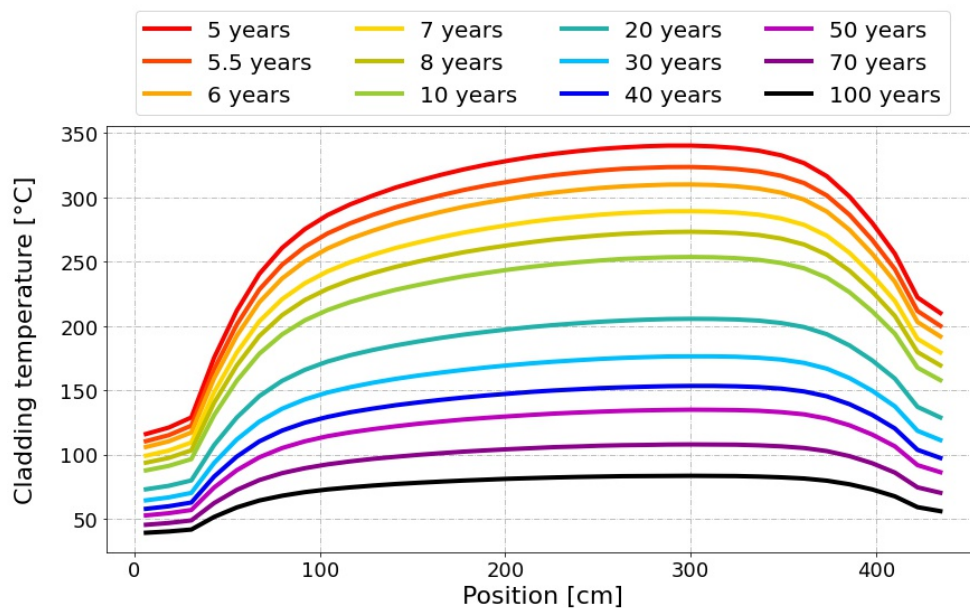


Figure 3.25: Temperature axial profiles in dry storage.

Evolution over 100 years for a concentration of 250 wt.ppm

For this first case, the hydrogen concentration is high compared to the solubility of hydrogen. Fig. 3.26, 3.27, 3.28, 3.29 and 3.30 show the hydride and hydrogen profiles in the cladding after respectively 5, 6, 10, 20 and 100 years of storage (incl. 5 years of wet storage). We can first note that most of the hydrides remain precipitated and the diffusion shows a limited effect in this simulation. The temperature of the fuel rod decreases rapidly (see Fig. 3.25), in particular over the first years:

- 340 °C at $t = 5$ years (beginning of the dry storage),
- 310 °C at $t = 6$ years,
- 254 °C at $t = 10$ years,
- 205 °C at $t = 20$ years and
- 83 °C at $t = 100$ years.

This temperature decrease induces a decrease in solubility and thus the amount of dissolved hydrogen progressively decreases too. This in turn results in lower concentration gradients and less diffusion. A limited effect of diffusion can be seen in this first simulation: in Fig. 3.30, on the uppermost part of the rod, we can observe that the total amount of hydrogen presents a slight dip around $x = 360$ cm and then a hump from $x = 380$ cm to the top of the rod. This mainly happens in the first 5 years of dry storage (Fig. 3.28), then after 15 years of dry storage (Fig. 3.29) the hydrogen solubility is already very low (< 14 wt.ppm) and does not enable further significant diffusion.

3.4 Hydrogen and hydride profiles - Predictions for full-length rods

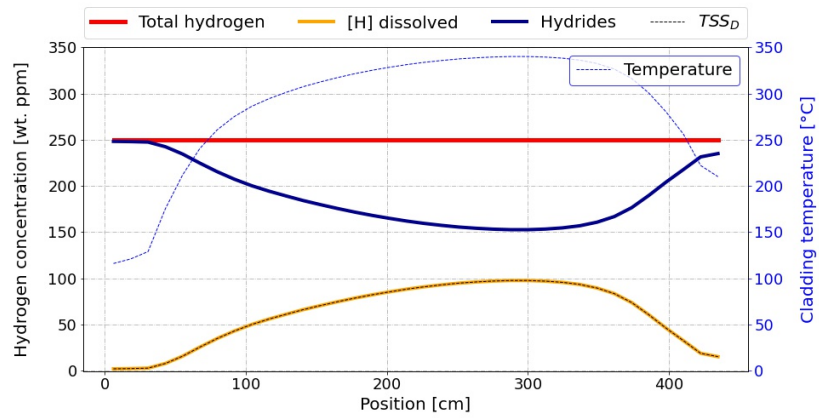


Figure 3.26: Hydrogen and hydride profiles at the beginning of the dry storage, for a total hydrogen concentration of 250 wt.ppm. The red line corresponds to the total hydrogen concentration, the blue line to the hydride concentration, the orange line to the dissolved hydrogen concentration (which overlaps with the TSS_D curve), and the thin dotted blue line to the cladding temperature (right-hand side y-axis).

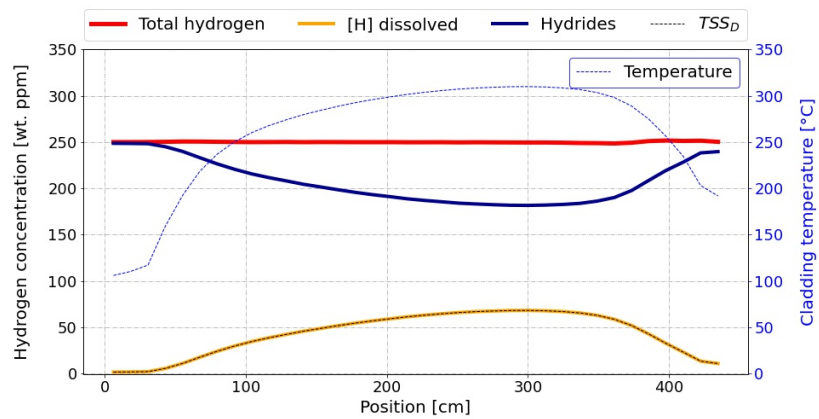


Figure 3.27: Hydrogen and hydride profiles after 1 year of dry storage, for a total hydrogen concentration of 250 wt.ppm.

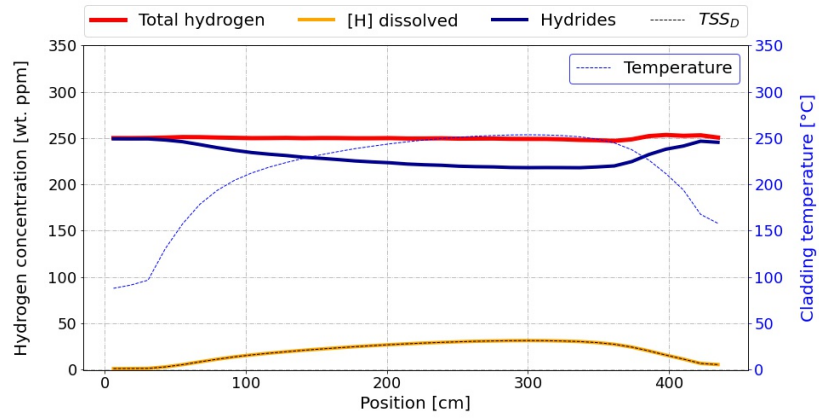


Figure 3.28: Hydrogen and hydride profiles after 5 years of dry storage, for a total hydrogen concentration of 250 wt.ppm.

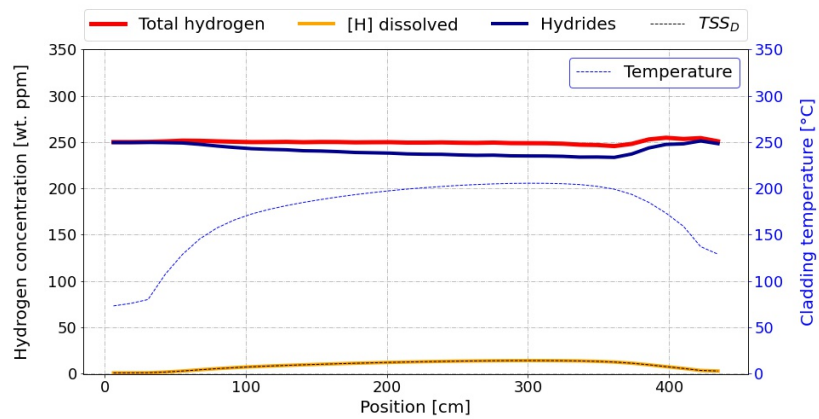


Figure 3.29: Hydrogen and hydride profiles after 15 years of dry storage, for a total hydrogen concentration of 250 wt.ppm.

3.4 Hydrogen and hydride profiles - Predictions for full-length rods

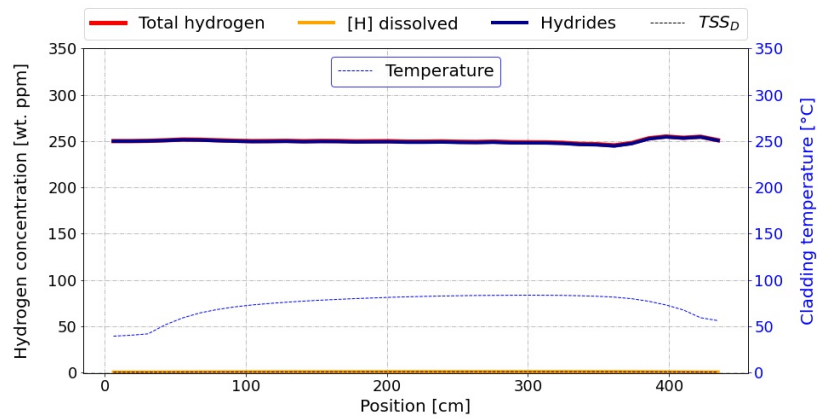


Figure 3.30: Hydrogen and hydride profiles after 95 years of dry storage, for a total hydrogen concentration of 250 wt.ppm. At this point, the temperature over the whole rod does not exceed 83 °C. This results in a nearly null solubility: the TSS_D curve and the dissolved hydrogen curve are both confounded with the x-axis. As no hydrogen is dissolved, the hydride concentration is equal to the total hydrogen concentration (blue curve overlapping the red curve). The effect of the diffusion during the 100 years of storage consists in the small hump at the top of the rod ($x > 380\text{cm}$).

Evolution over 100 years for a concentration of 100 wt.ppm

Fig. 3.31 to 3.35 are similar to the previous five figures, but correspond to a simulation for a total hydrogen content of 100 wt.ppm instead of 250 wt.ppm. At the beginning of the dry storage (Fig. 3.31) the TSS_D curve at $x = 300$ cm almost reaches the total amount of hydrogen (100 wt.ppm) so that nearly all hydrogen is dissolved and very few hydrides remain precipitated at this location. However, the temperature decrease over the following years results in more hydrides and the concentration of dissolved hydrogen remains equal to the TSS_D over the whole dry storage. Actually, as both the temperature profile and the concentration profile of dissolved hydrogen (given by the TSS_D) are identical in the two simulations (250 wt.ppm and 100 wt.ppm), the diffusion fluxes are also equals. Therefore, the hydrogen redistribution at the end of this simulation is identical to the previous simulation.

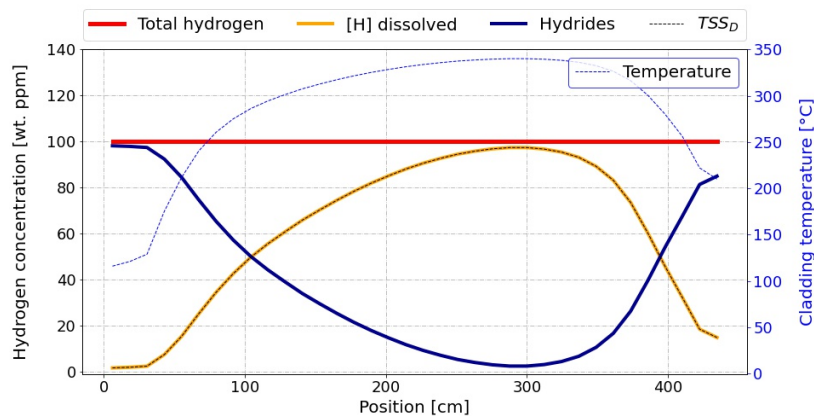


Figure 3.31: Hydrogen and hydride profiles at the beginning of the dry storage, for a total hydrogen concentration of 100 wt.ppm. At the hottest axial location ($x \approx 300$ cm), the hydrogen solubility is near 100 wt.ppm, so that the dissolved hydrogen concentration (orange curve) almost reaches the total hydrogen concentration (red curve), while the hydride concentration (blue curve) is nearly zero. The dissolved hydrogen concentration and the TSS_D curves are overlapping over the whole length of the rod.

3.4 Hydrogen and hydride profiles - Predictions for full-length rods

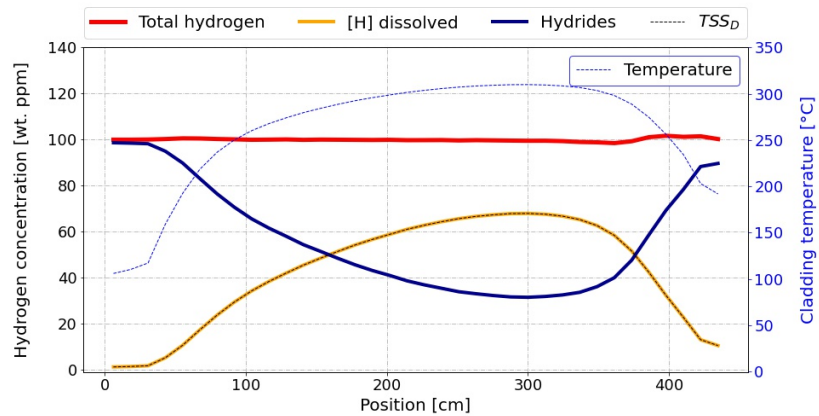


Figure 3.32: Hydrogen and hydride profiles after 1 year of dry storage, for a total hydrogen concentration of 100 wt.ppm. After only 1 year of storage, the temperature dropped by 30 °C at the hottest axial location and the hydrogen solubility by more than 30 wt.ppm. Thus, even at the hottest axial location, more than 30 wt.ppm hydrides are now precipitated.

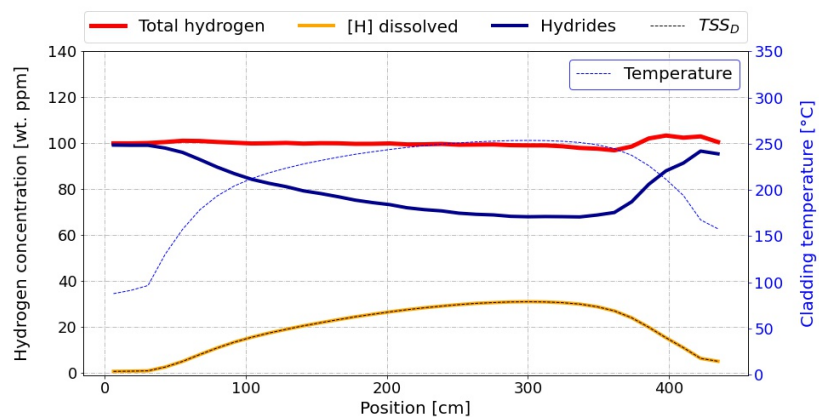


Figure 3.33: Hydrogen and hydride profiles after 5 years of dry storage, for a total hydrogen concentration of 100 wt.ppm.

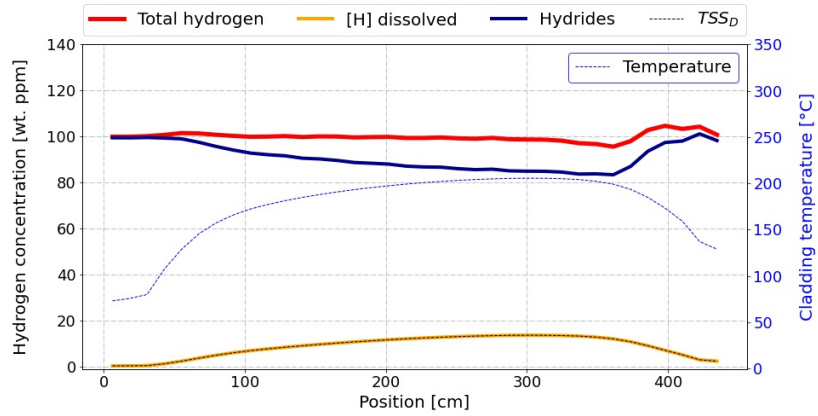


Figure 3.34: Hydrogen and hydride profiles after 15 years of dry storage, for a total hydrogen concentration of 100 wt.ppm. At this point, the dissolved hydrogen concentration does not exceed 20 wt.ppm at any axial location of the rod. Therefore, no significant further hydrogen diffusion should be expected over the remaining storage period.

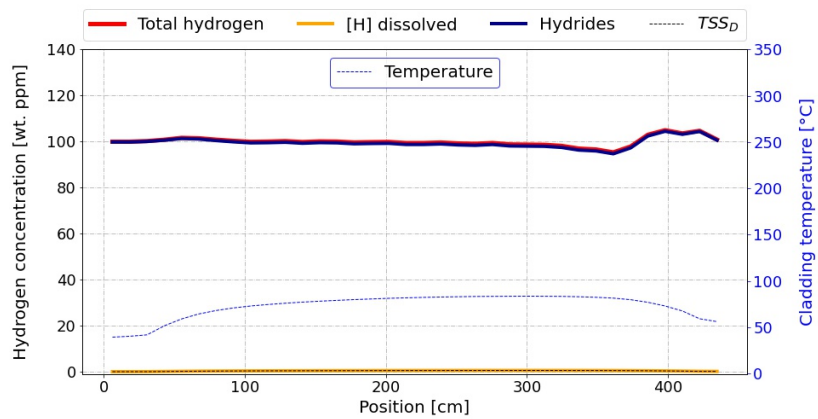


Figure 3.35: Hydrogen and hydride profiles after 95 years of dry storage, for a total hydrogen concentration of 100 wt.ppm. The effect of the diffusion during the dry storage can be seen on the upper part of the fuel rod: slight dip around $x = 360$ cm and hump for $x > 380$ cm.

Evolution over 100 years for a concentration of 50 wt.ppm

Fig. 3.36 to 3.40 show the results of a similar simulation but for a total hydrogen concentration of only 50 wt.ppm. The main difference is that the TSS_D profile corresponding to the initial temperature profile exceeds 50 wt.ppm (see Fig. 3.36) and therefore the concentration of dissolved hydrogen presents a hydride-free plateau at 50 wt.ppm, between $x = 100$ cm and $x = 400$ cm. After one year of dry storage (Fig. 3.37), the section free of hydride is reduced to $150 \text{ cm} < x < 375$ cm, and after 5 years of dry storage (Fig. 3.38) the TSS_D curve resides below 50 wt.ppm (even below 35 wt.ppm) at any location of the rod and therefore hydrides are precipitated over the whole length of the rod. The final hydride concentration can be seen in Fig. 3.40. As in the previous simulations, a slight dip can be observed around $x = 360$ cm and a hump above $x = 380$ cm. Diffusion of hydrogen at the bottom of the rod can also be observed (dip at $x = 100$ cm and hump between $x = 50$ cm and $x = 100$ cm), yet in lesser extent.

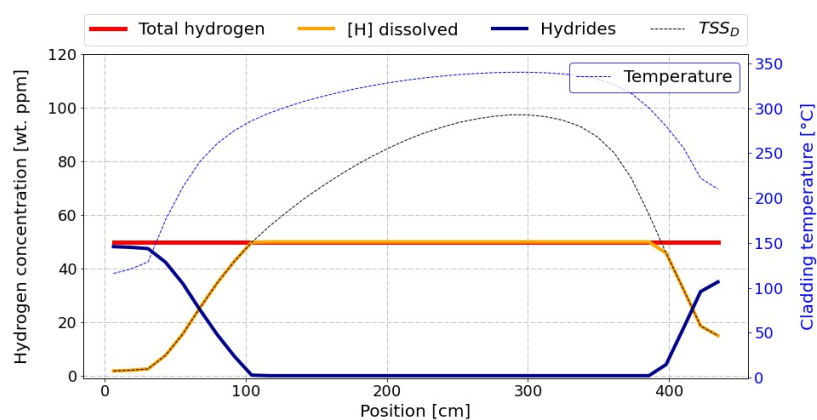


Figure 3.36: Hydrogen and hydride profiles at the beginning of the dry storage, for a total hydrogen concentration of 50 wt.ppm. For this rather low hydrogen concentration, the temperature at the beginning of the dry storage leads to the total dissolution of the hydrogen in a large section of the rod: between $x = 100$ cm and $x = 400$ cm the hydrogen solubility (TSS_D curve) exceeds 50 wt.ppm so that all hydrogen is dissolved (red and orange curves are overlapped and the blue curve is zero as no hydrides are precipitated). The TSS_D curve can be well seen on this section as it exceeds the total hydrogen concentration (50 wt.ppm) and is therefore not overlapping with the dissolved hydrogen curve.

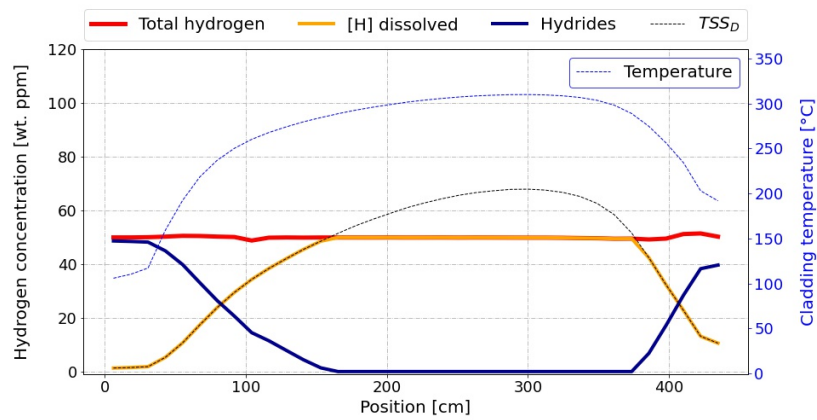


Figure 3.37: Hydrogen and hydride profiles after 1 year of dry storage, for a total hydrogen concentration of 50 wt.ppm. At this time, the hydrogen solubility in the central part of the rod still exceeds the total hydrogen content, so that the dissolved hydrogen concentration still presents a plateau at 50 wt.ppm for $150 \text{ cm} < x < 375 \text{ cm}$. In this rod section, there is no hydride. The effect of the hydrogen diffusion can already be observed: as small hump in the total hydrogen content can be seen around $x = 420 \text{ cm}$.

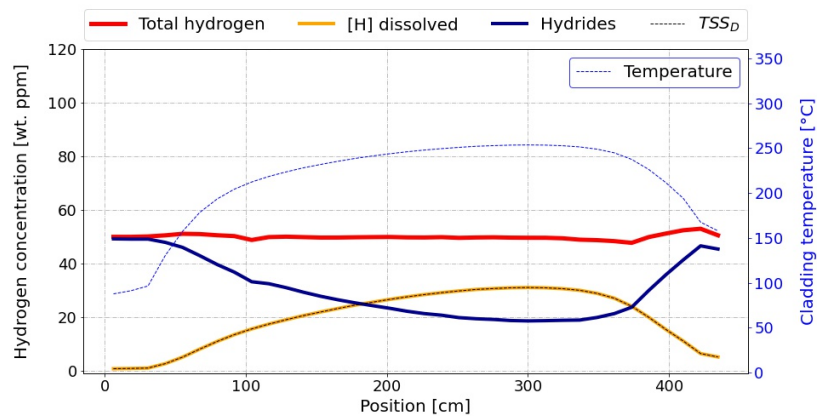


Figure 3.38: Hydrogen and hydride profiles after 5 years of dry storage, for a total hydrogen concentration of 50 wt.ppm. The temperature has sufficiently decreased at this point to result in hydrides precipitated in the whole rod: even at the hottest axial location, the hydrogen solubility dropped to around 35 wt.ppm, which is below the average 50 wt.ppm hydrogen concentration. The dissolved hydrogen concentration is therefore overlapping with the TSS_D over the whole length of the rod.

3.4 Hydrogen and hydride profiles - Predictions for full-length rods

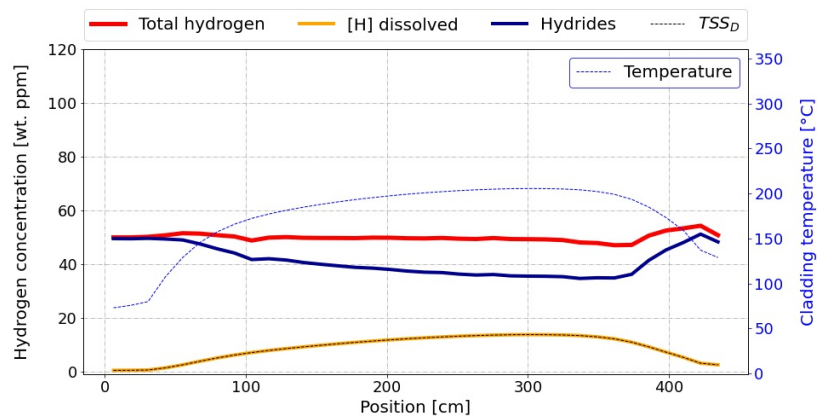


Figure 3.39: Hydrogen and hydride profiles after 15 years of dry storage, for a total hydrogen concentration of 50 wt.ppm. At this point, the dissolved hydrogen concentration does not exceed 20 wt.ppm at any axial location of the rod. Therefore, no significant further hydrogen diffusion should be expected over the remaining storage period.

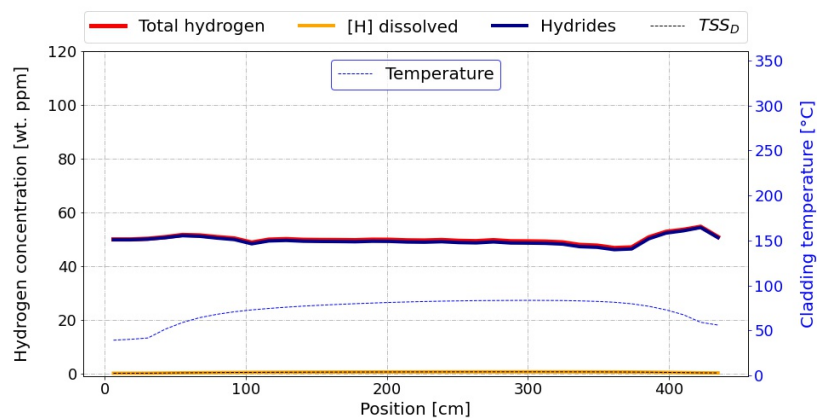


Figure 3.40: Hydrogen and hydride profiles after 95 years of dry storage, for a total hydrogen concentration of 50 wt.ppm. As the temperature is very low, the hydride profile is confounded with the total hydrogen profile. The effect of the hydrogen diffusion can be seen at both ends of the rod. In the upper part of the rod, the hydride profile presents a dip around $x = 360$ cm followed by a hump for $x > 380$ cm. In the lower part of the rod, a very slight dip can be seen around $x = 100$ cm and a hump for $x < 100$ cm.

3.4.5 Hydrogen and hydride profiles over 100 years of storage with an increased diffusion coefficient

The three simulations presented in the previous section have been obtained using the reference diffusion coefficient (see Equation 3.30). The results are consistent with expectations (higher temperature and higher dissolved hydrogen concentration in the middle part of the rod lead to hydrogen diffusion towards both ends of the rod) but the magnitude of the hydrogen diffusion appeared very low.

We should keep in mind that diffusion coefficient parameters have been derived from experiments at small scales (3 cm in [68], 15 cm in [70]), not necessarily with realistic fuel cladding configuration (geometry, material texture, heat treatment) and more often on unirradiated than on irradiated materials. It is thus questionable, how suitable the diffusion coefficient presented in Equation 3.30 (or any diffusion coefficient from the literature) is for the simulation of hydrogen diffusion at the scale of a full-length rod and over several decades. Finally, the presence or absence of hydrides (with various lengths and orientations) might also have an important impact on the diffusion.

Considering all those uncertainties of the diffusion, it is clear that no reliable prediction will be possible without experimental work for validation. If the hydrogen diffusion turns out to be even slower than observed in the previous simulation, the consequence on the final hydrogen distribution would be even more reduced. On the contrary, if the diffusion in real experiments turned out to be quicker/larger, this might have detrimental consequences (significant embrittlement of the cladding sections presenting increased hydrogen/hydride contents).

Therefore, we performed the same simulations as previously but with a diffusion coefficient increased by a factor 4. In the following, we present the results for the rods with hydrogen concentrations of 100 wt.ppm and 50 wt.ppm.

Evolution over 100 years for a concentration of 100 wt.ppm and a larger (factor 4) diffusion coefficient.

Fig. 3.41 to 3.45 present the evolution of the hydrogen and hydride profiles over 100 years of storage, for a hydrogen concentration of 100 wt.ppm and a diffusion coefficient increased by a factor 4 compared with the previous simulations. The initial state (beginning of the dry storage) shown in Fig. 3.41 is identical to Fig. 3.31: the only difference between both simulations is the diffusion coefficient, but at the beginning of the dry storage the diffusion has not played a role yet.

After 1 year of dry storage (Fig. 3.42), the effect of the increased diffusion coefficient can be well observed: the total hydrogen concentration already presents much larger variations than with the reference coefficient. In particular, the total hydrogen concentration in the upper part of the rod presents a clear dip around $x = 360$ cm and a hump for $x > 380$ cm. The amplitude of this variation is around 13 wt.ppm.

Hydrogen diffusion continues over the first years of storage. After 15 years of dry storage (Fig. 3.44), the dip of the total hydrogen concentration at $x = 360$ cm as well as the hump for $x > 380$ cm both reach nearly 20 wt.ppm of amplitude. The hydride profile in Fig. 3.45 presents the same characteristics, which indicates that no further diffusion occurs after the first 15 years of dry storage. We can note that the hydride profile also presents a small hump around $x = 60$ cm, which shows that hydrogen diffusion towards the lower end of the rod occurs.

The slight waves between $x = 100$ cm and $x = 300$ cm, as well as in the hump at $x = 410$ cm are due to numerical issues. The discretization in 36 zones (of approx. 12 cm each) is probably too coarse and the resolution algorithm (FTCS scheme) might be replaced by an enhanced method.

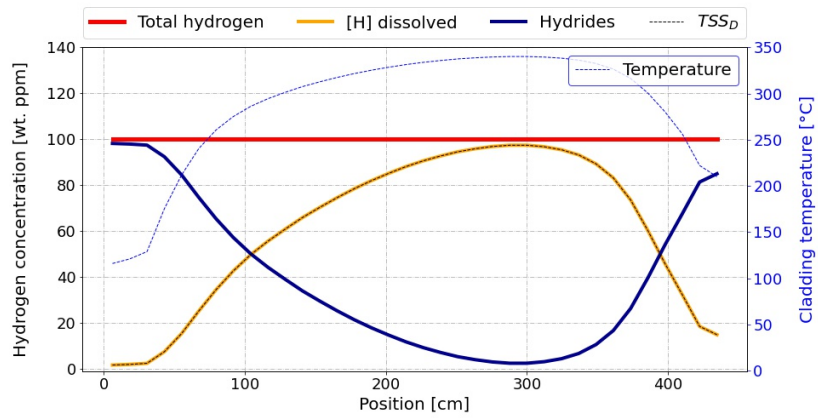


Figure 3.41: Hydrogen and hydride profiles at the beginning of the dry storage, for a total hydrogen concentration of 100 wt.ppm and a larger diffusion coefficient (factor 4). At this point, the diffusion has not played a role yet, thus the profiles are identical to the case with the reference diffusion coefficient.

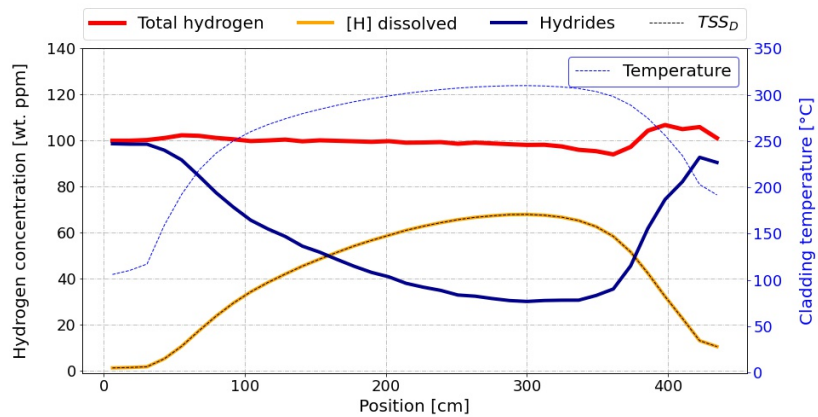


Figure 3.42: Hydrogen and hydride profiles after 1 year of dry storage, for a total hydrogen concentration of 100 wt.ppm and a larger diffusion coefficient (factor 4). The increased diffusion coefficient leads to a stronger hydrogen diffusion (larger variations in the total hydrogen curve).

3.4 Hydrogen and hydride profiles - Predictions for full-length rods

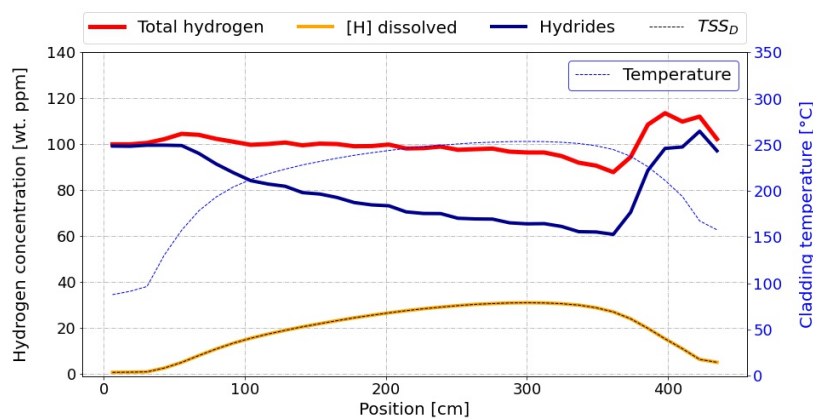


Figure 3.43: Hydrogen and hydride profiles after 5 years of dry storage, for a total hydrogen concentration of 100 wt.ppm and a larger diffusion coefficient (factor 4). At this point, the variations of the hydrogen concentration at the top of the rod reach an amplitude of about 30 wt.ppm. A clear (smaller) hump can also be seen at the bottom of the rod, around $x = 60$ cm.

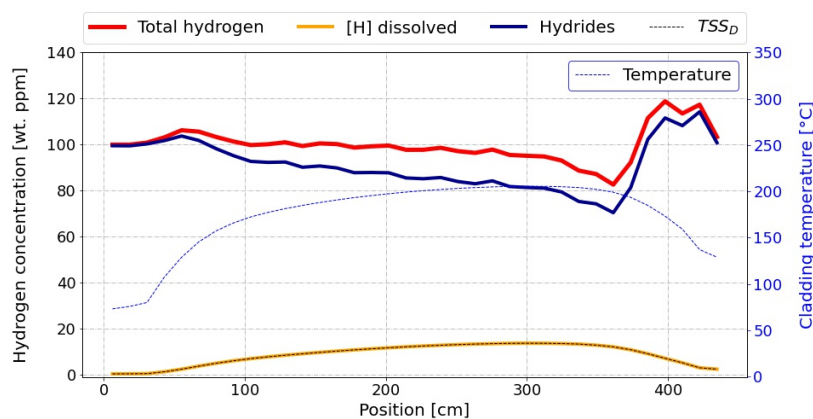


Figure 3.44: Hydrogen and hydride profiles after 15 years of dry storage, for a total hydrogen concentration of 100 wt.ppm and a larger diffusion coefficient (factor 4). At this point, the hydrogen concentration at the top of the rod varies between 80 wt.ppm at $x = 360$ cm and 120 wt.ppm at $x = 400$ cm. Between $x = 200$ cm and $x = 360$ cm, the hydrogen profile presents a continuous decrease: the high temperature gradient between $x = 360$ cm and $x = 400$ cm results in the hump at $x = 400$ cm and causes the dip at $x = 360$ cm, which in turn fosters diffusion from the region $x < 360$ cm.

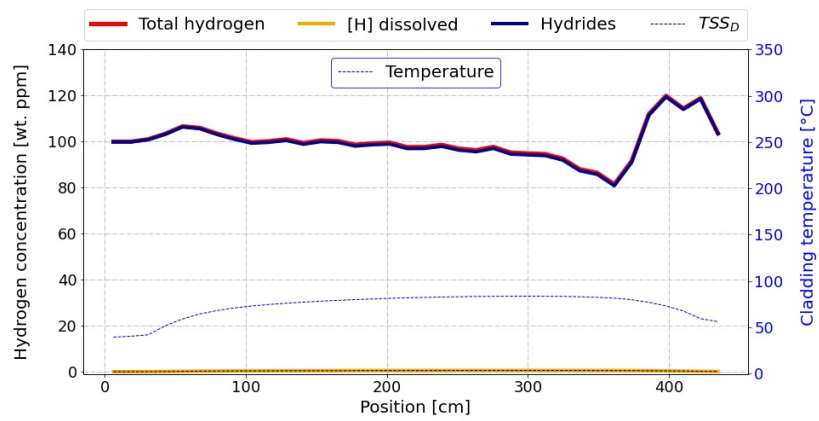


Figure 3.45: Hydrogen and hydride profiles after 95 years of dry storage, for a total hydrogen concentration of 100 wt.ppm and a larger diffusion coefficient (factor 4). The total hydrogen profile after 95 years of dry storage is identical to the profile after 15 years. This can be explained by the already sufficient decrease in temperature over the first 15 years of storage, resulting in a low solubility: the low concentration in dissolved hydrogen after 15 years of dry storage does not enable any further diffusion.

Evolution over 100 years for a concentration of 50 wt.ppm and a larger (factor 4) diffusion coefficient.

Fig. 3.46 to 3.46 present the results of the simulation for a hydrogen concentration of 50 wt.ppm and an increased diffusion coefficient (factor 4). The conclusions are similar to those of the previous simulation: the effect of the diffusion is clearer than with the reference coefficient, no significant diffusion occurs after 15 years of dry storage, the diffusion results in an important hydrogen redistribution at the top of the rod (30 wt.ppm between the maximum and the minimum concentrations), a slighter effect at the bottom of the rod (12 wt.ppm of amplitude) and a decrease in hydrogen concentration from $x = 200$ cm to $x = 360$ cm.

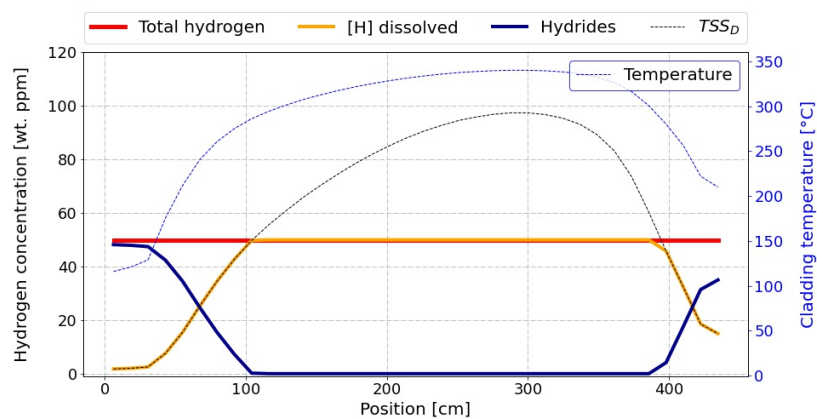


Figure 3.46: Hydrogen and hydride profiles at the beginning of the dry storage, for a total hydrogen concentration of 50 wt.ppm and a larger diffusion coefficient (factor 4). The profiles are identical to the case with the reference diffusion coefficient (no diffusion effect at this stage).

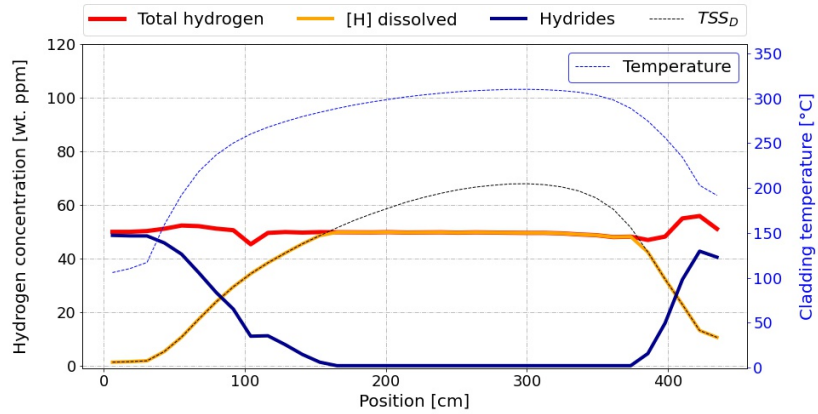


Figure 3.47: Hydrogen and hydride profiles after 1 year of dry storage, for a total hydrogen concentration of 50 wt.ppm and a larger diffusion coefficient (factor 4). After 1 year of dry storage, a clear hump has formed at the top of the rod, due to the concentration and temperature gradient between $x = 370$ cm and the top of the rod. This effect is more moderate at the bottom of the rod.

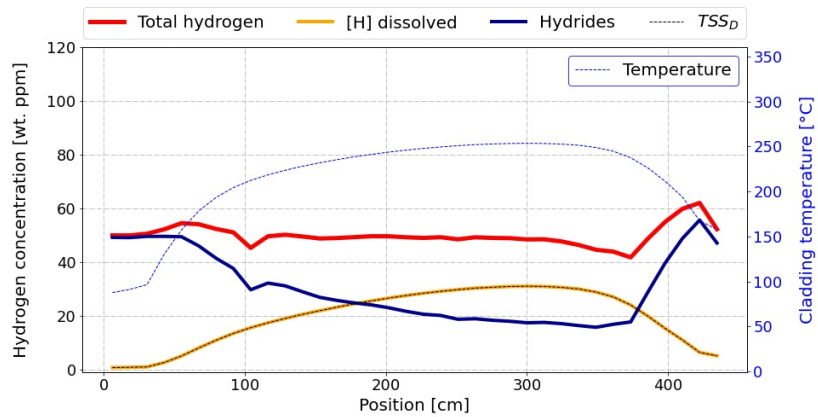


Figure 3.48: Hydrogen and hydride profiles after 5 years of dry storage, for a total hydrogen concentration of 50 wt.ppm and a larger diffusion coefficient (factor 4). The diffusion increases the hydrogen redistribution. The humps become higher and a decreasing hydrogen concentration profile forms between $x = 200$ cm and $x = 370$ cm.

3.4 Hydrogen and hydride profiles - Predictions for full-length rods

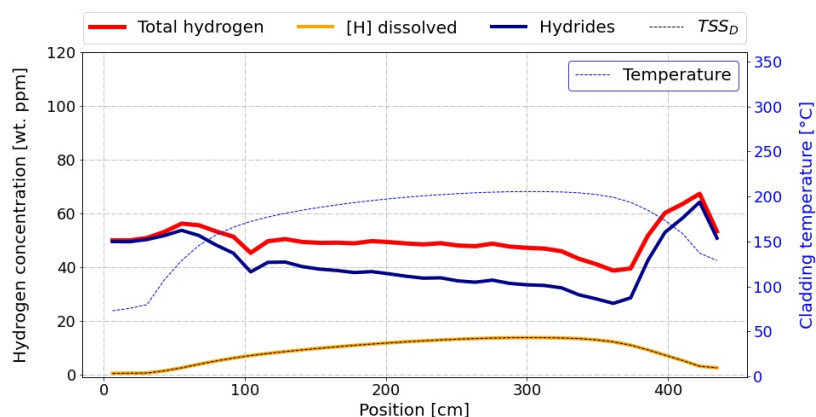


Figure 3.49: Hydrogen and hydride profiles after 15 years of dry storage, for a total hydrogen concentration of 50 wt.ppm and a larger diffusion coefficient (factor 4). At this point, the hydrogen redistribution consists in a hump reaching nearly 70 wt.ppm at $x = 420$ cm, a dip reaching 40 wt.ppm at $x = 360$ cm, and smaller dip and hump at the bottom of the rod (12 wt.ppm of amplitude).

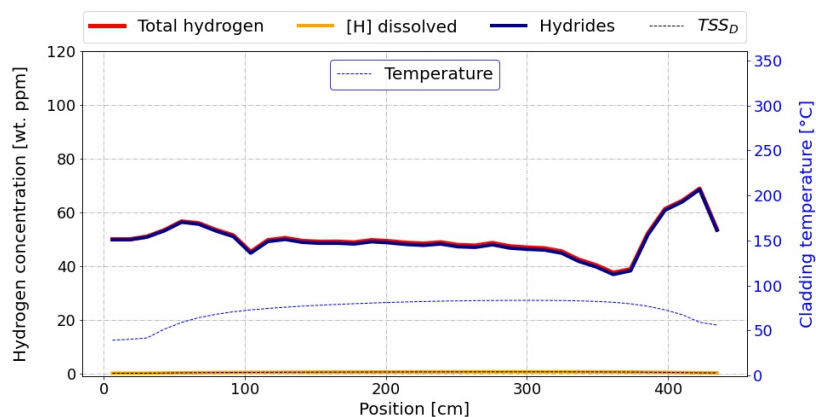


Figure 3.50: Hydrogen and hydride profiles after 95 years of dry storage, for a total hydrogen concentration of 50 wt.ppm and a larger diffusion coefficient (factor 4). The hydrogen profile is almost identical to the profile after 15 years of dry storage, which indicates that after 15 years of dry storage the temperature has sufficiently decreased to prevent further diffusion. This final hydrogen profile presents a large hump (70 wt.ppm) at the top of the rod combined with a dip (40 wt.ppm), a smaller hump (57 wt.ppm) at the bottom of the rod combined with a dip (45 wt.ppm), and a continuous decrease between $x = 200$ cm and $x = 360$ cm.

3.4.6 Hydrogen and hydride profiles after 100 years of storage for different diffusion coefficients

The following figures compare the final (after 100 years of storage) hydride profiles for different diffusion coefficients. After 100 years of storage, the peak cladding temperature has dropped under 100 °C and all hydrogen has precipitated in hydrides, preventing further diffusion. The diffusion coefficients considered here are:

- the reference coefficient (given in Equation 3.30),
- the reference coefficient with a factor 4 (as in the previous section),
- the reference coefficient with a factor 8 and
- the reference coefficient with a factor 10.

These four cases are applied to two rods: 100 wt.ppm and 50 wt.ppm of hydrogen.

Hydride profile after 100 years for an initial hydrogen concentration of 100 wt.ppm and different diffusion coefficients

Fig. 3.51 to 3.54 show the hydrogen profiles (which are equal to the hydride profiles at this stage) after 100 years of storage for a hydrogen concentration of 100 wt.ppm and different diffusion coefficients. Fig. 3.51 corresponds to the reference coefficient, which had already been described previously (Fig. 3.35). Fig. 3.52 corresponds to the result of a diffusion coefficient increased by factor 4 and has also been described in the previous section (Fig. 3.45). We can observe that the increased diffusion coefficient results in significantly larger hydrogen redistribution (larger variations in the hydrogen profile). This effect becomes even stronger in Fig. 3.53 and Fig. 3.54.

Table 3.6 summarizes the amplitudes of the upper and lower humps for the different diffusion coefficients.

3.4 Hydrogen and hydride profiles - Predictions for full-length rods

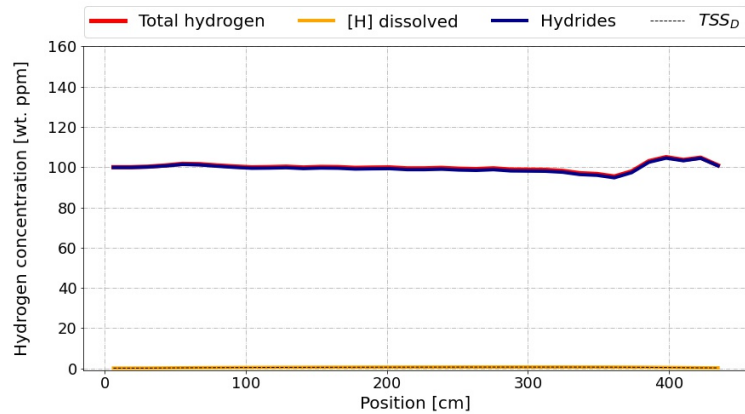


Figure 3.51: Hydrogen and hydride profiles after 100 years, for a total hydrogen concentration of 100 wt.ppm and the reference diffusion coefficient.

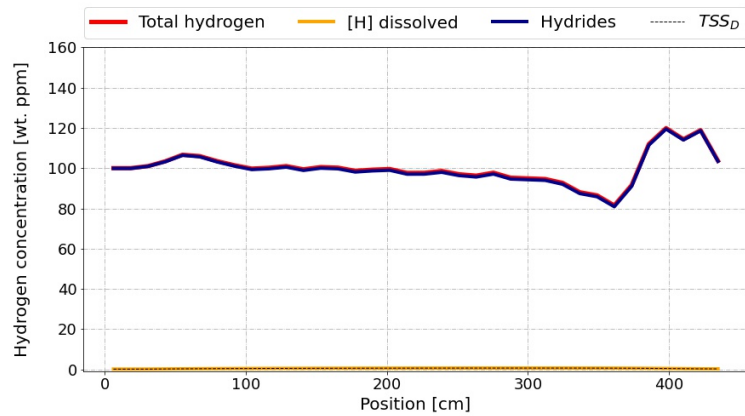


Figure 3.52: Hydrogen and hydride profiles after 100 years, for a total hydrogen concentration of 100 wt.ppm and a factor 4 for the diffusion coefficient.

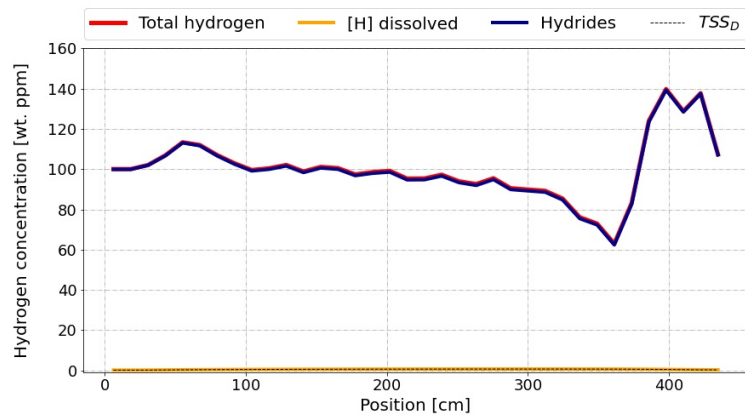


Figure 3.53: Hydrogen and hydride profiles after 100 years, for a total hydrogen concentration of 100 wt.ppm and a factor 8 for the diffusion coefficient.

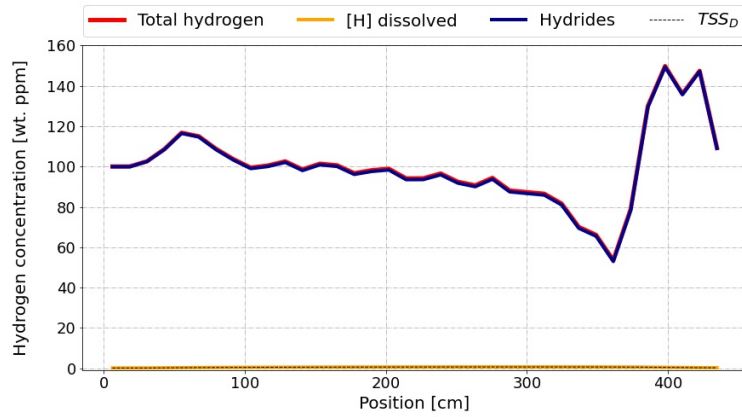


Figure 3.54: Hydrogen and hydride profiles after 100 years, for a total hydrogen concentration of 100 wt.ppm and a factor 10 for the diffusion coefficient.

Table 3.6: Effect of hydrogen diffusion on a rod with 100 wt.ppm hydrogen: humps and dips after 100 years of storage for different diffusion coefficients.

	Reference	Factor 4	Factor 8	Factor 10
$x = 60\text{cm}$	102	107	114	117
$x = 100\text{cm}$	100	100	100	100
Difference	2	7	14	17
$x = 420\text{cm}$	105	120	140	150
$x = 360\text{cm}$	96	82	65	55
Difference	9	38	75	95

Hydride profile after 100 years for an initial hydrogen concentration of 50 wt.ppm and different diffusion coefficients

Fig. 3.55 to 3.58 show the hydrogen profiles after 100 years of storage for a hydrogen concentration of 50 wt.ppm and for the different diffusion coefficients. The dependence of these profiles on the diffusion coefficient is similar to the previous case (rods with 100 wt.ppm) but more numerical instability can be seen for the highest diffusion coefficient (factor 10).

Table 3.7 summarizes the amplitudes of the upper and lower humps for the different diffusion coefficients.

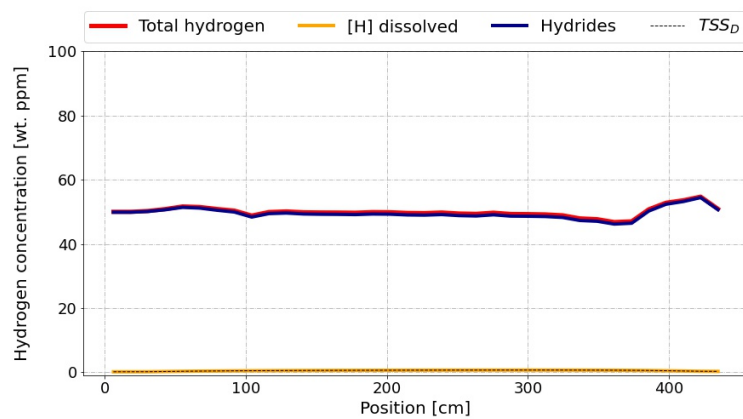


Figure 3.55: Hydrogen and hydride profiles after 100 years, for a total hydrogen concentration of 50 wt.ppm and the reference diffusion coefficient.

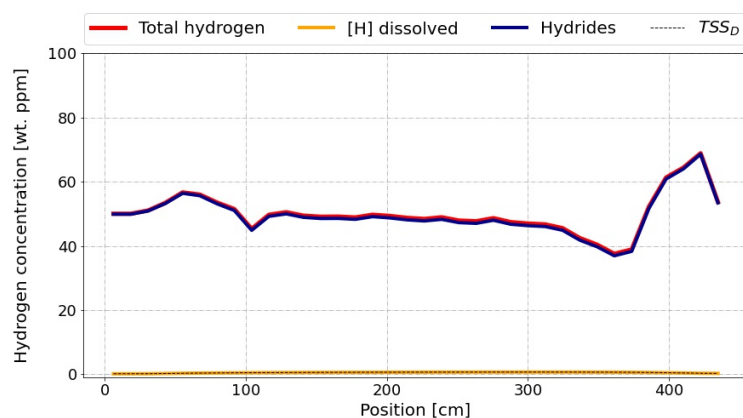


Figure 3.56: Hydrogen and hydride profiles after 100 years, for a total hydrogen concentration of 50 wt.ppm and a factor 4 for the diffusion coefficient.

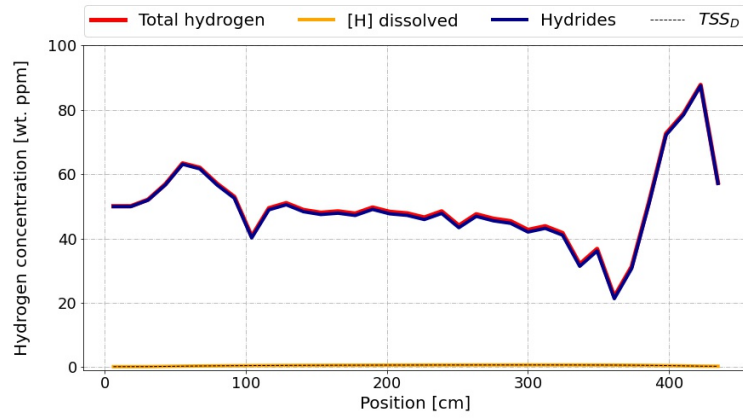


Figure 3.57: Hydrogen and hydride profiles after 100 years, for a total hydrogen concentration of 50 wt.ppm and a factor 8 for the diffusion coefficient.

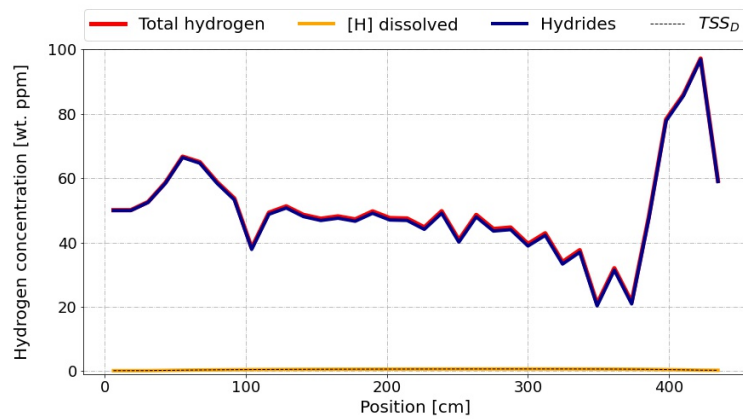


Figure 3.58: Hydrogen and hydride profiles after 100 years, for a total hydrogen concentration of 50 wt.ppm and a factor 10 for the diffusion coefficient.

Table 3.7: Effect of hydrogen diffusion on a rod with 50 wt.ppm hydrogen: humps and dips after 100 years of storage for different diffusion coefficients.

	Reference	Factor 4	Factor 8	Factor 10
$x = 60\text{cm}$	52	57	63	67
$x = 100\text{cm}$	49	46	42	40
Difference	3	11	21	27
$x = 420\text{cm}$	55	69	88	97
$x = 360\text{cm}$	47	38	23	22
Difference	8	31	65	75

3.4.7 Summary on the hydrogen diffusion in a full-length rod

In this section, we presented a model for hydrogen diffusion and precipitation at the scale of a full-length rod. We first defined and discussed the basic assumptions on which the model is built. Then, we described the numerical scheme used to implement the model. It corresponds to a Forward Time Centered Space (FTCS) method [108–110].

Afterwards, we used temperature profiles obtained in Chapter 2 to determine the cladding configuration at the beginning of the dry storage, in particular with regard to the profile of dissolved hydrogen (Fig. 3.22, 3.23 and 3.24).

The evolution of the hydrogen and hydride profiles over 100 years of storage has been simulated, for fuel cladding with different hydrogen contents: 250, 100 and 50 wt.ppm (resp. Fig. 3.26 to 3.30, Fig. 3.31 to 3.35 and Fig. 3.36 to 3.40), initially homogeneously distributed. The simulations rely on time-dependent fuel rod temperature profiles, determined in Chapter 2. We observed a limited effect of diffusion: the hydrogen redistribution did not exceed 10 wt.ppm. Furthermore, we noted that most hydrogen diffusion occurs during the first 5 years of dry storage (the temperature of the central part of the fuel rod was of approximately 250 °C at the end of the 5 years), and that no significant diffusion takes place after 15 years of storage: at this time, the maximum temperature has dropped to 205 °C and the concentration of dissolved hydrogen does not exceed 14 wt.ppm anymore.

In a next step, we performed the same simulations but with a diffusion coefficient increased by a factor 4 (Fig. 3.41 to 3.50). Due to the uncertainties on the diffusion mechanisms at the scale of a fuel rod, it seemed important to perform simulations with an increased diffusion coefficient. On the contrary, a reduced diffusion coefficient would result in even less effect on the final hydrogen distribution than with the reference coefficient, therefore this case has not been considered. As expected, the simulations with the increased diffusion coefficient led to larger hydrogen redistributions and revealed, in addition to the hydride concentration at the top of the rod already observed, another hydride concentration at the bottom of the rod, though of smaller

amplitude (Fig. 3.45).

Finally, we compared the hydride profiles after 100 years of storage, for cladding containing 100 wt.ppm and 50 wt.ppm, in four different cases: for the reference diffusion coefficient, or for coefficients increased by factors 4, 8 or 10. For the reference coefficient (Fig 3.51 and 3.55), only a small hydride accumulation (amplitude lower than 10 wt.ppm) was observed at the top of the rod. For the diffusion coefficient increased by a factor 10, we observed a hydride concentration at the bottom of the rod (approximately +20 wt.ppm), a gradual decrease in hydride concentration from the middle part of the rod towards the top, and another hydride accumulation at the top of the rod. This latter hydride accumulation reached nearly 100 wt.ppm of amplitude in the case of the fuel rod containing 100 wt.ppm (Fig.3.54).

3.5 Conclusion - Hydrogen and hydride behaviour

In this chapter, we discussed several aspects of the hydrogen behaviour in fuel cladding under storage conditions. Section 3.1 gave some theoretical input on the Zr-H binary system, on the diffusion mechanisms, and on the solubility limits TSS_P/TSS_D of hydrogen in zirconium alloys.

In section 3.2, we analysed a database on the Terminal Solid Solubility of hydrogen in zirconium alloys and derived correlations depending on the cladding materials and measurement methods. We observed that the distinction between TSS_P and TSS_D curves seems to be related to the cooling rate applied for the TSS_P measurements and might be a further hint to a kinetic effect described in [8,9].

In section 3.3, we implemented with Python a model (HNGD) describing the hydrogen and hydride behaviour in zirconium alloys, depending on the solubility limits TSS_P/TSS_D . We compared our results with the ones provided in the original articles describing the HNGD model, and we discussed the differences. The hydride growth rate was the main discrepancy but is not relevant for investigations on the hydrogen/hydride behaviour during dry storage, as the cooling rates in storage conditions are significantly lower than the hydride growth rate.

In section 3.4, we established a new model, adapted to the analysis of the hydrogen and hydride distributions in the cladding at the scale of a full-length rod. In particular, this model does not consider the TSS_P limit anymore, as the cooling rates involved during the dry storage are lower by a few orders of magnitude than the limiting cooling rates for hydride growth. The model takes into account temperature profiles calculated in Chapter 2, which are used to determine the Soret effect (hydrogen diffusion driven by temperature gradients) and the axial profile of dissolved hydrogen (resulting in hydrogen diffusion driven by concentration gradients, according to Fick's law). This model could not be validated, due to the lack of long-term experiments on full-scale fuel rods. Therefore, large uncertainties remain attached to the diffusion coefficient applied in the model and, more generally, on the diffusion mechanisms at this scale: impact of local defects, stress variations

along the axial dimension due to pellet cladding interaction, variations of the hydrogen concentration at the spacer grid positions.

However, the simulations provided qualitative estimations of the possible hydride configurations after several decades of dry storage. In particular, in the case of favourable hydrogen diffusion coefficients, significant hydride concentrations might be expected at the upper and lower end of the rod, which in turn might represent a risk of embrittlement for these regions.

4 Conclusion and outlooks

For the first time, we performed comprehensive simulations of the thermal history of spent fuel assemblies during long-term dry storage in casks, and related it to the hydrogen behaviour in fuel cladding at the scale of a full-length rod. In the following, more details are provided on the different steps involved in this project, as well as on possible further developments.

Temperature fields in storage casks

In this thesis, we presented and discussed different cask models and modelling assumptions to determine time-dependent temperature distributions of the cask, its components and inventories.

The semi-analytical model presented in section 2.2 showed that it is possible to obtain results within good orders of magnitude when compared to the more detailed model in section 2.3. Furthermore, it is straightforward to use and can be easily further developed or adapted to different boundary conditions and scenarios. For example, the model could also be applied for questions concerning cask temperature evolutions in final repositories.

However, for a comprehensive analysis of the cask content (assessment of the fuel cladding integrity), it is necessary to know the detailed time-dependent temperature distribution in the cask. The COBRA-SFS cask models presented in section 2.3 and section 2.4 meet these requirements: they present a high level of detail, including the definition of specific operation conditions (decay heats of each fuel assembly, axial power profiles, helium or vacuum conditions) and boundary conditions (room temperature, plenum models). The results consist of temperature profiles for each single rod and for all cask structures (rails, fuel compartments, cask body). Transients have been performed too, simulating the temperature evolution during the drying process. Finally, we performed sensitivity analyses and thus determined which

parameters are strongly affecting the temperature distribution:

- Ambient temperature

The increase of the ambient temperature leads to an increase of the whole cask (cask structures and spent fuel assemblies). In the case of steady-state calculations, we observed with both COBRA-SFS models that the temperature increase in the cask is nearly equal to the increase in ambient temperature. In transient calculations, depending on the time scale, different scenarios are expected: daily temperature variations (night/day) of the ambient temperature would affect mainly the cask body, whose large heat capacity would prevent significant temperature variations of the fuel assemblies. On the contrary, yearly variations (winter/summer) can be assimilated to steady-state and result in large temperature variations.

- Decay heat

Decay heat values are provided by calculations using the power history of the fuel assemblies and a set of nuclear data (cross sections). Both present uncertainties and therefore the decay heats also include uncertainties. We observed that $\pm 5\%$ decay heat resulted in ± 10 °C cladding temperature for the simulation of the TN-32B cask.

- Gap between the structures

Storage casks include different components (cask body, rails, baskets, fuel compartments), which should not be considered perfectly bonded: they are separated by thin gaps. These gaps induce additional thermal resistances, whose impact is not negligible. In particular, the gap between the inner surface of the cask body and the rail structures results in an overall increase of the temperature of the elements located in the cask inner cavity, including the fuel assemblies. In the case of a constant gap (most detrimental configuration), we observed a temperature increase of approximately 25 °C per mm of gap for the CASTOR model.

From the results of the cask modelling, we can conclude that the maximum

temperature will be reached either during the drying process or during the first months of dry storage:

If the vacuum drying lasts long enough, the temperature in the cask can exceed the equilibrium under helium atmosphere, thus a temperature peak would be reached at the end of the vacuum drying.

If the vacuum drying is rather short and the temperature maximum is only reached after helium refill, then there is a possibility that the temperature maximum will be reached later, despite the radioactive decay. Indeed, the seasonal temperature variations impact the ambient temperature of the cask and we observed that an increase of the ambient temperature results in a nearly equal increase in the temperature of the cask. This effect might exceed the effect of the decreasing decay heat, in particular if the cask loading occurs during a cold season quickly followed by a warmer one.

The question of the maximum temperature reached is important, as it determines how many hydrides will dissolve at the beginning of the dry storage, and possibly reprecipitate in a more detrimental configuration later.

Concerning the thermal modelling of storage casks, two major issues have been encountered:

- the difficult access to precise design data and
- the lack of publicly available experimental data.

The first point is relevant in the case of detailed cask modelling, as for instance with COBRA-SFS. For reliable, detailed temperature predictions, the precise knowledge of the cask design is required, including the geometry and the material properties. Thus, the CASTOR model presented in Chapter 2 cannot be considered as a specific model for the cask type CASTOR[®] V/19, but only as a generic model. In practice, this point could be solved, as the data exists.

The second point is a larger problem: experimental data is not only difficult to find publicly available, but also difficult to generate. Indeed, the containment function of a cask makes it difficult to re-open once closed. However, we might here note that measurements of the cask surface temperature should

not be an issue. These measurements results could significantly increase the reliability of the model, as it would directly help to validate the thermal modelling of the cask surface. This part of a cask model is particularly complex as it includes numerous factors affecting the heat transfers: the natural convection of air (with possible influence of the surrounding structures, casks, walls, air inlet/ventilation system of the facility), the cooling fins, the radiative heat transfers from the surrounding elements, heat conduction through the bottom of the cask to the ground.

As further steps, the cask models could be coupled with further programs: thermo-mechanical codes or hydrogen diffusion models. Indeed, these models concern mechanisms which are highly dependent on temperature and therefore require temperature distributions as input.

More comprehensive sensitivity analyses could be conducted with COBRASFS. This is planned for the TN-32B model, in the framework of the EPRI International Thermal Benchmark (phase 2).

Hydrogen and hydride behaviour

The determination of temperature distributions in storage casks enabled in the second part of the thesis to simulate the hydrogen/hydride behaviour in the cladding.

In section 3.2, we presented a data analysis on the Terminal Solid Solubility (TSS) of hydrogen in zirconium alloys, based on several experimental works. We derived correlations for different sets of data, corresponding to the different cladding materials and to the different measurement methods. The results gave further evidence of the influence of the cooling rate on the solubility limit for precipitation (TSS_P): the lower the cooling rates were, the less distinct the TSS_P and TSS_D were.

The TSS_P/TSS_D data analysis provided numerous correlations. As a further step, these correlations could be implemented in thermo-mechanical codes, for instance TESP-ROD [111, 112]. Furthermore, new experimental works on hydrogen solubility in zirconium alloys are regularly performed (with an upward trend in the accuracy of the measurements), so that the TSS_P/TSS_D

database should be updated on a regular basis.

In section 3.3, we presented a model describing the hydrogen dissolution and precipitation in zirconium alloys. Following [10], we implemented a suitable model with Python and performed different simulations. The model can be used to determine the local behaviour of hydrogen, depending on the temperature: hydride dissolution or precipitation (nucleation and growth). We observed some discrepancy between our results and the results in [10], in particular concerning the kinetics of the hydride precipitation by growth. In our case, hydride growth appeared slower. However, for investigations on the long-term dry storage of spent nuclear fuel, this will not be an issue as the cooling rates involved during dry storage are low enough to ensure the thermodynamic equilibrium (TSS_D) at any time. The model provided further understanding of the hydrogen dissolution and precipitation mechanisms, which helped developing a model for predictions at the scale of a full-length rod.

This model for full-scale rods is based on the assumption that the cooling rates during dry storage are low enough to ensure the thermodynamic equilibrium at any time. Therefore, the dissolved hydrogen profile in the rod is given by the TSS_D profile corresponding to the temperature axial profile, or by the total amount of hydrogen if this is less than the TSS_D . The dissolved hydrogen profile is then used to calculate locally the contribution of Fick's law to the hydrogen diffusion, while the temperature profile determines the Soret effect contribution. If hydrides are - locally - present, they constitute a source term for hydrogen in case of divergence of the hydrogen flux, or a sink term in case of negative divergence. The dissolved hydrogen profile remains in both cases unchanged. If all hydrogen is - locally - dissolved, the diffusion results in a change of the dissolved hydrogen profile, which impacts the Fick's law contribution.

Using this model, we simulated the evolution of the hydrogen and hydride profiles over 100 years of storage. We observed a limited accumulation of hydrides at the upper and lower ends of the rods. With increased diffusion coefficients, these hydrides accumulations might become significant with respect to the embrittlement issue. Experimental works on full-length fuel

rods and over long time scales (months) involving low cooling rates appear necessary to further validate this model. In the model at hand, we did not take into account possible variations in the diffusion coefficient due to local defects or varying stress along the axial dimension (pellet-cladding mechanical interaction).

We can provide here some further thoughts suggested by the present work:

- We found that the ratio of dissolved and precipitated hydrogen might be important if one investigates the impact of hydrides on the mechanical behaviour. While newer cladding materials present very good properties regarding corrosion and hydrogen pick-up in operation, the resulting lower hydrogen contents might constitute a detrimental characteristic in dry storage: for a hydrogen content of 50 wt.ppm, all hydrides might dissolve at the beginning of the dry storage. As the following cooling occurs very slowly, hydride precipitation would consist mainly in hydride growth, possibly radially oriented. Long radial hydrides represent the worst configuration with regard to the cladding mechanical properties and integrity.

In cladding types with higher hydrogen content, even at the beginning of the dry storage, part of the hydrides remain precipitated (mainly circumferentially, after reaction operations). The following hydride precipitation might then occur by growth of the already precipitated hydrides, and therefore avoid the formation of long radial hydrides.

- Zircaloy-2 with liner is seen as a low concern cladding type, due to the TSS_D difference between pure (or low-alloyed) Zr and Zircaloy-2: the liner presents a lower hydrogen solubility, which results in the radial diffusion of the hydrogen, from the Zircaloy-2 bulk to the liner [77]. Therefore, the main part of the hydrogen is concentrated in the liner, and the Zircaloy-2 might be less affected by hydride embrittlement. Similar arguments could be found for PWR claddings with liner. However, further experimental evidences have to be found.
- Hydrogen migration is expected to occur only during the first years of storage, and only if the cladding temperature is high enough: it re-

quires a significant amount of dissolved hydrogen, relatively high concentration gradients, and high temperature gradients. All these factors weaken with time: due to the decay heat decrease, the temperature decreases, which leads to smaller temperature gradients, lower dissolved hydrogen concentrations and lower concentration gradients. We observed in our simulations that after 15 years of dry storage, the maximum temperature is 205 °C, the hydrogen solubility does not exceed 14 wt.ppm, and therefore almost no more hydrogen diffusion takes place.

The simulations have been performed using rather hot rods, we can thus expect that for fuel assemblies with lower decay heats at the beginning of the dry storage, less diffusion would be observed due to lower temperature. On the contrary, MOX fuel might be of higher concern, due to higher decay heat and a slower radioactive decay: the cladding undergoes high temperatures for a long time, which could enable more hydrogen diffusion.

Many questions remain open concerning the development of the hydrogen diffusion model presented in section 3.4:

- What is the influence of local defects (hydride clusters, cracks) and of local variations of the hydrogen concentration (interpellet region, spacer grids positions) on diffusion?
- Is there a radial dependence of the axial diffusion (e.g. due to radial gradients of concentration or of stress)?
- What is the configuration of the hydrides: radial or circumferential orientation?

The influence of the temperature profile should be analysed. In the simulations presented in this thesis, we observed a larger accumulation of hydrides at the upper end of the rod than at the lower end. This is explained by the larger temperature and concentration gradients in the upper part of the rod. Further work should simulate the evolution of claddings presenting dif-

ferent temperature profiles, in particular to assess how detrimental sharper profiles could be, with regard to hydride accumulation and embrittlement.

Concerning the implementation of the diffusion model, enhanced resolution algorithms should be considered for further simulations, especially if finer discretizations (in time and space) are targeted. The Backward Time Centered Space (BTCS) scheme or the Crank - Nicolson scheme could be interesting candidates. Both are implicit and unconditionally stable, which is not the case of the explicit Forward Time Centered Space (FTCS) scheme used in the current model. [108–110]

In the present model, we considered only 36 axial zones for the discretization, as the temperature profiles provided by the COBRA-SFS CASTOR model consist of 36 values. In future versions of the model, we should consider a finer spatial discretization, as it might have a significant impact on the simulation of the diffusion. This would also enable to simulate for example the impact of local hydrogen concentrations (at the interpellet region, or at the spacer grid positions).

Furthermore, we did not consider a smooth/gradual evolution of the temperature over time, but only a few time points. For instance, the temperature profile calculated by COBRA-SFS at the beginning of the dry storage was used to determine the hydrogen fluxes applied during the first year of storage. These fluxes are recalculated only at the end of the first year of storage, when a new temperature profile is taken into account. In further developments of the model, we should consider a more gradual evolution of the temperature profile.

Finally, we should emphasize the fact that experimental work on full-length fuel rods and over long time scales appears necessary for the validation of hydrogen diffusion in cladding under storage conditions. BGZ foresees to conduct projects on this topic over the next years, as do the US DOE and EPRI (High Burnup Demonstration Project [113,114]). Therefore, we are confident that hydrogen/hydride behaviour models for fuel rod cladding under dry storage conditions will benefit from better validation possibilities in a near future.

5 Appendices

5.1 View factors

5.1.1 2-dimensional

View factor for two elementary surfaces:

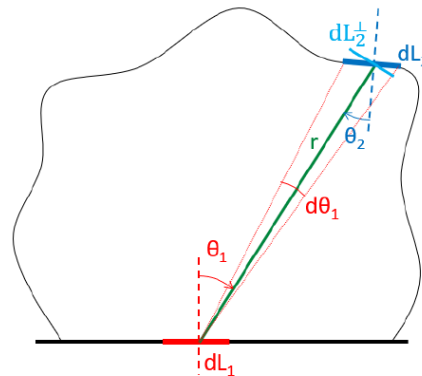
$$dF_{1 \rightarrow 2} = \frac{f(\theta_1) d\theta_1}{\int_{-\pi/2}^{+\pi/2} f(\theta_1) d\theta_1} \quad \text{with } f(x) = \cos(x) \quad (*\text{Apparent surface, see below})$$

$$= \frac{\cos(\theta_1) d\theta_1}{\int_{-\pi/2}^{+\pi/2} \cos(\theta_1) d\theta_1}$$

$$= \frac{\cos(\theta_1) d\theta_1}{2}$$

$$\begin{cases} dL_2^\perp = dL_2 * \cos(\theta_2) \\ dL_2^\perp = r * d\theta_1 \end{cases} \Rightarrow d\theta_1 = \frac{\cos(\theta_2) dL_2}{r}$$

$$dF_{1 \rightarrow 2} = \frac{\cos(\theta_1) \cos(\theta_2) dL_2}{2 * r}$$



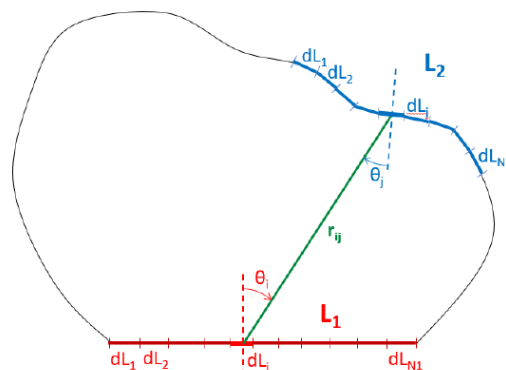
View factor for two standard surfaces:

$$F_{1 \rightarrow 2} = \frac{1}{S_1} \int_{S_1} \left(\int_{S_2} dF_{1 \rightarrow 2} \right) dL_1$$

$$F_{1 \rightarrow 2} = \frac{1}{S_1} \iint_{S_1 S_2} \frac{\cos(\theta_1) dL_1 \cos(\theta_2) dL_2}{2 * r}$$

Discretized formula:

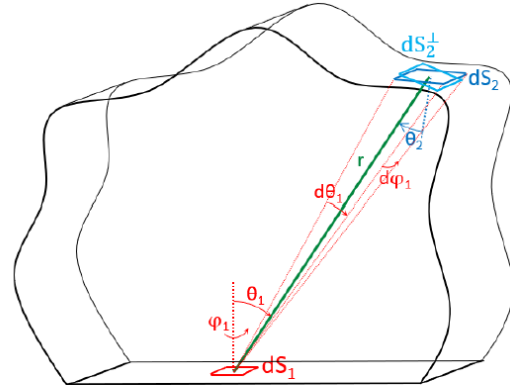
$$F_{1 \rightarrow 2} = \frac{1}{L_1} \sum_{i=1}^{N_1} dL_i \sum_{j=1}^{N_2} \frac{\cos(\theta_i) \cos(\theta_j) dL_j}{2 * r_{ij}}$$



5.1.2 3-dimensional

View factor for two elementary surfaces:

$$\begin{aligned}
 dF_{1 \rightarrow 2} &= \frac{f(\theta_1) d\Omega_1}{\iint f(\theta_1) d\Omega_1} \quad \text{with } f(x) = \cos(x) \\
 &= \frac{\cos(\theta_1) \sin(\theta_1) d\theta_1 d\varphi_1}{\int_0^{2\pi} \int_0^{\pi/2} \cos(\theta_1) \sin(\theta_1) d\theta_1 d\varphi_1} \\
 &= \frac{\cos(\theta_1) \sin(\theta_1) d\theta_1 d\varphi_1}{2\pi \left[\frac{\sin^2(\theta_1)}{2} \right]_0^{\pi/2}}
 \end{aligned}$$



$$\begin{cases} dS_2^\perp = dS_2 * \cos(\theta_2) \\ dS_2^\perp = r d\theta_1 * r \sin(\theta_1) d\varphi_1 \end{cases} \Rightarrow \sin(\theta_1) d\theta_1 d\varphi_1 = \frac{\cos(\theta_2) dS_2}{r^2}$$

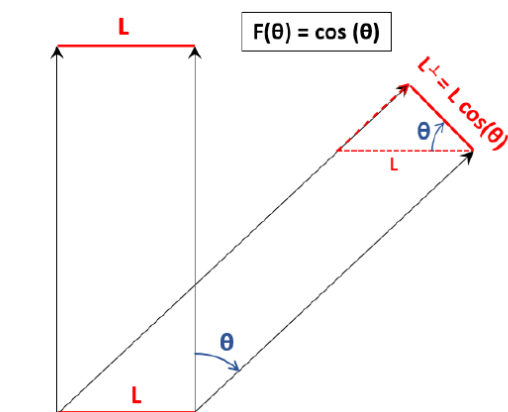
$$dF_{1 \rightarrow 2} = \frac{\cos(\theta_1) \cos(\theta_2) dS_2}{\pi * r^2}$$

View factor for two standard surfaces:

$$F_{1 \rightarrow 2} = \frac{1}{S_1} \int_{S_1} \left(\int_{S_2} dF_{1 \rightarrow 2} \right) dS_1$$

$$F_{1 \rightarrow 2} = \frac{1}{S_1} \iint_{S_1 S_2} \frac{\cos(\theta_1) dS_1 \cos(\theta_2) dS_2}{\pi * r^2}$$

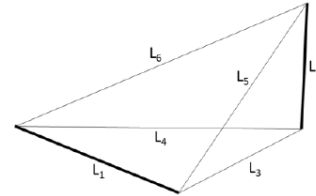
* Apparent surface



5.2 Hottel's crossed strings method [26].

The Hottel's correlation formula enables to calculate view factors for radiative heat transfer, without using the standard view factor definition (which involves integral expressions and leads in most cases to harsh calculations) but a rather simple expression based on string lengths:

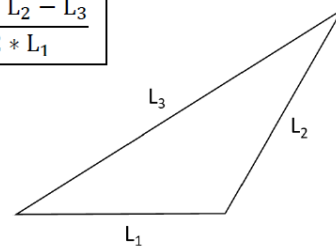
$$F_{12} = \frac{L_4 + L_5 - L_3 - L_6}{2 * L_1}$$



Demonstration:

We first demonstrate the following result (for a triangle):
We suppose that the sides are straight ($F_{ii} = 0$).

$$F_{12} = \frac{L_1 + L_2 - L_3}{2 * L_1}$$



$$\left. \begin{array}{l} F_{11} + F_{12} + F_{13} = 1 \\ F_{11} = 0 \end{array} \right\} L_1 F_{12} + L_1 F_{13} = L_1$$

$$\left. \begin{array}{l} F_{21} + F_{22} + F_{23} = 1 \\ F_{22} = 0 \end{array} \right\} \left. \begin{array}{l} L_2 F_{21} + L_2 F_{23} = L_2 \\ L_2 F_{21} = L_1 F_{12} \end{array} \right\} L_1 F_{12} + L_2 F_{23} = L_2$$

$$\left. \begin{array}{l} F_{31} + F_{32} + F_{33} = 1 \\ F_{33} = 0 \end{array} \right\} \left. \begin{array}{l} L_3 F_{31} + L_3 F_{32} = L_3 \\ L_3 F_{31} = L_2 F_{23} \end{array} \right\} L_1 F_{13} + L_2 F_{23} = L_3$$

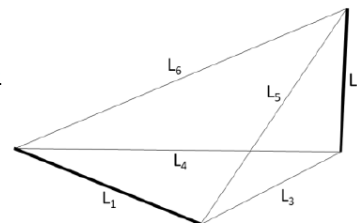
$$\Rightarrow (L_1 F_{12} + L_1 F_{13}) + (L_1 F_{12} + L_2 F_{23}) - (L_1 F_{13} + L_2 F_{23}) = L_1 + L_2 - L_3$$

$$\Rightarrow 2 * L_1 F_{12} = L_1 + L_2 - L_3$$

$$\Rightarrow F_{12} = \frac{L_1 + L_2 - L_3}{2 * L_1}$$

Then, using the upper formula, we can derive the Hottel's formula correlation:

$$\left. \begin{array}{l} F_{13} = \frac{L_1 + L_3 - L_4}{2 * L_1} \\ F_{16} = \frac{L_1 + L_6 - L_5}{2 * L_1} \\ F_{13} + F_{12} + F_{16} = 1 \end{array} \right\} F_{12} = 1 - F_{13} - F_{16} = \frac{L_4 + L_5 - L_3 - L_6}{2 * L_1}$$

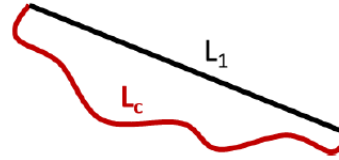


This formula was derived assuming that $F_{11} = 0$, i.e. that surface 1 is straight. However, the formula can be generalized to curved surfaces.

For a straight surface (L_1), the self view factor is null ($F_{11} = 0$). But this is not the case for a non-convex surface (L_c), where radiation emitted by the surface can hit the surface itself ($F_{cc} > 0$).

Self view factor of a curved surface:

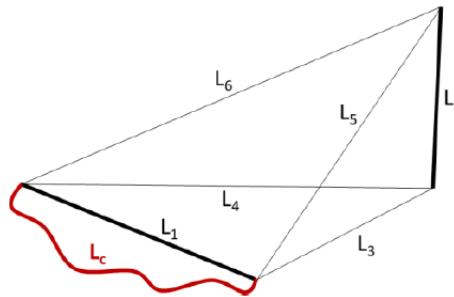
$$\left. \begin{aligned} F_{1c} &= 1 - F_{11} = 1 \\ L_c F_{c1} &= L_1 F_{1c} = L_1 \\ F_{cc} + F_{c1} &= 1 \end{aligned} \right\} \boxed{F_{cc} = 1 - L_1/L_c}$$



Hottel's Correlation Formula for curved surfaces:

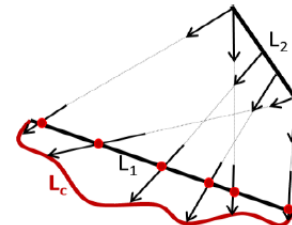
$$\left. \begin{aligned} L_c F_{c2} &= L_2 F_{2c} \\ F_{2c} &= F_{21} \\ L_1 F_{12} &= L_2 F_{21} \end{aligned} \right\} F_{c2} = \frac{L_2}{L_c} F_{21} = \frac{L_1}{L_c} F_{12}$$

$$F_{c2} = \frac{L_1}{L_c} * \frac{L_4 + L_5 - L_3 - L_6}{2 * L_1} = \frac{L_4 + L_5 - L_3 - L_6}{2 * L_c}$$



NB: $F_{c \rightarrow 2} \neq F_{1 \rightarrow 2}$ but $F_{2 \rightarrow c} = F_{2 \rightarrow 1}$

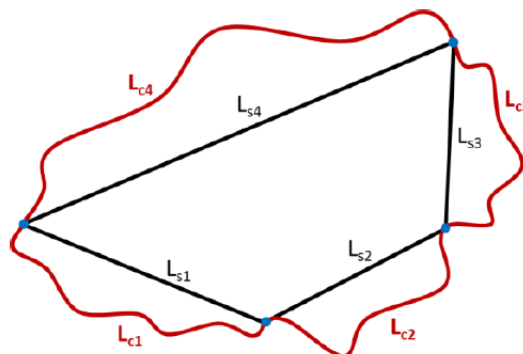
Indeed, surface L_c receives the same radiation from L_2 than L_1 . (see diagram beside)



Generalization to non-flat surfaces:

Consistent with the above, the formula can be extended for non-flat surfaces:

$$\left\{ \begin{aligned} F_{ci \rightarrow cj} &= \frac{\text{crossed strings} - \text{uncrossed strings}}{2 * L_{ci}} \\ & \quad i \neq j \\ F_{ci \rightarrow ci} &= \frac{L_{ci} - L_{si}}{L_{ci}} \end{aligned} \right.$$



5.2.1 Implementation with Python

```
def VF_Hottel(S1, S2):
    ''' Function calculating the view factor F12 using Hottel's correlation formula
        S1 : ((xm1, ym1), (xp1,yp1), l1) / S2 : ((xm2, ym2), (xp2,yp2), l2) '''

    if S1==S2:
        M1P1 = np.sqrt((S1[0][0]-S1[1][0])**2 + (S1[0][1]-S1[1][1])**2)
        F = round((S1[2]-M1P1)/S1[2], 5)

    else:
        # Calculation of crossed/uncrossed string lengths
        M1M2 = np.sqrt((S1[0][0]-S2[0][0])**2 + (S1[0][1]-S2[0][1])**2)
        P1P2 = np.sqrt((S1[1][0]-S2[1][0])**2 + (S1[1][1]-S2[1][1])**2)
        M1P2 = np.sqrt((S1[0][0]-S2[1][0])**2 + (S1[0][1]-S2[1][1])**2)
        P1M2 = np.sqrt((S1[1][0]-S2[0][0])**2 + (S1[1][1]-S2[0][1])**2)

        # Claculation of the view factor according to Hottel's formula
        F = round(abs((M1P2+P1M2)-(M1M2+P1P2))/(2*S1[2]),5)

    return F
```

```
def Hottels_matrix(*N):
    ''' Function calculating the view factor matrix for a set of surfaces S,
        according to Hottel's correlation formula'''

    factors=np.zeros((len(N),len(N)))          # Initialization of the matrix

    for i in list(range(len(N))):
        l = N[i][2]/2.54
        print("length",i+1,"=", l, "in")
        for j in list(range(len(N))):
            # factors[i][j] contains the view factor from surface i to surface j
            factors[i][j] = VF_Hottel(N[i], N[j])
    return factors
```

Example on Assembly 42 of the CASTOR model:

```
A = (0,0)
B = (7,0)
C = (7,11.75)
D = (7,23.5)
E = (0,23.5)
F = (0,11.75)

N1 = (A, B, 7)
N2 = (B, C, 11.75)
N3 = (C, D, 11.75)
N4 = (D, E, 7)
N5 = (E, F, 11.75)
N6 = (F, A, 11.75)

HM = Hottels_matrix(N5, N6, N1, N2, N3, N4)

print("Hottel's correlation formula:")
print(HM)

S1=frag_segm(A,B,2)
S2=frag_segm(B,C,2)
```

```
S3=frag_seg(C,D,2)
S4=frag_seg(D,E,2)
S5=frag_seg(E,F,2)
S6=frag_seg(F,A,2)
```

Output:

```
length 1 = 4.625984251968504 in
length 2 = 4.625984251968504 in
length 3 = 2.7559055118110236 in
length 4 = 4.625984251968504 in
length 5 = 4.625984251968504 in
length 6 = 2.7559055118110236 in

Hottel's correlation formula:

[[0.      0.      0.03858 0.17729 0.56826 0.21587]
 [0.      0.      0.21587 0.56826 0.17729 0.03858]
 [0.06476 0.36235 0.      0.36235 0.06476 0.14577]
 [0.17729 0.56826 0.21587 0.      0.      0.03858]
 [0.56826 0.17729 0.03858 0.      0.      0.21587]
 [0.36235 0.06476 0.14577 0.06476 0.36235 0.      ]]
```

5.3 Python semi-analytical model

```

H = 4.95          # Height of the cask [m]
R_int = 0.74      # Cask inner radius [m]
R_cask = 1.15     # Cask outer radius [m]

P_tot = 39000     # Total decay heat [W]
P_1 = (4/19)*P_tot # Relative distribution of power [W] between the 5 zones:
P_2 = (4/19)*P_tot # Zone 1 is the most external one, Zone 5 is the central one
P_3 = (4/19)*P_tot
P_4 = (3/19)*P_tot
P_5 = (4/19)*P_tot

em_int = 0.8      # Cladding emissivity
em_cask_o = 0.93  # Emissivity of the external side of the cask body
em_cask_i = 0.25  # Emissivity of the internal side of the cask body
em_room = 1.0     # Emissivity of the environment
sigma = 5.67E-8   # Stefan-Boltzmann constant [W/(m^2.K^4)]

```

```

def lbda_PE(T):
    """ Definition of the thermal conductivity of PE [W/(m.K)] """
    XXXXXXXXXXXXX
    return lbda_PE

lbda_GGG = 36     # Thermal conductivity of graphite iron [W/(m.K)]

def lbda_cask(T):
    """ Thermal conductivity of the homogenized cask body,
    depending on the temperature [W/(m.K)] """
    # Zones 100% iron
    R_GGG = np.log((80.1/74)*(95.3/88.1)*(115/103.3)) / (2*np.pi*lbda_GGG)

    # Zones PE + iron (in parallel)
    R_PE = np.log((88.1/80.1)*(103.3/95.3)) / (2*np.pi*(0.25*lbda_GGG + 0.75*lbda_PE(T)))

    # Total resistance
    R_tot = R_GGG + R_PE

    # Corresponding homogenized thermal conductivity
    lbda = np.log(115/74) / (2*np.pi*R_tot)

    return lbda

#####

S_FA = 19*24*24          # [cm^2]
S_He = np.pi*(R_int**2)*1E4 - S_FA # [cm^2]

def lbda_int(T):
    """ Calculation - interpolation - of the thermal conductivity for the homogenized
    internal cask zones, depending on the temperature [W/(m.K)] """
    XXXXXXXXXXXXX
    return lbda_int

```

```

R_1 = R_int          # Definition of the radii of the different zones [m]
R_2 = (0.8**0.5)*R_int
R_3 = (0.6**0.5)*R_int
R_4 = (0.4**0.5)*R_int
R_5 = (0.2**0.5)*R_int

```

```
##### Thermal resistances of the different zones
### Thermal resistances are written with W (for "Widerstand" in German)
### to distinguish them from radii R

def W_caskext(T):
    """ Calculation of the thermal resistance [K/W] from the cask body to the environment,
        depending on the cask body temperature """

    W = np.log((2*R_cask)/(R_1+R_cask))/(2*np.pi*H*lbda_cask(T)) # Material resistance
    W_par = 2.60E-3 # Parietal resistance
    W += W_par
    return W

def W_1cask(T_1, T_cask):
    """ Resistance [K/W] from zone 1 centre to cask body centre,
        depending on the cask body temperature and on T_1 """

    W = np.log((2*R_1)/(R_1+R_2))/(2*np.pi*H*lbda_int(T_1)) # R_th in zone 1
    W += np.log((R_1 + R_cask)/(2*R_1))/(2*np.pi*H*lbda_cask(T_cask)) # R_th in cask body
    return W

def W_21(T):
    """ Resistance from zone 2 centre to zone 1 centre [K/W] """
    return np.log((R_1+R_2)/(R_2+R_3))/(2*np.pi*H*lbda_int(T))

def W_32(T):
    return np.log((R_2+R_3)/(R_3+R_4))/(2*np.pi*H*lbda_int(T))

def W_43(T):
    return np.log((R_3+R_4)/(R_4+R_5))/(2*np.pi*H*lbda_int(T))

def W_54(T):
    return np.log((R_4+R_5)/(R_5))/(2*np.pi*H*lbda_int(T))
```

```
##### Heat capacity of the cask body

c_PE = 2150 # [J/(kg.K)]
m_PE = 2514 # [kg]
m_GGG = 85906 # [kg]

def C_cask(T):
    """ Calculation - interpolation - of the cask body heat capacity [J/K],
        depending on the cask body temperature """
    XXXXXXXXXXXXXXXXXXXX
    return C_cask

##### Volumes of the different materials in the cask cavity

h = 400 # Fuel height [cm]
r_fuel = 0.403 # Fuel pellet radius [cm]
r_clad_o = 0.475 # Outer cladding radius [cm]
r_clad_i = 0.411 # Inner cladding radius [cm]
r_gt_o = 0.616 # Outer cladding radius [cm]
r_gt_i = 0.555 # Inner cladding radius [cm]

V_1clad = h*np.pi*(r_clad_o**2-r_clad_i**2) # Volume of a single rod cladding [cm^3]
V_1gt = h*np.pi*(r_gt_o**2-r_gt_i**2) # Volume of a single guide tube [cm^3]

V_clad = 19*((18*18-24)*V_1clad + 24*V_1gt)*10**(-6) # Volume of the whole cladding
material in the loaded cask [m^3]
```

5.3 Python semi-analytical model

```
V_alum = h*6*(9+10+10+10+11.75+4+11.75+8.25+10+11.75+10+10+10+9)*10**(-6) # Al vol. [m^3]
V_steel = h*(12*72.5 + 7*98 + 8 + 8 + 28)*10**(-6) # Steel volume [m^3]
V_fuel = 19*(18*18-24)*h*np.pi*(r_fuel**2)*10**(-6) # Total fuel volume [m^3]
V_He = h*(np.pi*R_int**2)*10**(-2) - V_clad - V_alum - V_steel - V_fuel # He volume [m^3]

##### Heat capacities of the different elements in the cask cavity

Ro_clad = XXXX # [kg/m^3]
C_clad = XXXX # [J/kg.K]

Ro_alum = XXXX # [kg/m^3]
C_alum = XXXX # [J/kg.K]

Ro_steel = XXXX # [kg/m^3]
C_steel = XXXX # [J/kg.K]

Ro_fuel = XXXX # [kg/m^3]
C_fuel = XXXX # [J/kg.K]

Ro_He = XXXX # [kg/m^3]
C_He = XXXX # [J/kg.K]

# Total thermal capacity of the internal part of the cask [J/K]
C_int = V_clad*Ro_clad*C_clad + V_alum*Ro_alum*C_alum \
        + V_steel*Ro_steel*C_steel + V_He*Ro_He*C_He \
        + V_fuel*Ro_fuel*C_fuel

# Capacity of each of the 5 internal zones [J/K]
C_i = C_int/5
```

```
def T_room_tab(T_list, t, dt):
    """ T_room_tab(T_list, t, dt) creates a list of room temperature according to
        - a time step: dt,
        - a total duration t, and
        - a list of room temperature changes: T_list=[(t_0, Temp_0), (t_1, Temp_1),
            (t_2, Temp_2), ...] """

    current_time = 0 # Time counter
    T_tab = [] # Initialization of the T_room table
    list_len = len(T_list) # Number of given temperature changes
    index = 0 # Index i of (t_i, Temp_i) tuple in T_list,
    # valable at the current_time

    while current_time <= t: # We fill the T_tab as long as time t is not reached.
        if index == (list_len-1): # If the last tuple is reached,
            T_tab.append(T_list[index][1]) # we just keep adding the corresponding T_room,
            current_time += dt # until t is reached.
        else: # If there are still T_room changes later,
            while current_time < T_list[index+1][0]: # as long as the next isn't reached,
                T_tab.append(T_list[index][1]) # we add the current T_room to T_tab.
                current_time += dt
            index += 1 # When it is reached, then we change index
            # to consider the next tuple in T_list.

    return T_tab # Finally, we return the T_tab list completed.
```

```

def temp_eq(T_room, dt = 10, delta = 1E-6):
    """ temp_eq(T_room) calculates the equilibrium temperatures for the different zones
    of the cask, for a given room temperature T_room.
    There are two other optional parameters:
    - the time step dt for the calculation
    - the convergence criterion delta
    The values of these parameters have the following defaults values:
    dt = 10 s and delta = 10e-6 """

    # Initialisation (arbitrary) of the temperatures
    T_cask = 100
    T_1 = 240
    T_2 = 280
    T_3 = 320
    T_4 = 360
    T_5 = 400

    # Initialisation (arbitrary) of the heat fluxes
    Phi_out = 0.0
    Phi_1cask = 0.0
    Phi_21 = 0.0
    Phi_32 = 0.0
    Phi_43 = 0.0
    Phi_54 = 0.0

    var = delta**2+1 # Variable used for the convergence criterion,
                    # initially not matching the criterion
    while var > delta**2: # While the convergence criterion is not satisfied,
                          # we calculate the next step.

        # Calculation of the new flux values
        Phi_out = (T_cask - T_room)/W_caskext(T_cask) \
            + 2*np.pi*R_cask*H*sigma*(em_cask_o*((T_cask+273)**4) - em_room*((T_room+273)**4))

        Phi_1cask = (T_1 - T_cask)/W_1cask(T_1, T_cask) \
            + 2*np.pi*R_1*H*sigma*(em_int*((T_1+273)**4) - em_cask_i*((T_cask+273)**4))

        Phi_21 = (T_2 - T_1)/W_21((T_2+T_1)/2) \
            + 2*np.pi*R_2*H*em_int*sigma*(((T_2+273)**4)-((T_1+273)**4))

        Phi_32 = (T_3 - T_2)/W_32((T_3+T_2)/2) \
            + 2*np.pi*R_3*H*em_int*sigma*(((T_3+273)**4)-((T_2+273)**4))

        Phi_43 = (T_4 - T_3)/W_43((T_4+T_3)/2) \
            + 2*np.pi*R_4*H*em_int*sigma*(((T_4+273)**4)-((T_3+273)**4))

        Phi_54 = (T_5 - T_4)/W_54((T_5+T_4)/2) \
            + 2*np.pi*R_5*H*em_int*sigma*(((T_5+273)**4)-((T_4+273)**4))

        # Calculation of the new temperature values
        T_cask_n = T_cask + dt*(Phi_1cask - Phi_out)/C_cask(T_cask)
        T_1_n = T_1 + dt*(P_1 + Phi_21 - Phi_1cask)/C_i
        T_2_n = T_2 + dt*(P_2 + Phi_32 - Phi_21)/C_i
        T_3_n = T_3 + dt*(P_3 + Phi_43 - Phi_32)/C_i
        T_4_n = T_4 + dt*(P_4 + Phi_54 - Phi_43)/C_i
        T_5_n = T_5 + dt*(P_5 - Phi_54)/C_i

        # Calculation of the evolution between the two last time steps
        # (sum of the squared differences)
        # This value is compared to the convergence criterion delta to decide
        # whether to continue the calculation or not
        var = (T_cask_n - T_cask)**2 + (T_1_n - T_1)**2 + (T_2_n - T_2)**2\

```

5.3 Python semi-analytical model

```
+ (T_3_n - T_3)**2 + (T_4_n - T_4)**2 + (T_5_n - T_5)**2

T_cask = T_cask_n # Temperature values are updated
T_1 = T_1_n
T_2 = T_2_n
T_3 = T_3_n
T_4 = T_4_n
T_5 = T_5_n

# The function returns the list of the temperatures of the cask zones,
# rounded with one decimal
return [round(T_cask, 1), round(T_1, 1), round(T_2, 1), round(T_3, 1), round(T_4, 1),
        round(T_5, 1)]
```

```
def temp(T_init, T_room_list, t, dt, scale = "lin"):
    """ temp(T_init, T_room_list, t, dt) plots the temperature evolution over time for:
        - the 5 internal zones of the cask,
        - the cask body
        - the environment (room temperature)

    Parameters are:
        - T_init: list of 6 initial temperatures, [T_cask_init, T_1_init, ..., T_5_init]
        - T_room_list: list of T_room changes, [(t_0, Temp_0), (t_1, Temp_1), ...]
        - t: total duration for the calculation
        - dt: time step for the calculation
        - scale: linear (defaults) or logarithmic time scale

    CPU time: ~ 50 s for 10^6 time steps """

    n = round(t/dt) # number of time steps

    # Values for heat flux initialisation
    Phi_init = [0.0, 0.0, 0.0, 0.0, 0.0, 0.0]

    # Initialisation of the temperatures and time
    T_room = T_room_tab(T_room_list, t, dt) # Creation of the T_room list
    T_cask = [T_init[0]] # Other temperature lists are initialized with T_init values
    T_1 = [T_init[1]]
    T_2 = [T_init[2]]
    T_3 = [T_init[3]]
    T_4 = [T_init[4]]
    T_5 = [T_init[5]]
    t = [0] # Time list initialisation

    # Initialisation of the heat fluxes
    Phi_out = Phi_init[0]
    Phi_1cask = Phi_init[1]
    Phi_21 = Phi_init[2]
    Phi_32 = Phi_init[3]
    Phi_43 = Phi_init[4]
    Phi_54 = Phi_init[5]

    for i in list(range(n)): # Then we go through all the time steps

        # Flux are first calculated using current temperature values
        # read in the temperature lists.
        # The first term is thermal conduction, the following are
        # radiation exchange terms (Stefan-Boltzmann law).
        Phi_out = (T_cask[i] - T_room[i])/W_caskext(T_cask[i]) \
            + 2*np.pi*R_cask*H*sigma*(em_cask_o*((T_cask[i]+273)**4)\
            - em_room*((T_room[i]+273)**4))
```

```

Phi_1cask = (T_1[i] - T_cask[i])/W_1cask(T_1[i], T_cask[i]) \
+ 2*np.pi*R_1*H*sigma*(em_int*((T_1[i]+273)**4) - em_cask_i*((T_cask[i]+273)**4))

Phi_21 = (T_2[i] - T_1[i])/W_21((T_2[i]+T_1[i])/2) \
+ 2*np.pi*R_2*H*em_int*sigma*(((T_2[i]+273)**4)-((T_1[i]+273)**4))

Phi_32 = (T_3[i] - T_2[i])/W_32((T_3[i]+T_2[i])/2) \
+ 2*np.pi*R_3*H*em_int*sigma*(((T_3[i]+273)**4)-((T_2[i]+273)**4))

Phi_43 = (T_4[i] - T_3[i])/W_43((T_4[i]+T_3[i])/2) \
+ 2*np.pi*R_4*H*em_int*sigma*(((T_4[i]+273)**4)-((T_3[i]+273)**4))

Phi_54 = (T_5[i] - T_4[i])/W_54((T_5[i]+T_4[i])/2) \
+ 2*np.pi*R_5*H*em_int*sigma*(((T_5[i]+273)**4)-((T_4[i]+273)**4))

# Then, the new temperature value for each zone is calculated and
# added to the corresponding temperature list.
T_cask.append(T_cask[i] + dt*(Phi_1cask - Phi_out)/C_cask(T_cask[i]))
T_1.append(T_1[i] + dt*(P_1 + Phi_21 - Phi_1cask)/C_i)
T_2.append(T_2[i] + dt*(P_2 + Phi_32 - Phi_21)/C_i)
T_3.append(T_3[i] + dt*(P_3 + Phi_43 - Phi_32)/C_i)
T_4.append(T_4[i] + dt*(P_4 + Phi_54 - Phi_43)/C_i)
T_5.append(T_5[i] + dt*(P_5 - Phi_54)/C_i)

# And the time list is also updated.
t.append((i+1)*dt/3600)

if scale == "log": # Plot with logarithmic time scale
    fig, ax1 = plt.subplots(figsize=(8.5, 8))

    ax2 = ax1.twinx() # we will use 2 y-axes:

    # one for the temperature evolution of the cask zones
    ax1.semilogx(t, T_5, label="T_5")
    ax1.semilogx(t, T_4, label="T_4")
    ax1.semilogx(t, T_3, label="T_3")
    ax1.semilogx(t, T_2, label="T_2")
    ax1.semilogx(t, T_1, label="T_1")
    ax1.semilogx(t, T_cask, label="T_cask")
    ax1.tick_params(axis='y', colors='black')

    # one for the T_room temperature evolution
    ax2.semilogx(t, T_room, color='blue', linestyle='dashed', label="T_room")
    ax2.tick_params(axis='y', colors='blue')

else: # Plot with linear scale
    fig, ax1 = plt.subplots(figsize=(12, 8))

    ax2 = ax1.twinx()

    ax1.plot(t, T_5, label="T_5", color="red", linewidth=3.5)
    ax1.plot(t, T_4, label="T_4", color="blue", linewidth=3.5)
    ax1.plot(t, T_3, label="T_3", color="seagreen")
    ax1.plot(t, T_2, label="T_2", color="olivedrab")
    ax1.plot(t, T_1, label="T_1", color="darkgoldenrod")
    ax1.plot(t, T_cask, label="T_cask", color="brown")
    ax1.tick_params(axis='y', colors='black')

    ax2.plot(t, T_room, color='blue', linestyle='dashed', label="T_room")
    ax2.tick_params(axis='y', colors='blue')

```

5.3 Python semi-analytical model

```
leg1 = ax1.legend(loc='upper left')
leg2 = ax2.legend(loc='lower left')
leg1.get_frame().set_edgecolor('black')
leg2.get_frame().set_edgecolor('blue')

ax1.set_xlabel("Time [h]", fontsize=16)
ax2.set_ylabel("Room temperature \[°C]", color="blue", fontsize=16)
ax1.set_ylabel("Temperatures in the cask \[°C]", fontsize=16)
ax1.grid(True, linestyle='-.')
ax1.set_xlim([0,81])
ax1.set_ylim([40,400])

plt.show()
```

5.4 Python model, sensitivity analysis

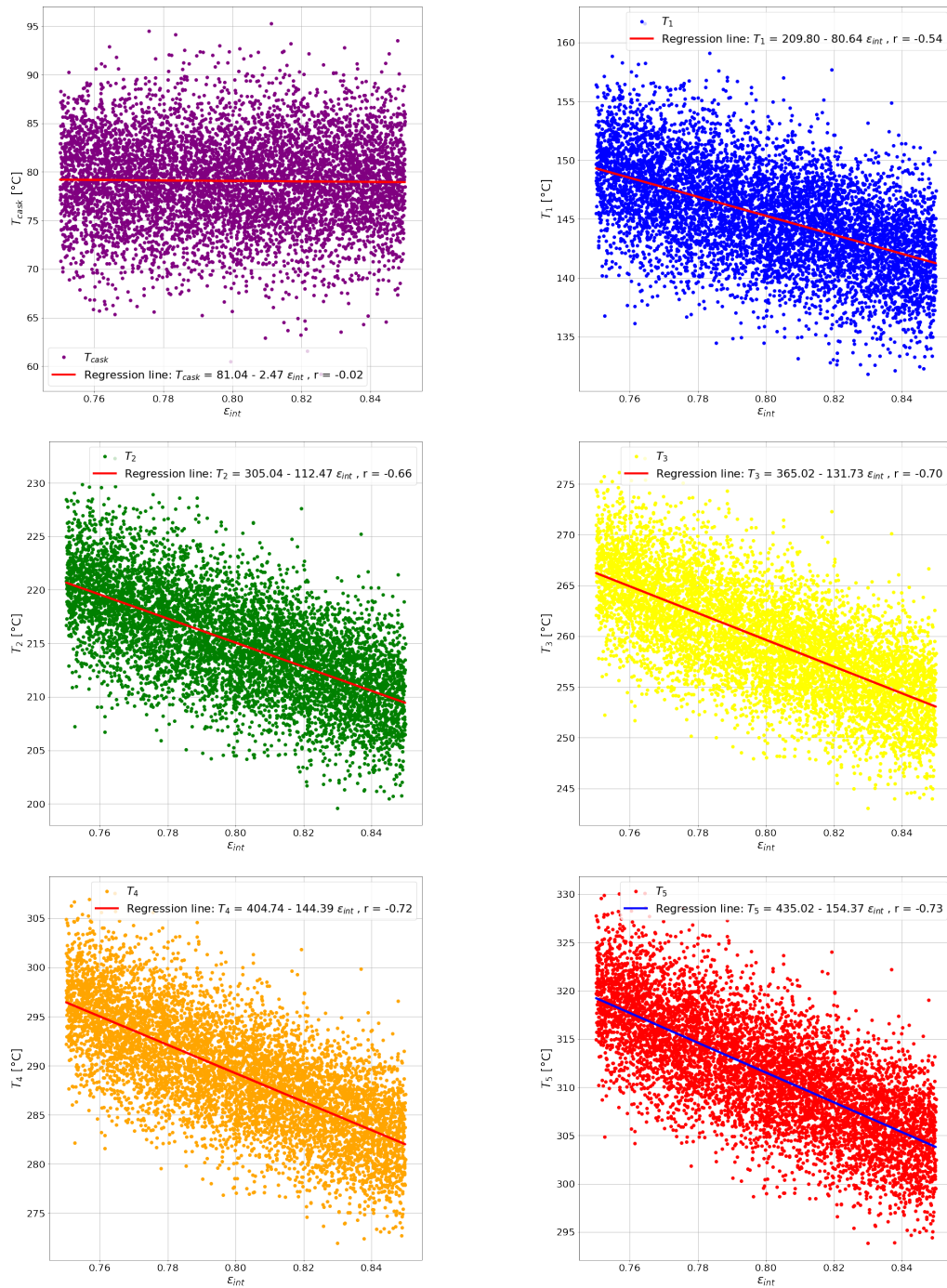


Figure 5.1: Correlation to ϵ_{int} .

5.4 Python model, sensitivity analysis

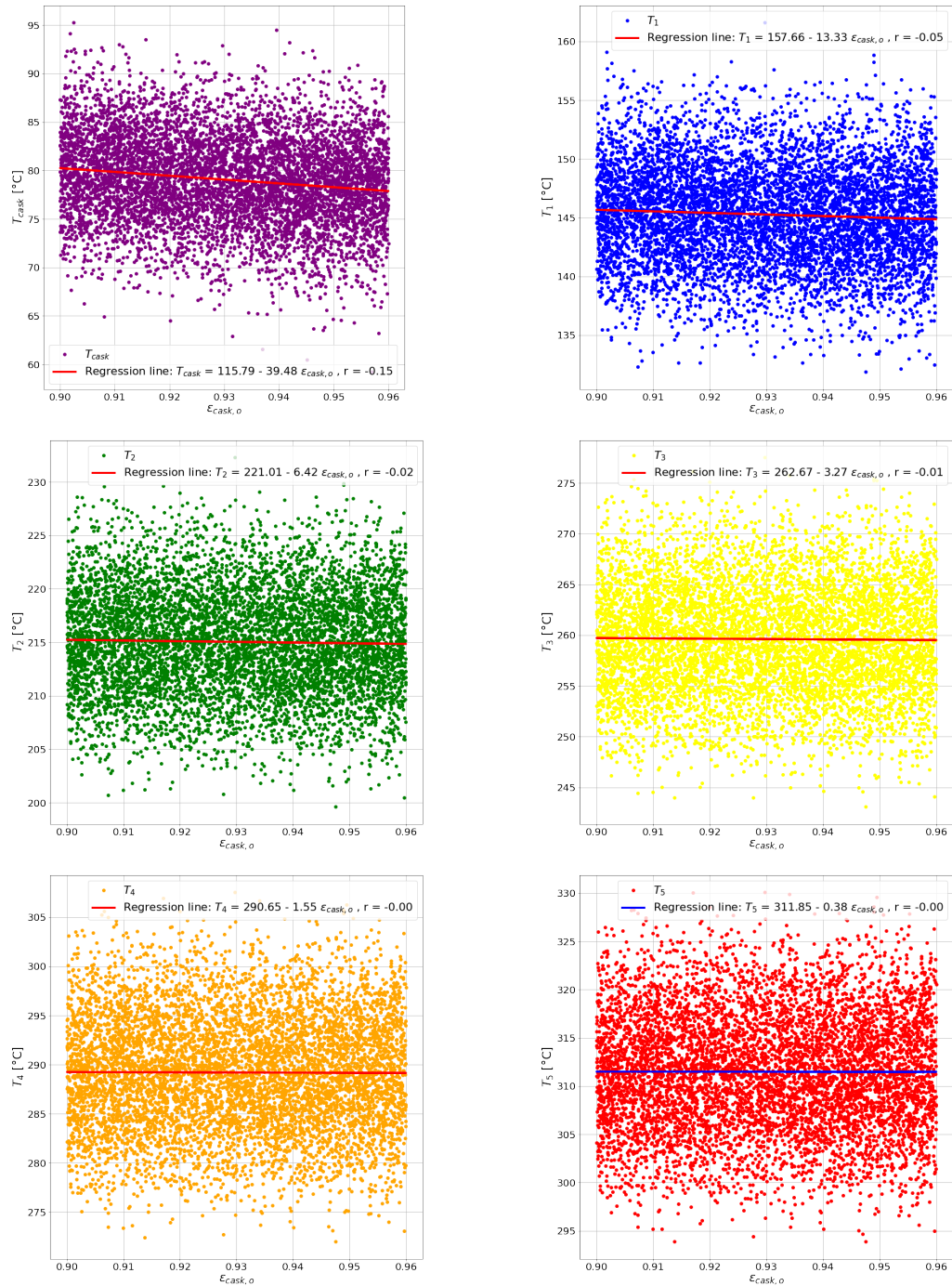


Figure 5.2: Correlation to $\epsilon_{cask,o}$.

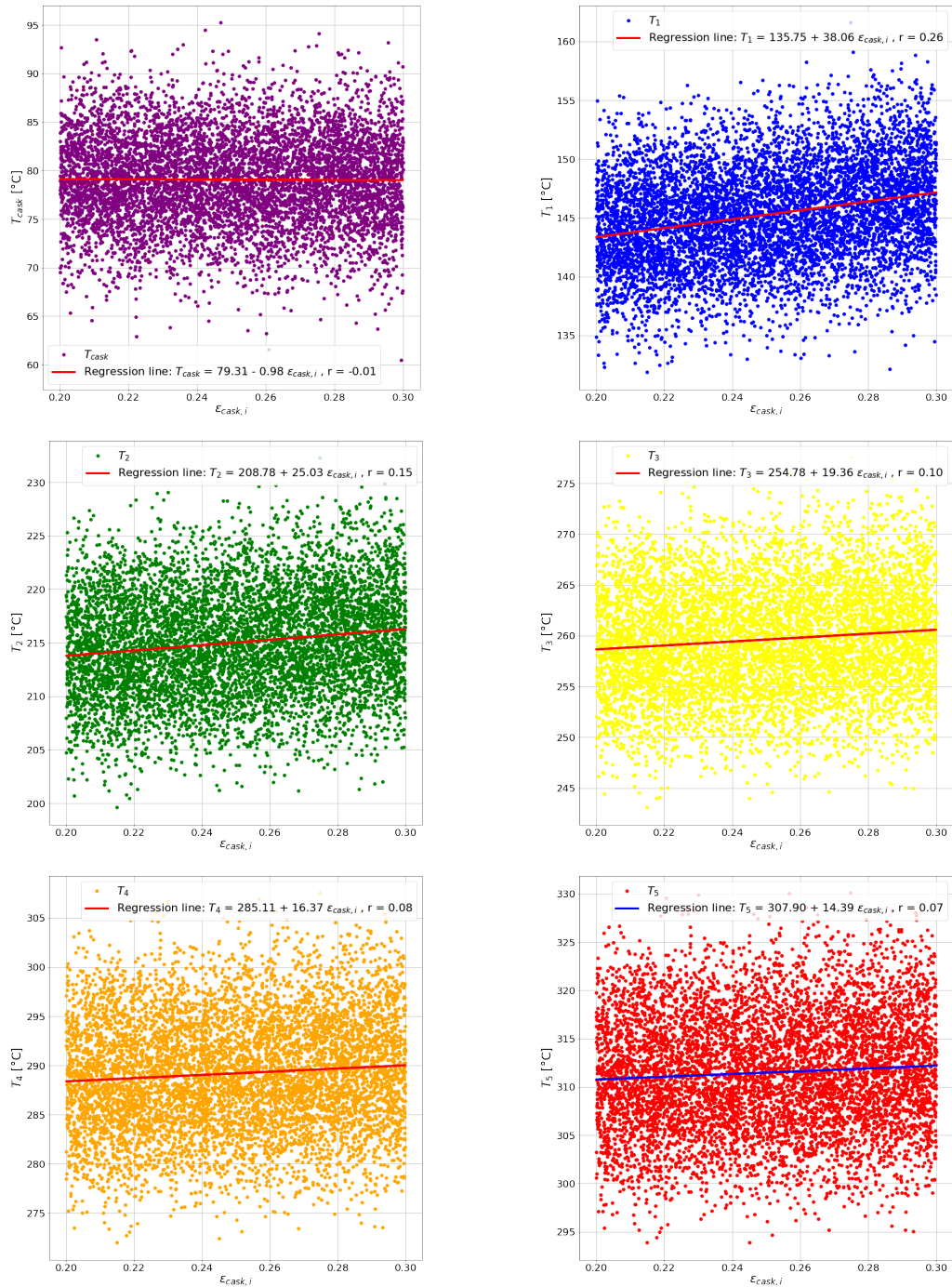


Figure 5.3: Correlation to $\epsilon_{cask,i}$.

5.4 Python model, sensitivity analysis

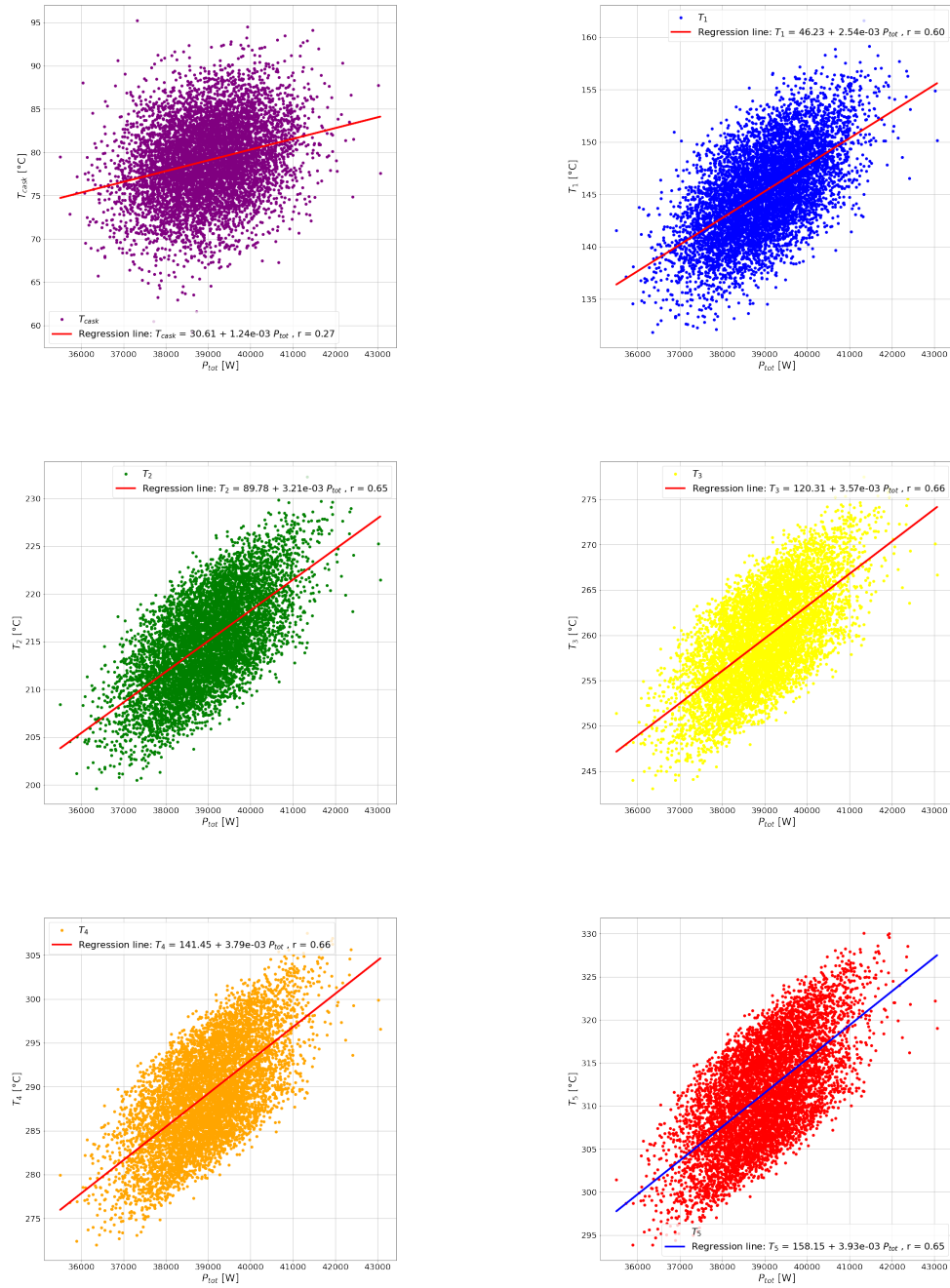


Figure 5.4: Correlation to P_{tot} .

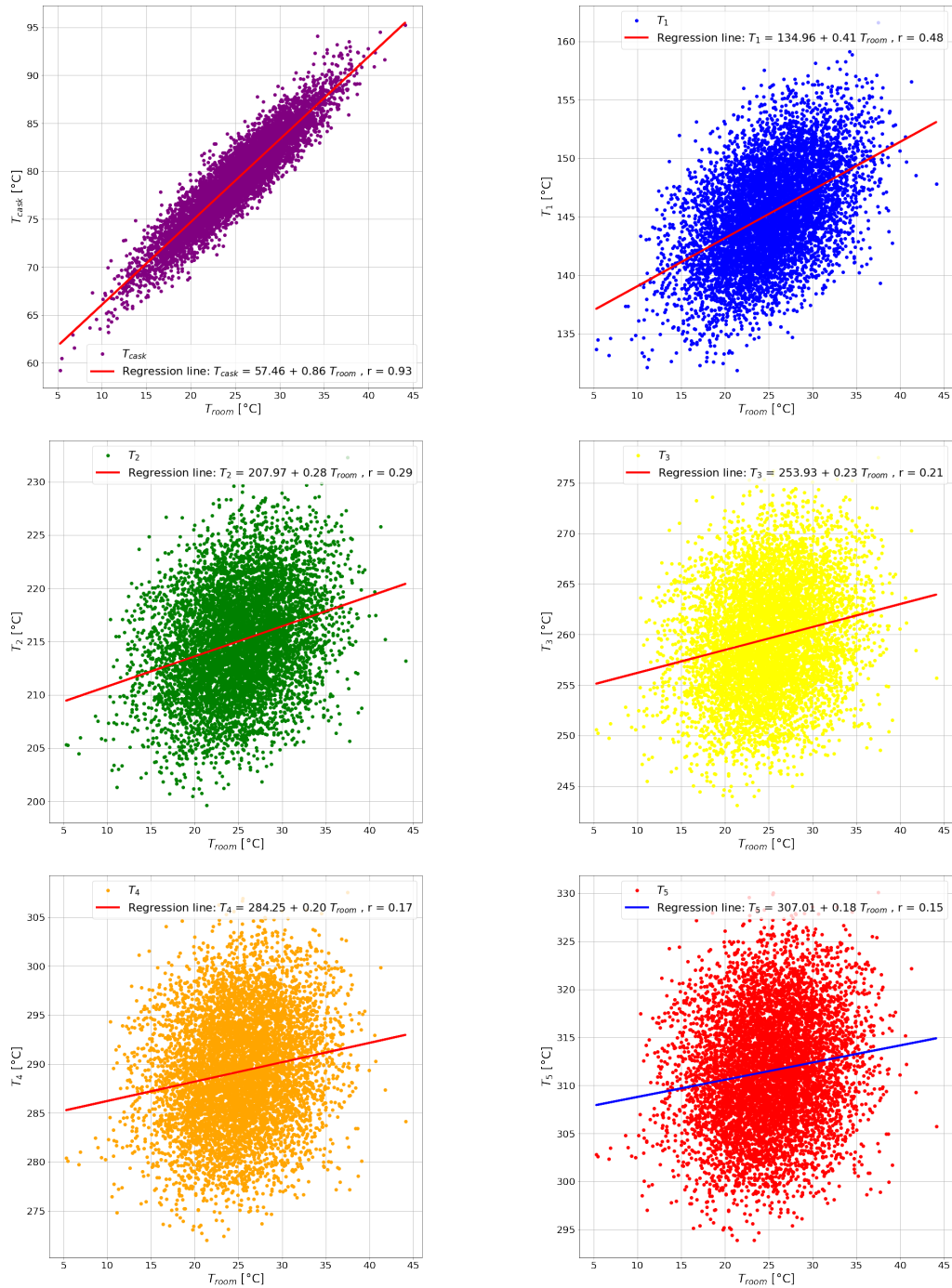


Figure 5.5: Correlation to T_{room} .

5.4 Python model, sensitivity analysis

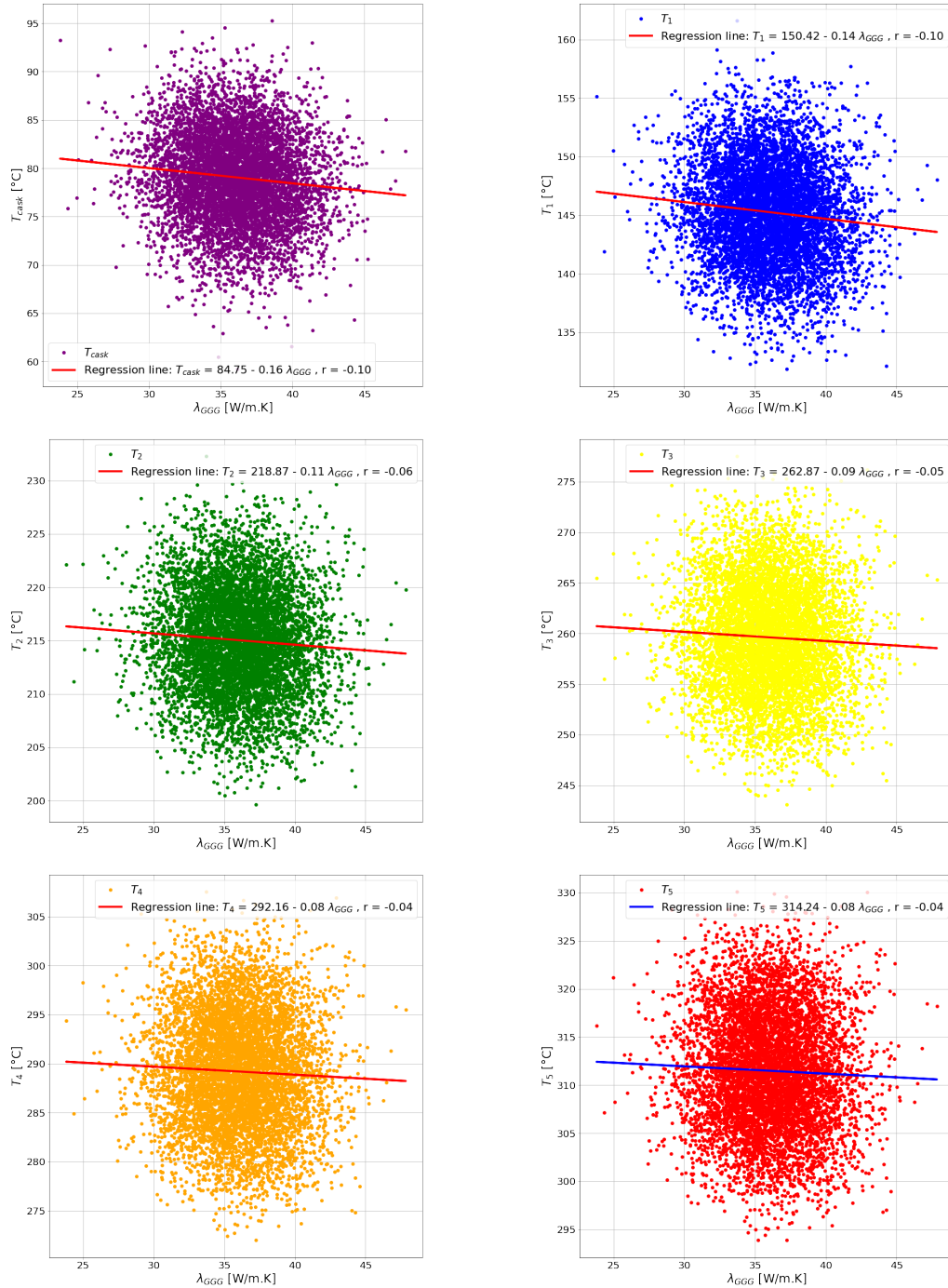


Figure 5.6: Correlation to λ_{GGG} .

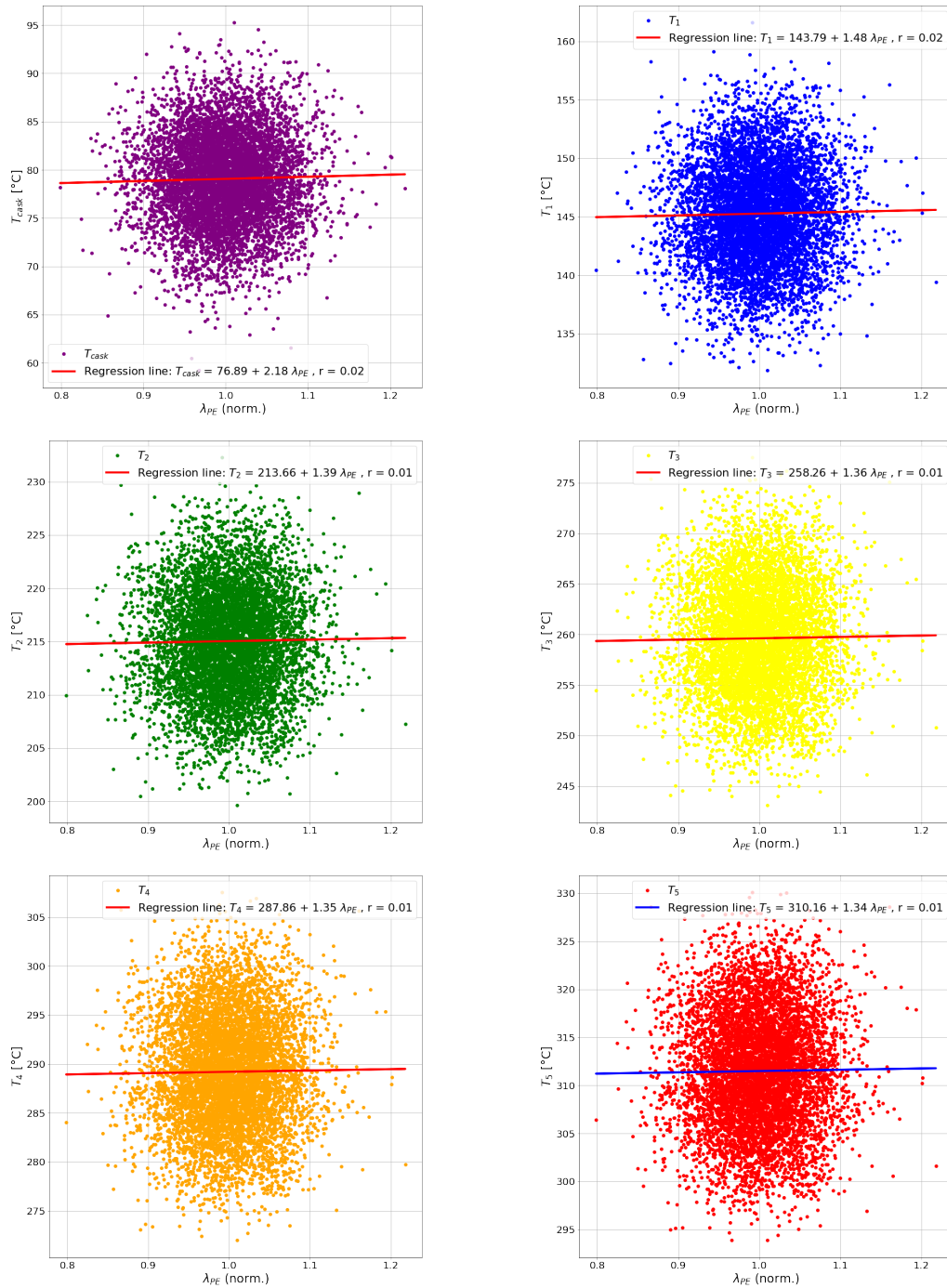


Figure 5.7: Correlation to λ_{PE} .

5.4 Python model, sensitivity analysis

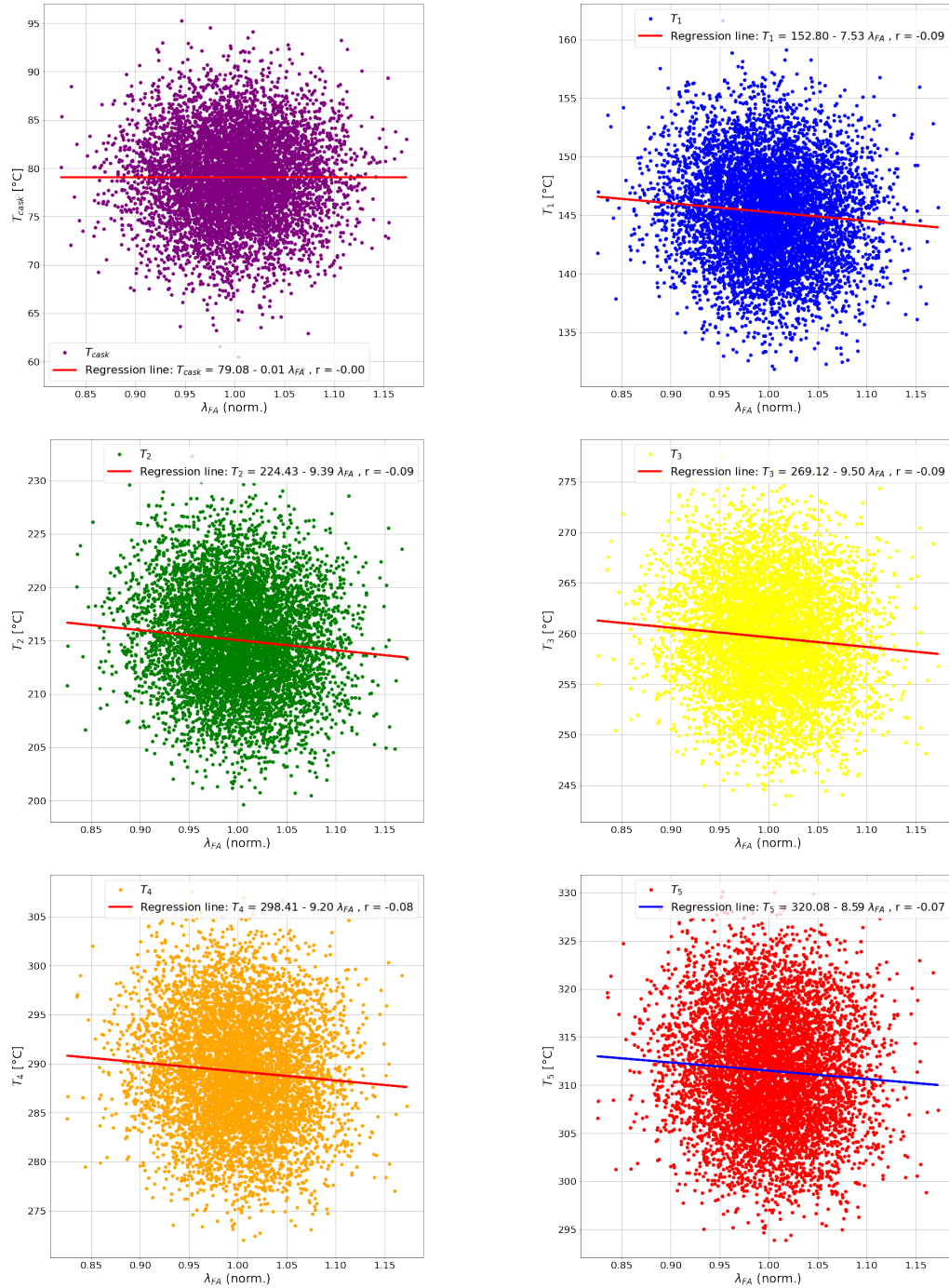


Figure 5.8: Correlation to λ_{BE} .

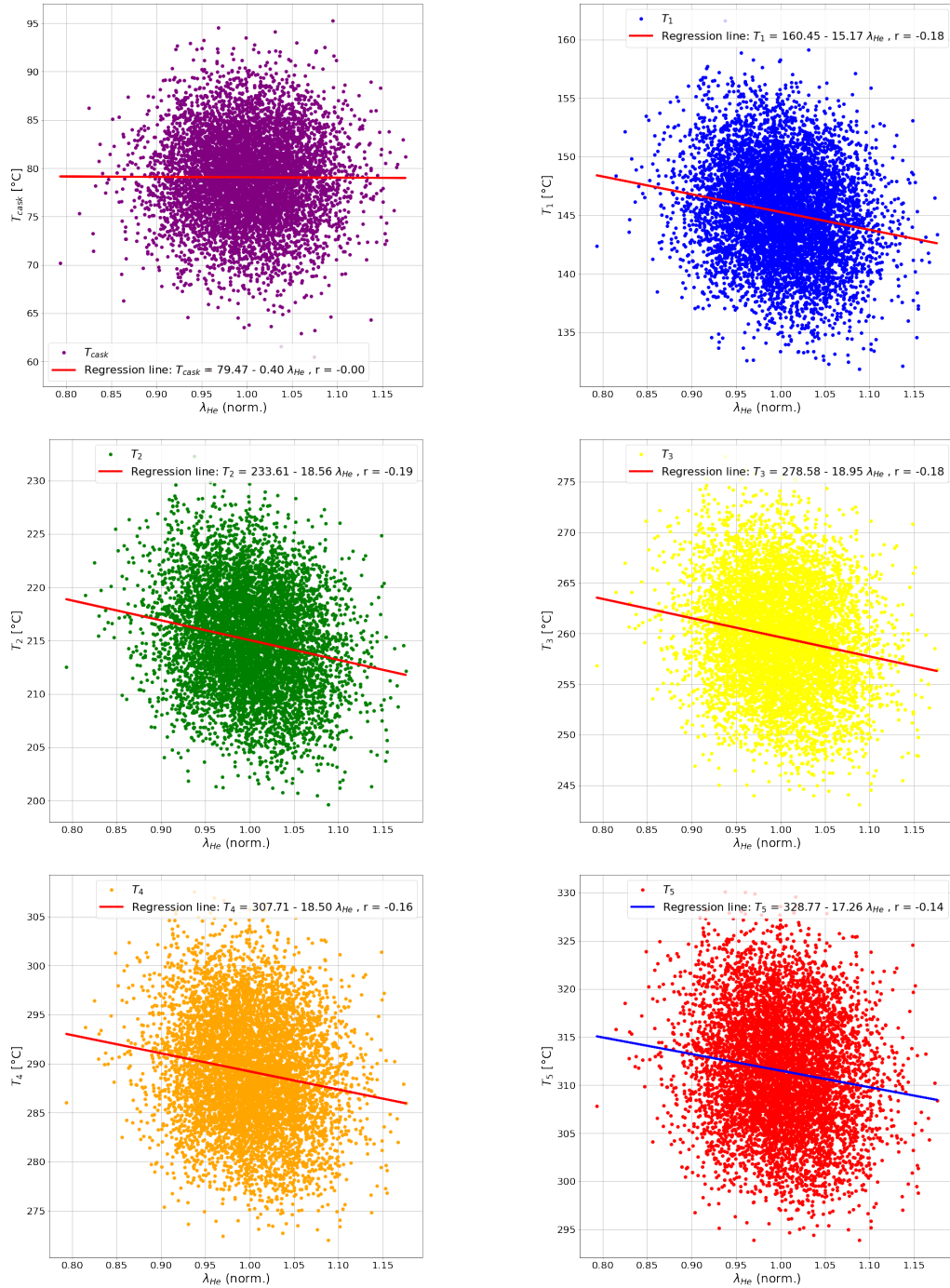


Figure 5.9: Correlation to λ_{He} .

5.4 Python model, sensitivity analysis

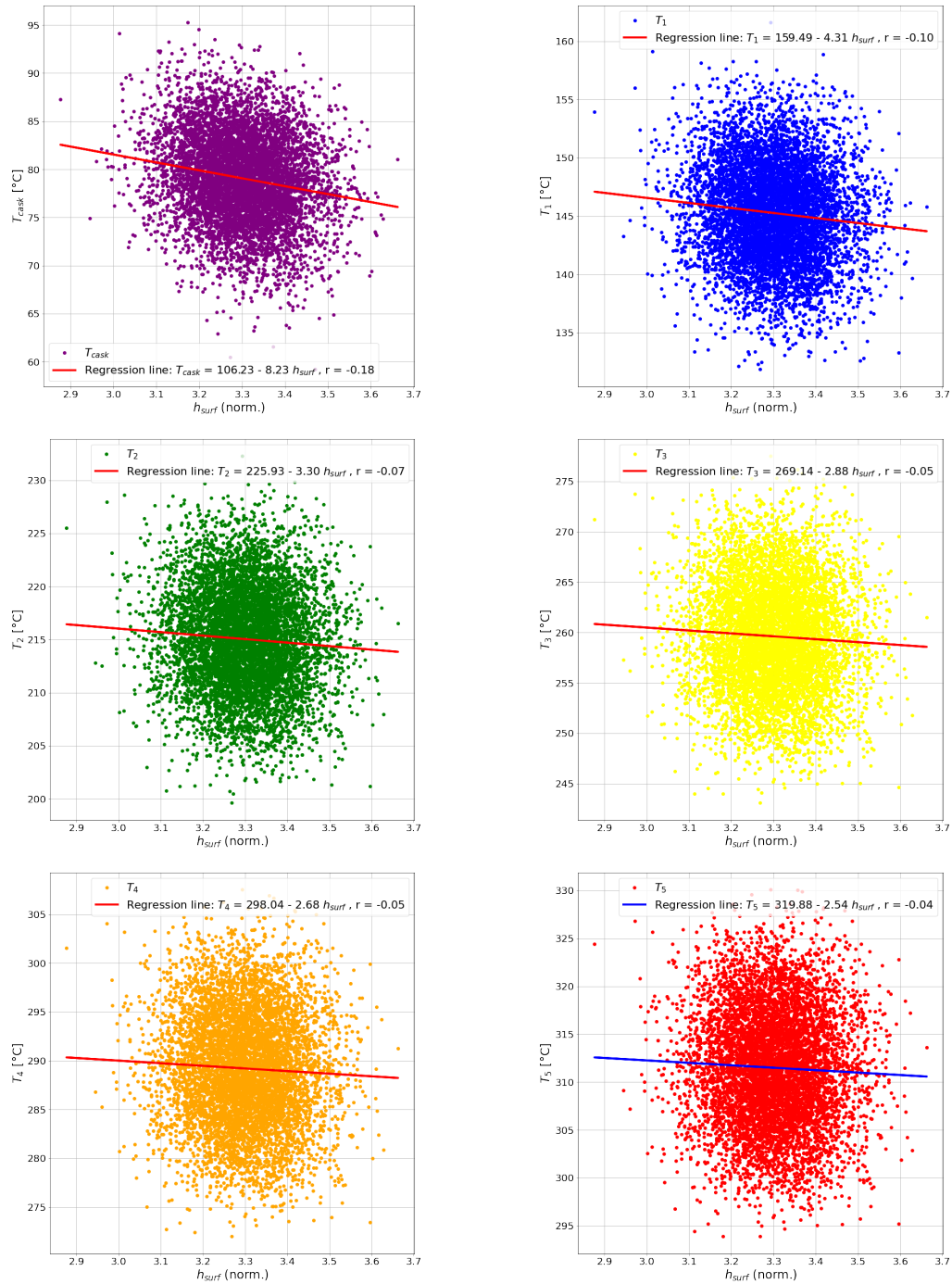


Figure 5.10: Correlation to h_{surf} .

5.5 Construction of a COBRA-SFS cask model

This section presents the different steps for building a new cask model with COBRA-SFS. Four stages may be distinguished:

1. A preliminary work to gather information on the cask to model: geometry, material properties, fuel type, operation conditions.
2. The drawing of a cask diagram on which the model will be based and the writing of the first input file. At this stage, no test with COBRA-SFS is possible: first, all input groups have to be written.
3. The debugging of the input file to obtain a file that can be entirely read by COBRA-SFS without stopping.
4. The model verification and validation: correct further errors once the code is running and yields results, and adjust parameters.

Preliminary work

The first phase can be straightforward or rather tricky, depending on the cask to model and the access to the corresponding information. Indeed, for most casks the detailed design data is proprietary and the publicly available data is limited. Thus, in the case of the CASTOR model, the data had to be taken from a limited number of sources [28, 29] and some approximations were necessary. In the case of the TN-32B model, this phase was much easier, as all the necessary data was publicly available and provided within the EPRI benchmark specifications [20].

Cask diagram and writing of the input file

The second phase is probably the most demanding (and burdensome) task, requiring at least a few weeks, if not months. First a cask diagram has to be drawn, which defines how the cask is divided into small elements (slab nodes, gas channels, fuel assemblies and rods). All these elements are identified with numbers (see Fig. 2.18 for the CASTOR model and Fig. 2.33 for the TN-32B

model), which are then used to write the input file. The definition of this diagram is important with many regards: a too high number of elements will increase unnecessarily the calculation time while a too reduced number of elements might lead to weak accuracy. Ideally, one should have an idea of the expected temperature distributions and gradients, or main heat paths, in order to define appropriate elements. Furthermore, the numbering of those elements is important: a “logical” numbering can make the following input file writing much easier and reduce the risk of errors. Indeed, most of the input groups (see Table 2.5 for the summary) have to be defined and manually written in the input file, which at the end usually represents some thousand lines (3116 for the CASTOR model and 2716 for the TN-32B model). COBRA-SFS input files are rigorously structured, with exacting format requirements: Each input group is divided in subgroups: for example, the group PROP consists of subgroups PROP.1, PROP.2, PROP.3, etc. The first subgroups of each group is used to define which further subgroups will be required for this input group. Afterwards, COBRA-SFS expects an exact number of lines according to the information given in the first subgroup. On each line, parameters have precise positions: for instance, indexes 1 to 5 are attributed to the first parameter, then the second parameter will have to be placed at indexes 6 to 15, the third parameter at indexes 16 to 25, and so on. A more detailed presentation of the main groups, based on input file extracts from the CASTOR model, is given in Appendix 5.6.

Debugging of the input file

Once all input groups have been written, the debugging phase can be started. This third phase can be achieved very quickly or within several days, depending on the experience of the user. By the first trial of running COBRA-SFS on a new input file, it is highly likely that the code will prematurely stop due to major errors¹ in the input file. An experienced user might then identify the errors more rapidly than a beginner, using the error messages returned by COBRA-SFS. Furthermore, the number of errors in-

¹*Major errors* means here that the input cannot be understood by COBRA-SFS, for example due to a missing subgroup, too many or too few lines in a given subgroup, or a parameter written out of its assigned indexes.

cluded in the input file is expected to decrease when the experience of the user increases.

When running the code with a file including major errors, the terminal returns an error message, which can usually help to identify the problem. Furthermore, even if COBRA-SFS cannot read the whole input file, it returns an output file, which is also useful to correct errors in the input. Indeed, this output file ends with a “Summary of input options” as shown in Fig. 5.11, which consists of the first subgroup of each input group (PROP.1, CHAN.1, RODS.1, etc.). This summary remains incomplete as long as one of the input group presents a major error. Thus, by looking at the last input group printed in this summary, the user can determine in which group the error is located. The errors that have been encountered in this work included:

- Inconsistencies between information in the first subgroup and information in the following subgroups: for instance, 3 correlations are announced in subgroup 1, but only 2 are defined in the following.
- Inconsistencies in the number of connections or neighbours announced and the number defined: 10 connections from node n to fluid channels are announced but then only 9 are defined, or 0 thermal connection from node n with other nodes is announced, yet two connections are then defined.
- A whole subgroup is forgotten: an option-parameter in subgroup 1 is given a value which leads to the necessary writing of an additional subgroup that would not be required for other values of the parameter in subgroup 1. Or, on the contrary, one parameter in subgroup 1 is changed so that a subgroup is not expected anymore by the code, but the user forgets to remove it from the input.
- A number is written (partially) out of its allocated indices: this can happen for instance if a space is inadvertently added or deleted, or if a subgroup admitting a maximum number of elements from a list receives more elements.

```

3614 summary of input options
3615 group n1 n2 n3 n4 n5 n6 n7 n8 n9 n10 n11 n12 n13 n14 n15
3616 prop 6 6 0 0 0 0 0 0 0 0 0 0 0 0 0
3617 chan 47 36 0 0 0 0 0 0 0 0 0 0 0 0 0
3618 rods 5 1 0 0 1 0 0 0 0 0 0 0 0 0 0
3619 slab 36 14 568 0 0 0 0 0 0 0 0 0 0 0 0
3620 radg 47 2 7 0 0 0 0 0 0 0 0 0 0 0 0
3621 heat 2 0 1 0 0 0 0 0 0 0 0 0 0 0 0
3622 drag 2 8 0 0 0 0 0 0 0 0 0 0 0 0 0
3623 bdry 12 1 36 2 0 0 0 0 0 0 0 0 0 0 0
3624 oper 1 0 3 0 0 0 0 0 0 0 0 0 0 0 1
3625 rest 47 0 0 0 0 0 0 0 0 0 0 0 0 0 0
3626 calc 1 0 0 1 0 0 0 0 0 0 0 0 0 0 0
3627 outp 11113 0 0 0 0 0 0 0 2 0 0 1 0 0 0
3628 endd 0 0 0 0 0 0 0 0 0 0 0 0 0 0 0

```

Figure 5.11: Summary of input options printed in the output file of COBRA-SFS. If the input file presents structural errors in any subgroups, the output file will end with this summary only partially printed. This provides an indication on the faulty group. If all groups can be read by COBRA-SFS, the summary includes the first line (subgroup 1) of each group and ends with “endd”.

Model verification and validation

Finally, when all major errors have been removed, COBRA-SFS can read the whole input file and yields an output file including first calculation results. The fourth phase starts at this point. It first consists in looking for further errors, which do not interrupt the COBRA-SFS calculations but can nonetheless induce significant errors in the results. An example of this step is presented in more detail in Appendix 5.7, based on the TN-32B model.

Afterwards, the validation can be performed: in the best case by comparison with experimental data (TN-32B model, see section 2.4.2.1), otherwise by comparison with other simulation works (CASTOR model, see section 2.3.3).

5.6 COBRA-SFS input groups - Writing of an input file

COBRA-SFS requires a rigorously structured input file, organised in groups and subgroups. This section goes through the input groups required for the CASTOR model. For a more detailed description of COBRA-SFS input files, the user is referred to the User's Manual [19], Chapter 6. In an attempt to make the description easier to read, numbers have been put in bold. These numbers correspond to COBRA-SFS inputs and can be found in the corresponding Listings.

5.6.1 Group PROP

Listing 5.1 shows the structure of input group PROP, which describes the fluid (helium) and solid material properties. In the first subgroup², PROP.1,

- the first 4 characters are dedicated to the name of the group “**prop**”,
- at indices 6-10, the user should indicate a number (**6** in Listing 5.1) corresponding to the *number of elements of the fluid properties table* (helium properties), i.e. the number of lines to be read in PROP.3, and
- at indices 11-15, the user should indicate the *number of solid materials* (also **6** in Listing 5.1) for which properties will be entered on PROP.4, i.e. the number of lines in PROP.4.

COBRA-SFS enables to define properties for two different fluids. In this case, the user has to set the *number of elements of the fluid properties table* to 0, which tells COBRA-SFS that two sets of fluid properties have to be defined. Then, COBRA-SFS will expect a subgroup PROP.2, whose only role is to define how many lines both fluid properties sets (in PROP.3) will have.

In the case of Listing 5.1, this *number of elements of the fluid properties table* is equal to **6** so that COBRA-SFS knows that there is only one fluid in the model. As a consequence, no subgroup PROP.2 is included in the input

²The name of the subgroups are usually set in comment, as it is otherwise difficult to recognize to which group/subgroup a part of the input file corresponds.

file but directly the subgroup PROP.3, which must have 6 lines.

As for subgroup PROP.1, the 6 lines of subgroup PROP.3 have a rigorous format: on each line, we should list the enthalpy, thermal conductivity, specific heat, specific volume and viscosity corresponding to a given temperature. Each of these quantities must be written in the right character index range (for instance, temperature is between 11 and 20). Most units used in COBRA-SFS are imperial units, thus almost all parameters in the input files have to be written with imperial units.

Finally, PROP.4 defines the solid material properties of 6 different materials. Those materials first receive ID numbers (**1** to **6**), which are used later in the input to assign materials to the different volume elements of the model. For instance, on the first line, **steel** gets the ID number **1** and the rest of the line defines its specific heat (**0.1194** Btu lbm⁻¹ °F⁻¹), density (**486.94** lbm ft⁻³) and thermal conductivity (in Btu h⁻¹ ft⁻¹ °F⁻¹) given by the coefficients of a polynomial expression (up to the third order).

3	prop	6	6						*prop.1
4		1.	0.	100.0	.0780	1.24	83.33	.1410	*prop.3
5		2.	200.	348.0	.0970	1.24	119.76	.1533	
6		3.	400.	596.0	.1150	1.24	156.25	.1641	
7		5.	600.	844.0	.1290	1.24	192.31	.1727	
8		10.	800.	1092.0	.1380	1.24	229.36	.1823	
9		15.	1000.	1340.0	.1380	1.24	265.25	.1907	
10	1steel	0.1194	486.94	4.6367	7.329E-03	-1.415E-06			*prop.4
11	2 alum	0.2140	168.56	121					
12	3GGG40	0.1194	443.24	1.592863	0.0563635	-5.099E-05	1.446E-08		
13	4G4+Md	0.3537	214.43	-2.468565	0.0374328	-4.208E-05	1.607E-08		
14	5G4+Md	0.3456	222.32	-2.328516	0.0380856	-4.238E-05	1.602E-08		
15	6PE Md	0.5135	58.370	-5.238807	0.0245205	-3.599E-05	1.717E-08		

Listing 5.1: Input group PROP.

5.6.2 Group CHAN

Following the group PROP, the group CHAN has to be written in the input to describe the helium channels. Listing 5.2 and 5.3 show the structure of this group. Subgroup CHAN.1 first indicates how many fuel assemblies are included in the model (**47**) and how many axial zones the model considers (**36**).

We should mention here that for COBRA-SFS an *assembly* consists in a group of channels, with or without fuel rods (we might therefore speak

of *rodded assemblies* and *unrodded assemblies* to make the distinction in the following). In practical terms, COBRA-SFS assemblies include on the one hand the usual fuel assemblies (including 19x19 helium channels for the CASTOR model), on the other hand the free spaces delimited by the basket structures and modelled as single (large) helium channels. These *assemblies* can be seen in Fig 2.18 where they are numbered in red. Assemblies 1 to 19 correspond to rodded fuel assemblies, while assemblies 20 to 47 are helium channels between basket structures³.

Subgroup CHAN.3 is then used to specify the length of the channel/fuel region: in this model, it was set to **173.5433** in (440.8 cm), which corresponds to the height of the fuel assemblies.

Subgroups CHAN.5, CHAN.6 and CHAN.7 are then used to describe the geometry of the channels within the assemblies. For this model, we described two types of rodded assemblies: one for the external fuel assemblies (such as FA 1) and one for the internal fuel assemblies (such as FA 6 or FA 10). The external fuel assemblies were defined with slightly larger helium channels on the side facing the curved cask body.

CHAN.5 indicates first the ID number of a fuel assembly, then the ID number of its configuration (type of assembly) and finally its number of channels. Thus, in Listing 5.3, the first line indicates that FA **19** corresponds to assembly type **1** (external fuel assemblies) and has **361** channels. Two lines below, FA **20** is described as being of type **3** (first type of *unrodded assembly*) and consists of only **1** channel.

CHAN.6 is used to assign a heat flux profile (defined later in group OPER), a heat transfer correlation (defined later in group HEAT) and a friction factor correlation (defined later in DRAG) to each assembly, using again in each case an ID number. CHAN.7 is one of the longest subgroups in COBRA-SFS: it is used when a new type of assembly has to be defined and lists all channels included in the assembly. In Listing 5.2, FA 1 is the first assembly of type 1 described in CHAN.5, thus type 1 has to be defined in CHAN.7. For the following assemblies of the same type (such as FA 19 in Listing 5.3), it is then sufficient to indicate in CHAN.5 that they are of type 1. The description of an assembly type includes for each channel of the assembly: its

³COBRA-SFS requires the rodded assemblies to be all numbered first and the unrodded assemblies to be numbered only afterwards.

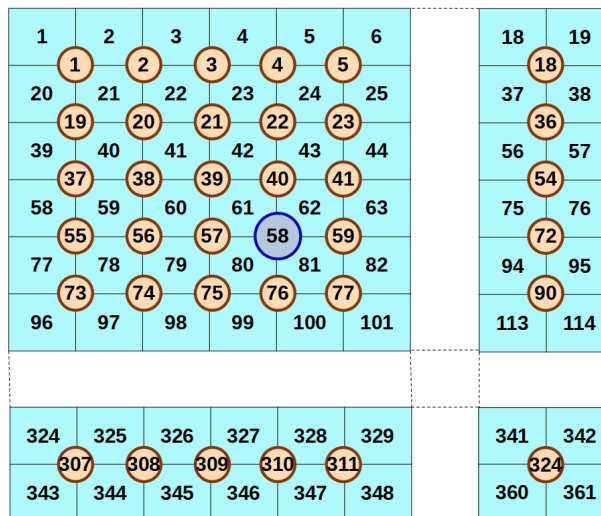


Figure 5.12: Numbering of the channels and rods (NB: number 58 corresponds to a guide tube) of a 18x18-24 fuel assembly. This numbering is used in groups CHAN and RODS to describe which channels and rods are neighbours and later in group SLAB to identify which channels are facing the solid nodes of the model.

later, together with an axial heat generation profile), and 4 neighbouring helium channels (see the numbering in Fig. 5.12) of ID numbers **1**, **2**, **20** and **21**. Each of the 4 neighbour channels is in contact with a quarter (factor **0.25**) of the rod. On line 900, rod **58** is actually a guide tube. This explains that it presents a larger diameter of **0.486** in and a heat generation factor set to **0.00**.

Once an assembly type has been defined, the following assemblies of the same type are easier to describe: for instance, on line 1167, assembly **2** of the model is simply defined as being of type **1** and having **324** rods. The definition of the unrodded assemblies is even simpler as there is no rod to describe. Thus, on lines 1509 to 1536, the 28 unrodded assemblies (ID numbers **20** to **47**) are simply listed with their ID numbers, **0** as assembly type (default ID for unrodded assemblies) and **0** as number of rods.

Finally, subgroup RODS.4 (line 1537) is used to define fuel rod properties (fuel thermal conductivity, fuel specific heat, fuel density, pellet diameter, cladding thermal conductivity, cladding specific heat, cladding density, cladding thickness, gap resistance).

5.6 COBRA-SFS input groups - Writing of an input file

```

841 rods      5      1      0      0      1                                *rods.1
842      1      1    324                                *rods.2
843      1  .374  1.00      1 0.25      2 0.25      20 0.25      21 0.25
844      2  .374  1.00      2 0.25      3 0.25      21 0.25      22 0.25

899      57  .374  1.00      60 0.25      61 0.25      79 0.25      80 0.25
900      58  .486  0.00      61 0.25      62 0.25      80 0.25      81 0.25
901      59  .374  1.00      62 0.25      63 0.25      81 0.25      82 0.25

1165     323  .374  1.00      340 0.25      341 0.25      359 0.25      360 0.25
1166     324  .374  1.00      341 0.25      342 0.25      360 0.25      361 0.25
1167      2      1    324                                *rods.2 FA 2
1168      3      1    324                                *rods.2 FA 3
1169      4      1    324                                *rods.2 FA 4

1502     13      2    324                                *rods.2 FA 13
1503     14      2    324                                *rods.2 FA 14
1504     15      1    324                                *rods.2 FA 15
1505     16      1    324                                *rods.2 FA 16
1506     17      1    324                                *rods.2 FA 17
1507     18      1    324                                *rods.2 FA 18
1508     19      1    324                                *rods.2 FA 19
1509     20      0      0                                *rods.2 FA 20
1510     21      0      0                                *rods.2 FA 21

1534     45      0      0                                *rods.2 FA 45
1535     46      0      0                                *rods.2 FA 46
1536     47      0      0                                *rods.2 FA 47
1537      3.0  .059 647.0.324  10.  0.1 409..02441000.  .374      *rods.4

```

Listing 5.4: Input group RODS.

5.6.4 Group SLAB

The next input group is SLAB (Listing 5.5) and is the most important in terms of line number (1276 for the CASTOR model) and complexity. First, in subgroup SLAB.1, the number of solid-to-solid (**36**) and solid-to-fluid (**14**) connections to be defined respectively in subgroups SLAB.2 and SLAB.5 is indicated, as well as the total number of solid nodes (**568**) of the model. Then the solid-to-solid connections are described (subgroups SLAB.2 and SLAB.3) and afterwards the solid-to-fluid connections (subgroups SLAB.5 to SLAB.7).

```

1538 slab      36      14    568                                *slab.1
1539      1      5.875      5.875      0.00 0.00 0.00 0.00      *slab.2 (1-2)
1540      2      0.056      0.056      182.1 0.48 0.18 3.54      *slab.2 (1-215)
1541      3      5.875      0.5      0.00 0.00 0.00 0.00      *slab.2 (2-3)

```

1562	24	0.063	0.381					409.7	0.18	0.25	3.15					*slab.2 (199-345)
1563	25					236.6		0.00	0.00	0.00	0.00					*slab.2 (317-318)
1564	26					131.5		0.00	0.00	0.00	0.00					*slab.2 (317-353)
1565	27					19489.5		0.00	0.00	0.00	0.00					*slab.2 (353-354)
1574	36					8.7		0.00	0.00	0.00	0.00					*slab.2 (497-533)
1575	1	11.821	0.0	1	3	2	1	215	2	347	9					*slab.3 FA 1
1576	2	11.821	0.0	1	2	3	3	216	4							*slab.3
1577	3	10.155	0.0	1	2	4	3	211	6							*slab.3
2105	531	36.278	0.0	1	2	532	35	567	36							*slab.3
2106	532	36.278	0.0	1	1	568	36									*slab.3
2107	533	30.000	0.0	1												*slab.3
2108	534	30.000	0.0	1												*slab.3
2142	568	30.000	0.0	1												*slab.3
2143	1.5356		0.3675													*slab.5 basket->chan1
2144	2.3929		0.501													*slab.5 basket->chan2
2145	3.7858		0.2505													*slab.5 basket->chan10
2156	144.774		0.2515													*slab.5 cask->chan 172
2157	1	10	1	1	1	1	2	2	1	3	2	1	4	2		*slab.6 FA1
2158			1	5	2	1	6	2	1	7	2	1	8	2		*slab.7
2159			1	9	2	1	10	3								*slab.7
2160	2	10	1	10	3	1	11	2	1	12	2	1	13	2		*slab.6
2161			1	14	2	1	15	2	1	16	2	1	17	2		*slab.7
2162			1	18	2	1	19	1								*slab.7
2163	3	0														*slab.6
2810	352	10	3	343	12	3	324	13	3	305	13	3	286	13		*slab.6
2811			3	267	13	3	248	13	3	229	13	3	210	13		*slab.7
2812			3	191	13	3	172	14								*slab.7
2813	0															

Listing 5.5: Input group SLAB.

5.6.4.1 Solid-to-solid connections

In subgroup SLAB.2, all solid-to-solid connections necessary in the model have to be defined. For instance, on line 1540, connection type **2** is described by a *geometry factor* F_G (ratio length/width of the heat path, equal to **0.056** here) for each of the two solid nodes, a thermal resistance (**182.1** sft °F Btu⁻¹) for the gap between the two nodes as they are not perfectly connected⁵, the emissivities of both nodes (**0.48** and **0.18**) and the length of node (**3.54** in) facing the gap.

⁵Even very thin gaps can have a strong impact on the thermal behaviour, inducing an additional thermal resistance. We can consider as perfectly connected two nodes belonging to a common structure. Two nodes welded could also be expected to be efficiently thermally connected. Bolted structures might induce some gaps and therefore gap resistances might be defined. For two elements not fixed together, the definition of a gap resistance appears necessary.

Once the solid-to-solid connections have been defined, all nodes are listed in subgroup SLAB.3 and the connection types are used to describe the connections between the nodes. Thus, on line 1575 of Listing 5.5, node **1** is first assigned material type **1** (defined in group PROP as steel), then its area (**1.821** in, important for axial conduction) is defined, a volumetric heat generation rate (**0.0** Btu h⁻¹ ft⁻³), an ID number for a heat generation profile (**1** here, but not relevant as no heat is generated in the node) and the number (**3**) of connected nodes⁶: node **2** (connection type **1**), node **215** (connection type **2**) and node **347** (connection type **9**). At any moment, it is possible to define a new connection type in SLAB.2 (one additional line) if it appears that one type had been initially overlooked, but then one should not forget to increase the number of connections announced in SLAB.1 (**36**).

Geometry factors

The geometry factors are defined as $F_G = W/L$, with W the distance from the node centre to the edge facing the adjacent node and L_{node} the length of the node at the face in contact with the adjacent node. They are used by COBRA-SFS in combination with the thermal conductivities of the nodes (defined in SLAB.3) to calculate the corresponding thermal resistance: $R_{th} = F_{G,1}/\lambda_1 + F_{G,2}/\lambda_2 (+R_{gap})$, where the indices 1 and 2 refer to the two nodes involved in the connection and R_{gap} to a potential gap resistance. Geometry factors offer the main advantage that the resulting thermal resistances use the thermal conductivities defined in group PROP, which can be defined as temperature-dependent. Furthermore, in case of changes in the material properties defined in group PROP, the thermal resistances are automatically changed in group SLAB. However, it is possible to directly define a thermal resistance (common for both nodes of the connection), as for instance on line 1563 of Listing 5.5, where connection type **25** consists in a thermal resistance of **236.6** s ft °F Btu⁻¹. This might be useful in particular cases, such as nodes corresponding to homogenized material. Indeed, one can define only one material type (i.e. one set of ma-

⁶A connection between two nodes needs to be defined only once and is therefore only described in the input line of the node presenting the lowest ID number.

terial properties) per node so that it is not possible to distinguish a radial thermal conductivity and an azimuthal thermal conductivity. In order to take into account the different conductivities according to the direction, one can define thermal resistances instead of geometry factors. We should note that for the axial heat transfers, COBRA-SFS determines the thermal resistances using the axial length of the nodes, the area of the nodes and the thermal conductivities defined in group PROP. There is no means to define directly a thermal resistance and it is therefore important to define in PROP the type of homogenization (in parallel or in series) corresponding to the axial direction. In this case, it might be useful to define thermal resistances instead of geometry factors for the radial and azimuthal thermal connections.

5.6.4.2 Solid-to-fluid connections

After the description of the solid-to-solid connections, solid-to-fluid connections are defined in SLAB.5. Thus, on line 2143 of Listing 5.5, connection type **1** is defined by a geometry factor (**0.5356**) for the solid node involved in the connection and by the length of node facing the channel (**0.3675** in). In comment at the end of the line, one can see that this first connection corresponds to the connection of a basket structure node with the channel 1 (corner channel). A second connection type (ID number **2**) had to be defined (line 2144) for the connection between the basket structure and channel 2 as the length of node seeing channel 1 is smaller than the length of node seeing channel 2. Similarly to the solid-to-solid connections, it is possible to define a thermal resistance instead of the geometrical factor.

Using the connections defined in SLAB.5, all solid nodes with connections to channels are listed and their connections are described in SLAB.6 and SLAB.7. These descriptions include the number of channels connected to the node and for each connection the FA number, the channel number and the connection type number.

For instance, on lines 2810 to 2812, node **352** has **10** connections with channels: channel **343** from FA **3** is connected by connection type **12**, channels **324**, **305**, **286**, **267**, **248**, **229**, **210** and **191** from FA **3** are connected by

connection type **13** and channel **172** from FA **3** is connected by connection type **14**.

Finally, after all nodes with connections have been listed, a **0** is entered (line 2813) to indicate the end of this input group.

Definition of the nodalization

As mentioned in section 5.5, the definition of the cask diagram is very important, as the model relies on this diagram. Too many nodes increases the calculation time and the risk of errors in the definition of the thermal connections, but a too reduced number of nodes might lead to a weak accuracy. The above description of the SLAB group gives a further insight into the importance of the definition of the nodalization. Both the geometry of the nodes and their numbering should be defined carefully.

Indeed, as the thermal resistances are simply based on the ratio length/width of the nodes, we should try to define nodes which make this definition appropriate for the description of the conductive heat transfers. For instance, bent nodes should be avoided, as well as adjacent nodes of different widths (width meaning here the dimension perpendicular to the heat flux direction).

Finally, the numbering of the nodes is important, as it constitutes the basis for the whole description of the connections in subgroups SLAB.3, SLAB.6 and SLAB.7. A logical numbering significantly facilitates the writing of these subgroups.

5.6.5 Group RADG

RADG is the following group, shown in Listing 5.6, and aims to describe the radiative heat transfers. In RADG.1, the user indicates the number of assemblies (**47**) for which radiative heat transfers will be specified, the number (**2**) of radiative heat transfer groups for rodded assemblies (read from an extra file, *tape10⁷*) and the number (**7**) of radiative heat transfer

⁷These radiative heat transfer groups involve in general a large amount of view factors, as many radiating surfaces have to be taken into account (nodes from the basket structure and all fuel rods).

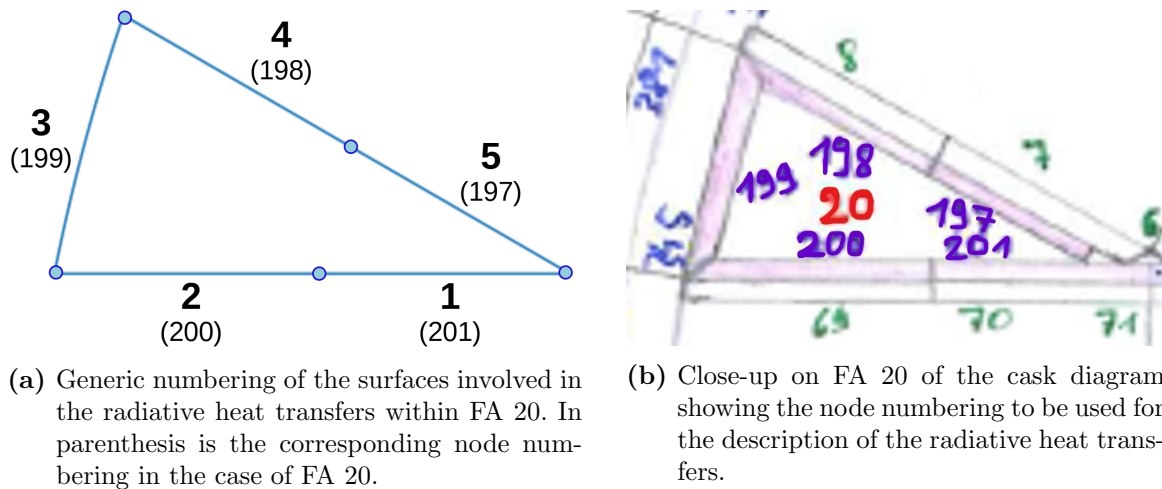


Figure 5.13: Surfaces to take into account for the description of the first radiative heat transfer group, corresponding to FA 20-32.

added for the latter when they are assigned to assemblies in RADG.10. For instance:

- on line 2882, assembly **2** corresponds to the radiative heat transfer group **1** read in *tape10* (therefore there is no minus sign), which includes **8** nodes: **9, 10, 12, 13, 15, 16, 349** and **350**. The order of the eight nodes is important. COBRA-SFS expects for instance that the first two nodes are facing the first row of rods (in the case of the CASTOR model, node 9 faces rods 1 to 9 and node 10 faces rods 10 to 18).
- on line 2900, assembly **20** corresponds to the first radiative heat transfer group defined in RADG.2/RADG.3, which is indicated by **-1**. This group involves **5** nodes: **197, 198, 199, 200** and **201**. In this case too, the order of the list is important: Fig. 5.13a shows the generic node indices used in RADG.3 for the view factor and Fig. 5.13b shows the actual node ID numbers when this group is applied to assembly 20.

5.6.6 Group HEAT

HEAT is the next input group and is used to define the convective heat transfer correlations to apply within the assemblies (rodded or not) and which describe the heat transfers between the fluid and the solid structures. The heat transfer correlations are specified in the form

$$H = (a_1 Re^{a_2} Pr^{a_3} + a_4) \frac{k}{D_e} \quad (5.1)$$

where a_1 , a_2 , a_3 and a_4 are empirical coefficients, Re the Reynolds number, Pr the Prandtl number, k the thermal conductivity of the fluid and D_e the hydraulic diameter of the channel.

The sets of coefficients (a_1 , a_2 , a_3 and a_4) are entered in pairs, one set corresponding to turbulent flow and one pair corresponding to laminar flow:

$$H_{turbulent} = (a_{t1} Re^{a_{t2}} Pr^{a_{t3}} + a_{t4}) \frac{k}{D_e} \quad \text{and} \quad H_{laminar} = (a_{l1} Re^{a_{l2}} Pr^{a_{l3}} + a_{l4}) \frac{k}{D_e}$$

The local heat transfer coefficient for a node is evaluated by COBRA-SFS as the maximum obtained with the laminar and turbulent equations using the local Reynolds and Prandtl numbers: $H_{axial} = \max(H_{laminar}, H_{turbulent})$.

In Listing 5.7, HEAT.1 (line 2928) indicates that **2** correlations will be defined, that turbulent mixing and energy exchange between fluid flowing in adjacent channels can be neglected⁹ (option value set to **0**) and that heat conduction in the fluid will be taken into account (further option, set to **1**).

Two pairs of correlations corresponding to Equation 5.1 are then defined on the following two lines:

- $H_{turbulent} = \mathbf{3.66} \cdot \frac{k}{D_e}$ and $H_{laminar} = \mathbf{3.66} \cdot \frac{k}{D_e}$
- $H_{turbulent} = (\mathbf{0.023} Re^{\mathbf{0.8}} Pr^{\mathbf{0.4}}) \frac{k}{D_e}$ and $H_{laminar} = \mathbf{3.66} \cdot \frac{k}{D_e}$

⁹COBRA-SFS originates from the COBRA code family, which was used to represent liquid or two-phase coolant flow in reactor cores. The models for turbulent energy exchange between adjacent channels are not really relevant in the case of the low velocity gas flow in storage cask and the COBRA-SFS User's Manual recommends to neglect these energy exchanges.

where q_b'' is the heat flux from node i at temperature T_i to node $i+1$ at temperature T_{i+1} , C_1 , C_2 and C_3 are coefficients to be specified by the user, σ is the Stefan-Boltzmann constant, and ϵ_i and ϵ_{i+1} are the surface emissivities of the nodes. This expression enables to take into account all three types of heat transfers if necessary:

- $C_2 = 1$ and $C_3 = 0$ leads to $q_{cond} = C_1 (T_i - T_{i+1})$ for the first part of Equation 5.2, which describes simple thermal conduction (Equation 2.3).
- Using C_2 and C_3 together with C_1 , it is possible to describe heat transfers by convection (Equation 2.5), involving heat transfer coefficient correlations as presented in Table 2.2 for instance.
- The second part of Equation 5.2 corresponds to radiative heat transfers (Equation 2.8). If the emissivities are set to 0.0, radiative heat transfers are disabled.

Axial profiles of room temperature can be defined in BDRY.3. These profiles are then used as boundary condition on the boundary nodes (nodes 533 to 568 in Fig. 2.18) of the model. In principle, it is possible to apply a different room temperature profile for each of the boundary nodes as well as an optional boundary heat flux. For the models presented in this thesis, we simply defined one temperature profile, which is applied to all boundary nodes. Thus, on line 2966 of Listing 5.9, temperature profile **1** is defined using **2** temperature points: at the relative height of **0.0** (bottom of the cask) is a temperature of **77** °F and at the relative height of **1.0** (top of the cask) is a temperature of **77** °F. This corresponds to a simple flat profile of **77** °F (25 °C).

Then the 36 boundary nodes announced in BDRY.1 are listed in BDRY.5 and BDRY.6 with some information: the length of node facing the boundary, the boundary temperature profile seen by the node, the optional boundary heat flux and the thermal boundary connection type.

2953	bdry	12	1	36	2					*bdry . 1
2954	1	5.61e-6			1	0	.93			*bdry . 2
2955	2	1.2e-6								

2956	3	5.0e-4												
2957	4	3.2e-6					.48	.25						
2966	1	2	0.0	77	1.0	77								*bdry.3
2967	533	17.957		1										*bdry.5
2968	1	1.0	1	1.0	1									*bdry.6
2969	534	17.957		1										*bdry.5
2970	1	1.0	1	1.0	1									*bdry.6
3037	568	17.957		1										*bdry.5
3038	1	1.0	1	1.0	1									*bdry.6
3039	1	0	2667	0	6	140	140							*bdry.8 low plenum
3040	1	1.0	2	0										*bdry.11
3041	2	1.0	3	0										*bdry.11
3042	3	1.0	4	0										*bdry.11
3043	4	1.17	5	0										*bdry.11
3044	5	1.17	6	72	317	3	13.9	318	3	13.9	319	3	13.9	
3045					320	3	13.9	321	3	13.9	322	3	13.9	
3046					323	3	13.9	324	3	13.9	325	3	13.9	
3067					422	3	13.9	423	3	13.9	424	3	13.9	
3068	6	1.42	7	0										*bdry.11
3069	2	0	2667	0	5	77	77							*bdry.8 up plenum
3070	1	1.0	8	0										*bdry.11
3071	2	1.38	9	36	317	3	15.6	318	3	15.6	319	3	15.6	
3072					320	3	15.6	321	3	15.6	322	3	15.6	
3073					323	3	15.6	324	3	15.6	325	3	15.6	
3095					422	3	25.7	423	3	25.7	424	3	25.7	
3096	5	2.45	12	0										*bdry.11
3097	0													*bdry.13

Listing 5.9: Input group BDRY.

Plenum modelling

BDRY group is also used to define the plenum models. The plena are optional features of the cask model and aim to describe in more detail the upper and lower boundary conditions of the cask. Indeed, the upper (resp. lower) plenum thermally connects the helium outlet (resp. inlet) at the top (resp. bottom) of the channels with the environment through a 1-dimensional series of axial and/or radial zones modelling the top (resp. bottom) of the cask. For instance, the different lids closing the cask can be modelled with the upper plenum. It is also possible to define connections between some solid nodes and one or several of the axial and radial plenum zones. This is represented in Fig 5.14.

In the User's Manual, COBRA-SFS developers recommend to proceed with caution with the plenum modelling. For instance, it is recommended to

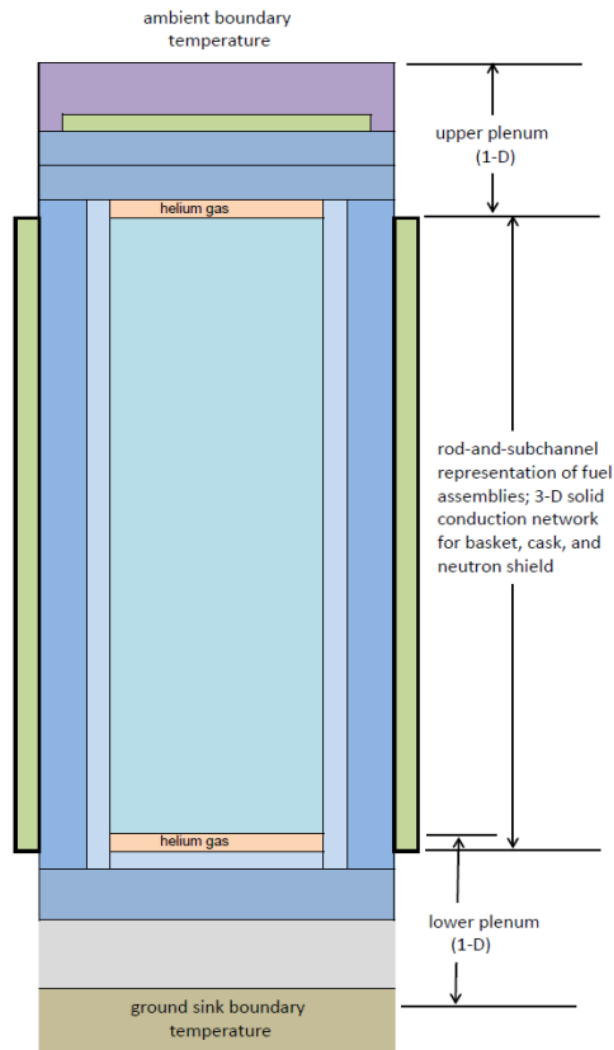


Figure 5.14: Plenum modelling in a COBRA-SFS cask model. Taken from [19].

conduct the verification steps without plenum models until the slab node network has been verified. Furthermore, radial heat transfers in the plenum regions should be included only when absolutely necessary. In most cases, the axial heat transfers should be sufficient as most of the heat removal from the top/bottom of the cask is expected to occur along the axial direction (radial heat transfers are important too, but mainly in the central part of the cask, which is extensively described in the group SLAB). As a general advise, it is recommended to represent the plenum regions as simply as possible.

In Listing 5.9, the lower plenum is defined starting at line 3039. It is identi-

fied as plenum **1** (the upper plenum starts on line 3069, where it is identified as plenum **2**), has a radial heat transfer area of **0** in², an axial heat transfer area of **2667** in², includes **0** radial region (no radial heat transfer from the plenum) and **6** axial regions, and the boundary temperature is **140** °F (60 °C). The 6 axial regions are then described on the following lines in BDRY.11.

5.6.9 Group OPER

Group OPER is mainly used to define axial decay heat profiles (in OPER.16 and OPER.17) as well as the initial state of the system at the beginning of the steady-state iterative solution (OPER.2). In Listing 5.10, the decay heat profile includes **36** (OPER.16) pairs of entries (axial position, heat generation factor), which are listed in OPER.17:

(0.000, 0.000), **(0.071, 0.000)**, **(0.085, 0.392)**, **(0.113, 0.659)**, **(0.140, 0.893)** and **(0.168, 1.022)** are the first six pairs of entries, written on the first OPER.17 line (line 3101).

3098	oper	1	0	3	0	0	0	0	0	0	0	0	0	0	1	*oper .1
3099				145.0	1.E-07	0.0023028		185.0	-.000001		0.0					*oper .2
3100			36													*oper .16
3101				0.0000	.0000	.0710	.0000	.0850	.3920	.1130	.6590	.1400	.8930	.1681	.022	*oper .17
3102				0.1961	.0820	.2231	.1170	.2511	.1270	.2791	.1280	.3061	.1320	.3341	.132	*oper .17

Listing 5.10: Input group OPER.

Originally, group OPER was also used to set the decay heat values of the fuel assemblies. This should be done by specifying an absolute value (in MBtu h⁻¹ ft⁻²) in OPER.2 and individual factors for all fuel assemblies in OPER.8. This approach is still working, but a new group (REST) has been added, which simplifies the definition of the individual decay heat values.

5.6.10 Group REST

Group REST appeared with the release of a new version of the code and enables to specify the decay heat for each fuel assembly in Watt¹¹. In List-

¹¹Previously, the decay heats had to be specified in group OPER using an average heat generation rate in MBtu h⁻¹ ft⁻² and factors to apply to the fuel assemblies.

ing 5.11, REST.1 indicates that decay heats will be defined for **47** assemblies. Then, in REST.2, the decay heats are listed for the 47 assemblies: the first 19 assemblies have a decay heat of **2052** W (rodded fuel assemblies), while the other 28 (unrodded) assemblies do not generate any heat (**0.00** W).

```

3107 rest      47                                     *rest .1
3108 2052 2052 2052 2052 2052 2052 2052 2052 2052 2052 2052 2052 *rest .2
3109 2052 2052 2052 2052 2052 2052 2052 0.00 0.00 0.00 0.00 0.00 *rest .2
3110 0.00 0.00 0.00 0.00 0.00 0.00 0.00 0.00 0.00 0.00 0.00 0.00 *rest .2
3111 0.00 0.00 0.00 0.00 0.00 0.00 0.00 0.00 0.00 0.00 0.00 0.00 *rest .2

```

Listing 5.11: Input group REST

5.6.11 Groups CALC and OUTP

In Listing 5.12, the last two input groups are shown. Group CALC fixes calculational parameters and options: convergence criteria, maximum number of iterations, dumping factors. It also enables to set transient information in case of a transient simulation: total duration of the transient, number and duration of the time steps.

Group OUTP is the last input group and enables to control what should be printed in the output file: summary of the input entries, all or part of the fuel rods, all or part of the channels, all or part of the solid nodes, all or part of the timesteps in case of transients and assembly average information.

Finally, the input file ends when the flag *endd* is entered.

```

3112 calc      1      0      1                                     *calc .1
3113          1E-04 1E-04 1E-04 1E-04          1.0   .7  1.0  1.2   .5  0.0 *calc .2
3114          0  400                                     *calc .3
3115 outp 11113          2          1 *outp .1
3116 endd

```

Listing 5.12: Input groups CALC and OUTP.

5.7 COBRA-SFS model verification

In Appendix 5.5, we presented the different steps of the development of a new COBRA-SFS model. In particular, the third step consists in looking for errors in the input file once it has become readable by COBRA-SFS. As COBRA-SFS does not provide any visualization tool¹², we developed some scripts with Python to plot temperature distributions in assemblies as well as temperature differences between symmetrical assemblies. Indeed, the symmetry axes of the TN-32B cask offer efficient means to identify errors in the input file: if the model (input file) is correct, a symmetrical power distribution between the fuel assemblies should lead to a symmetrical temperature field in the cask. Therefore, in the first input file, we assigned the same power to all 32 assemblies. Figures 5.15 to 5.21 show the evolution of the symmetry checks on the model. Each Figure includes two diagrams: (a) represents the temperature difference between the North and South halves of the cask, each rod being individually processed and depicted, while (b) represents the difference between the West and East halves.

The first symmetry check, represented in Fig. 5.15, revealed three problems:

- An overall gradient in the temperature difference:

In Fig. 5.15a, the temperature difference is close to zero (red) near the symmetry axis but increases progressively when moving towards the upper right side of the cask. The maximum temperature difference reaches about 2.5 °C (light blue) between FA 4 and FA 32, the latter being warmer.

In Fig. 5.15b, we can also observe this gradient: the temperature difference is close to zero (blue) near the symmetry axis, but increases when moving towards the upper left side, where it reaches about 2 °C.

- A local mismatch between FA 5 and FA 23 (blue spot on FA 5):

¹²The fact is that even though the input file is very detailed - involving geometrical descriptions of the constitutive elements of the model - the overall geometry of the modelled cask remains “unknown” to COBRA-SFS. Through the input file, COBRA-SFS might know how slender or not an element is and to which other elements it is connected, but it has no means to know the overall spatial configuration of the cask.

This problem can also be observed in Fig. 5.15b, with the red spot on FA 23 which points out a mismatch between FA 23 and FA 28. Considering the information from Fig. 5.15a and 5.15b, we can deduce that the problem most probably comes from FA 23.

- A local mismatch between FA 4 and FA 32 (red spot on FA 4):

This problem can also be observed in Fig. 5.15b, with the red spot on FA 29 which points out a mismatch between FA 29 and FA 32. Considering the information from Fig. 5.15a and 5.15b, we can deduce that the problem most probably comes from FA 32.

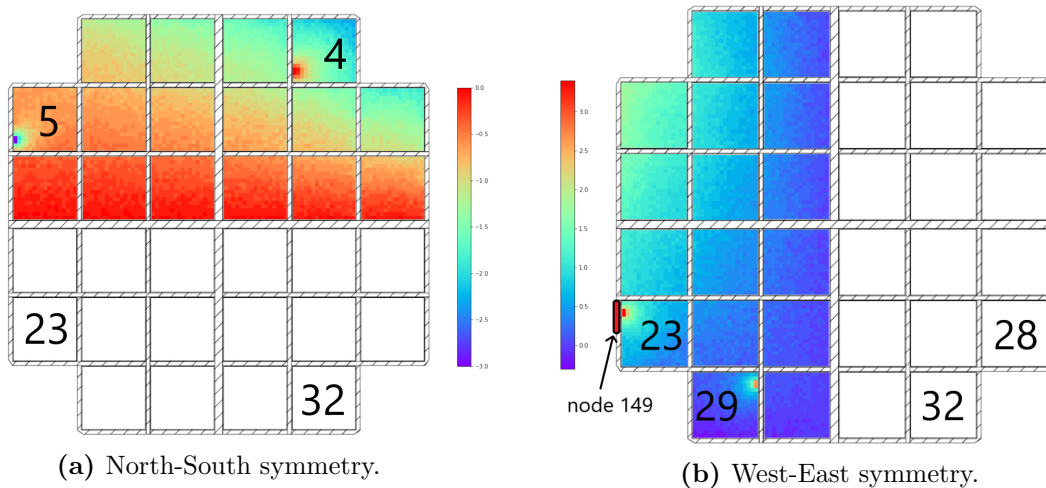


Figure 5.15: First symmetry maps: the coloured halves show the temperature difference between one rod and its symmetrical one. On these first maps, we could observe two local mismatches and an overall gradient. An input file free of errors should result in a perfect symmetry, i.e. in homogeneously coloured maps.

The global gradient might indicate a problem in the cask body (input group SLAB) or boundary conditions (group BDRY): the effect of the error is rather smooth in the internal part of the cask and increases from the centre to the exterior. The second and third points are easier to address, as the problems are well localized. The errors most probably concern the description of the basket structures (input group SLAB) at the local mismatches or the description of the helium channels or fuel rods (groups CHAN and RODS) of the corresponding assemblies.

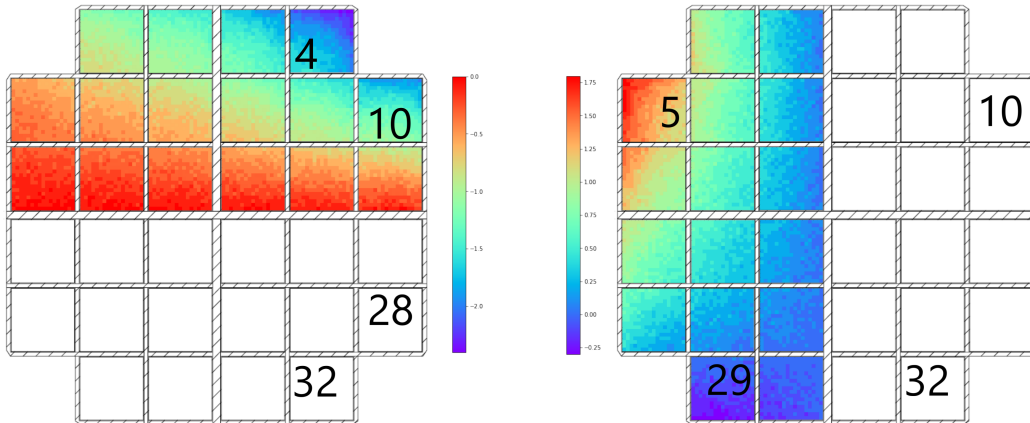
We first solved the second and third points: the localization of the errors in the input file was more straightforward, as we could restrain the search at a few precise nodes, rods and channels. It appeared that both mismatches were related to a single error in input group SLAB. In the listing of the solid nodes and their connections with helium channels (subgroups SLAB.6 and SLAB.7, see Fig. 5.16), the node 149 was supposed to be connected to the helium channels 1, 19, 37, 55, 73, 91, 109, 127 and 145 (fringe channels) of assembly 23. However, 32 had been written instead of 23 for the connection between slab 149 and helium channel 73 (see the red circle in Fig. 5.16). This resulted in:

- a missing heat removal path for channel 73 of FA 23 (the connection was not written and thus did not exist), explaining the local hot spot (red point on FA 23 of Fig 5.15b) around this channel,
- an undue heat removal path for channel 73 of FA 32 (this undue connection came in addition to the right connection with the slab node facing channel 73 of FA 32), explaining the local cold spot (red points on FA 4 in Fig 5.15a and FA 29 in Fig 5.15b, both symmetrical points of the cold spot of FA 32) around this channel.

2088	148	9	23	307	1	23	289	2	23	271	2	23	253	2	*slab.6	
2089			23	235	2	23	217	2	23	199	2	23	181	2	*slab.7	
2090			23	163	2										*slab.7	
2091	149	9	23	145	2	23	127	2	23	109	2	23	91	2	*slab.6	
2092			32	73	2	23	55	2	23	37	2	23	19	2	*slab.7	
2093			23	1	1										*slab.7	
2094	150	18	24	18	1	24	36	2	24	54	2	24	72	2	*slab.6	Assy 24
2095			24	90	2	24	108	2	24	126	2	24	144	2	*slab.7	
2096			24	162	2	25	145	2	25	127	2	25	109	2	*slab.7	
2097			25	91	2	25	73	2	25	55	2	25	37	2	*slab.7	
2098			25	19	2	25	1	1							*slab.7	

Figure 5.16: Error in group SLAB responsible for the local mismatches in the symmetry of the temperature distribution.

Once this error had been corrected, the new symmetry check was free of local mismatches but still presented the overall gradient of temperature difference. The new symmetry maps are shown in Fig. 5.17. As explained above, the source of this gradient was expected to be either in the description of the cask body (group SLAB) or in the definition of the boundary conditions (group BDRY) on the cask outer surface.



(a) North-South symmetry, maximum difference: 2.4 °C between FA 4 and FA 32. (b) West-East symmetry, maximum difference: 1.8 °C between FA 5 and FA 10.

Figure 5.17: New symmetry maps, after correction of the error leading to the local mismatches. The overall gradients can still be observed.

We finally found it in the subgroup BDRY.5: in this subgroup, the boundary nodes are listed and a temperature profile is assigned to each of them. In this model, all surface nodes are supposed to be connected with the same temperature $T_{room} = 24$ °C (flat profile). However, 600 had been written instead of 610 as node identity number. This led to the lack of a connection between the node 610 and the environment and, on the contrary, a double connection of node 600 with the environment. As a consequence, the heat removal from the region around node 610 was less efficient than it was supposed to be, which led to higher temperatures around FA 31 and FA 32 (see Fig. 5.18 for the position of nodes 600 and 610). This can be observed in Fig. 5.17a: the blue colour at FA 4 indicates that FA 4 is around 2 °C colder than FA 32. This also slightly appears in Fig. 5.17b, where the purple colour on FA 29 indicates that FA 29 is 0.25 °C colder than FA 32. On the other hand, the heat removal was excessive through node 600, which led to lower temperatures around FA 10. This can be well observed in Fig. 5.17b, where the red colour on FA 5 indicates that FA 5 is 1.75 °C warmer than FA 10. In Fig. 5.17a, the heat removal through node 600 slightly increases the temperature difference between FA 10 and FA 28, but the main effect is rather related to the error on node 610.

We might remark that the influence of those inexact heat removal paths is

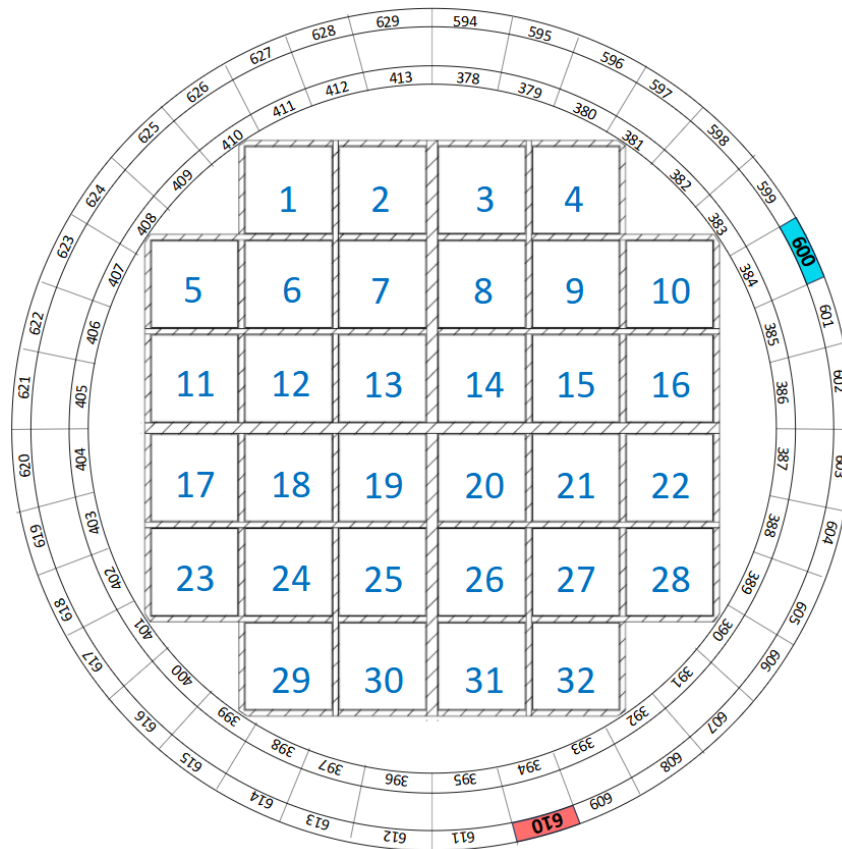
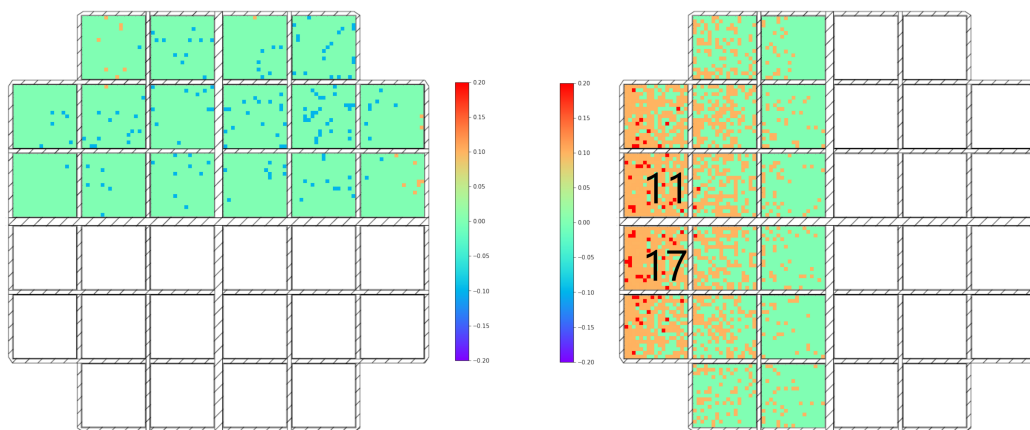


Figure 5.18: Localisation of nodes 600 (blue) and 610 (red) affected by the error in group BDRY. No thermal connection was set between node 610 and the environment, leading to a heat accumulation around FA 32, while an enhanced heat removal path was set for node 600, resulting in lowered temperatures around FA 10.

stronger on the corner assemblies (FA 4, FA 10, FA 32) than on non-corner external assemblies (such as FA 31). In particular, FA 32 is more impacted by the missing heat removal path through node 610 than FA 31. This is probably due to the fact that conduction plays here an important role in the heat removal and that the basket structure around FA 32 is directly connected to the cask body (at node 392, see Fig. 2.33), which is not the case for the basket structure around FA 31.

After correction of this second error, we obtained the symmetry maps shown in Fig. 5.19. The former gradient of temperature difference had disappeared as expected but a new gradient appeared. Indeed, the East-West symmetry

map (Fig. 5.19b) showed a clear gradient, the West half of the cask being too hot compared to the East half. However, the differences involved here were significantly more satisfying than at the previous step: the orange colour code corresponds to $+0.1\text{ }^{\circ}\text{C}$ and red to $+0.2\text{ }^{\circ}\text{C}$, to be compared with the $\pm 2\text{ }^{\circ}\text{C}$ observed in the previous symmetry check. The North-South symmetry map (Fig. 5.19a) only presented few mismatching points, but without clear gradient. All mismatches indicated either a $+0.1\text{ }^{\circ}\text{C}$ difference (orange points) or a $-0.1\text{ }^{\circ}\text{C}$ difference (blue points).



(a) North-South symmetry: only a few disseminated asymmetries, involving small temperature differences ($\pm 0.1\text{ }^{\circ}\text{C}$). (b) West-East symmetry: low gradient along the West-East axis (maximum temperature difference: $0.2\text{ }^{\circ}\text{C}$).

Figure 5.19: New symmetry check, after correction of the error on the boundary node leading to the initial overall gradient. The new West-East map presents another gradient of temperature difference, but with a much smaller amplitude ($0.2\text{ }^{\circ}\text{C}$). Colour code: green stands for zero temperature difference, light blue for $-0.1\text{ }^{\circ}\text{C}$, orange for $+0.1\text{ }^{\circ}\text{C}$ and red for $+0.2\text{ }^{\circ}\text{C}$.

As the new gradient was oriented along the West-East axis, it could be assumed that the corresponding error was affecting a node near to this axis, either from the basket structure or from the cask body. We did not succeed in finding the error directly in the input file, but finally found it using the summary of the node connections given at the beginning of the COBRA-SFS output file. This is a rather tedious task, but it can enable to find some errors and constitutes a further verification of the model. In practical terms, we printed a section of the output file listing each of the 629 nodes of the model (54 pages) including for each node its neighbour nodes and

channels, together with the identification numbers of the thermal connection types and the fuel assembly numbers to which the channels belong. Then we checked all this information, fuel assembly after fuel assembly, connection type after connection type, as well as the material types and the node surfaces. We highlighted the verified information/numbers as we went along. Two of the 54 pages can be found in Appendix 5.8: the first page, which lists the first nodes of the model (those nodes include connections both to helium channels and to other nodes), and the page including node 424 (presenting connections only to other solid nodes), which appeared to be responsible for the gradient shown in Fig. 5.19b. We can see on the page including node 424 (Fig. 5.23 of Appendix 5.8) that node 424 presented two connections with node 460: one connection with the ID number 55 and one connection with the ID number 56. The first connection was supposed to be with node 425. On the following line, describing the connections of node 425, we can see that node 425 was missing the connection with node 424.

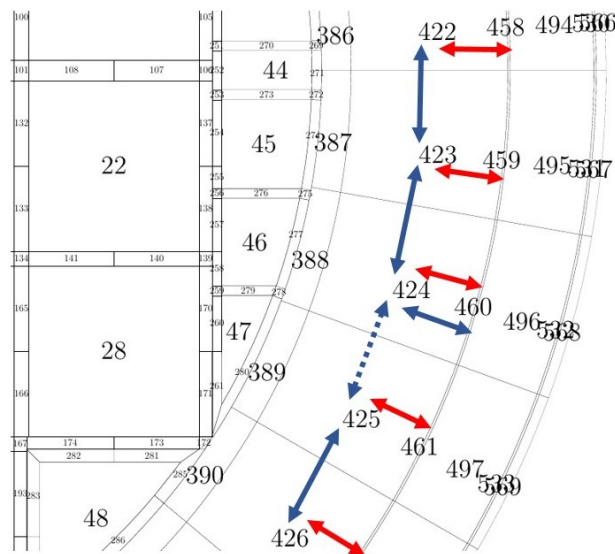


Figure 5.20: Localization of the error responsible for the low West-East gradient: in the description of the thermal connections between solid nodes (subgroup SLAB.3), 460 was written instead of 425 in the listing of the nodes connected to node 424. This led to a missing tangential connection between nodes 424 and 425 (dotted blue arrow) and to an undue connection (blue arrow) between nodes 424 and 460 (in addition to the right connection which is represented with the red arrow).

Figure 5.20 shows a close-up of the cask diagram (Fig. 2.33), centered on

node 424. We can see the consequence of the error on node 424: a thermal connection between nodes 424 and 425 is missing while an undue connection between nodes 424 and 460 is defined. The missing connection probably does not significantly impact the thermal behaviour, as most of the heat transfer in this region is expected to be along the radial direction (removal of the heat generated by the fuel assemblies inside the cask, radially through the cask body and to the environment). On the other hand, the undue connection between nodes 424 and 460 increases the heat removal through this radial path, which explains the gradient of temperature difference, with the East half of the cask slightly colder than the West half.

After correction of the error on node 424, we obtained the symmetry maps shown in Fig. 5.21. At this point, the remaining mismatches between symmetrical rods were all of $\pm 0.1^\circ\text{C}$. There might still be minor errors in the model explaining these asymmetries, but numerical convergence issues might also be responsible for it. However, as no more error could be identified within a reasonable time and considering the very low magnitude of the mismatches, the model was considered as satisfying.

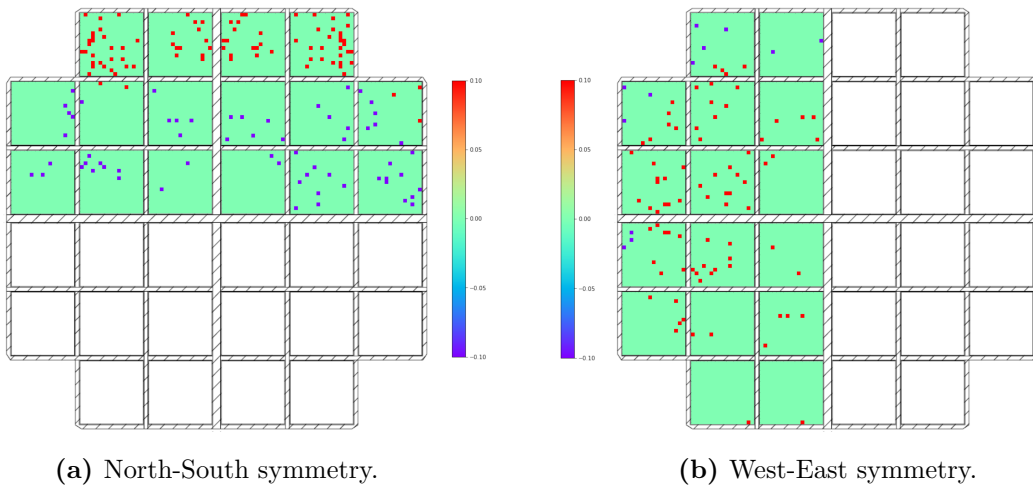


Figure 5.21: Symmetry maps after correction of the thermal connections around node 424. Colour code: green stands for zero temperature difference, blue for -0.1°C and red for $+0.1^\circ\text{C}$.

5.8 COBRA-SFS output - Verification of the node connections

```

5484 slab thermal connections
5485 -----
5486 slab mat.      area      heat gen.      power      solid connections      fluid connections
5487 no.  typ.      (in2)      (btu/cu.ft.-h)  profile      (connected node,type)  (adjacent assembly,channel,type)
5488 1    1          0.21      0.000        1    ( 2, 1) ( 12, 1) ( 410, 10) ( 0, 0)  ( 0, 0, 0) ( 0, 0, 0) ( 0,
5489 2    1          2.81      0.000        1    ( 3, 2) ( 198, 11) ( 1, 1) ( 0, 0)  ( 1, 1, 1) ( 1, 2, 2) ( 1,
5490      3, 2)      ( 0, 0) ( 0, 0) ( 0, 0) ( 0, 0)  ( 1, 4, 2) ( 1, 5, 2) ( 1,
5491      6, 2)      ( 0, 0) ( 0, 0) ( 0, 0) ( 0, 0)  ( 1, 7, 2) ( 1, 8, 2) ( 1,
5492 3    1          2.81      0.000        1    ( 4, 1) ( 199, 12) ( 200, 13) ( 201, 14)  ( 1, 10, 2) ( 1, 11, 2) ( 1,
5493      12, 2)      ( 2, 2) ( 0, 0) ( 0, 0) ( 0, 0)  ( 1, 13, 2) ( 1, 14, 2) ( 1,
5494      15, 2)      ( 0, 0) ( 0, 0) ( 0, 0) ( 0, 0)  ( 1, 16, 2) ( 1, 17, 2) ( 1,
5495 4    1          0.48      0.000        1    ( 5, 3) ( 13, 1) ( 201, 15) ( 3, 1)  ( 0, 0, 0) ( 0, 0, 0) ( 0,
5496 5    1          3.26      0.000        1    ( 6, 4) ( 4, 3) ( 0, 0) ( 0, 0)  ( 1, 18, 1) ( 1, 36, 2) ( 1,
5497      54, 2)      ( 0, 0) ( 0, 0) ( 0, 0) ( 0, 0)  ( 1, 72, 2) ( 1, 90, 2) (
5498      1,108, 2)  ( 0, 0) ( 0, 0) ( 0, 0) ( 0, 0)  ( 1,126, 2) ( 1,144, 2) (
5499      1,162, 2)  ( 0, 0) ( 0, 0) ( 0, 0) ( 0, 0)  ( 2,145, 2) ( 2,127, 2) (
5500      2,109, 2)  ( 0, 0) ( 0, 0) ( 0, 0) ( 0, 0)  ( 2, 91, 2) ( 2, 73, 2) ( 2,
5501      55, 2)      ( 0, 0) ( 0, 0) ( 0, 0) ( 0, 0)  ( 2, 37, 2) ( 2, 19, 2) ( 2,
5502 6    1          3.26      0.000        1    ( 7, 3) ( 5, 4) ( 0, 0) ( 0, 0)  ( 1,180, 2) ( 1,198, 2) (
5503      1,216, 2)  ( 0, 0) ( 0, 0) ( 0, 0) ( 0, 0)  ( 1,234, 2) ( 1,252, 2) (
5504      1,270, 2)  ( 0, 0) ( 0, 0) ( 0, 0) ( 0, 0)  ( 1,288, 2) ( 1,306, 2) (
5505      1,324, 1)  ( 0, 0) ( 0, 0) ( 0, 0) ( 0, 0)  ( 2,307, 1) ( 2,289, 2) (
5506      2,271, 2)  ( 0, 0) ( 0, 0) ( 0, 0) ( 0, 0)  ( 2,253, 2) ( 2,235, 2) (
5507      2,217, 2)  ( 0, 0) ( 0, 0) ( 0, 0) ( 0, 0)  ( 2,199, 2) ( 2,181, 2) (
5508 7    1          0.56      0.000        1    ( 8, 3) ( 20, 3) ( 48, 3) ( 6, 3)  ( 0, 0, 0) ( 0, 0, 0) ( 0,
5509 8    1          3.26      0.000        1    ( 9, 4) ( 7, 3) ( 0, 0) ( 0, 0)  ( 1,324, 1) ( 1,323, 2) (
5510      1,322, 2)  ( 0, 0) ( 0, 0) ( 0, 0) ( 0, 0)  ( 1,321, 2) ( 1,320, 2) (

```

Figure 5.22: Part of COBRA-SFS output file summarizing the solid node information. This page shows the information corresponding to the first 8 nodes. As a further means of verification (and error identification) of the thermal connections defined in group SLAB, this summary has been printed and all node information has been checked (progressively highlighted).

5.8 COBRA-SFS output - Verification of the node connections

6589	411	3	9.20	0.000	1	0, 0) (412, 53) (447, 54) (217, 46) (410, 53)	(0, 0, 0) (0, 0, 0) (0,
6590	412	3	9.20	0.000	1	(413, 53) (448, 54) (218, 47) (220, 48)	(0, 0, 0) (0, 0, 0) (0,
6591						(221, 47) (411, 53) (0, 0) (0, 0)	(0, 0, 0) (0, 0, 0) (0,
6592	413	3	9.20	0.000	1	(449, 54) (223, 49) (224, 47) (226, 50)	(0, 0, 0) (0, 0, 0) (0,
6593						(378, 53) (412, 53) (0, 0) (0, 0)	(0, 0, 0) (0, 0, 0) (0,
6594	414	4	55.68	0.000	1	(415, 55) (449, 55) (450, 56) (378, 54)	(0, 0, 0) (0, 0, 0) (0,
6595	415	4	55.68	0.000	1	(416, 55) (451, 56) (379, 54) (414, 55)	(0, 0, 0) (0, 0, 0) (0,
6596	416	4	55.68	0.000	1	(417, 55) (452, 56) (380, 54) (415, 55)	(0, 0, 0) (0, 0, 0) (0,
6597	417	4	55.68	0.000	1	(418, 55) (453, 56) (381, 54) (416, 55)	(0, 0, 0) (0, 0, 0) (0,
6598	418	4	55.68	0.000	1	(419, 55) (454, 56) (382, 54) (417, 55)	(0, 0, 0) (0, 0, 0) (0,
6599	419	4	55.68	0.000	1	(420, 55) (455, 56) (383, 54) (418, 55)	(0, 0, 0) (0, 0, 0) (0,
6600	420	4	55.68	0.000	1	(421, 55) (456, 56) (384, 54) (419, 55)	(0, 0, 0) (0, 0, 0) (0,
6601	421	4	55.68	0.000	1	(422, 55) (457, 56) (385, 54) (420, 55)	(0, 0, 0) (0, 0, 0) (0,
6602	422	4	55.68	0.000	1	(423, 55) (458, 56) (386, 54) (421, 55)	(0, 0, 0) (0, 0, 0) (0,
6603	423	4	55.68	0.000	1	(424, 55) (459, 56) (387, 54) (422, 55)	(0, 0, 0) (0, 0, 0) (0,
6604	424	4	55.68	0.000	1	(460, 55) (460, 56) (388, 54) (423, 55)	(0, 0, 0) (0, 0, 0) (0,
6605	425	4	55.68	0.000	1	(426, 55) (461, 56) (389, 54) (424, 55)	(0, 0, 0) (0, 0, 0) (0,
6606	426	4	55.68	0.000	1	(427, 55) (462, 56) (390, 54) (425, 55)	(0, 0, 0) (0, 0, 0) (0,
6607	427	4	55.68	0.000	1	(428, 55) (463, 56) (391, 54) (426, 55)	(0, 0, 0) (0, 0, 0) (0,
6608	428	4	55.68	0.000	1	(429, 55) (464, 56) (392, 54) (427, 55)	(0, 0, 0) (0, 0, 0) (0,
6609	429	4	55.68	0.000	1	(430, 55) (465, 56) (393, 54) (428, 55)	(0, 0, 0) (0, 0, 0) (0,
6610	430	4	55.68	0.000	1	(431, 55) (466, 56) (394, 54) (429, 55)	(0, 0, 0) (0, 0, 0) (0,
6611	431	4	55.68	0.000	1	(432, 55) (467, 56) (395, 54) (430, 55)	(0, 0, 0) (0, 0, 0) (0,
6612							
6613							

Figure 5.23: Further page from the summary of the solid node information, including node 424. The description of this node presented an error leading to a slight asymmetry of the temperature map of the cask (see section 5.7, Fig. 5.19). The systematic check of all nodes and connections on this printed summary enabled to identify the missing connection between nodes 424 and 425, as well as the undue connection between nodes 424 and 460.

List of Figures

1.1	Overview of the temperature range and time scales involved over the fuel assembly life.	3
1.2	Ductile-to-Brittle Transition Temperature (DBTT).	4
2.1	Thermal conduction in cylindrical geometry with heat production inside the inner cylinder.	9
2.2	Thermal conduction in a uniaxial configuration.	11
2.3	Equivalent thermal resistances and conductivities for two materials in parallel or in series.	12
2.4	Equivalent conductivity λ_{eq} for two materials (conductivities λ_1 and λ_2) in parallel or in series.	13
2.5	Surface energy balance for an opaque (no transmission) material. Taken from [24].	17
2.6	Radiation network for two surfaces that see each other and nothing else. Taken from [24].	19
2.7	Radiative heat transfer between two surfaces in two different configurations.	20
2.8	Crossed and uncrossed strings between two surfaces exchanging radiative heat.	21
2.9	Radiative heat transfer in a closed half cylinder of diameter \mathcal{L}	23

2.10 CASTOR [®] V/19 cask from GNS. Taken from [28].	25
2.11 Diagram of the semi-analytical cask model.	27
2.12 Temperature evolution with a step of 1 hour at 600 °C.	31
2.13 Temperature evolution with a step of 30 min at 800 °C.	32
2.14 Evolution of the cask temperature under generic daily fluctuations of the room temperature.	33
2.15 Scatterplot showing the temperatures of the 6 zones of the Python model with regard to the total power.	36
2.16 Scatterplot showing the temperatures of the 6 zones of the Python model with regard to the room temperature.	37
2.17 Correlation matrix.	42
2.18 Diagram of the generic model.	47
2.19 Generic cask model inspired by the CASTOR [®] V/19 and built using COCOSYS. Taken from [29].	51
2.20 Modelling work inspired by the CASTOR [®] V/19 and performed using ANSYS CFX. Taken from [29].	52
2.21 Comparison of the COBRA-SFS model with COCOSYS and CFX models. Taken from [42].	53
2.22 Comparison of the temperature calculated with the Python model and with COBRA-SFS, for a homogeneous load of 39 kW and a room temperature of 25 °C.	55
2.23 Comparison of COBRA-SFS and Python models on a transient calculation corresponding to the drying process.	57
2.24 Temperature distribution in a quarter of the central fuel assembly, determined by the ANSYS CFX model. Taken from [29].	59

LIST OF FIGURES

2.25 Temperature map for a quarter of the COBRA-SFS CASTOR model.	59
2.26 Temperature profiles of the hottest rod, an “external” rod and the cask body, for different room temperatures.	60
2.27 Picture of a CASTOR [®] V/19 under water during loading operations. Adapted from [43].	61
2.28 Temperature profiles in the central fuel assembly for a model a) without gap, b) with small gaps (0.5 - 1 mm) and c) with larger gaps (1 - 2.5 mm).	62
2.29 Temperature profile along a diagonal line through a TN-32 cask, modelled using ANSYS. Taken from [44].	64
2.30 Temperature distribution [°C] at the hottest axial position (294 to 306 cm) for a total power load of 39 kW equally distributed between the 19 fuel assemblies and for a room temperature of 25 °C. Taken from [42].	65
2.31 Temperature evolution from cooling pond to dry storage.	67
2.32 Temperature evolution over 100 years of storage.	69
2.33 Diagram of the TN-32B model.	80
2.34 Power of the 32 fuel assemblies loaded in the TN-32B cask.	84
2.35 Comparison of the measured and simulated temperature profiles of guide tubes from 7 fuel assemblies loaded in the TN-32B cask.	86
2.36 Comparison of the measured and simulated surface temperature of the TN-32B cask.	88
2.37 Temperature variation with decay heat.	89
2.38 Temperature variation of the cask surface with decay heat.	91

2.39	Temperature variation with room temperature.	92
2.40	Temperature variation of the cask surface with room temperature.	93
2.41	Analogy between temperatures and electrical potentials.	93
3.1	Axial and circumferential stresses in a cylinder.	98
3.2	Hydrogen content in cladding with regard to the burnup. Taken from [54, 55].	99
3.3	Influence of hydrogen content and temperature on Zircaloy-4 fracture toughness. Taken from [56].	100
3.4	Threshold stress for hydride reorientation, depending on the hydrogen content and on the peak temperature. Taken from [12].	102
3.5	Phase diagram for Zr-H binary system. Adapted from [65].	104
3.6	Generic curves representing the Terminal Solid Solubility for Dissolution (TSS_D) and Precipitation (TSS_P) of hydrogen in zirconium as function of the temperature.	106
3.7	Experimental results on a sample loaded with 541 wt.ppm hydrogen. Taken from [9].	108
3.8	Particle current density vector.	110
3.9	Hydrogen diffusion and hydride morphology under temperature, concentration and stress gradients.	115
3.10	Plot of all TSS_P and TSS_D points from the database as a function of the temperature and with uncertainties.	118
3.11	Orthogonal Distance Regression (ODR) problem. Taken from [104].	126

LIST OF FIGURES

3.12 Plot of all TSS _P and TSS _D values from the database corresponding to Zircaloy-2.	128
3.13 Plot of all TSS _P and TSS _D values from the database corresponding to Zircaloy-4.	129
3.14 Plot of all TSS _P and TSS _D values from the database measured using Differential Scanning Calorimetry (DSC).	131
3.15 Precipitation (nucleation/growth) and dissolution domains considered by the HNGD model.	135
3.16 Simulation results from the HNGD model developed at the Pennsylvania State University. Adapted from [10].	136
3.17 Verification case for hydride dissolution.	140
3.18 Verification case for hydride nucleation.	142
3.19 Verification case for hydride growth.	143
3.20 Thermal cycles simulated with the HNGD model, involving the total dissolution of hydrogen in a zirconium alloy and different cooling rates.	144
3.21 Thermal cycles simulated with the HNGD model, involving partial dissolution of hydrogen in a zirconium alloy and different cooling rates.	145
3.22 Hydrogen and hydride profiles at the beginning of the dry storage, for a total hydrogen concentration of 250 wt.ppm.	152
3.23 Hydrogen and hydride profiles at the beginning of the dry storage, for a total hydrogen concentration of 100 wt.ppm.	153
3.24 Hydrogen and hydride profiles at the beginning of the dry storage, for a total hydrogen concentration of 50 wt.ppm.	153
3.25 Temperature axial profiles in dry storage.	155

3.26 Hydrogen and hydride profiles at the beginning of the dry storage, for a total hydrogen concentration of 250 wt.ppm.	157
3.27 Hydrogen and hydride profiles after 1 year of dry storage, for a total hydrogen concentration of 250 wt.ppm.	157
3.28 Hydrogen and hydride profiles after 5 years of dry storage, for a total hydrogen concentration of 250 wt.ppm.	158
3.29 Hydrogen and hydride profiles after 15 years of dry storage, for a total hydrogen concentration of 250 wt.ppm.	158
3.30 Hydrogen and hydride profiles after 95 years of dry storage, for a total hydrogen concentration of 250 wt.ppm.	159
3.31 Hydrogen and hydride profiles at the beginning of the dry storage, for a total hydrogen concentration of 100 wt.ppm.	160
3.32 Hydrogen and hydride profiles after 1 year of dry storage, for a total hydrogen concentration of 100 wt.ppm.	161
3.33 Hydrogen and hydride profiles after 5 years of dry storage, for a total hydrogen concentration of 100 wt.ppm.	161
3.34 Hydrogen and hydride profiles after 15 years of dry storage, for a total hydrogen concentration of 100 wt.ppm.	162
3.35 Hydrogen and hydride profiles after 95 years of dry storage, for a total hydrogen concentration of 100 wt.ppm.	162
3.36 Hydrogen and hydride profiles at the beginning of the dry storage, for a total hydrogen concentration of 50 wt.ppm.	163
3.37 Hydrogen and hydride profiles after 1 year of dry storage, for a total hydrogen concentration of 50 wt.ppm.	164
3.38 Hydrogen and hydride profiles after 5 years of dry storage, for a total hydrogen concentration of 50 wt.ppm.	164

LIST OF FIGURES

3.39 Hydrogen and hydride profiles after 15 years of dry storage, for a total hydrogen concentration of 50 wt.ppm. 165

3.40 Hydrogen and hydride profiles after 95 years of dry storage, for a total hydrogen concentration of 50 wt.ppm. 165

3.41 Hydrogen and hydride profiles at the beginning of the dry storage, for a total hydrogen concentration of 100 wt.ppm and a larger diffusion coefficient (factor 4). 168

3.42 Hydrogen and hydride profiles after 1 year of dry storage, for a total hydrogen concentration of 100 wt.ppm and a larger diffusion coefficient (factor 4). 168

3.43 Hydrogen and hydride profiles after 5 years of dry storage, for a total hydrogen concentration of 100 wt.ppm and a larger diffusion coefficient (factor 4). 169

3.44 Hydrogen and hydride profiles after 15 years of dry storage, for a total hydrogen concentration of 100 wt.ppm and a larger diffusion coefficient (factor 4). 169

3.45 Hydrogen and hydride profiles after 95 years of dry storage, for a total hydrogen concentration of 100 wt.ppm and a larger diffusion coefficient (factor 4). 170

3.46 Hydrogen and hydride profiles at the beginning of the dry storage, for a total hydrogen concentration of 50 wt.ppm and a larger diffusion coefficient (factor 4). 171

3.47 Hydrogen and hydride profiles after 1 year of dry storage, for a total hydrogen concentration of 50 wt.ppm and a larger diffusion coefficient (factor 4). 172

3.48 Hydrogen and hydride profiles after 5 years of dry storage, for a total hydrogen concentration of 50 wt.ppm and a larger diffusion coefficient (factor 4). 172

3.49 Hydrogen and hydride profiles after 15 years of dry storage, for a total hydrogen concentration of 50 wt.ppm and a larger diffusion coefficient (factor 4).	173
3.50 Hydrogen and hydride profiles after 95 years of dry storage, for a total hydrogen concentration of 50 wt.ppm and a larger diffusion coefficient (factor 4).	173
3.51 Hydrogen and hydride profiles after 100 years, for a total hydrogen concentration of 100 wt.ppm and the reference diffusion coefficient.	175
3.52 Hydrogen and hydride profiles after 100 years, for a total hydrogen concentration of 100 wt.ppm and a factor 4 for the diffusion coefficient.	175
3.53 Hydrogen and hydride profiles after 100 years, for a total hydrogen concentration of 100 wt.ppm and a factor 8 for the diffusion coefficient.	175
3.54 Hydrogen and hydride profiles after 100 years, for a total hydrogen concentration of 100 wt.ppm and a factor 10 for the diffusion coefficient.	176
3.55 Hydrogen and hydride profiles after 100 years, for a total hydrogen concentration of 50 wt.ppm and the reference diffusion coefficient.	177
3.56 Hydrogen and hydride profiles after 100 years, for a total hydrogen concentration of 50 wt.ppm and a factor 4 for the diffusion coefficient.	177
3.57 Hydrogen and hydride profiles after 100 years, for a total hydrogen concentration of 50 wt.ppm and a factor 8 for the diffusion coefficient.	178

LIST OF FIGURES

3.58 Hydrogen and hydride profiles after 100 years, for a total hydrogen concentration of 50 wt.ppm and a factor 10 for the diffusion coefficient.	178
5.1 Correlation to ϵ_{int}	206
5.2 Correlation to $\epsilon_{cask,o}$	207
5.3 Correlation to $\epsilon_{cask,i}$	208
5.4 Correlation to P_{tot}	209
5.5 Correlation to T_{room}	210
5.6 Correlation to λ_{GGG}	211
5.7 Correlation to λ_{PE}	212
5.8 Correlation to λ_{BE}	213
5.9 Correlation to λ_{He}	214
5.10 Correlation to h_{surf}	215
5.11 Summary of input options printed in the output file of COBRA-SFS.	219
5.12 Numbering of the channels and rods of a 18x18-24 fuel assembly.	224
5.13 Surfaces to take into account for the description of the first radiative heat transfer group, corresponding to FA 20-32.	231
5.14 Plenum modelling in a COBRA-SFS cask model. Taken from [19].	237
5.15 First symmetry maps.	241
5.16 Error in group SLAB responsible for the local mismatches in the symmetry of the temperature distribution.	242

5.17 Second symmetry maps.	243
5.18 Localisation of nodes 600 and 610 affected by the error in group BDRY.	244
5.19 Third symmetry maps.	245
5.20 Localization of the error responsible for the low West-East gradient.	246
5.21 Fourth symmetry maps.	247
5.22 Part of COBRA-SFS output file summarizing the solid node information.	248
5.23 Further page from the summary of the solid node information, including node 424.	249

List of Tables

1.1	Main temperature dependent phenomena affecting the cladding at the different steps of the fuel assembly life.	5
2.1	Thermal conductivity λ [$\text{W m}^{-1} \text{K}^{-1}$] of some materials at 20 °C and 1 bar [23].	8
2.2	Correlations for free convection from various surfaces to air at atmospheric pressure [24].	15
2.3	Parameters used in the Python semi-analytical model.	28
2.4	Parameters used in the sensitivity analysis of the Python model.	34
2.5	Summary of input groups for COBRA-SFS [19].	45
2.6	Impact of the gap thicknesses on the temperature of the central fuel assembly.	63
2.7	Temperatures in the CASTOR [®] cask for different loading schemes.	71
2.8	Temperatures in the CASTOR [®] cask for loadings involving special fuel assemblies.	74
3.1	Characteristic length of diffusion at different temperatures and for different diffusion times. [68]	114
3.2	TSS _D /TSS _P database references.	117

3.3	Composition [wt.%] of Zircaloy-2, Zircaloy-4, Zr-2.5Nb, M5 [®] , N18 and HiFi [®] . [85–92]	119
3.4	Arrhenius fit functions for TSS _D and TSS _P calculated with the ODR method. The standard deviations are indicated for each coefficient.	132
3.5	Parameters used in the reproduction of the HNGD model. [10, 107]	139
3.6	Effect of hydrogen diffusion on a rod with 100 wt.ppm hydrogen: humps and dips after 100 years of storage for different diffusion coefficients.	176
3.7	Effect of hydrogen diffusion on a rod with 50 wt.ppm hydrogen: humps and dips after 100 years of storage for different diffusion coefficients.	179

Nomenclature

Latin symbols

$C_{diss/prec}$	Concentration (dissolved/precipitated)	wt.ppm
D	Diffusion coefficient	$\text{m}^2 \text{s}^{-1}$
D_e	Hydraulic diameter	m
E	Activation energy	J mol^{-1}
K_{Ic}	Fracture toughness	$\text{MPa m}^{-1/2}$
Nu	Nusselt number	-
Pr	Prandtl number	-
Q^*	Heat of transport	J mol^{-1}
R	Gas constant	$8.3145 \text{ J mol}^{-1}$
Re	Reynolds number	-
$r_{x,y}$	Pearson's correlation coefficient	-
T	Temperature	K
$wt.ppm$	Weight ppm	mg kg^{-1}

Greek symbols

λ	Thermal conductivity	$\text{W m}^{-1} \text{K}^{-1}$
σ	Stefan-Boltzmann constant	$5.67 \cdot 10^{-8} \text{ W m}^{-2} \text{K}^{-4}$

π	Pi	-
ϵ	Emissivity	-
ρ	Density	kg m^{-3}

Mathematical symbols and operators

$ x $	Absolute value of x
\bar{x}	Mean value of x
$cov(X, Y)$	Covariance of variables X and Y
$var(X)$	Variance of X
$\sigma(X)$	Standard deviation of X
\hat{Y}	Estimator of Y
$\text{div}(\vec{x})$	Divergence of \vec{x}
$\overrightarrow{\text{grad}} x$ or $\vec{\nabla} x$	Gradient of x
Δx	Laplacian of x (divergence of the gradient)
\mathbb{R}^1	Set of real numbers
\mathbb{R}^p	p-dimensional vector space over the field of the real numbers

Indices

alum	Aluminium
bottom	Bottom (of the rod)
clad	Cladding
cond	Conductive
conv	Convective
diss	Dissolved

NOMENCLATURE

eq	Equivalent
ext	External
gap	Gap (between two distinct elements)
GGG	Ductile cast iron (globularer Grauguss in German)
GT	Guide tube
HM	Heavy metal
int	Internal
max	Maximum
par	Parietal
PE	Polyethylene
prec	Precipitated
prod	Produced
rad	Radiative
room	Room (temperature)
th	Thermal
top	Top (of the rod)
tot	Total
vol	Volumetric
SS	Solid solution
surf	Surface

Abbreviations

BISON	Finite element-based nuclear fuel performance code (INL)
BTCS	Backward Time Centered Space
BWR	Boiling Water Reactor
CANDU	CANada Deuterium Uranium

CASTOR [®]	Cask for storage and transport of radioactive material, GNS trademark
CFD	Computational Fluid Dynamics
COBRA-SFS	COoling & Boiling in Rod Arrays - Spent Fuel Storage
COCOSYS	Containment Code System
DBTT	Ductile-to-Brittle Transition Temperature
DEM	Dynamic Elastic Modulus
DOE	US Department Of Energy
DSC	Differential Scanning Calorimetry
EDF	Electricité De France
EPRI	Electric Power Research Institute (USA)
ESCP	Extended Storage Collaboration Program
FA	Fuel Assembly
FTCS	Forward Time Centered Space
GNS	Gesellschaft für Nuklear-Service mbH (Germany)
GRS	Gesellschaft für Anlagen- und Reaktorsicherheit (GRS) gGmbH (Germany)
HCP	Hexagonal Close-Packed
HiFi [®]	Registered trademark for zirconium alloy by Westinghouse
HighFeZry	Zirconium alloy with relatively high iron content
HNGD	Hydride Nucleation-Growth-Dissolution
IAEA	International Atomic Energy Agency
INL	Idaho National Laboratory (USA)
IRSN	Institut de Radioprotection et de Sûreté Nucléaire (France)
LWR	Light Water Reactor
MOX	Mixed Oxide fuel
M5 [®]	Registered trademark for zirconium alloy by Framatome
N18	Zirconium alloy type developed in China

NOMENCLATURE

NFI	Nuclear Fuel Industries, Ltd. (Japan)
NIST	National Institute of Standards and Technology (USA)
NPP	Nuclear Power Plant
NRC	Nuclear Regulatory Commission (USA)
ODR	Orthogonal Distance Regression
PE	Polyethylene
PNNL	Pacific Northwest National Laboratory (USA)
ppm	parts per million
PWR	Pressurized Water Reactor
RBMK	Реактор Большой Мощности Канальный
resp.	Respectively
TESPA-ROD	Temperature and Strain Probabilistic Analysis, fuel performance code developed by GRS
TSS	Terminal Solid Solubility
TSS _D	Terminal Solid Solubility for dissolution
TSS _P	Terminal Solid Solubility for precipitation
XRD	X-Ray Diffraction
Zr	Zirconium
Zr-2.5Nb	Zirconium alloy with 2.5% Niobium
Zry-2	Zircaloy-2, zirconium alloy used for BWR fuel cladding
Zry-4	Zircaloy-4, zirconium alloy used for PWR fuel cladding

Bibliography

- [1] Bertrand Barré, Pascal Anzieu, Richarch Lenain, and Jean-Baptiste Thomas. Nuclear Reactor Systems: A technical, historical and dynamic approach. EDP Sciences, 2021.
- [2] Commissariat à l'énergie atomique (CEA). Nuclear fuels. DEN Monographs. Le Moniteur, 2009.
- [3] Storage of nuclear spent fuel: concepts and safety issues. Technical report, IRSN, June 2018. IRSN Report No 2019-00181.
- [4] M. Péridis and M. Stuke. Comparison of numerical and semi-analytical analyses of temperature fields of loaded dry casks. Kerntechnik, 85:444–451, 2020.
- [5] Donghak Kook, Jongwon Choi, Juseong Kim, and Yongsoo Kim. Review of Spent Fuel Integrity Evaluation for Dry Storage. Nuclear Engineering and Technology, 45(1):115–124, 2013.
- [6] Brady Hanson, Halim Alsaed, Christine Stockman, David Enos, Ryan Meyer, and Ken Sorenson. Gap Analysis to Support Extended Storage of Used Nuclear Fuel, Rev. 0. Technical report, US Department of Energy, January 2012. Used Fuel Disposition Campaign, PNNL-20509.
- [7] Melissa Teague, Sylvia Saltzstein, Brady Hanson, Ken Sorenson, and Goeff Freeze. Gap Analysis to Guide DOE R&D in Supporting Extended Storage and Transportation of Spent Nuclear Fuel: An FY2019 Assessment. Technical report, US Department of Energy, December

-
2019. Spent Fuel and Waste Science and Technology, SAND2019-15479R.
- [8] Peter Kaufholz, Maik Stuke, Felix Boldt, and Marc Péridis. Influence of kinetic effects on terminal solid solubility of hydrogen in zirconium alloys. Journal of Nuclear Materials, 510:277–281, 2018.
- [9] E. Lacroix, A.T. Motta, and J.D. Almer. Experimental determination of zirconium hydride precipitation and dissolution in zirconium alloy. Journal of Nuclear Materials, 509:162–167, 2018.
- [10] Florian Passelaigue, Evrard Lacroix, Giovanni Pastore, and Arthur T. Motta. Implementation and Validation of the Hydride Nucleation-Growth-Dissolution (HNGD) model in BISON. Journal of Nuclear Materials, 544:152683, 2021.
- [11] Mahmut N. Cinbiz, Donald A. Koss, and Arthur T. Motta. The influence of stress state on the reorientation of hydrides in a zirconium alloy. Journal of Nuclear Materials, 477:157–164, 2016.
- [12] Ji-Min Lee, Ho-A. Kim, Dong-Hak Kook, and Yong-Soo Kim. A study on the effects of hydrogen content and peak temperature on threshold stress for hydride reorientation in Zircaloy-4 cladding. Journal of Nuclear Materials, 509:285–294, 2018.
- [13] Kimberly B. Colas. Fundamental Experiments on Hydride Reorientation in Zircaloy. PhD thesis, The Pennsylvania State University, 2012.
- [14] Arthur T. Motta, Laurent Capolungo, Long-Qing Chen, Mahmut Nedim Cinbiz, Mark R. Daymond, Donald A. Koss, Evrard Lacroix, Giovanni Pastore, Pierre-Clément A. Simon, Michael R. Tonks, Brian D. Wirth, and Mohammed A. Zikry. Hydrogen in zirconium alloys: A review. Journal of Nuclear Materials, 518:440–460, 2019.
- [15] GNS Gesellschaft für Nuklear-Service mbH. <https://www.gns.de/language=en/24394>, last accessed on 22.01.2022.

- [16] D.R. Rector, C.L. Wheeler, and N.J. Lombardo. COBRA-SFS: A Thermal-Hydraulic Analysis Computer Code - Volume I: Mathematical Models and Solution Method, November 1986.
- [17] D.R. Rector, J.M. Cuta, N.J. Lombardo, T.E. Michener, and C.L. Wheeler. COBRA-SFS: A Thermal-Hydraulic Analysis Computer Code - Volume II: User's Manual, November 1986.
- [18] N.J. Lombardo, J.M. Cuta, T.E. Michener, D.R. Rector, and C.L. Wheeler. COBRA-SFS: A Thermal-Hydraulic Analysis Computer Code - Volume III: Validation Assessments, December 1986.
- [19] T.E. Michener, J.M. Cuta, D.R. Rector, and H.E. Jr. Adkins. COBRA-SFS: A thermal-hydraulic analysis code for spent fuel storage and transportation casks, Cycle 4a, October 2017.
- [20] James Fort, Brady Hanson, and David Richmond. International Thermal Modeling Benchmark Description for a High-Burnup Used Fuel Dry Storage System. Technical report, Electric Power Research Institute (EPRI), November 2020. An Extended Storage Collaboration Program Activity, Technical Report 3002018498, <https://www.epri.com/research/products/000000003002018498>, last accessed on 25.02.2022.
- [21] Evrard Lacroix. Modeling Zirconium Hydride Precipitation and Dissolution in Zirconium Alloys. PhD thesis, The Pennsylvania State University, 2019.
- [22] Clément Lemaignan. Science des matériaux pour le nucléaire. Génie Atomique. EDP Sciences, 2004.
- [23] J. Carvill. 3 - Thermodynamics and heat transfer. In J. Carvill, editor, Mechanical Engineer's Data Handbook, pages 102–145. Butterworth-Heinemann, Oxford, 1993.
- [24] J.P. Holman. Heat Transfer - Tenth Edition. McGraw-Hill, 2010.

- [25] Philip Kosky, Robert Balmer, William Keat, and George Wise. Chapter 14 - Mechanical Engineering. In Exploring Engineering (Fifth Edition), pages 317–340. Academic Press, 2021.
- [26] Isidoro Martínez. Radiative View Factors, 2021. <http://webserver.dmt.upm.es/~isidoro/tc3/Radiation%20View%20factors.pdf>, last accessed on 23.10.2021.
- [27] R. Weh and W. Sowa. Advanced techniques for storage and disposal of spent fuel from commercial nuclear power plants, July 1999.
- [28] GNS Gesellschaft für Nuklear-Service mbH. CASTOR[®] V/19 Transport und Lagerbehälter für Brennelemente (DWR), 2019. Produkt Infoblatt.
- [29] J. Stewering, S. Schwarz, and M. Sonnenkalb. Berechnung der Brennstabhüllrohrtemperaturen in einem generischen Transport- und Lagerbehälter. Technical report, GRS, April 2014. GRS - A - 3739.
- [30] André Leber, Wilhelm Graf, and Roland Hüggenberg. Validation of CFD-Methods to Predict Heat Transfer and Temperatures during the Transport and Storage of Casks under a Cover. September 2004.
- [31] R. Diersch, G Dreier, and H. Stelzer. CASTOR V - The Package System for Transport and Storage of Spent Fuel Assemblies. <http://archive.wmsym.org/1997/sess18/18-05.htm>, last accessed on 27.01.2022.
- [32] Regulations for the Safe Transport of Radioactive Material, 2018. IAEA Safety Standards, No. SSR-6 (Rev. 1).
- [33] Title 10 of the Code of Federal Regulations (10 CFR), 2020. Part 71 - Packaging and Transportation of Radioactive Material, Section 73.
- [34] The NumPy community. NumPy v1.21 Manual, numpy.corrcoef. <https://numpy.org/doc/stable/reference/generated/numpy.corrcoef.html>, last accessed on 13.12.2021.

- [35] H. Hayashi, K. Ogata, T. Baba, and K. Kamimura. The Correlation Coefficient: An Overview. Critical Reviews in Analytical Chemistry, 36(1):41–59, 2006.
- [36] The SciPy community. SciPy documentation v1.7.1, `scipy.stats.linregress`. <https://docs.scipy.org/doc/scipy/reference/generated/scipy.stats.linregress.html>, last accessed on 13.12.2021.
- [37] National Institute of Standards and Technology (NIST), U.S. Department of Commerce. NIST Chemistry Webbook, Thermophysical Properties of Fluid Systems. <https://webbook.nist.gov/chemistry/fluid/>, last accessed on 24.11.2021.
- [38] Felix Boldt and Maik Stuke. Benchmark for thermo-mechanical fuel rod behaviour during dry storage - Specifications Version 3, December 2019.
- [39] U. Hesse, W. Denk, and H. Deitenbeck. OREST - eine direkte Kopplung von HAMMER und ORIGEN zur Abbrandsimulation von LWR-Brennstoffen. Technical report, GRS, November 1986. GRS - 63.
- [40] W. Klein-Heßling, S. Arndt, G. Weber, H. Wolff, S. Schwarz, and C. Spengler. COCOSYS - Short description, May 2008. https://www.grs.de/sites/default/files/fue/COCOSYS%20Kurzbeschreibung_Shortdescription.pdf, last accessed on 28.11.2021.
- [41] Ansys CFX. <https://www.ansys.com/products/fluids/ansys-cfx>, last accessed on 28.11.2021.
- [42] M. Péridis, F.-N. Sentuc, M. Sonnenkalb, J. Stewering, and M. Stuke. Analysis of 3-dimensional temperature fields of loaded dry storage casks, Proceedings of the 19th International Symposium on the Packaging and Transportation of Radioactive Materials (PATRAM). August 2019.

-
- [43] GNS. Behälterbeladung. <https://www.gns.de/language=de/21562/behaelterbeladung>, last accessed on 10.10.2021.
- [44] M. Higley, M. Hadj-Nacer, and M. Greiner. Temperature Prediction of a TN-32 Cask with Non-Concentric Basket Subjected to Vacuum Drying, proceedings of the 19th International Symposium on the Packaging and Transportation of Radioactive Materials (PATRAM). August 2019.
- [45] 2. Technology Systems Manual. Section 3.1 - Reactor Vessel and Internals. <http://www.nrc.gov/docs/ML1122/ML11223A212.pdf>, last accessed on 24.11.2021.
- [46] David Richmond and Maik Stuke. International Thermal Benchmark Activity Initial Results and Updates, November 2021. ESCP Winter Meeting.
- [47] Jean-Marc Delhaye. Thermohydraulique des réacteurs. Génie Atomique. EDP Sciences, 2013.
- [48] Y.-E. Kim, J.-W. Park, and J. Cleveland. Thermophysical properties database of materials for light water reactors and heavy water reactors. Technical report, IAEA, June 2006.
- [49] S. Yagnik, R. Yang, and E. Kolstad. In-pile determination of zirconium oxide thermal conductivity using LWR cladding. Technical report, Halden, 1998. HPR-349, INIS Vol. 35, Issue 23.
- [50] M. Murabayashi, S. Tanaka, and Y. Takahashi. Thermal Conductivity and Heat Capacity of Zircaloy-2, -4 and Unalloyed Zirconium. Journal of Nuclear Science and Technology, 477:661–662, 1975.
- [51] K.E. Gilchrist. Thermal property measurements on Zircaloy-2 and associated oxide layers upto 1200 °C. Journal of Nuclear Materials, 62(2):257–264, 1976.
- [52] Commissariat à l'énergie atomique (CEA). Corrosion and Alteration of Nuclear Materials. DEN Monographs. Le Moniteur, 2010.

- [53] Franck Bigot. Avis IRSN N° 2014-000032. 30/01/2014.
- [54] Marcio Soares Dias, João Roberto De Mattos, and Edison Andrade. The Gd-isotopic fuel for high burnup in PWR's. October 2017.
- [55] H. Hayashi, K. Ogata, T. Baba, and K. Kamimura. Research Program to Elucidate Outside-in Failure of High Burnup Fuel Cladding. Journal of Nuclear Science and Technology, 43(9):1128–1135, 2006.
- [56] S. Fourgeaud, J. Desquines, M. Petit, C. Getrey, and G. Sert. Mechanical characteristics of fuel rod claddings in transport conditions. Packaging, Transport, Storage & Security of Radioactive Material, 20(2):69–76, 2009.
- [57] R.N Singh, R Kishore, S.S Singh, T.K Sinha, and B.P Kashyap. Stress-reorientation of hydrides and hydride embrittlement of Zr–2.5 wt% Nb pressure tube alloy. Journal of Nuclear Materials, 325(1):26–33, 2004.
- [58] S.I. Hong and K.W. Lee. Stress-induced reorientation of hydrides and mechanical properties of Zircaloy-4 cladding tubes. Journal of Nuclear Materials, 340(2):203–208, 2005.
- [59] Masaki Aomi, Toshikazu Baba, Toshiyasu Miyashita, Katsuichiro Kamimura, Takayoshi Yasuda, Yasunari Shinohara, Toru Takeda, Magnus Limback, Bruce Kammenzind, and S. Dean. Evaluation of Hydride Reorientation Behavior and Mechanical Properties for High-Burnup Fuel-Cladding Tubes in Interim Dry Storage. Journal of Astm International, 5, October 2008.
- [60] M.C. Billone, T.A. Burtseva, Z. Han, and Y.Y. Liu. Embrittlement and DBTT of High Burnup PWR Fuel Cladding Alloys. Technical report, Argonne National Laboratory, 2013.
- [61] R.N. Singh, R. Lala Mikin, G.K. Dey, D.N. Sah, I.S. Batra, and P. Stähle. Influence of temperature on threshold stress for reorientation of hydrides and residual stress variation across thickness of Zr–2.5Nb alloy pressure tube. Journal of Nuclear Materials, 359(3):208–219, 2006.

- [62] Hyun-Jin Cha, Ki-Nam Jang, Ji-Hyeong An, and Kyu-Tae Kim. The effect of hydrogen and oxygen contents on hydride reorientations of zirconium alloy cladding tubes. Nuclear Engineering and Technology, 47(6):746–755, 2015.
- [63] Ju-Jin Won, Su-Jeong Min, and Kyu-Tae Kim. Cooldown-Induced Hydride Reorientation of Hydrogen-Charged Zirconium Alloy Cladding Tubes. Metals and Materials International, 21:31–42, 2015.
- [64] V. Tikare, P. Weck, P. Schultz, B. Clark, J. Mitchell, M. Glazoff, and E. Homer. Documentation of Hybrid Hydride Model for Incorporation into Moose-Bison and Validation Strategy. Technical report, Sandia National Laboratories, August 2014. FCRD-UFD-2014-000063 Rev. 0.
- [65] R.L. Beck. Zirconium-Hydrogen Phase System. Am. Soc. Metals, Trans. Quart., 55, 1962.
- [66] J.J. Kearns. Terminal solubility and partitioning of hydrogen in the alpha phase of zirconium, Zircaloy-2 and Zircaloy-4. Journal of Nuclear Materials, 22(3):292–303, 1967.
- [67] A. Sawatzky and B.J.S. Wilkins. Hydrogen solubility in zirconium alloys determined by thermal diffusion. Journal of Nuclear Materials, 22(3):304–310, 1967.
- [68] A. Sawatzky. The diffusion and solubility of hydrogen in the alpha phase of Zircaloy-2. Journal of Nuclear Materials, 2(1):62–68, 1960.
- [69] G.F. Slattery. The Terminal Solubility of Hydrogen in Zirconium Alloys between 30 and 400 °C. Journal of the Institute of Metals, 43-7, 95, 1967.
- [70] B.F. Kammenzind, D.G. Franklin, W.J. Duffin, and H.R. Peters. Hydrogen pickup and redistribution in alpha-annealed Zircaloy-4. June 1996.

- [71] Z.L. Pan, I.G. Ritchie, and M.P. Puls. The terminal solid solubility of hydrogen and deuterium in Zr-2.5Nb alloys. Journal of Nuclear Materials, 228(2):227–237, 1996.
- [72] A. McMinn, E.C. Darby, and J.S. Schofield. The Terminal Solid Solubility of Hydrogen in Zirconium Alloys. Zirconium in the Nuclear Industry: 12th International Symposium, pages 173–195, January 2000.
- [73] P Vizcaíno, A.D Banchik, and J.P Abriata. Solubility of hydrogen in Zircaloy-4: irradiation induced increase and thermal recovery. Journal of Nuclear Materials, 304(2):96–106, 2002.
- [74] K. Une and S. Ishimoto. Dissolution and precipitation behavior of hydrides in Zircaloy-2 and high Fe Zircaloy. Journal of Nuclear Materials, 322(1):66–72, 2003.
- [75] Katsumi Une and Shinji Ishimoto. Terminal Solid Solubility of Hydrogen in Unalloyed Zirconium by Differential Scanning Calorimetry. Journal of Nuclear Science and Technology, 41:949–952, September 2004.
- [76] R.N. Singh, S. Mukherjee, Anuja Gupta, and S. Banerjee. Terminal solid solubility of hydrogen in Zr-alloy pressure tube materials. Journal of Alloys and Compounds, 389(1):102–112, 2005.
- [77] K. Une, S. Ishimoto, Y. Etoh, K. Ito, K. Ogata, T. Baba, K. Kamimura, and Y. Kobayashi. The terminal solid solubility of hydrogen in irradiated Zircaloy-2 and microscopic modeling of hydride behavior. Journal of Nuclear Materials, 389(1):127–136, 2009. Thermochemistry and Thermophysics of Nuclear Materials.
- [78] Rui Tang and Xiaoxue Yang. Dissolution and precipitation behaviors of hydrides in N18, Zry-4 and M5 alloys. International Journal of Hydrogen Energy, 34(17):7269–7274, 2009. IWBT 2008.
- [79] O. Zanellato, M. Preuss, J.-Y. Buffiere, F. Ribeiro, A. Steuwer, J. Desquines, J. Andrieux, and B. Krebs. Synchrotron diffraction

- study of dissolution and precipitation kinetics of hydrides in Zircaloy-4. Journal of Nuclear Materials, 420(1):537–547, 2012.
- [80] Ju-Seong Kim and Yong-Soo Kim. Effect of thermal history on the terminal solid solubility of hydrogen in Zircaloy-4. International Journal of Hydrogen Energy, 39(29):16442–16449, 2014.
- [81] M.S. Blackmur, J.D. Robson, M. Preuss, O. Zanellato, R.J. Cernik, S.-Q. Shi, F. Ribeiro, and J. Andrieux. Zirconium hydride precipitation kinetics in Zircaloy-4 observed with synchrotron x-ray diffraction. Journal of Nuclear Materials, 464:160–169, 2015.
- [82] Katsumi Une, Kazuhiro Nogita, Shinji Ishimoto, and Keizo Ogata. Crystallography of Zirconium Hydrides in Recrystallized Zircaloy-2 Fuel Cladding by Electron Backscatter Diffraction. Journal of Nuclear Science and Technology, 41:731–740, July 2004.
- [83] Marie-Noëlle Sanz, Bernard Salamito, Sylvie Corbel-Copin, Anne-Emmanuelle Badel, and Stéphane Cardini. Physique : Tout-en-un - 2^e année PC-PSI. J'intègre (Paris). Dunod, 2004.
- [84] G P Marino. HYDIZ: a 2-dimensional computer program for migration of interstitial solutes of finite solubility in a thermal gradient (LWBR Development Program). June 1974.
- [85] A. Kecek, K. Tuček, S. Holmström, and P. Van Uffelen. Development of M5 Cladding Material Correlations in the TRANSURANUS Code: Revision 1. Technical report, JRC, 2016. JRC100644, EUR 28366 EN.
- [86] J.M. Wright, M. Limbäck, D. Schrire, M. Owaki, and M. Nilsson. Commercial introduction and experience with the advanced high iron cladding HiFi[®] in Boiling Water Reactors, Proceedings of the TOP-FUEL 2018 conference, Prague, Czech Republic. 30 September - 4 October 2018.
- [87] C. Song. Irradiation effects on Zr-2.5Nb in power reactors. CNL Nuclear Review, 5(1):17–36, 2016.

- [88] B.X. Zhou, M.Y. Yao, Z.K. Li, X.M. Wang, J. Zhou, C.S. Long, Q. Liu, and B.F. Luan. Optimization of N18 Zirconium Alloy for Fuel Cladding of Water Reactors. Journal of Materials Science & Technology, 28(7):606–613, 2012.
- [89] Clément Lemaignan and Arthur Motta. Zirconium Alloys in Nuclear Applications, volume 10. September 2006.
- [90] Shannon M. Bragg-Sitton. Advanced LWR Nuclear Fuel Cladding System Development: Technical Program Plan, Revision 1. Technical report, Idaho National Laboratory, December 2012. INL/MIS-12-25696.
- [91] Hans G. Weidinger. Zr-Alloy, the Nuclear Material for Water Reactor Fuel. A Survey and Update with Focus on Fuel for Pressurized Water Reactor Systems. 17-21 September 2007. 7th International Conference on WWER Fuel Performance, Modelling and Experimental Support.
- [92] Western Alloys. Zr-Sn-Nb Alloys. <https://www.tantalum-niobium.com/zirconium/zr-sn-nb-alloy.html>, last accessed on 12.02.2022.
- [93] C.L. Whitmarsh. Review of Zircaloy-2 and Zircaloy-4 Properties Relevant to N.S. Savannah Reactor Design. July 1962.
- [94] Liliana I. Duarte, Francesco Fagnoni, Robert Zubler, Weijia Gong, Pavel Trtik, and Johannes Bertsch. Effect of the inner liner on the hydrogen distribution of zircaloy-2 nuclear fuel claddings. Journal of Nuclear Materials, 557:153284, 2021.
- [95] Framatome. M5 Advanced Cladding, World Class Material Designed for Unmatched Corrosion Resistance and Hydrogen Uptake. <https://www.framatome.com/solutions-portfolio/docs/default-source/default-document-library/product-sheets/a0532-p-us-g-en-037-05-18-m5.pdf>, last accessed on 14.01.2022.
- [96] K. Kakiuchi, K. Ohira, N. Itagaki, Y. Otsuka, Y. Ishii, and A. Miyazaki. Irradiated Behavior at High Burnup for HiFi Alloy. Journal of Nuclear Science and Technology, 43(9):1031–1036, 2012.

-
- [97] Westinghouse. TRITON11TM Westinghouse 11x11 BWR fuel design. https://www.westinghousenuclear.com/Portals/0/Triton%20A4_v7.pdf, last accessed on 13.01.2022.
- [98] ASTM International. Standard Test Method for Dynamic Young's Modulus, Shear Modulus, and Poisson's Ratio by Sonic Resonance, 2008. ASTM Standards, E 1875-08.
- [99] Z.L. Pan, N. Wang, and Z. He. Measurements of elastic modulus in Zr alloys for CANDU applications, 2010. 11th International Conference on CANDU Fuel, Niagara Falls, Ontario, Canada, October 17-20.
- [100] M. N. Cinbiz, D. A. Koss, A. T. Motta, J.-S. Park, and J. D. Almer. In situ synchrotron X-ray diffraction study of hydrides in Zircaloy-4 during thermomechanical cycling. Journal of Nuclear Materials, 487:247–259, 2017.
- [101] R. S. Daum, Y. S. Chu, and A. T. Motta. Identification and quantification of hydride phases in Zircaloy-4 cladding using synchrotron x-ray diffraction. Journal of Nuclear Materials, 392:453–463, 2009.
- [102] The SciPy community. Orthogonal distance regression (scipy.odr). <https://docs.scipy.org/doc/scipy/reference/odr.html>, last accessed on 30.01.2022.
- [103] Paul T. Boggs, Richard H. Byrd, Janet E. Rogers, and Robert B. Schnabel. User's Reference Guide for ODRPACK Version 2.01, Software for Weighted Orthogonal Distance Regression, June 1992.
- [104] Paul T. Boggs, Richard H. Byrd, and Robert B. Schnabel. A stable and efficient algorithm for nonlinear orthogonal distance regression. SIAM Journal on Scientific and Statistical Computing, 8(6):1052–1078, 1987.
- [105] K. Madsen, H.B. Nielsen, and O. Tingleff. Methods for non-linear least squares problems, 2nd Edition, April 2004.
- [106] Antonio Faleiros, T.N. Rabelo, Gilmar Thim, and Marinalva Oliveira. Kinetics of Phase Change. Materials Research, 3, July 2000.

- [107] Idaho National Laboratory. BISON-Specific Input Syntax and Reference Manual. https://mooseframework.inl.gov/bison/syntax/bison_only_index.html, last accessed on 21.01.2022.
- [108] Tsegaye Simon and Purnachandra Rao Koya. Application of Some Finite Difference Schemes for Solving One Dimension Diffusion Equation. American Scientific Research Journal for Engineering, Technology, and Sciences (ASRJETS), 27(1):140–154, 2016.
- [109] Westfälische Wilhelms-Universität Münster, Institut für Theoretische Physik. Chapter 7 - The Diffusion Equation. https://www.uni-muenster.de/imperia/md/content/physik_tp/lectures/ws2016-2017/num_methods_i/heat.pdf, last accessed on 18.01.2022.
- [110] Oliver Ong. Review of finite-difference schemes for the 1D heat/diffusion equation. <https://oliver-ong.github.io/Papers/Heat-diffusion%20-%20Review%20of%20finite-difference%20schemes.pdf>, last accessed on 18.01.2022.
- [111] GRS gGmbH. TESPA-ROD: Temperature, Strain and Pressure Analysis of a fuel ROD. Contact: Felix Boldt, <https://www.grs.de/en/research-and-assessment/reactor-safety/tespa-rod-temperature-strain-and-pressure-analysis-fuel-rod>, last accessed on 20.01.2022.
- [112] F. Boldt. Implementation of Hydrogen Solid Solubility Data and Precipitation Threshold Stresses in the Fuel Rod Code TESPA-ROD. Journal of Engineering and Radiation Science, 5(2), April 2019. ASME.
- [113] High-Burnup Dry Storage Cask Research and Development Project - Final Test Plan. Technical report, Electric Power Research Institute (EPRI), February 2014. Contract No.: DE-NE-0000593.
- [114] S.J. Saltzstein, K.B. Sorenson, B.D. Hanson, R.W. Shimskey, N.A. Klymyshyn, R.A. Webster, P.J. Jensen, P.J. MacFarlan, M. Billone,

J. Scaglione, R. Montgomery, and B. Bevard. EPRI/DOE High-Burnup Fuel Sister Rod Test Plan Simplification and Visualization. Technical report, US Department of Energy, September 2017. Spent Fuel and Waste Science and Technology, SAND2017-10310R.